1-1-2014

Applications of EPR with an Emphasis on Tau Fibril Structure

Virginia Meyer
University of Denver

Applications of EPR with an Emphasis on Tau Fibril Structure

_____

A Dissertation

Presented to

the Faculty of Natural Sciences and Mathematics

University of Denver

_____

In Partial Fulfillment

of the Requirements for the Degree

Doctor of Philosophy

_____

By

Virginia Meyer

June 2014

Advisor: Martin Margittai

Author: Virginia Meyer
Title: Applications of EPR with an Emphasis on Tau Fibril Structure
Advisor: Martin Margittai
Degree Date: June 2014

Abstract

Substances containing unpaired electrons have been studied by electron paramagnetic resonance (EPR) for nearly 70 years. With continual development and enhancement of EPR techniques, questions have arisen regarding optimum method selection for a given sample based on its properties. In this work, radiation defects, natural lattice defects, solid organic radicals, radicals in solution, and spin-labeled proteins were analyzed using CW, pulse, and rapid scan EPR to compare methods. Studies of solid BDPA, E′ in quartz, N_s^0 in diamond, and a-Si:H, showed that rapid scan could overcome many obstacles presented by other techniques, cementing rapid scan as an effective alternative to CW and pulse methods.

Relaxation times of six nitroxide radicals were characterized from 0.25-34 GHz, guiding synthesis of improved nitroxides for *in vivo* imaging experiments. Processes contributing to T_1 of DPPH in polystyrene were found through variable temperature measurements at X- and Q-band, resolving previously-reported discrepancies in relaxation properties and providing new insight into this commonly-used standard.

In the history of EPR, the study of proteins is relatively new. Double electron-electron resonance (DEER) has emerged as a powerful technique for the study of amyloid fibrils, a class of protein aggregates implicated in a number of neurodegenerative disorders. Microtubule-associated protein tau forms fibrils linked to Alzheimer's disease through seeded conversion of monomer. Self-assembly is

mediated by the microtubule binding repeats in tau, and there are either three or four repeats present depending on the isoform. DEER was used to show that filaments of 3R and 4R tau are conformationally distinct and that 4R fibrils adopt a heterogeneous mixture of conformations. Populations of 4R fibril conformations, which were independently validated using a model system, can be modulated by introduction of mutations to the primary sequence or by varying fibril growth conditions. These findings provided unprecedented insights into the seed selection of tau monomers and established conformational compatibility as an important driving force in tau fibril propagation.

Lastly, DEER acquisition was improved through addition of paramagnetic metal to spin-labeled protein, decreasing collection time, and through use of a novel spin label with increased T_2, thereby lengthening the available acquisition window.

Acknowledgements

I would like to thank Drs. Sandra and Gareth Eaton for welcoming me into their lab 4 years ago and for their continued support of my projects and generosity with EPR resources. Thank you especially for your advice on experimental design and data interpretation, and also for countless hours troubleshooting instrument issues and ensuring DEER experiments were performed without incident.

Thank you to Dr. Margittai for inviting me into his lab 2 ½ years ago; I have learned so much from the opportunities you have given me and am indebted to you for the successes we have seen studying tau fibrils using DEER.

The work described in this dissertation was financially supported through NIH R01 NS076619 awarded to Martin Margittai, NIH NIBIB EB000557 awarded to Gareth and Sandra Eaton, and NIH NIBIB P41 EB002034 awarded to Howard J. Halpern.

Thank you to Dr. Michael Swanson for teaching me DEER and providing continual advice and support. Also thanks to Dr. Ayisha Siddiqua for her patience and guidance as I learned the biochemistry techniques utilized in this dissertation. Thank you also to the colleagues who have made these projects possible, especially Drs. Deborah Mitchell, Joshua Biller, and Paul Dinkel and to Michael Holden for all of his hard work.

Lastly, I would like to acknowledge my family for their unwavering support as I completed my doctoral requirements. Thank you to my parents for their constant reassurance and positivity and to my husband, Matthew Krause, for keeping me balanced and encouraging me through every challenge I encountered over the past five years. Finally, thank you to my dogs, Boston and Eva, for making me smile every day.

Table of Contents

List of Tables

List of Figures

List of Abbreviations, Acronyms, and Constants

3R	3-repeat
4R	4-repeat
a	Scan rate
$\bar{A}$	Average nitrogen hyperfine
A	Hyperfine splitting
A_i	Nitrogen nuclear hyperfine
A_x	Coefficient of contribution to T_1
a-Si:H	Amorphous hydrogenated silicon
AWG	Arbitrary waveform generator
Aβ	Beta-amyloid peptide
B	Magnetic field, general
B*	Resonant magnetic field
B_0	Static magnetic field
B_1	Applied magnetic field
BCA	Bicinchoninic acid
BDPA	1,3-bisdiphenylene-2-phenylallyl
B_i	Applied magnetic field along x, y, or z axis
BL21 (DE3)	Expression-optimized *E. coli*
BW	Bandwidth
c′	Slip coefficient
CBD	Corticobasal degeneration

CCD	Charge-coupled device
CD	Circular dichroism
CLR	Cross loop resonator
CW	Continuous wave
C_α	Cysteine carbon attached to spin label
DEER	Double electron-electron resonance
DEFit	Dipolar evolution fitting
d_i	DEER time constants (i = 0, 1, 2, 3)
DNA	Deoxyribonucleic acid
DNP	Dynamic Nuclear Polarization
dNTP	Deoxinucleoside triphosphates
DpnI	Restriction enzyme
DPPH	2,2-diphenyl-1-picrylhydrazyl
DTPA	N-bis(2-(bis-(carboxymethyl)amino)ethyl)-glycine
DTT	Dithiothreitol
dx	DEER step size
E. coli	*Escherichia coli*
E′	Lattice defect in quartz
E_a	Activation energy
EB	Elution buffer
EDTA	Ethylenediaminetetraacetic acid
ELDOR	Electron double resonance

EM	Electron microscopy
ENDOR	Electron-nuclear double resonance
EPR	Electron paramagnetic resonance
E_z	Zeeman energy
FID	Free induction decay
FPT	Freeze-pump-thaw
FRET	Fluorescence resonance energy transfer
FWHM	Full-width at half maximum
g	g-value
g_e	Free-electron g-value
GLADD	Global analysis of DEER data
h	Plank's constant
Habc	Helical domain of syntaxin 1A
HEPES	4-(2-hydroxyethyl)-1-piperazineethanesulfonic acid
HS	High sensitivity
I	Nuclear spin
i.d.	Inner diameter
IPTG	Isopropyl-β-D-thiogalactopyranoside
IR	Inversion recovery
J	Total angular momentum quantum number
J(ω)	Spectral density function
J_8	Transport integral

k	Boltzmann's constant
L	Orbital angular momentum quantum number
LB	Lysogeny broth/Luria-Bertani
M_0	Net magnetization
MAPT	Gene encoding tau protein
mHCTPO	4-hydro-3-carbamoyl-2,2,5,5-tetra-perdeuteromethyl-pyrrolin-1-oxyl-d_{12}
M_i	Magnetization along x, y, or z axis
m_I	Nitrogen nuclear spin state
MOPS	3-(N-morpholino)propanesulfonic acid
m_s	Spin projection quantum number
MTSL	(1-oxyl-2,2,5,5-tetramethyl-Δ3-pyrroline-3-methyl)methanethiosulfonate
MW	Molecular weight
MWCO	Molecular weight cutoff
n	Number of symmetry equivalent nuclei
Nco1	Restriction enzyme
NFT	Neurofibrillary tangles
NMR	Nuclear magnetic resonance
N_s^0	Nitrogen substitution defect
N_x	Population of states
o.d.	Outer diameter
OD	Optical density
OX63	Methyl tris(8-carboxy-2,2,6,6-tetra(hydroxyethyl)-benzo(1,2-d:4,5 -d′)bis(1,3)-dithiol-4-yl)-tripotassium salt

P	Power
PAGE	Polyacrylamide gel electrophoresis
PCR	Polymerase chain reaction
PDB	Protein data bank
PDT	4-oxo-2,2,6,6-tetra-perdeuteromethyl-piperidinyl-oxyl-d_{16}
PELDOR	Pulsed ELDOR
PFU	*Pyrococcus furiosus* DNA polymerase
PIPES	Piperazine-*N*,*N*'-bis(2-ethanesulfonic acid)
PMCA	Protein misfolding cyclic amplification
ppb	Parts per billion
ppm	Parts per million
PSP	Progressive supranuclear palsy
Q	Resonator quality factor
r	Distance between spins
R	Gas constant
RNA	Ribonucleic acid
S	Total spin quantum number
SDS	Sodium dodecyl sulfate
SEM	Standard error of the mean
SHQ	Super high quality factor
SL	Spin label
SNARE	Soluble NSF attachment protein receptor

SNR	Signal-to-noise
SR	Saturation recovery
SRT	Shot repetition time
Syn	Syntaxin 1A
T	Temperature
T_1	Spin-lattice relaxation time
T_{1e}	Electron T_1
T_{1n}	Nuclear T_1
T_2	Spin-spin relaxation time
T4L	T4 Lysozyme
TEM	Transmission electron microscopy
TFA	Trifluoroacetic acid
ThT	Thioflavin T
T_m	Phase memory time
TPHIO	1,1,3,3-tetraphenylisoindolin-2-yloxyl
Tris	2-amino-2-hydroxymethyl-propane-1,3-diol
trityl	Triarylmethyl
TWT	Traveling-wave tube amplifier
UPEN	Uniform penalty
UV-Vis	Ultraviolet-visible
VHF	Very high frequency
w	Scan width

WT	Wild-type
Xho1	Restriction enzyme
XL1-blue	Transformation-optimized *E. coli*
α	Tikhonov fitting parameter
γ	Gyromagnetic ratio
ΔB_{pp}	Peak-to-peak linewidth
Δ_{loc}	Local mode energy gap
θ_D	Debye temperature
μ	Electron magnetic moment
μ_B	Bohr magneton
ν	Frequency
τ	Time between pulses
τ_c	Tumbling correlation time
τ_c^0	Pre-exponential factor
τ_p	Pulse length
τ_r	Resonator ringdown
τ_R	Rotational correlation time
ω	Larmor frequency

Chapter 1: Electron Paramagnetic Resonance

Electron paramagnetic resonance (EPR) is a spectroscopic technique capable of providing both qualitative and quantitative information about samples containing unpaired electrons as radicals or paramagnetic centers. A number of discrete EPR techniques have been developed to study properties of these samples, many of which were utilized for the work reported in this dissertation. Thorough examinations of these techniques can be found elsewhere, allowing a more concise introduction to be presented here.

1.1 Samples

EPR shares many of the same physical principles as nuclear magnetic resonance (NMR). Whereas NMR probes nuclear spin states of an atom, EPR is used to study electron spin. EPR samples must therefore contain an unpaired electron, a characteristic of transition state metals, lattice defects, and organic radicals. The experiments presented in this dissertation include a sampling of lattice defect centers and organic radicals. This research started as a comparison of EPR techniques for the study of a variety of samples to determine the most appropriate technique based on properties of the sample. Over time, the focus evolved to application of EPR to biological samples, including improvements to data acquisition. The overall motivation, therefore, is to characterize a variety of unique samples using the different EPR techniques available in the Eaton lab.

1.2 Techniques

Determining which EPR technique to employ for a specific sample requires an understanding of the properties of the sample, in addition to the relevant information to be gained from the analysis. Many physical properties differ between paramagnetic species, including stability, sensitivity to pH and O_2 concentration, relaxation times, number of spins/concentration/size, and lossiness [1]. Each of these factors guide selection of EPR method, which consequently includes choice of microwave frequency, resonator capabilities (e.g. dual frequency, high sensitivity, high *Q*, filling factor), and detection system. The techniques available in the Eaton lab are explained in the following sections, and Chapter 2 describes the instruments used to perform these experiments.

1.2.1 The EPR Signal

The EPR phenomenon is observable for systems with nonzero electron spin, S [2]. The spin exists in a defined energy level, and introduction of an external magnetic field, B_0, splits this energy into two states (Figure 1.1). This is called the Zeeman Effect. The lower energy state, or β state, corresponds to the energy associated with alignment of the projection of the net magnetization vector along the direction of the field. The higher energy state, or α state, corresponds to alignment of the spins against the magnetic field. An electron has $m_s = \pm ½$, where -½ describes the β states and +½ describes the α states. The separation between the states is called the Zeeman Energy:

$$\Delta E_Z = h\nu = g\mu_B B_0 \qquad (1.1)$$

As with any electromagnetic radiation, energy is proportional to frequency, ν, where h is Planck's constant. The Bohr magneton, μ_B, is a constant that describes the magnetic dipole moment of an electron. The g-value, g, describes the coupling of spin and orbital angular momentum according to the following equation:

$$g = 1 + \frac{J(J+1) + S(S+1) - L(L+1)}{2J(J+1)} \tag{1.2}$$

For a free electron, L = 0 and J = S, reducing Equation 1.2 to g = 2. Relativistically, g = 2.00232, and this value serves as a first approximation of the g-value for many radicals studied by EPR [3]. Local environments and anisotropy can have a substantial effect on the g-value and, subsequently, the resonant field and appearance of the EPR signal [2, 3]. Anisotropic g-values arise from anisotropic electron distributions and result in dependence of the EPR spectrum on orientation of the molecule within the magnetic field. A system with axial symmetry will have two g-values, $g_{\parallel}$ and $g_{\perp}$, while lower symmetry species have g-values that are different along each axis, g_{xx}, g_{yy}, and g_{zz} [3]. Anisotropy in g-values is averaged for rapidly tumbling radicals in solution. g-values are similar to chemical shifts in NMR spectroscopy and are likewise a tool for distinguishing between different samples [3, 4]. Table 1.1 provides g-values, isotropic and anisotropic, for the samples studied in this work.

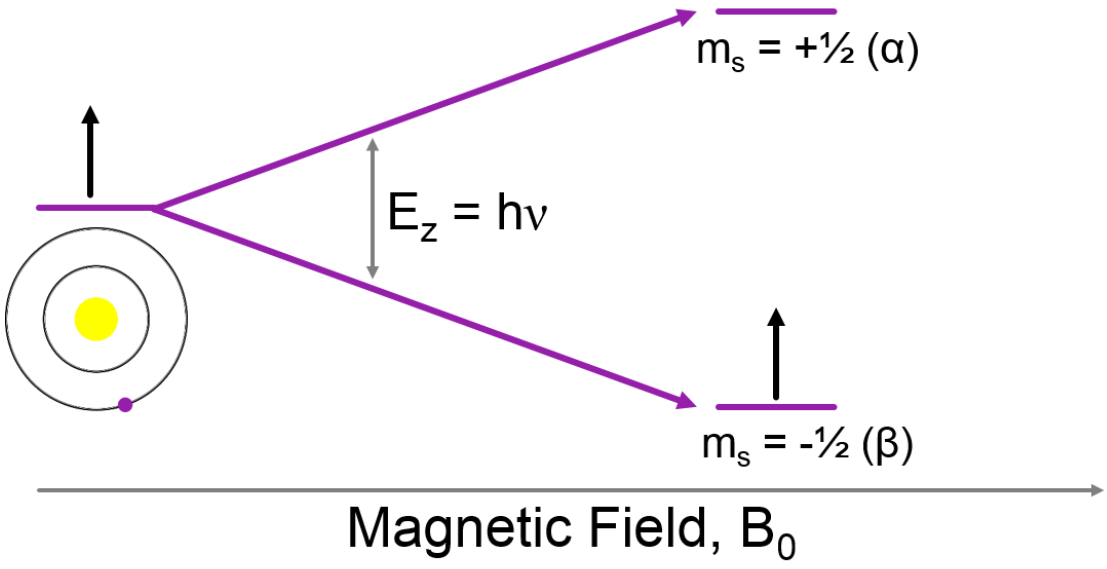

Figure 1.1. An electron in a magnetic field experiences the Zeeman Effect. The applied field splits the energy level into two states aligned along (β) or against (α) the magnetic field. The energy separation between the states is called the Zeeman Energy (E_z).

Hyperfine splitting, another spectral feature shared by NMR and EPR, is also a valuable tool for sample identification. Atomic nuclei with nonzero magnetic moments project a local magnetic field on nearby electrons that modulates the field imposed by the instrument magnet. This effect splits the signal into multiple signals according to Equation 1.3:

$$\#\text{ of hyperfine lines} = 2nI + 1 \qquad (1.3)$$

where n is the number of symmetry-equivalent nuclei in the molecule and I is the nuclear spin. If the contribution from the nuclei increases the magnetic field felt by the electron, then the signal is shifted downfield and the converse if the magnetic field is decreased [2]. Like g-values, hyperfine interactions, A, can be isotropic or anisotropic [3]. These properties used together provide unique fingerprints for the molecular structures of samples studied by EPR.

Radical	Matrix	g (g_{xx}, g_{yy}, g_{zz})	Ref.	Section
E′ defect in quartz	solid	2.00179, 2.00053, 2.00030	[5]	3.1
Irradiated tooth	solid	2.0032, 1.9973, 2.0016	[6]	3.2
N_s^0 diamond	solid	∥ 2.0029, ⊥ 2.0031	[7]	4.1
Hydrogenated silicon	solid	∥ 2.0042, ⊥ 2.0065	[8]	4.2
BDPA-solid	solid	2.00263, 2.00260, 2.00257	[9]	5.1
BDPA-dissolved	water	2.0026	[10]	6.1
DPPH	solid	2.0036 ± 0.0003	[11]	5.2
Galvinoxyl	hexane	2.00457	[12]	6.1
Thianthrene	TFA	2.0084	[13]	6.1
Tempone	decalin	2.0060	[14]	6.2
Nitronyl	benzene	2.0065	[3]	6.2
TPHIO	decalin	2.0059	[14]	6.2
MTSL	water	2.00551	[15]	7
Spirocyclohexyl-SL	benzene	2.0060	[16]	8.4

Table 1.1. g-values for paramagnetic species presented in this dissertation. Anisotropic g-values are given for solid samples and appear as presented in the provided reference.

1.2.2 Continuous Wave

Continuous wave (CW) EPR is the most commonly used technique and provides a direct measurement of the resonance condition in Equation 1.1. This method requires scanning the magnetic field during continuous excitation of the sample using microwave radiation at frequency ν. The resonance condition is met when the field position matches the applied frequency for a sample with a given g-value (Equation 1.1). At this point in the spectrum, the absorbed radiation excites the spins to the upper level spin state that is a consequence of the Zeeman Effect. The EPR signal will appear as the derivative of absorption due to the phase-sensitive detection method necessary to measure modest signals against often difficult noise conditions [2]. EPR signals are

naturally weak as a result of the relatively small Zeeman Energy separating spin states. The populations of the states, N_x, prior to excitation are described by the Boltzmann distribution:

$$\frac{N_B}{N_A} = e^{g\mu_B B_0/kT} \tag{1.4}$$

N_A refers to the upper level α state and N_B to the lower level β state. For a resonance centered at g = 2 measured at X-band (9.5 GHz), the populations of the upper and lower states are nearly equal, differing by only 0.15% according to Equation 1.4. This value assumes room-temperature measurement, but the relative populations can be altered by increasing frequency and decreasing temperature [3]. Signal intensity is increased over 10-fold by running the same sample at Q-band (34 GHz) and 80 K, where the separation of states is around 2%. Although these parameters greatly improve the signal to noise ratio (SNR), the net magnetization is still quite small, demonstrating the sensitivity of EPR to the detection of very small signals.

A number of phenomena can affect the properties (shape, linewidth, amplitude, etc.) of a CW spectrum. Spin relaxation is the most important contribution to the EPR signal for the research presented here. Relaxation of excited spins is described by T_m, T_2, and T_1. Spins existing within a magnetic field are not static but precessing about the z-axis, which is aligned parallel to the direction of the applied field (Figure 1.2A). Keeping in mind the slight difference in populations of α and β state spins, the projection of the net spin magnetization is along the z-axis, aligned with the field (Figure 1.2B). Considering the net magnetization of spins in the 3-dimensional magnetic field of Figure 1.2B provides a useful setting by which relaxation can be described.

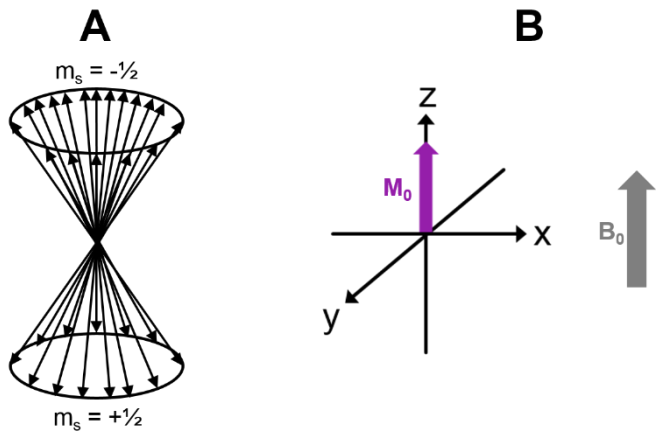

Figure 1.2. Spin alignment within the magnetic field. Spins precess about the z-axis, with a slightly higher population in m_s = -½ (A). The projection of the net magnetization (M_0) is therefore along the z-axis, aligned with the magnetic field (B_0, B).

Spin dephasing, T_m. In a pulse experiment, spins aligned with the magnetic field that absorb photons of microwave irradiation delivered by a pulse are flipped from the z-axis into the xy-plane, perpendicular to the direction of the field. The spins immediately begin to dephase within the xy-plane, creating a free-induction decay (FID) signal. The FID is a measure of the disappearance of magnetization signal with time [17]. T_m describes only the dephasing of the spins, and if there are additional interactions of the spins with the surroundings, this value may be altered [18]. Processes contributing to variation in T_m include instantaneous diffusion, spectral diffusion, nuclear spin diffusion, rapidly relaxing neighboring species, and molecular motions. T_m has been used interchangeably with T_2 in some articles in the literature, but the two processes are only truly identical if the experimental decay can be fit by a single exponential function and conditions are chosen to exclude confounding effects [18].

Spin-spin relaxation, T_2. The interaction of nuclear spins with the dephasing electron spins is described by T_m. For a system containing few nuclear spins, T_2 provides a reasonable estimate of T_m. In this case, dephasing is defined by dipole-dipole interactions between excited and ground-state spins, leading to mutual spin flips between coupled electrons [19]. T_2 can then be described according to Equation 1.5:

$$T_2 = \frac{hr^3}{2\pi\mu^2} \tag{1.5}$$

where h is Planck's constant, r is the distance between spins, and μ is the magnetic moment of the electron [20]. T_2 is a contribution to T_m, and in some cases, including radicals tumbling rapidly in solution, $T_m = T_2$. Throughout the remainder of this dissertation, T_2 will be used to describe this process.

T_2 can have a large effect on the appearance of the EPR signal in a CW experiment. Faster relaxation times correspond to broader CW spectra, and if T_2 is too short, the signal may not be visible by CW. Generally, if the CW spectrum cannot be seen, other EPR techniques will also be silent. Conversely, slower relaxation leads to narrow CW spectra. The CW linewidth can be described in terms of T_2 using Equation 1.6 [2]:

$$\Delta B_{pp} = \frac{2}{\sqrt{3}\gamma T_2} \tag{1.6}$$

ΔB_{pp} is the linewidth (peak-to-peak) and γ is the gyromagnetic ratio. This equation is valid only for a Lorentzian-shaped CW line which contains no unresolved hyperfine interactions. If the lineshape is Gaussian, as differentiated by a series of descriptive equations, the unresolved hyperfine changes ΔB_{pp} so that it is not proportional to T_2

[21]. Additionally, Equation 1.6 only holds if the incident microwave power is low enough to avoid spin saturation. If the EPR line is saturated, T_1 becomes a significant contribution to linewidth.

Spin-lattice relaxation, T_1. Considering again the net magnetization of spins within a magnetic field (Figure 1.3B); T_1 refers to the return to equilibrium along the z-axis following microwave perturbation. Whereas T_2 is an entropic process, T_1 is enthalpic, and is caused by loss of energy to the lattice [19]. The lattice is described as the environment surrounding the electron that is capable of absorbing this lost energy. The earliest studies of relaxation times were performed on solids, so the lattice referred exclusively to the crystal lattice [22]. Although the term, "lattice" is still used, the definition has been extended to include solvents and other neighboring species. A variety of processes contribute to the magnitude of T_1, many of which are described in greater detail in sections 5.2.3 and 6.2.4.

As mentioned above, the CW linewidth is not described by Equation 1.6 if the spins are saturated by the microwave power. Saturation refers to the process by which spins in the β state have been excited into the α state and have not relaxed sufficiently to repromote with additional incident radiation. This phenomenon leads to decreased intensity of the CW signal. To fully understand the cause of power saturation, it is important to introduce the Bloch equations, which describe the net magnetization vector in terms of relaxation times [23]. The Bloch equations have a variety of different forms based on the simplified relationship $dM/dt = \gamma(M \times B)$, where M is the net magnetization vector, B is the magnetic field, and γ the gyromagnetic ratio. The cross product can be

expanded into 3 dimensions, and the simplest derivation for description of saturation is shown in Equations 1.7A-C [23].

$$\frac{dM_x}{dt} = \gamma \left(M_y B_z - M_z B_y\right) - \frac{M_x}{T_2} \tag{1.7A}$$

$$\frac{dM_y}{dt} = \gamma \left(M_x B_z - M_z B_x\right) - \frac{M_y}{T_2} \tag{1.7B}$$

$$\frac{dM_z}{dt} = \gamma \left(M_x B_y - M_y B_x\right) + \frac{M_0 - M_z}{T_1} \tag{1.7C}$$

It is clear from the Bloch equations in this form that if B_i is too large, the magnetizations along x and y (M_x, M_y) approach zero. This occurs if the rate of absorption is of the same order or greater than the relaxation rate. Samples with long relaxation times commonly saturate at a low power, leading to distortion of the CW signal. The saturation factor, derived from the Bloch equations, must be ~1 to collect an undistorted lineshape [2]:

$$s = \frac{1}{1 + \gamma^2 B_1^2 T_1 T_2} \tag{1.8}$$

Whereas B_i refers to the directionality of the magnetic field in Equations 1.7A-C, B_1 in Equation 1.8 is the applied magnetic field perpendicular to the z-axis. For a sample that satisfies Equation 1.6, the CW linewidth can be linked to relaxation time for the saturation-broadened line as described by Equation 1.9 [2]:

$$(\Delta B_{pp})^2 = \frac{4}{3}\left(\frac{1}{\gamma^2 T_2^2} + B_1^2 \frac{T_1}{T_2}\right) \tag{1.9}$$

To determine whether a specific applied field, B_1, is responsible for spin saturation, it is common to collect a power saturation curve, in which the CW signal intensity is plotted as a function of the square root of the incident power [24]. Because B_1 is proportional to $\sqrt{P}$, the power at which saturation begins is seen as a deviation from linearity in the curve. A power saturation curve for a hydrogenated silicon sample is shown in Figure 4.11.

When considering which method is appropriate for a particular sample, CW EPR is ideal for quantitative measurements of g-values, hyperfine splitting, and spin concentration, in addition to samples with very wide spectra or short relaxation times that cannot be measured directly using pulse methods. CW is typically the method of choice for standard observation of paramagnetic species.

1.2.3 Rapid Scan

By design, CW EPR is a slow technique due to the necessity for spins to relax sufficiently to collect an undistorted spectrum. Performing a slow enough scan requires the following criteria be met:

$$\frac{d\delta}{dt} \ll \frac{1}{\sqrt{T_1 T_2}} \text{ where } \delta = \frac{B_0 - B^*}{B_1} \tag{1.10}$$

B_0 refers to the field along the z-axis, B^* is the resonant field, and B_1 is the applied field [23]. Equation 1.10 reveals that during a successful CW experiment, the square of the ratio of the applied magnetic field to the rate of change in magnetic field is much greater than the reciprocal of the product of the relaxation times, T_1 and T_2. This is commonly not the case for samples with very long relaxation times. As a result, the CW signal

must either be collected at very low power or contain distortions that are not always obvious. Solving Equation 1.10 for an immobilized nitroxide radical, such as the MTSL spin label used for DEER measurements at 80 K (Chapter 7, T_1 = 700 μs and T_2 = 2 μs), slow scan is achieved by scanning 1 G/s at 1 μW incident power. As T_1 increases below 80 K, however, slow-passage CW is inaccessible using the same parameters. For samples with a significant contribution from spectral diffusion, T_2 can be replaced by this faster process [25].

If the CW signal is scanned through resonance too rapidly according to the conditions in Equation 1.10, the spectrum contains passage effects. These were described by Bloch in 1946 [23], and the first use of this phenomenon to interpret spectra followed several years later [26]. Since then, a number of researchers have contributed to the theoretical understanding of rapid passage [22, 27, 28], including a thorough examination by Weger [29]. Exploitation of passage effects to obtain useful information on samples with long relaxation times and to improve SNR has been attempted by various groups [30-32]. Rapid scan EPR, developed in the Eaton lab [33], involves scanning the magnetic field (or frequency [34]) rapidly through resonance, using deconvolution to obtain the absorbance signal [35]. The principles of rapid scan EPR are equivalent to those of rapid scan NMR [20], including recovery of the absorption signal through deconvolution [36].

The CW distortions caused by passage effects include the appearance of the derivative signal as absorption and flipping of the spectrum when scanning from high to low field [2]. Distortions are more evident when the power and modulation amplitude

are varied. In rapid scan, the field is scanned much faster than a CW experiment, and this often results in "wiggles" trailing the absorbance-like signal [37]. Passage effect distortions of this kind are not always seen, but were first reported in 1956 [38]. If present, the number of wiggles in the spectrum increases with increasing scan rate.

Rapid scan wiggles decay in a time proportional to T_2, including contributions from inhomogeneous broadening. The spectra can therefore be simulated to obtain information about the relaxation properties of the sample [39]. As shown previously, this is also a feature of CW EPR, and it is possible to obtain T_2 and T_1 through linewidth simulation as a function of incident power (Equation 1.9) and power saturation experiments. However, there are important advantages of using rapid scan over CW. It is often difficult to know whether the CW signal for a specific sample is being distorted, either by passage effects or use of too large a modulation amplitude. Rapid scan is not susceptible to these kinds of distortions, so the derived lineshape is more accurate than CW [40]. Additionally, there can be physical properties of a sample, such as heterogeneity, that are undetectable by CW but become clear when rapid scan is used for comparison [41].

SNR is improved for rapid scan over CW for several reasons. Because the field is scanned quickly, the sample is on resonance for a very short time, and the spins do not saturate as readily. A higher B_1 can therefore be applied using rapid scan, improving the SNR. This effect can be quite large for samples with extremely long relaxation times [42]. The rapid field sweep also allows for acquisition of many more signal averages than are possible using CW in the same amount of time. Characterization of

the improvement in SNR using rapid scan was the end goal of many experiments presented here.

Due to the long history of CW EPR, most magnetic resonance spectroscopists are well-versed in interpretation of a CW spectrum. Interpretation of rapid scan data is slightly more complex, requiring deconvolution to recover the absorption spectrum from the rapid scan signal. The process of deconvolution was developed by Mark Tseitlin in the Eaton lab for sinusoidal magnetic field scans [35]. For direct comparison to CW, the derivative spectrum can be found from the absorption signal via pseudomodulation [43, 44].

There are many advantages to rapid scan over other EPR techniques. Although it is a relatively new method, the Eaton lab has already demonstrated the benefits of rapid scan for spin trapping and *in vivo* imaging [45, 46].

1.2.4 Pulse

T_1 and T_2 relaxation can be calculated from both CW and rapid scan EPR, or can be measured directly using pulsed EPR. Most pulse techniques rely on the formation of a spin echo, which was first described in 1950 by Erwin Hahn, for whom the echo is named [47]. Hahn described the spin echo for NMR in terms of the Bloch equations (Equations 1.7A-C) and the distributions of spins within the magnetic field. The first spin echo used for an EPR experiment was described several years later by Richard Blume [48], who furthermore demonstrated that T_1 and T_2 measured by pulse techniques matched the values predicted by Bleombergen, Pound, and Purcell [20].

Any two microwave pulses form an echo, which develops through changes to the magnetization of the spins [49]. Figure 1.3 shows the evolution of the magnetization in a two-pulse sequence. The first pulse is a π/2 pulse, or a 90° pulse, which flips the net magnetization from the z-axis, aligned with the magnetic field, into the xy-plane (Figure 1.3A). Focusing on the xy-plane, the spins begin to diphase immediately following the π/2 pulse, creating an FID. The sample is then subjected to a π pulse, or 180° pulse, which flips the spins within the plane but does not alter the direction in which the spins are dephasing. The spins are now moving back together, and the position at which the echo reaches a maximum amplitude corresponds to complete spin convergence. With no additional perturbation, the spins continue dephasing along the same path, completing the echo. Figure 1.3B breaks down each of these changes in magnetization within the xy-plane.

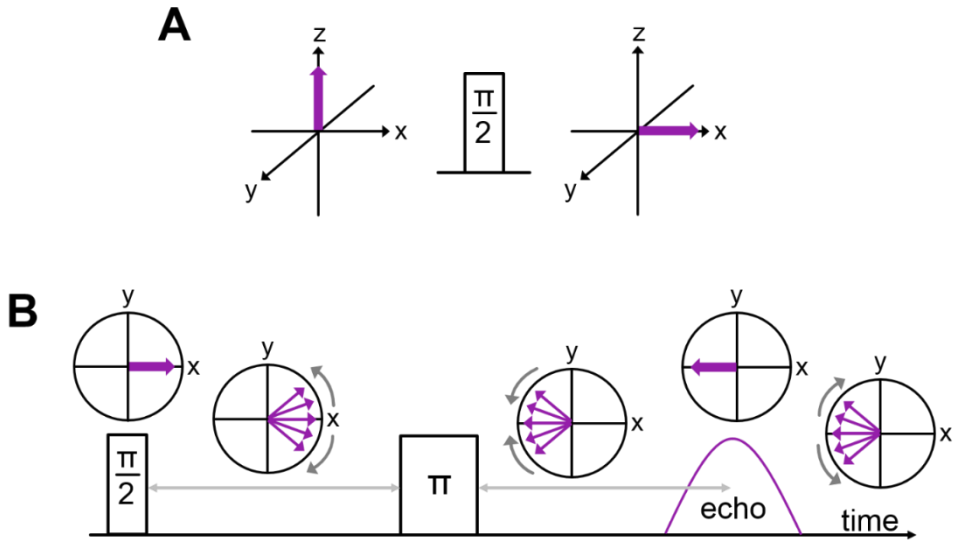

Figure 1.3. Changes in net spin magnetization for a two-pulse experiment. The π/2 pulse flips the magnetization from the z-axis 90° into the xy-plane (A). The spins dephase in the plane, followed by a 180° π pulse, after which the spins refocus, creating an echo (B).

The spin echo is utilized in several ways when performing a pulse experiment. A field-swept echo-detected spectrum can be recorded to determine the maximum echo height at which relaxation measurements would give the best SNR. Additionally, relaxation may vary based on g-value, which can be determined using field sweep. This type of measurement does not resolve the hyperfine splitting as well as CW, which employs phase-sensitive detection, because the pulses excite a smaller number of spins. Once the desired field position is determined, an echo is collected, and the required detector gate is selected based on the full-width at half-maximum (FWHM) height of the echo (Figure 1.4, dashed). The gate determines the position in the echo at which the relaxation signal will be recorded. Using a narrow gate decreases the bandwidth which broadens the signal somewhat. Encompassing the entire echo within the gate decreases SNR by broadening the bandwidth, but provides more detailed spectral features [50]. For this reason, the FWHM is used as a compromise between SNR and spectral resolution.

Spin echo decay. The echo formed from two pulses reaches a maximum amplitude at the same time after the center of the second pulse as the time between the center of the first two pulses (Figure 1.3B). In a spin echo decay experiment, the distance between the two pulses is gradually increased (Figure 1.4). The echo amplitude decreases with increasing time between pulses, until the echo is no longer detectable. The echo decays in a time proportional to T_2. Measuring T_2 by echo decay is advantageous because the signal is not subject to distortions or broadening like CW

linewidths. However, if the T_2 is short relative to the instrument dead time, the signal cannot be recorded and this technique is unusable.

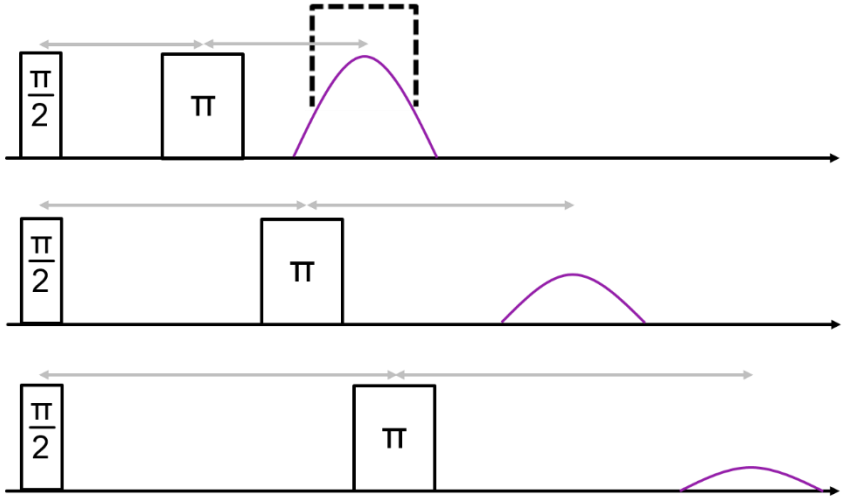

Figure 1.4. Spin echo decay is used to measure T_2. The echo achieves maximum amplitude at the time equivalent to the distance between the center of the pulses. Increasing this distance causes the echo to decay in a time proportional to T_2. For experimental measurement of relaxation times, the gate is set (dashed line) at the FWHM echo amplitude.

Inversion recovery. Inversion recovery (IR) is a method by which T_1 is measured using a three-pulse sequence. An additional π pulse positioned before the π/2 pulse inverts the net magnetization along the z-axis. The spins begin to relax to equilibrium along the direction of the magnetic field with a time constant, T_1. During this relaxation, the additional two pulses are applied, forming an echo that measures the magnetization along the z-axis [18]. The echo is inverted due to the initial π pulse, and as a result, the decay of the echo is also flipped and appears as a recovery.

Because any two pulses form an echo, the additional pulse employed in IR creates unwanted echoes. The IR experiment creates 5 echoes: the desired IR echo, an echo from the first and second pulse, from the first and last pulse, from the first echo

and last pulse, and a stimulated echo that is formed from all three pulses [44]. Pulse detection includes phase cycling, to remove the unwanted echoes [51]. IR experiments typically employ 2-step phase cycling, while experiments using more than three pulses may require additional phase cycling.

The pulse lengths used in IR make this technique susceptible to interference from spectral and spin diffusion [52]. Oftentimes, the spins that are excited are not the spins that are measured, meaning that the excitation energy is transferred to neighboring spins [18]. Diffusion processes can have a large effect on measured values of T_1. The spectrum must be adequately narrow for full inversion by the initial π pulse, which is true of few spin systems [44]. Interference from diffusion was not a problem for the narrow nitroxide radicals studied in Chapter 6, but was evident from the high concentration diamond sample in Chapter 4 and DPPH in polystyrene in Chapter 5. IR is not the preferred method for measurement of very broad spectra or very long relaxation times, but is useful for adequately dilute systems or rapidly tumbling radicals.

Saturation recovery. Saturation recovery (SR) measures T_1 using a single pulse and does not require formation of a spin echo. Additionally, SR uses CW excitation and detection, making this method intermediate between pulse and CW in both theory and instrumentation. A long, low-power pulse is used to excite all of the spins that communicate via spin diffusion. The spins then return to equilibrium along the z-axis, and this is detected at low power with a nonsaturating continuous stream of microwave irradiation [18]. The length of the saturating pulse is dictated by expected values of T_1.

Pulse lengths are typically set to ~10 times T_1 (though not always [17]) and are on the order of μs, whereas pulse lengths for spin echo methods are ns in length.

There are several advantages to SR over IR for T_1 measurements. Spectral diffusion is suppressed through excitation of more spins [18], so T_1 may be longer (and more accurate) when measured by SR compared to IR. Agreement of T_1 values measured by SR and IR serves as an indication that spectral diffusion is minimal. The absence of additional relaxation processes also means that SR curves fit well to single exponential functions in most cases [17]. The difficulty with accurate fitting of multiexponentials is expanded on in Section 4.2.4. Samples with very short T_2 relaxation may be inaccessible using pulse techniques that require formation of a spin echo. For this reason, SR is advantageous because it is not limited by T_2 [18].

It is important to mention some significant disadvantages to SR. CW detection is not as sensitive as spin echo detection, resulting in poor SNR for SR. For a very weak or noisy sample, the advantages of SR over IR may not compensate for the reduced SNR. Several weak samples, including irradiated teeth (Chapter 3), were attempted by SR but no signal was seen. Additionally, CW excitation and detection requires nearly perfect resonator tuning, which is achievable but difficult. Lastly, if the pulse lengths and power settings are not chosen correctly, interpretation of the recovery may become complicated [17]. This can typically be avoided through iteration of varying pulse lengths and powers. It is clear that SR may be the method of choice for strong samples with significant contributions from spectral diffusion or very short T_2.

Double electron-electron resonance (DEER). A unique quality of pulsed EPR is that pulse sequences can be designed to measure desired interactions between spins. This feature expands the capabilities of pulsed EPR to more than measurements of relaxation times. DEER is a pulse technique used to measure distances between two or more spin labels, with particular application to proteins. Proteins can be difficult to study using other available methods. X-ray crystallography relies on the ability of the protein to form a single crystal, and if this is achieved, the crystal structure may differ from the structure in solution. NMR has an inherent size limitation of roughly 30 kDa [53] for the study of proteins due not only to the complicated spectra that arise, but more importantly the decrease in tumbling rate of larger proteins. DEER overcomes these obstacles, as it can be used to study a protein in any state (crystalline, solid, solution, or membrane), and tumbling rate is unimportant as the spins are immobilized by measuring at low temperature.

DEER, sometimes referred to as PELDOR (pulsed-ELDOR), is a four-pulse sequence that utilizes two excitation frequencies to differentiate between spins. ELDOR was originally developed to overcome cross relaxation, the dominant process for nearby spins excited with a single frequency [44]. DEER was first described in 1981 using a three-pulse sequence in which H atoms were selectively excited at one frequency and the effect monitored by frozen hydroquinone radicals at a second frequency [54]. Several years later, the technique was used to study distances between rigid biradicals [55]. Recently, applications have focused more on the study of polymers and proteins [56], as it is a powerful tool to study conformational differences.

The nature of the DEER signal has been described both mathematically [57] and theoretically [56] by two scholars who have been instrumental to evolution of the technique. Figure 1.5 was inspired by Gunnar Jeschke's review on DEER of protein systems. DEER measures the distance between spins in a rigid system that are separated by no more than ~6 nm (Figure 1.5A). Advancements to the maximum measureable distances are described in Chapter 8. Performing a pulse experiment on just one of these spins at a single frequency, ν_1, creates the expected echo shown in the purple trace. This echo decays with time in the normal manner. If, however, the purple spin is close enough to exist within the local magnetic field of a second spin, the green spin, additional information can be obtained. A π pulse at frequency ν_2 selectively excites the green spin, and the local magnetic field is inverted (Figure 1.5B). As the green spin relaxes, the purple spin will experience a constantly changing magnetic field, which is a combination of the applied field, B_1, and the field of the green spin. This changing magnetic field results in modulation of the echo observed from the purple spin. The readout from a DEER experiment is therefore modulation over time.

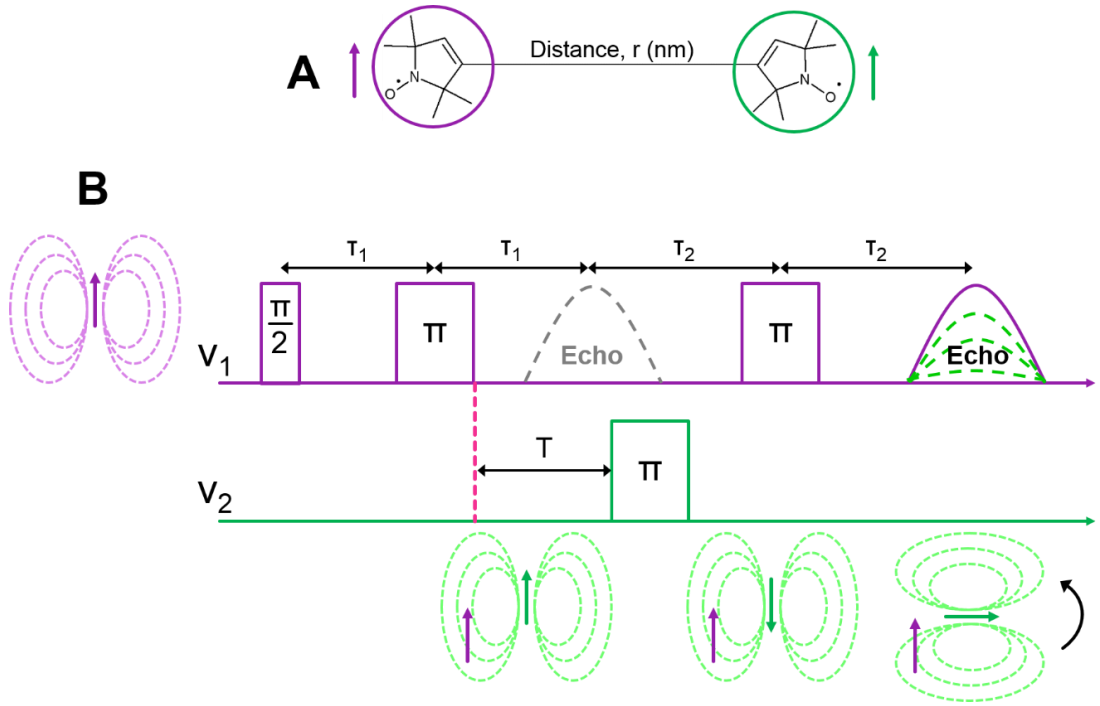

Figure 1.5. Nature of the DEER signal. Spin labels in the system to be studied are separated by a defined distance (A). A spin echo is formed in the typical way for one of the spins at a frequency, ν_1 (B, purple). The second spin is selectively excited using frequency, ν_2 (B, green) and time, T, is stepped. As the second spin relaxes, the echo of the first spin is modulated due to variation in the magnetic field felt by the first spin.

Modulation of the spin echo appears as an oscillation of defined frequency. There are several programs available for fitting the oscillations to obtain a distance distribution, each with unique features. These are described in Section 2.3.3. For many systems, including tau, the modulation may include overlap of several frequencies. This indicates the presence of more than one distance between spin labels.

A successful DEER experiment depends on dipole-dipole couplings of the spin labels such that the magnetic field of one spin (B, green) affects that of a second, nearby spin (A, purple). This interaction changes the Zeeman Energy, or the splitting of energy

levels, of the spin that is being effected (spin A). The dipolar interaction is described by Equation 1.11:

$$E_D = {}^{\mu_A \mu_B}/_{r^3} \tag{1.11}$$

where μ_A and μ_B refer to the magnetic dipole moments of the two spins and r is the distance between them. With Equation 1.11, the new Zeeman energy (E_A) becomes:

$$E_A = E_Z \pm E_D \tag{1.12}$$

The Zeeman energy of spin A, therefore, depends on the magnitude of the applied magnetic field, the magnetic moment of both itself and spin B, and the distance from spin B. The dipolar interaction can be measured with a three-pulse sequence, but the strength of the interaction between spin labels closer than 2.5 nm falls within the instrument dead-time of a three-pulse DEER experiment; Dipole interaction with the second spin label decays within tens of ns, the same order of the pulses themselves [58]. The echo will still be present, but modulation due to spin interaction will be gone before the echo is detected. For any DEER signal to be measured using a three-pulse sequence, the pulses would have to overlap, leading to large distortions. This problem is absent in four-pulse DEER, which is now standard, because the amount of time the echo is present is extended by a second refocusing pulse.

Pulses at different frequencies correspond to different locations in the field-swept echo-detected spectrum of the spin label (Figure 1.6). If the spin labels are different, the pulse positions on the spectrum are straightforward to determine: the observer frequency (ν_1) is ideally located at the maximum signal of spin A with minimum contribution from B spins. The pump frequency (ν_2) then corresponds to the

maximum signal of the B spins. For nitroxides, the three-line spectrum is orientation-dependent in the rigid lattice. At the typical observer frequency, only one transition (the high field along z) is excited, whereas all lines are excited at the pump frequency [56]. Separation of pulse frequencies must be sufficient to excite just the A spins or just the B spins. Pulse overlap arises when either the pulse length required (Equation 1.13 [18]) to achieve this separation is too long, or the spectrum is too narrow.

$$BW_{excitation} = \frac{1.6}{2\gamma\tau_p} \tag{1.13}$$

Here, the excitation bandwidth is in terms of G within the field-swept echo-detected spectrum, and τ_p is the required pulse length to achieve this bandwidth (BW). As usual, γ is the gyromagnetic ratio in Hz/T. Pulse overlap is not a problem for frozen nitroxide radicals because the spectrum is wider than the excitation bandwidth of the pulse [44]. Solving Equation 1.13 for bandwidth using a typical π pulse length of 40 ns, the corresponding spectral bandwidth is ~6 G. Experiments presented in this dissertation were conducted with a frequency difference of 37 MHz, corresponding to 13 G in the spectrum, which is greater than twice the pulse bandwidth. The maximum difference between frequencies is dictated by the resonator bandwidth [44] and is ~100 MHz. This limit can be extended by using a bimodal resonator [59].

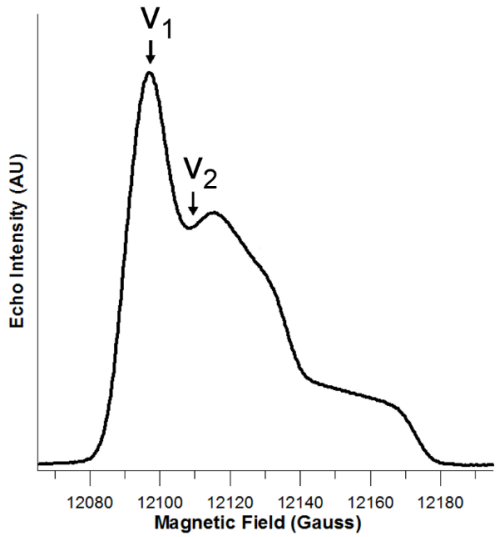

Figure 1.6. Field-swept echo-detected spectrum at Q-band for a double nitroxide system. The positions of the pulses are defined by ν_1 and ν_2, and the pulse lengths are calculated to give ~6 G bandwidth. The difference between the two frequencies corresponds to ~13 G.

DEER is useful for obtaining long-range distance information. It is more sensitive than distance measurements by CW, where the distance limit is ~1.5 nm [58]. The advantages of DEER over X-ray crystallography and NMR have been mentioned, and in cases where these techniques can be used, DEER provides a powerful complement to structural data. Additionally, it is not always necessary to attach unnatural spin labels to the protein studied. Van Doorslaer, et al. attached MTSL to the natural cysteines in neuroglobin, a heme-containing protein, and measured the distance between the nitroxide and the heme iron [60]. If spin labels must be attached, MTSL is relatively small in size and does not alter protein structure to the extent that large fluorophores might. As instrumentation and application of DEER becomes more commonplace, structural information will become available for proteins that are difficult to study by other means.

Chapter 2: EPR Methods

2.1 Spectroscopy

Bruker Biospin instrumentation was used for most analyses, along with homebuilt spectrometers and components. The Eaton lab has instruments capable of microwave frequencies including VHF (250 MHz), L-band (1.0, 1.5, and 1.9 GHz), S-band (2.5 and 3.0 GHz), X-band (9.5 GHz), and Q-band (34.5 GHz). Only X- and Q-band frequencies were used in the studies reported in this dissertation. Direct relaxation measurements were performed by two-pulse spin echo decay to determine T_2 and by either three-pulse inversion recovery (IR) or long-pulse saturation recovery (SR) to determine T_1. Pulse lengths and microwave powers were adjusted for each experiment to provide the maximum signal. Parameters used for individual experiments are listed in figure captions where appropriate.

2.1.1 EMX

Two Bruker EMX systems were used for collection of CW spectra at X-band. The EMX is equipped with an ER4122-SHQ (super high quality factor) resonator and the EMX plus with an ER4119-HS (high-sensitivity) resonator. The EMX was used for evaluation of the half-field transition for DPPH, purging efficiency of BDPA in solution, and additional basic CW measurements. The EMX plus was used for samples that required additional sensitivity (~2X), including the irradiated teeth, solid BDPA, and

biological samples. All DEER samples were checked for signal using the EMX plus prior to freezing.

2.1.2 E500T

The Bruker E500T was customized for rapid scan in the Eaton lab. Spectrometer components have varied in recent years, and the setup described here was used for the experiments presented in this dissertation. The instrument was equipped with either a Bruker FlexLine ER4118X-MD5 dielectric resonator or an ER4118X-MD4 pulse ENDOR resonator. The MD5 resonator has fewer metal components than the ENDOR resonator, which decreases eddy currents induced by rapid field scans. ENDOR scan coils were used to achieve scan widths up to 70 G, and the resonator was oriented such that the field from these coils was aligned with B_0. The coils were originally driven using a Tektronix AWG2021 arbitrary waveform generator operating at 1% duty cycle to avoid coil burnout. In later experiments, a locally designed coil driver was used, capable of higher duty cycles [61]. The maximum rate of a sinusoidal rapid scan is defined by Equation 2.1:

$$\text{rate} = \pi w f \tag{2.1}$$

where w is the scan width in G and f is the scan frequency [41]. A SpecJetII digitizer was used for rapid signal acquisition with the instrument operated in transient mode. The video amplifier in the Bruker microwave bridge had 200 MHz bandwidth. The bandwidth required for an undistorted rapid scan signal is given approximately by Equation 2.2:

$$BW_{signal} = \frac{Na}{\sqrt{3}\pi B_{pp}} \quad (2.2)$$

where N is ~5, a is the rate calculated from Equation 2.1 in G/s, and B_{pp} is the linewidth of the sample in G. The limiting bandwidth is typically from the resonator, for which it is defined in terms of microwave frequency, ν, and resonator *Q* by Equation 2.3:

$$BW_{resonator} = \frac{\nu}{Q} \quad (2.3)$$

From Equation 2.3, it is clear that decreasing resonator *Q* gives higher bandwidth and is often necessary to collect unbroadened rapid scan spectra. For samples with high dielectric loss, this can provide another advantage over CW EPR. In CW, matrices with high dielectric loss can absorb enough microwave irradiation to be immeasurable. Rapid scan can tolerate more lossiness than CW, but must still allow critical coupling of the resonator when operated in reflection mode, as was done in the work reported here. Methods by which *Q* was lowered are described for individual samples in later chapters. *Q* was originally calculated using Equation 2.4 [62]:

$$Q = 2\pi\nu\tau_r \quad (2.4)$$

where ν is the microwave frequency and τ_r is the resonator ringdown, measured on a LeCroy oscilloscope as the time for the signal to decay by 1/e after a pulse. It was determined that this method was not accurate for measuring very low *Q* values as the ringdown was shorter than the response time of the scope circuit. An HP 8719D network analyzer was instead used in later experiments.

2.1.3 ELEXSYS E580

The Bruker E580 is a multi-frequency pulse spectrometer capable of CW, SR, spin echo decay, IR, and DEER measurements. The resonators used at X-band were an ER4118X-MS5 split ring and an ER4118X-MD5-W1 dielectric, and at Q-band an ER5107D2 dielectric resonator. Tuning varied depending on experiment: CW and SR required critically coupled resonators, X-band echo decay and IR were performed with resonators overcoupled to $Q \sim 150$ as measured using Equation 2.4, and DEER was performed with the Q-band resonator fully overcoupled ($Q \sim 500$). All experiments used Bruker Xepr software. SR utilized PulseSpel, a programming option in Xepr that allows user-defined parameters. For SR, the E580 is equipped with a locally-designed video amplifier and filter (Richard Quine), in addition to those in the Bruker bridge. These are selected depending on the expected T_1 to avoid signal distortions from bandwidth limitations.

The E580 was equipped with an Oxford CF935 cryostat for variable temperature measurements using either liquid N_2 ($\geq$ 80 K) or liquid He (20-80 K). Low temperatures were used for echo decay, IR, and particularly DEER. DEER measurements also require a second microwave source, which was an E580-400U ELDOR unit along with a SuperQ-FT bridge capable of two frequencies. Pulses were formed using a Bruker PatternJet. A nominal 1 kW travelling wave tube (TWT) amplifier was used for X-band pulse, while a 1 W amplifier is incorporated into the Q-band pulse bridge. Bruker SpecJet I and II were both utilized for data acquisition. SpectJet II allowed faster

repetition rates, which was necessary for DEER using a paramagnetic metal and at room temperature, both of which had very short shot repetition times (SRTs).

2.1.4 Homebuilt Pulse Instrument

The Homebuilt pulse spectrometer has been described in detail [63]. Except the Bruker PatternJet, X-band components used for the E580 system were also available on the Homebuilt, including the cryostat system. X-band DEER could be performed on the Homebuilt system using a locally built cross-loop resonator (CLR, George Rinard) and a Wavetek 965 second microwave source. This instrument was primarily used for echo decay and IR.

2.1.5 Homebuilt Saturation Recovery

Like the Homebuilt pulse system, the Homebuilt saturation recovery instrument has been described [64]. The microwave source on this instrument is a klystron, which is slightly less stable than the E580 Gunn diode. The resonator was a five-loop four-gap resonator made by Medical Advances, Inc [65]. The recovery signal was visualized on a LeCroy oscilloscope, recorded using a SpecJet, and transferred with locally-written software. This instrument was primarily used to compare with values of T_1 measured by IR.

2.2 Sample Preparation

Although the samples studied here differ greatly in composition, many aspects of sample preparation and handling were common to all. Unless otherwise stated, EPR tubes are quartz with outer diameters (o.d.) of 4 mm (X-band) and 1.6 mm (Q-band). Samples are usually degassed to remove oxygen which can affect CW linewidths and

relaxation times. Solid samples were degassed with simple vacuum evacuation, while liquid samples required either continuous N_2 purge or freeze-pump-thaw (FPT). For purging at X-band, liquid was drawn into thin-walled Teflon tubing (0.97 inner diameter (i.d.)) which was sealed at both ends with critoseal. This was folded over and supported in a 4 mm tube alongside the purge line (also Teflon) that delivered N_2 to exchange O_2 through the tubing. For purging at Q-band, the sample was drawn into 0.3 mm i.d. Teflon tubing supported in a 1.6 mm tube that was open at both ends, and the full resonator assembly was purged with N_2. Samples were purged prior to measurements for several hours until T_2 reached a maximum value and remained stable. Purging was continued for the duration of the measurements. Alternatively, oxygen was often removed by application of several FPT cycles followed by flame sealing of the tube. This technique was commonly used with highly volatile liquids for which purging would change the sample concentration. Minimizing radical degradation, which was slowed by storage of sensitive samples in the dark at -20 °C, often required many FPT preparations. Specific challenges with regard to oxygen removal and sample degradation are discussed where appropriate.

2.3 Data Analysis

Many of the programs used for data analysis were locally written. Prof. Sandra Eaton wrote the FORTRAN and Mathcad programs, and Mark Tseitlin wrote the rapid scan MATLAB programs.

2.3.1 FORTRAN

CWLV is a FORTRAN-based program used for integration and background subtraction of CW spectra. Solution spectra could be simulated in EPR2 to determine hyperfine coupling constants and contributions from Lorentzian and Gaussian lineshapes. Solution spectra with incomplete motional averaging are treated in ASYM, which is based on the Kivelson model of linewidth [66]. CWLV was used for a variety of samples, while EPR2 and ASYM were primarily used for nitroxide radicals.

Relaxation times were determined using Multifit and UPEN. Multifit is based on Provencher's algorithms [67] and compares the quality of fits to single, double, and triple exponentials, assigning a weighting to each component. UPEN analyzes data in terms of distributions of relaxation times [68]. These programs were used for a number of samples, and almost all relaxation data are reported from Multifit.

2.3.2 Mathcad

Programs were written in Mathcad for determination of the relaxation processes contributing to T_1 for solid samples. These programs were based on Equation 2.5 [18], in which each of the processes, direct, Raman, local mode, Orbach, and thermal, is a possible contribution to the relaxation rate:

$$\frac{1}{T_1} = A_{dir}T + A_{Ram}\left[\left(\frac{T}{\theta_D}\right)^9 J_8\left(\frac{\theta_D}{T}\right)\right] + A_{loc}\left[\frac{e^{\Delta_{loc}/T}}{\left(e^{\Delta_{loc}/T} - 1\right)^2}\right] + A_{Orb}\frac{\Delta_{Orb}^3}{e^{\Delta_{Orb}/T}-1} + A_{therm}\left[\frac{2\tau_c}{1+\omega^2\tau_c^2}\right] \qquad (2.5)$$

Not all of these processes are appropriate for every sample, so the adjustment of the coefficients is discussed for affected samples.

2.3.3 MATLAB

Rapid scan data were simulated and deconvolved using MATLAB. Simulations [39] were achieved through integration of the Bloch equations (Equations 1.7A-C). The required input parameters were magnetic field scan width and frequency, resonator *Q*, resonance field offset from the center of the scan, and T_2. T_2 is the only parameter not established by the experimental parameters, so this value was adjusted until a good match of the simulation to experimental data was reached. The optimal value was often compared to T_2 calculated from CW linewidth to check for agreement.

Sinusoidal deconvolution of rapid scan signals has been described in detail [35]. The signal obtained by rapid scan is a convolution of the absorption signal from the sample and the rapid scan driving function that describes the change in excitation phase over time (sinusoidal in this case). Deconvolution involves multiplication of the complex conjugate of the signal by the driving function, followed by division of the Fourier transform of the driving function and reverse Fourier transformation.

MATLAB also served as the platform of DEER interpretation programs, including DEERAnalysis, GLADD, and DEFit. All DEER data were analyzed using DEERAnalysis2009 or 2011 [69], and the other programs were used for comparison. To obtain a distance distribution from the dipolar oscillation, the background must be subtracted from the raw DEER data. This background is caused by spins on neighboring proteins. The distances to these neighboring spins are much longer than the distances measured by DEER between spins on the same protein, so the background can be subtracted using a simple polynomial function. This method is used in DEERAnalysis

and DEFit. The background subtracted data is then fit with a function that provides probable distance distributions. GLADD (Global Analysis of DEER Data) is a program that determines the most probable background subtraction and distance distribution simultaneously [70]. The program uses no *a priori* background correction and fits data to single, double, or triple Gaussian models.

The main difference between the three programs is the fitting of the dipolar oscillation curve. The frequency of the oscillation is fit in DEERAnalysis [71], whereas DEFit (dipolar evolution fitting) uses Monte Carlo/SIMPLEX algorithms to fit to experimental data in the time domain. Like GLADD, DEFit uses Gaussian functions for distance distributions, whereas a variety of models are available in DEERAnalysis. In DEERAnalysis, Tikhonov regularization fits the DEER data to a simulated signal from a given distance distribution [56]. This procedure allows fitting of multiple oscillation frequencies without requiring the number of frequencies be specified beforehand. The L-curve gives a general estimation of the best compromise between sharpness of the distance peaks and smoothness of fit function. The smoothing parameter value is found where the two lines forming the L intersect. Some characteristic L-curves are shown in Figures 7.10A and 7.11A.

MATLAB was used to estimate SNR for DEER data using a program written by Deborah Mitchell. The program reads the background-subtracted raw data from DEERAnalysis and uses a Butterworth filter to smooth the original signal. The noise is determined based on the difference between the smoothed and the original signal, and the SNR is calculated. For purposes here, this program provides an acceptable estimate

of SNR. For a more accurate calculation, the filter parameter that dictates the degree of smoothing requires optimization or calibration.

Chapter 3: Irradiation Defects

It is well known that exposure to high-energy radiation creates free radicals, and this class of samples have been studied extensively by EPR. Radiation-induced defects affect a variety of samples and have been used practically for both dosimetry and archaeological dating.

3.1 E′ Defect in Quartz

3.1.1 Introduction

As with any crystal lattice, quartz has intrinsic defects, including oxygen vacancies and metal impurities. The E′ defect in irradiated quartz refers to introduction of an electron to the oxygen vacancy site where it resides in a dangling sp^3 orbital on SiO_3^-. Because quartz is one of the most abundant minerals on Earth, this defect has great importance to the field of geological dating [72]. Quartz has also been studied in depth for its applications to electronics and optics [6].

Many irradiated samples have characteristically long spin relaxation times. This quality makes obtaining an undistorted CW spectrum difficult due to spin saturation at relatively low powers. Spins do not saturate as easily in rapid scan EPR as in CW because the rapid scan magnetic field is on resonance for a very short time, and the spins do not absorb as much energy for the same incident power [42]. The aim of this project, and many presented in this dissertation, is to use rapid scan to collect an undistorted signal for samples that are difficult to study using CW.

3.1.2 Materials and Methods

E′ defects were formed in a fused quartz rod provided by Wilmad Glass using irradiation to 240 kGy with ^{60}Co γ rays at Cobe Labs [73]. The rod measured 2 mm in diameter by 10 mm long and was either supported in a 4 mm tube or fitted directly into a sample holder. CW measurements were collected at X-band on the Bruker E580 spectrometer, varying both power and modulation to monitor line shape distortion. Rapid scan and pulsed measurements of irradiated quartz were completed by Deborah Mitchell.

3.1.3 Results and Discussion

The dependence of lineshape on power was striking with the irradiated quartz sample. At low powers, signal saturation is minimized and the spectrum appears as the typical derivative, but at higher powers, the spectrum looks more like an inverted absorption spectrum (Figure 3.1A). At intermediate powers, the spectrum is a mixture of these two signals (Figure 3.1B), making the CW difficult to interpret. Differences in modulation frequency also affect the CW spectrum, and the most prominent effects are seen at the extremes of power and modulation amplitude. At moderate power and modulation amplitude, changes in modulation frequency affect only the amplitude of the signal. At high modulation amplitude, line broadening is expected for any modulation frequency, however this effect is more pronounced at 100 kHz than at 50 kHz (Figure 3.2A). Decreasing the modulation amplitude and collecting the spectrum at a power close to that at which the spectrum inverts (see Figure 3.1B) also demonstrates modulation frequency dependence (Figure 3.2B). As the modulation

frequency is increased, the spectrum becomes more representative of the derivative rather than absorption spectrum. The CW lineshape was also examined using a range of modulation amplitudes. In addition to broadening the linewidth, over-modulation affects the appearance of the spectrum to varying degrees (Figure 3.3). It is clear from these experiments that collection of an undistorted CW spectrum for this sample is difficult. If appropriate parameters are not selected, the lineshape obtained can be misleading. This work was included in reference [40].

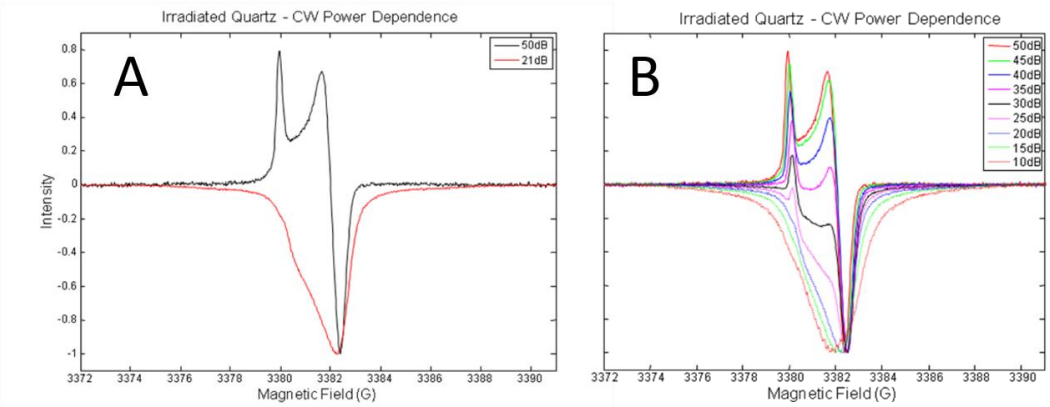

Figure 3.1. Power dependence of irradiated quartz CW spectrum. The sample readily saturates, causing the spectrum to appear as an inverted dispersion signal, even at moderate power (A, adopted from [40]). A more detailed power dependence is shown in (B). The high-power dispersion signal fully broadens at 10 dB, and no distinct spectral features are observable. For this spectrometer, 0 dB is 200 mW, so 10 dB = 20 mW and 50 dB = 2 μW. Spectra were collected with 100 kHz modulation frequency and 0.1 G modulation amplitude.

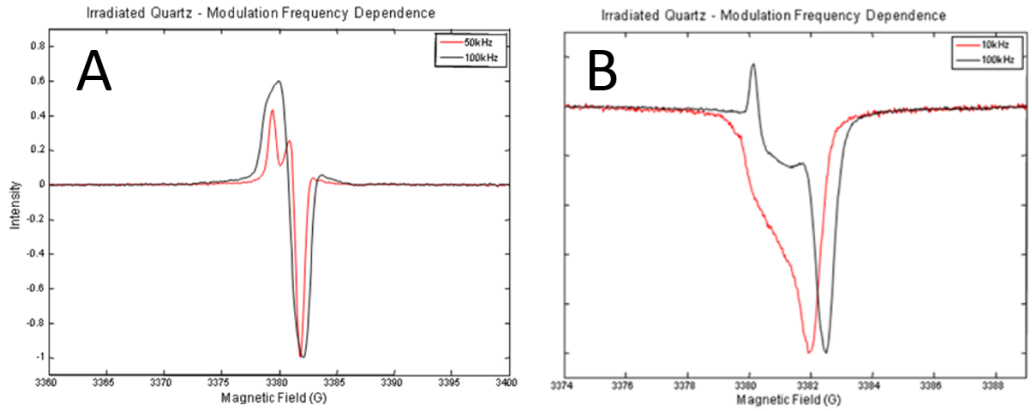

Figure 3.2. Modulation frequency dependence of irradiated quartz CW spectrum. The modulation amplitude was 2.0 G in (A) and 0.1 G in (B). Modulation frequencies of 50 and 100 kHz are compared in (A) and 10 and 100 kHz are compared in (B). The modulation amplitude in (A) is large for this sample, but was chosen to highlight the effect of modulation frequency. Power was 30 dB (200 μW).

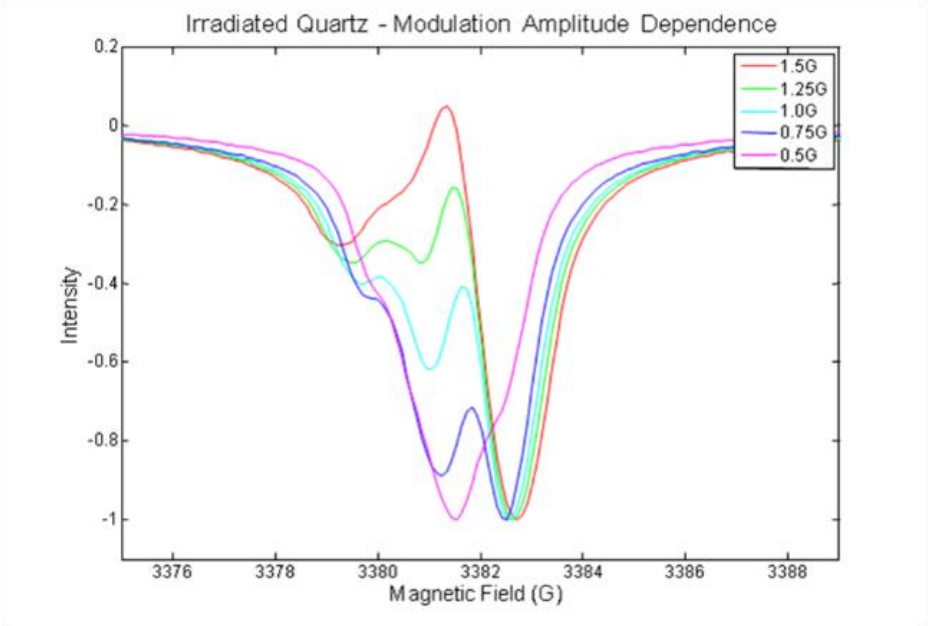

Figure 3.3. Modulation amplitude dependence of irradiated quartz CW spectrum. Modulation frequency was constant at 100 kHz, and power was 20 dB (2 mW). The variation in lineshape is less when modulation frequency is 50 kHz.

3.2 Teeth

3.2.1 Introduction

Teeth are an attractive sample for both dating and dosimetry due to the persistence of the radicals that form upon irradiation and the simple relationship between EPR signal and radiation dosage [6]. Early applications of EPR to dating examined uptake of uranium in the tooth of a mammoth [74]. It was recognized around twenty years prior to that study that irradiation causes EPR-active defects in tooth enamel itself [75], however the source of the signal was not fully understood. Although originally attributed to CO_3^{3-} [76], it was shown that spectral properties align more accurately with the presence of CO_2^- radicals [77]. Biological tooth dosimetry has been used to examine effects of radiation-involved disasters, including atom-bomb survivors in Nagasaki and Hiroshima and residents of Chernobyl during the reactor meltdown, as well as cancer patients exposed to radiation therapy [6]. This unique application of EPR holds future potential as a diagnostic tool to determine radiation exposure in humans.

This work is part of a larger project at Dartmouth College to develop a simple, portable spectrometer for low level detection of radiation exposure. Irradiated tooth was characterized by CW EPR, and the signal was then compared to that obtained using rapid scan. Rapid scan offers a fast and accurate technique to test large populations for exposure. Results have not been published, but studies continue for determination of the most appropriate standard for this type of application (Zhelin Yu).

3.2.2 Materials and Methods

Several teeth irradiated to 15 Gy were provided by Prof. Harold Swartz at the Geisel School of Medicine at Dartmouth College. The teeth were broken into pieces with a hammer and placed into an X-band EPR tube, filling the active space. CW spectra were collected on the Bruker EMX Plus system at varying powers to monitor changes in the line shape. The teeth were reanalyzed after addition of 0.5% K_3CrO_8 doped in K_3NbO_3 (prepared by Jacqueline Toomey) for possible use as a dosimetry standard. T_2 and T_1 measurements of the teeth were performed on the Homebuilt pulse system. The size and shape of the spin echo were monitored as a function of distance between pulses and location of the acquisition gate.

3.2.3 Results and Discussion

The irradiated teeth gave a weak but detectable signal, the shape of which was power dependent (Figure 3.4). The majority of the signal seen in this figure is background associated with organic radicals. The background saturates at a different power than the irradiation signal, as seen in the figure. It should be noted that this dose of radiation (15 Gy) exceeds the amount eventually hoped to be detected. Obtaining a useful CW spectrum of the chromium doped standard with the teeth was difficult because the strong chromium signal overpowered the weak tooth signal. Attempts to use a smaller crystal improved the spectrum slightly (Figure 3.5A). Using a powder sample of the standard changed the g-value enough that the chromium signal overlapped with the teeth (Figure 3.5B).

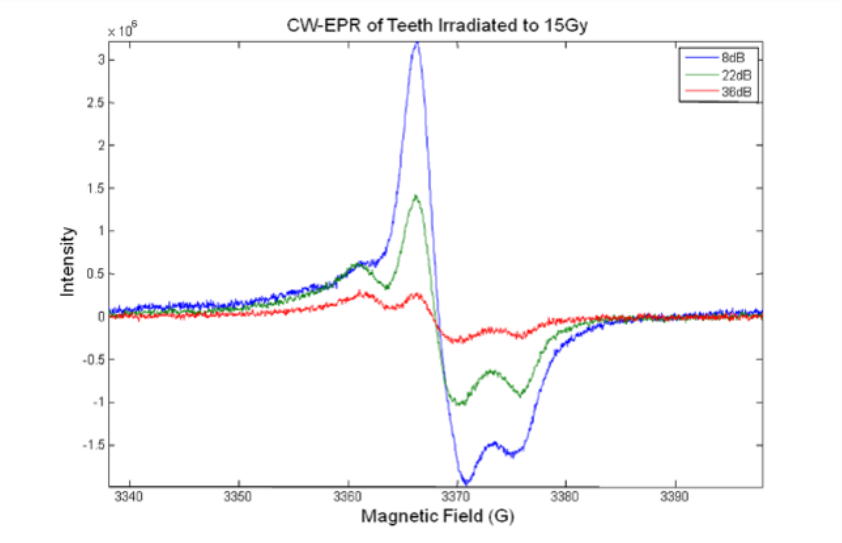

Figure 3.4. Power dependence of irradiated teeth CW spectrum. All were collected in 50 scans, using modulation frequency of 100 kHz and 1.0 G amplitude. The small feature around 3360 G is the irradiation signal, while the large remaining signal is background.

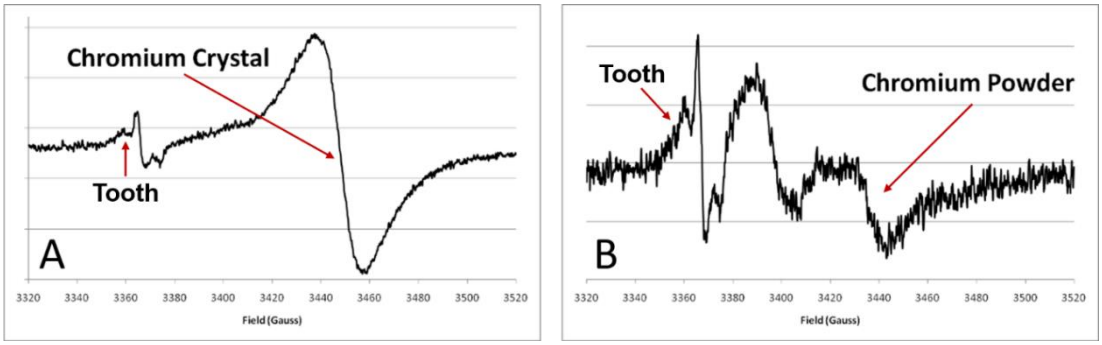

Figure 3.5. CW of irradiated teeth with chromium as a standard. Use of a standard helps identify radiation dosage. The signal from the crystal in (A) overpowered the tooth signal, while the powder in (B) contained remnants of small crystals, distorting the tooth signal. Spectra were collected using the same parameters: 100 kHz modulation frequency, 1.0 G modulation amplitude, 50 scans, 22 dB (1.3 mW).

Relaxation times of irradiated tooth samples have been previously reported [78], and measurements of T_1 and T_2 were repeated here for the 15 Gy sample. In the prior study, T_1 was shown to be double exponential at room temperature, with slight variation in the second component depending on irradiation dosage. The recovery curves for the

15 Gy sample also fit well to a double exponential function, and the measured values were of the same order as those found in the prior study. The lowest concentration, 10 Gy, was not examined at room temperature previously, so a more direct comparison cannot be made. T_2 measurements were not reported as a single exponential at room temperature in the paper, although it is stated that relaxation times were similar for both temperatures. The T_2 value measured for the 15 Gy sample was similar to those reported at 130 K. The similarities in relaxation times of this sample compared to prior studies is not surprising, as it was observed that radiation dosage has minimal effect on relaxation.

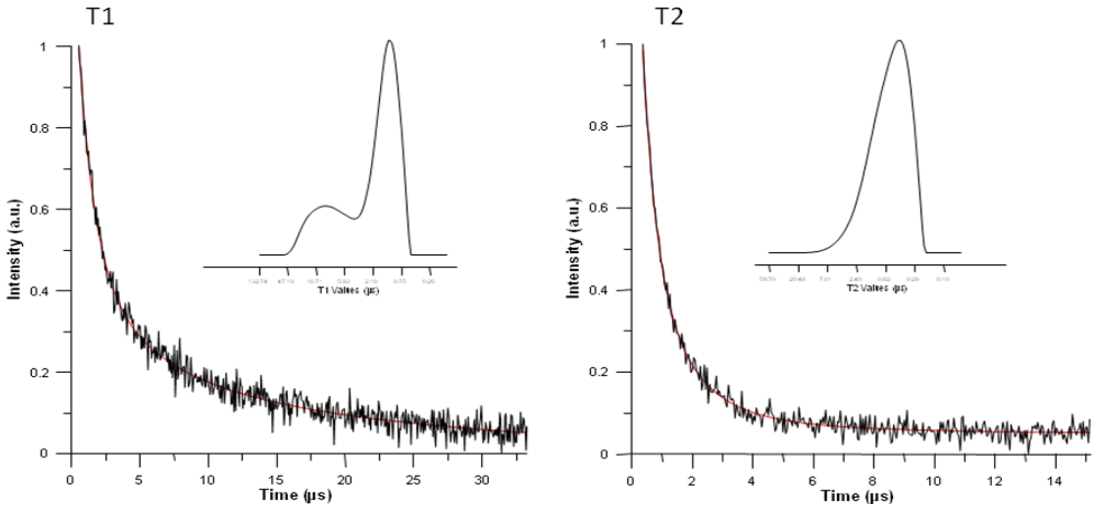

Figure 3.6. T_1 and T_2 measurements of irradiated teeth analyzed with two programs. UPEN (inset) shows a clear double exponential fit for T_1 and single for T_2. For T_1, the time window should be extended for more accurate measurement of the long component. T_1 relaxation was about 12 and 1.3 µs, and T_2 relaxation was about 500 ns.

3.3 Conclusions

The numerous obstacles in collecting an undistorted, representative CW spectrum of irradiated samples can be overcome using rapid scan. Scanning quickly

through resonance avoids spin saturation, so the SNR is improved by operating at higher microwave powers. Because of its long relaxation times, irradiated quartz is also a good candidate for pulsed EPR. An undistorted echo-detected lineshape can be collected using pulsed EPR in less time than CW EPR, but not as fast as with rapid scan and with decreased SNR. Analysis of the irradiated quartz provided a proof-of-concept that rapid scan would benefit collection of undistorted lineshapes and also lead to improved SNR [40].

Using EPR to acquire information on radiation exposure is a practical application that may become increasingly important in the future. Several methods have been attempted; fingernails could be used, but present several problems, including dielectric loss of the adjacent finger tissue and the EPR signal arising from cutting the fingernail [79]. Additionally, radiation is not as persistent in fingernails as in teeth. Teeth are not without problems, however, including background from X-rays and exposure to sunlight (primarily incisors). Relaxation times are only mildly dosage dependent in teeth, which necessitates the use of a standard for calibration. As shown in this study and unpublished results obtained by Zhelin Yu, differences in relaxation and power saturation can lead to successful separation of tooth background from the irradiation signal by using rapid scan. Radiation becomes of clinical concern ≥ 3 Gy, below which the EPR SNR becomes very poor. Rapid scan will not only be fast and accurate (based on selective saturation of the signal of interest), but has the potential to greatly improve SNR. These studies provide a starting point for developments of radiation detection that will potentially benefit many people.

Chapter 4: Other Lattice Defects

Natural lattice defects have similar characteristics to defects formed from irradiation. With the exception of most metal ion defects, lattice defects are present in very low concentrations and are characterized by long relaxation times. Both of these factors make CW EPR less attractive for this type of sample. Solid defect centers are becoming increasingly important for quantum computing [80] and electronics [81], and thorough characterization of magnetic properties has application in these fields [82].

4.1 Diamond N_s^0

4.1.1 Introduction

The diamond lattice is extremely rigid and compact, and while impurities can be present in very low concentration, they can have a substantial effect on the structure and properties of diamond. Nitrogen is the most common natural impurity in diamond and can also be artificially inserted through high temperature or pressure [83]. The bond angle and distance distortions caused by insertion of N atoms to the C lattice produces an EPR signal [84]. This defect is termed N_s^0.

EPR has been utilized to examine characteristics of diamond defects for over 70 years [85]. Although this type of study is not new to the field, unique properties of the N_s^0 defects are still being discovered using EPR. More recent discoveries include description of chemically-distinct centers characterized by variation in bond length distortion [86], evidence of high H concentration in diamonds from space that alter the

deposition of N atoms [87], and the participation of Ni atoms in formation of these defect centers [88]. For this project, signals obtained by CW, pulse, and rapid scan were compared, including demonstration that rapid scan is highly beneficial for another sample affected by long relaxation times. Parts of this work have been published in reference [42].

4.1.2 Materials and Methods

Diamond samples containing varying concentrations of N_s^0 defects were provided [89] by Prof. Mark E. Newton at the University of Warwick. Concentrations studied were 300 ppm (yellow, narrow rod), 8 ppm (green, cubic), 200 ppb (smoky gray, rectangular), and 20 ppb (colorless, rectangular). The higher-concentration samples slid easily into 4 mm tubes, and the 20 ppb was fit firmly into 4 mm o.d. Teflon tube for analysis. This was the only sample that was also studied by rapid scan and CW. All measurements at 20 ppb were collected by Deborah Mitchell.

Pulse measurements were performed at X-band on the Bruker E580 spectrometer with the split-ring resonator. Depending on the nature of the defect center and the local environment surrounding that center, the field-swept echo-detected spectra can look very different (Figure 4.1). The large nitrogen hyperfine splittings result in three sets of lines, and there are several inequivalent sites in the crystal that give rise to multiple lines. Despite these differences, relaxation measurements were predominantly performed on the central peak for comparison between samples.

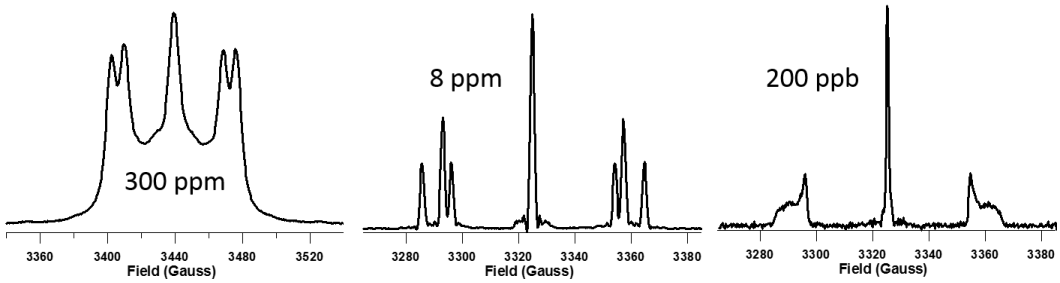

Figure 4.1. Field-swept echo-detected spectra of diamond with different concentrations of nitrogen defect centers. The g-values and nitrogen hyperfine splittings depend largely on the local environment, which is a product of the temperature and pressure at which the defect was created.

4.1.3 Results and Discussion

Spin-spin relaxation time, T_2. Table 4.1 provides a summary of results for T_1 and T_2 measurements. T_2 measurements generally fit well to single-exponential functions (Figure 4.2). At 8 ppm, the center field line T_2 values were double exponential, but the low field line gave single exponential T_2 values. The weightings in Multifit of the double exponential components for the central line show that the shorter T_2 is dominant, which is confirmed by the proximity to the single exponential value. Echo dephasing becomes quite long at low concentration, and despite a 10-fold decrease in defect centers, there was not much difference in T_2 between 200 and 20 ppb. At 300 ppm, T_2 was very short and may have been dominated by spectral diffusion or instantaneous diffusion. In this case, spectral diffusion refers to any number of processes that alter the magnetization properties of a single spin, while instantaneous diffusion involves a second, dipolar-linked spin. Both of these phenomena are affected by concentration, so for the 300 ppm sample, they are difficult to distinguish. However, the increase in T_2 values with pulse length for this sample (Table 4.2) supports a contribution from instantaneous diffusion. This variation in T_2 was also seen for the lower concentration

samples, but to a lesser extent as expected for a concentration-dependent process (Table 4.3). This trend holds for the low field line of the 8 ppm sample as well (Table 4.4). Measurements were repeated at least twice to confirm values.

Sample	T_1 – Double Exponential Fit	T_1 – Single Exponential Fit	T_m – Double Exponential ($\pi/2$ = 80 ns)	T_m – Single Exponential ($\pi/2$ = 80 ns)
300 ppm	900 µs, 21 µs	93 µs	N/A	320 ns
8 ppm	2.7 ms, 360 µs	930 µs	4.4 µs, 1.1 µs	1.4 µs
200 ppb	N/A	2.4 ms	N/A	200 µs
20 ppb	N/A	2.3 ms	N/A	230 µs ($\pi/2$ = 160 ns)

Table 4.1. Summary of relaxation data for diamond samples. T_1 was recorded using $\pi/2$ = 80 ns, but unlike T_2 (T_m), pulse length did not affect relaxation times.

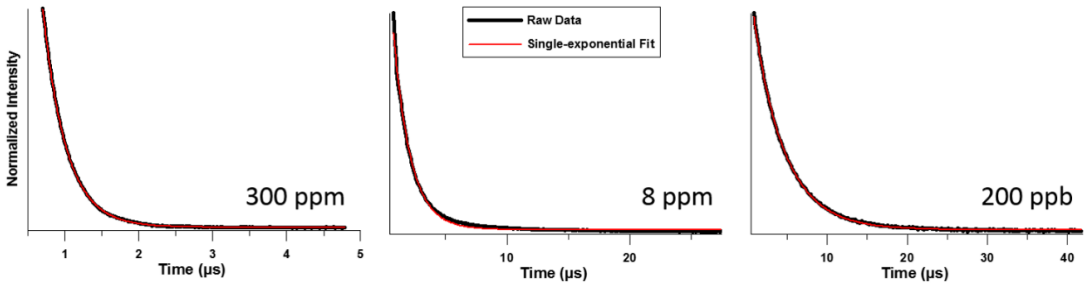

Figure 4.2. Electron spin echo decay for diamond samples. Experimental data (black) fit well to single-exponential fit functions (red). Parameters were similar for all measurements: $\pi/2$ = 80 ns, 512 points, 96 shots/point, SRT = 8 ms, collected in 1 scan with 2-step phase cycling. Power was adjusted to give maximum echo amplitude, and the gate was FWHM of the echo. The step size was adjusted so that the time window was approximately 10X the relaxation time.

π/2 Pulse Length (ns)	Power (dB)	T_m (ns) – single exponential
20	20	290
40	24	280
80	27	320
160	31	420
200	33	460

Table 4.2. T_m (T_2) values with varying pulse lengths for 300 ppm N_s^0 in diamond. The increase in relaxation with pulse length indicates a contribution from instantaneous diffusion. Power is reported in dB, where 0 dB = 200 mW.

π/2 Pulse Length (ns)	Power (dB)	T_m (μs) – double exponential	T_m (μs) – single exponential
20	13	4.0, 0.9	1.1
40	19	4.3, 1.0	1.2
80	26	4.4, 1.1	1.4
160	32	9.9, 1.7	1.9
200	34	9.3, 1.8	2.2

Table 4.3. T_m (T_2) values with varying pulse lengths for 8 ppm N_s^0 in diamond. Instantaneous diffusion remains a dominant contribution to relaxation at this concentration. While the decay curve could be fit using a double exponential function, the short component was dominant, closely correlating to the single-exponential values.

π/2 Pulse Length (ns)	Power (dB)	T_m (μs) – single exponential
20	12	3.1
40	20	3.3
80	26	3.9
160	33	4.5
200	35	4.6

Table 4.4. T_m (T_2) values with varying pulse lengths for 200 ppb N_s^0 in diamond. Instantaneous diffusion is decreased at this concentration compared with the other samples.

Spin-lattice relaxation time, T_1. T_1 measurements were double exponential recoveries at the high concentrations and were single exponential at the low concentrations. The 300 ppm sample was particularly difficult to interpret; four different time windows were run to try to accurately characterize the obvious double-exponential fit to the raw data. The longer the window, the longer the recovery time required to fit the experimental data (Figure 4.3). Consequently, T_1 was determined using saturation recovery (SR) to eliminate contributions from spectral diffusion. The measurements were repeated three times using varying saturating and observe pulses to ensure appropriate parameters were used. Each run gave the same results, and the measured recovery time did not depend on the length of the saturating pulse. Unlike the inversion recovery (IR) data, the SR fit fairly well to a single exponential, but a double-exponential function fit better (Figure 4.4). The 8 ppm sample was studied for both the center field and low field lines. The low field line gave a single exponential recovery, but the center field line fit best with a double exponential (Figure 4.5). All IR and SR

data were examined using both Multifit and the UPEN program. Although IR UPEN distributions were very broad for the 300 and 8 ppm samples, the analysis supports the conclusion that T_1 by IR is multiexponential, based on both programs (Figures 4.6 and 4.7). The UPEN distributions for SR (300 ppm only) were better-defined and clearly showed two exponentials that corresponded to the double-exponential T_1 values in Multifit.

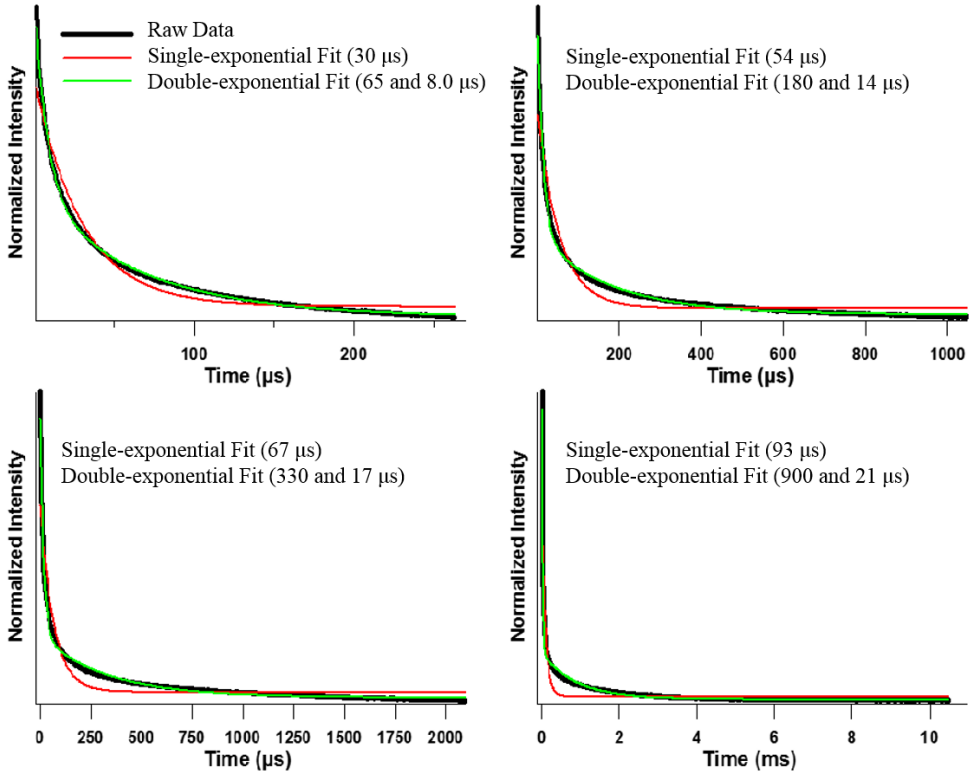

Figure 4.3. T_1 curves collected by inversion recovery using different time windows (x-axis) for 300 ppm N_s^0 in diamond. The experimental data (black) are clearly multiexponential (single fit in red, double fit in green). Accurate values were difficult to obtain due to increasing T_1 with the time window. Parameters for T_1 experiments were similar to T_m (T_2, see Figure 4.2), except that phase cycling was omitted for long relaxation times.

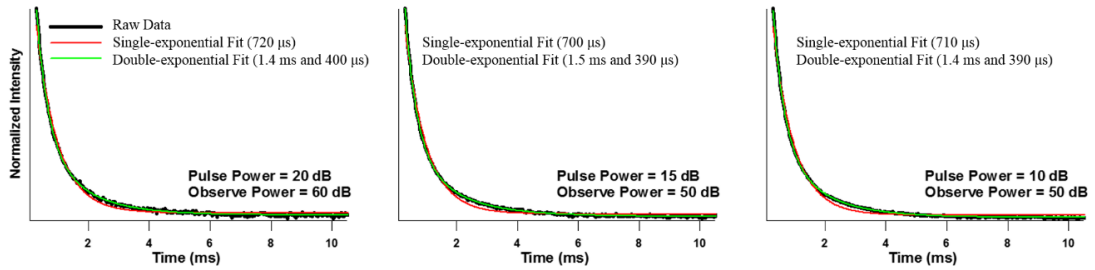

Figure 4.4. T_1 values determined by saturation recovery for 300 ppm N_s^0 in diamond. The panels refer to different power setting parameters, all which gave consistent T_1 values. The curves fit well to single exponential functions compared to inversion recovery, indicating a strong contribution from spectral diffusion to the inversion recovery. The values were most similar to values obtained with the longest time window used in Figure 4.3.

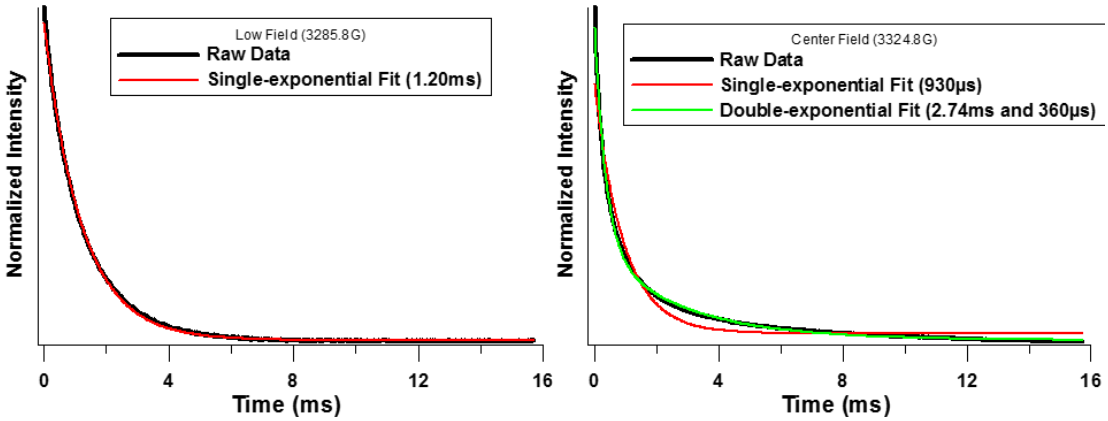

Figure 4.5. T_1 values determined by inversion recovery for the low and center fields of 8 ppm N_s^0 in diamond. Interestingly, the low field fit well to a single exponential, while the high field required a double exponential. Variation in relaxation properties with g-value is expected as different transitions are sampled. Several transitions overlap in the center of the spectrum but are resolved in the low-field lines.

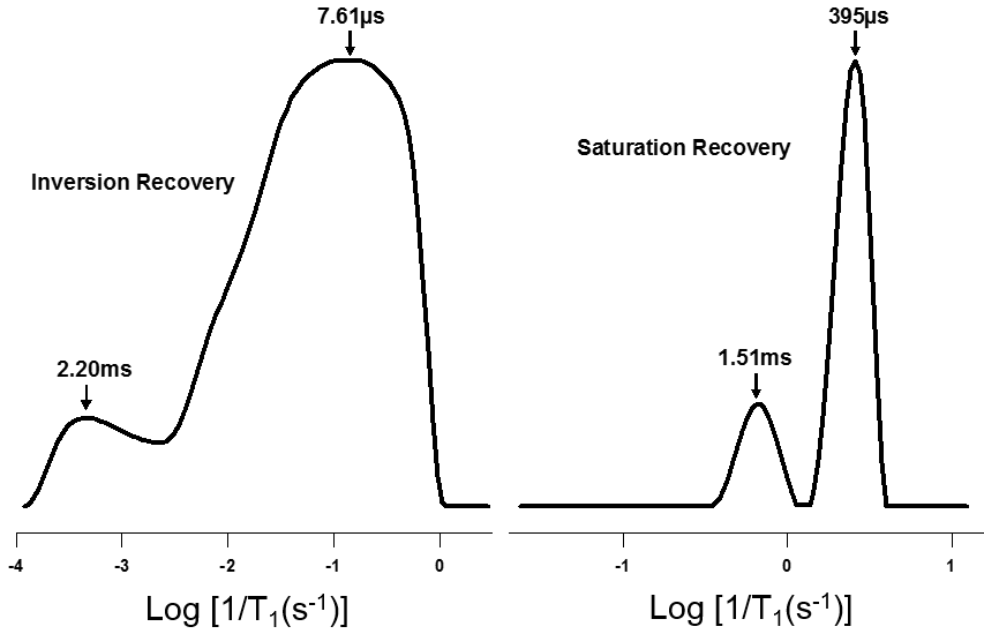

Figure 4.6. T_1 values analyzed using UPEN for both inversion recovery and saturation recovery of 300 ppm N_s^0 in diamond. These results corroborate the Multifit results from Figures 4.3 and 4.4.

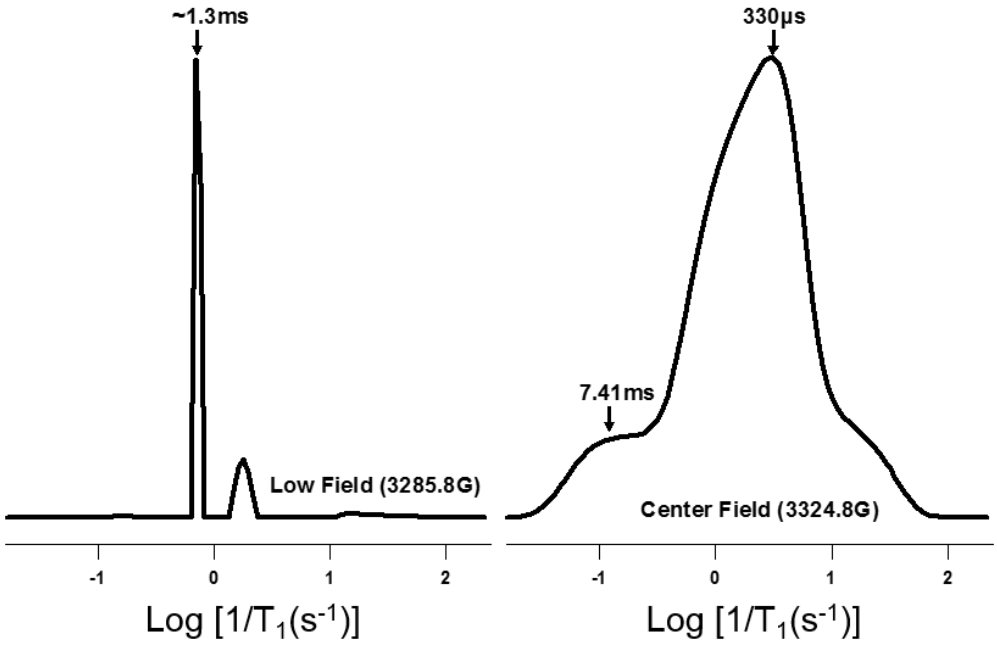

Figure 4.7. T_1 values analyzed using UPEN for the low and center fields of 8 ppm N_s^0 in diamond. The low field data did not give reproducible UPEN results, however the pattern was always a high probability, narrow distribution with a lower probability broad distribution. The values obtained with UPEN matched closely with the Multifit results in Figure 4.5.

The center field lines of the 200 and 20 ppb samples fit well to single exponential functions, a finding confirmed in UPEN. Low and high field lines were also examined for the 20 ppb sample (collected by Deborah Mitchell). Unlike the 8 ppm sample, the IR data at different field positions fit well to single exponentials. UPEN values matched Multifit very well and were single, narrow distributions for low concentration samples (Figure 4.8).

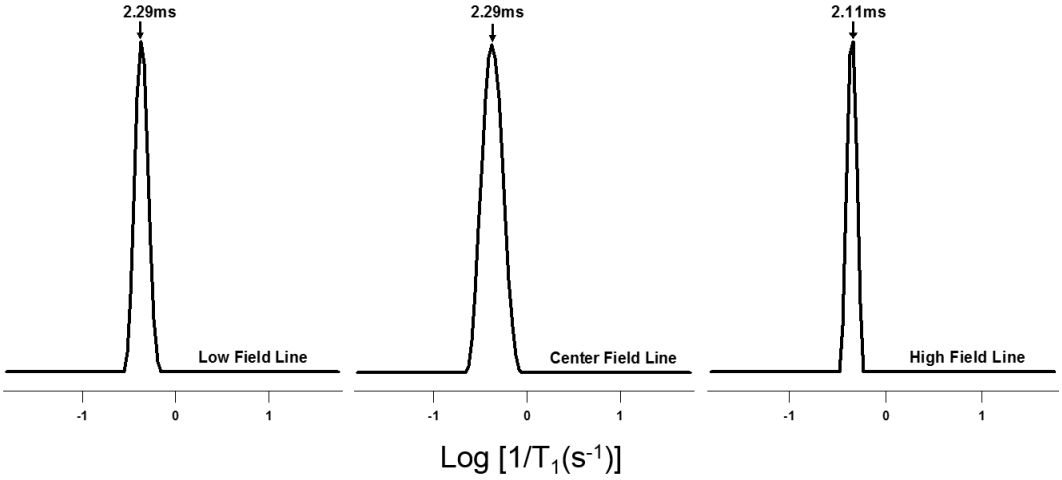

Figure 4.8. T_1 values analyzed using UPEN for the low and center fields of 20 ppb N_s^0 in diamond. These values matched the single exponential values in Multifit very well. UPEN analysis of 200 ppb N_s^0 in diamond looked very similar to these results.

4.1.4 Conclusions

Only the 200 ppb N_s^0 in diamond sample was used for comparison of different EPR techniques, but examination of the set of four concentrations provided an opportunity for a more thorough characterization of the relaxation properties of this type of defect. A number of processes can contribute to T_2, but the echo decay is well-defined by a single exponential function, as seen for these samples. In an immobilized sample, T_2 can be described by Equation 4.1:

$$\text{Signal Amplitude } (2\tau) = e^{-\left(2\tau/T_2\right)^x} \quad (4.1)$$

where τ refers to the time between the two pulses, and x varies depending on the dephasing mechanism, falling within 0.5-3 [90]. The diamond samples showed strong contributions from instantaneous diffusion, a phenomenon for which x = 1 [18]. This effect was more dominant at high concentrations, as described by Klauder and Anderson [91]. Additional processes contributing to T_2 were not analyzed in detail.

Like T_2, T_1 was also influenced by concentration. In addition to more than an order of magnitude increase in relaxation time, T_1 curves transitioned from complicated multiexponential functions at 300 ppm to single exponentials at 20 ppb. For radicals in solution, the effect of concentration is intuitive: high concentration leads to an increased number of mutual spin flips, providing an additional pathway through which electrons relax. Relaxation of radical centers in solids is more complicated. Bowman and Kevan described this process for samples similar to diamond; tunneling of nuclei in the vicinity of the radical modulates the dipolar interaction between the two species, altering the electron relaxation pathway [92]. It is likely that local mode vibrations are also large contributors to relaxation, as they are characteristic of disordered systems. Variable temperature measurements could be used to accurately assign relaxation processes for diamond, in addition to confirming the presence of a tunneling process.

4.2 Hydrogenated Silicon (a-Si:H)

4.2.1 Introduction

Amorphous hydrogenated silicon (a-Si:H) can be deposited into thin films and is primarily used in the production of solar cells, including those found on calculators

as well as larger cells [93]. Paramagnetism arises from dangling bonds on the normally 4-coordinate Si molecules in the solid, which have previously been studied by EPR [8]. In addition to demonstrating the applicability of rapid scan to analysis of a-Si:H, this sample was studied to gain a better understanding of the relaxation properties of this substance. In unpublished work communicated to Prof. Gareth Eaton by Prof. Song-I Han at the University of California Santa Barbara and Prof. Daniella Goldfarb at the Weizmann Institute of Science, relaxation times of a-Si:H were measured at low temperatures (6 and 8 K) with some variation in T_1 values depending on the fitting procedure used. It was suggested that a double exponential fit is more accurate for this system and that the faster relaxation arises from spectral diffusion. This sample was therefore examined at low temperature in addition to ambient temperature. Some of this work was published in reference [42].

4.2.2 Materials and Methods

a-Si:H was prepared [93] by Sonya Calnan and Bernd Stannowski (Competence Centre Thin-Film and Nanotechnology for Photovoltaics Berlin) and provided by Alexander Schnegg at the Institute for Silicon Photovoltaics. The sample was a fine silver dust contained in a 4 mm tube.

CW measurements were recorded on the EMX system and room-temperature pulse measurements on the E580, both at X-band. Pulse measurements between 20-70 K were recorded using liquid He on the Homebuilt pulse spectrometer. Most of the measurements at 50 K were collected by Joshua Biller. Rapid scan was performed by Deborah Mitchell.

4.2.3 Results and Discussion

CW measurements. The CW spectrum of a-Si:H was a single line with ΔB_{pp} ~ 6.0 G. The powder was so fine and lightweight that encouraging all of the sample to the bottom of the tube was difficult. This may have contributed to the relatively poor SNR seen in Figure 4.9, which was collected using 1000 averages. The level of noise in this sample was ideal for comparison between rapid scan and other EPR techniques. To ensure the CW modulation parameters (100 kHz frequency and 1.0 G amplitude) were not broadening the lineshape, CW was also collected using 30 kHz modulation frequency and 0.8 G amplitude (Figure 4.10). Both linewidths measured 6.0 G. The higher modulation was therefore used to measure as much signal as possible for collection of a power saturation curve (Figure 4.11). This curve shows that a-Si:H saturates at relatively low power. The SNR limited measurement down to around 30 dB, but another power saturation curve collected by Deborah Mitchell went to lower power. The second analysis (not shown) clearly shows a 2-step curve with saturation occurring around 5 mW.

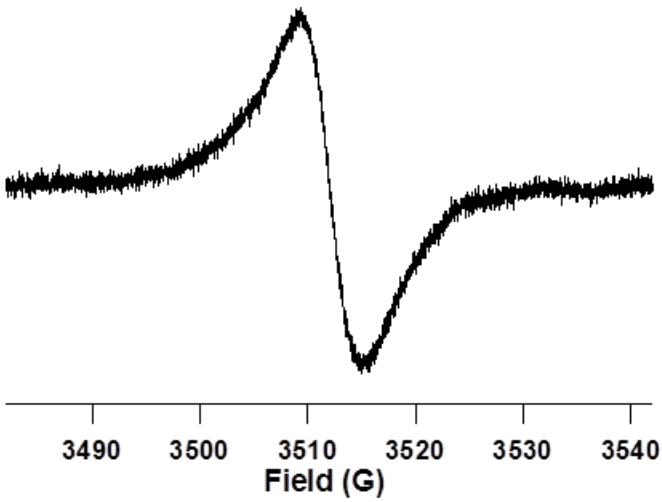

Figure 4.9. CW spectrum of a-Si:H collected with 1000 scans at room temperature. Modulation frequency was 100 KHz and modulation amplitude 1.0 G. The spectrum was collected at 4 dB (80 mW) power, which is within the saturation region in which the signal does not increase linearly with √P.

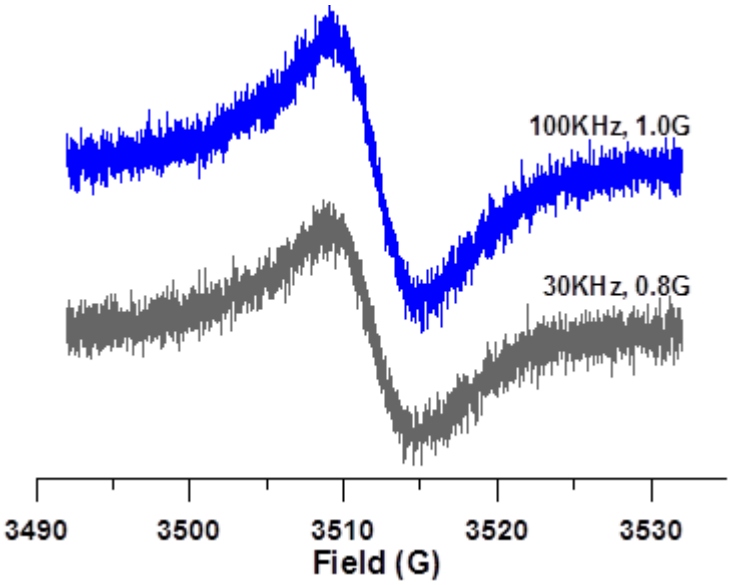

Figure 4.10. CW spectra of a-Si:H with different modulation parameters. The spectral linewidth was checked for broadening. Both spectra had a measured linewidth of 6.0 G.

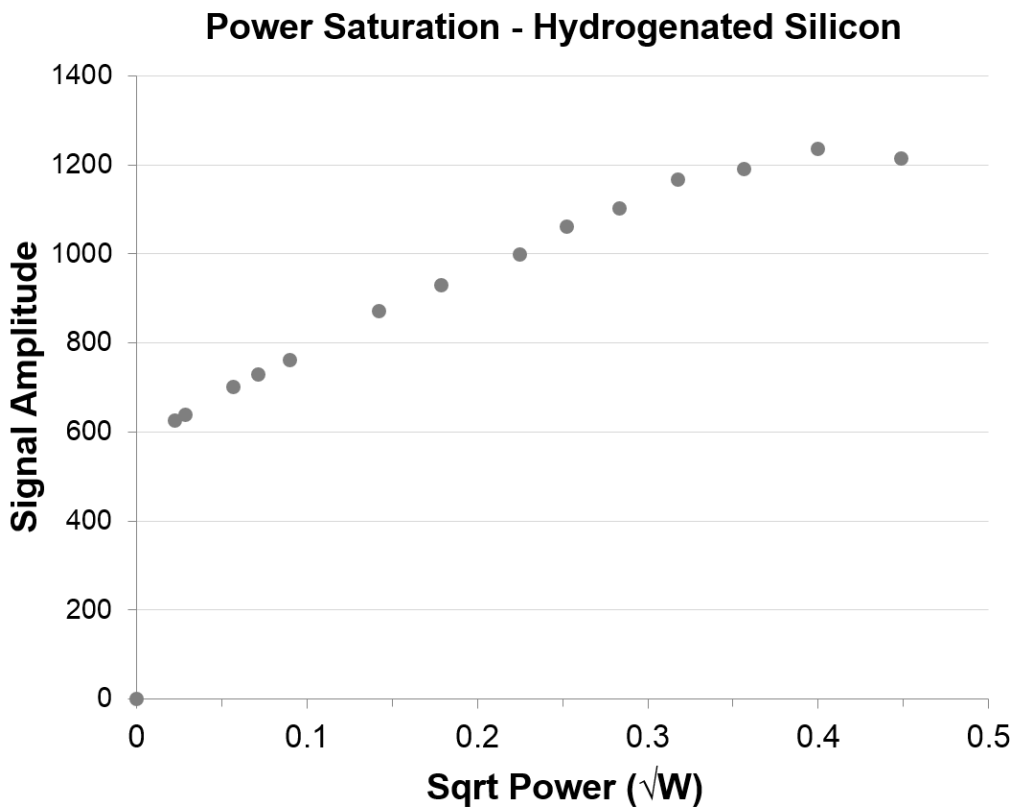

Figure 4.11. CW power saturation curve of a-Si:H. It is clear the sample saturates at relatively low power, but the region below 0.5 mW is not well defined. A second power saturation curve collected by Deborah Mitchell showed that the a-Si:H saturates around 5 mW.

Relaxation measurements. Room-temperature pulse measurements had fair SNR. Unlike the diamond samples, both T_2 and T_1 fit well to single exponential functions (Figure 4.12). T_1 was also analyzed using a double exponential, and the values were very similar to the single exponential. Results from UPEN recapitulated these findings; the distribution is primarily single exponential, with an additional shoulder suggesting a possible second contribution with similar relaxation (Figure 4.13).

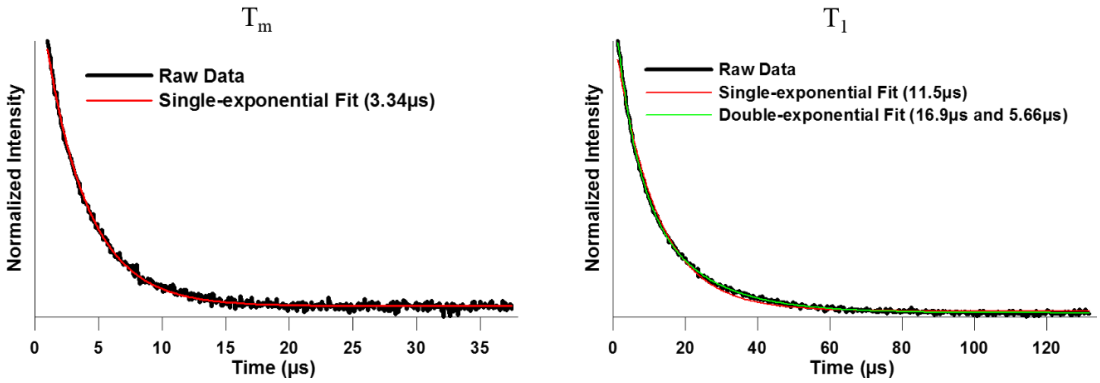

Figure 4.12. T_1 and T_m (T_2) curves for a-Si:H at room temperature. T_2 data fit well to a single-exponential function. T_1 data fit very well to a double-exponential function, and the single-exponential fit was also reasonable. The weighting of the two exponentials in Multifit was approximately equal. The signal to noise was such that the use of two significant figures for the relaxation values may be appropriate (SNR = 90). Pulse parameters were: $\pi/2$ = 40 ns, 2-step phase cycling, SRT = 500-1000 μs, 512 points, 96 shots/point. T_2 was collected in 100 scans, and T_1 in 113.

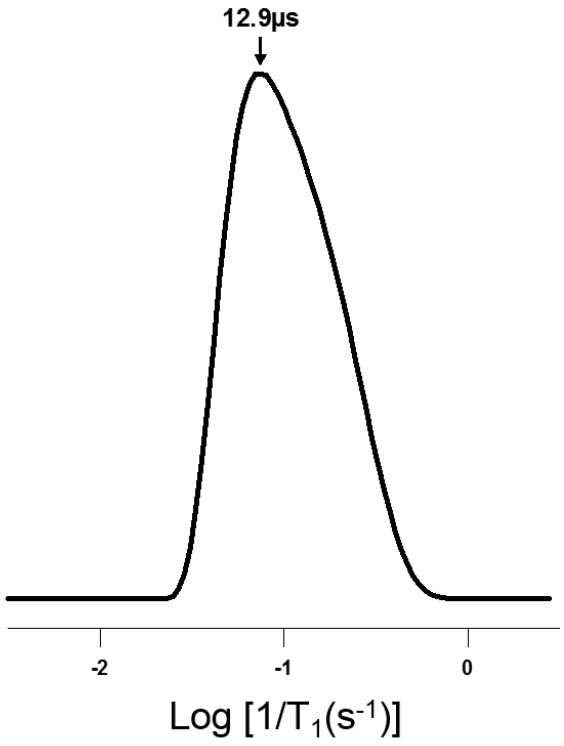

Figure 4.13. UPEN analysis of inversion recovery data for a-Si:H at room temperature. The distribution is slightly lopsided, suggesting more than one exponential. T_1 results agree between UPEN and Multifit (compare to Figure 4.12).

Relaxation becomes slightly more complicated at lower temperature. A field-swept echo-detected spectrum, which was a single peak FWHM ~10 G, was recorded prior to each measurement to find the field position of maximum echo amplitude. At 30 K, T_2 was recorded at varying pulse lengths to determine the contributions from instantaneous or spectral diffusion (Table 4.5). The consistent values of T_2 indicate little to no diffusion for this sample. Pulse lengths were varied at other temperatures as well, with similar results. T_2 fit reasonably well to single exponential functions at all temperatures, but a double exponential was slightly better, in contrast to the room-temperature spectrum (Figure 4.12 compared to 4.14).

Sample Name	π/2, π Pulses (ns)	Power (dB)	Double Exponential (S/N)	Single Exponential (S/N)
vm86029a	20, 40	13	3.0, 0.8 (129)	2.0 (69)
vm86029g	20, 40	13	3.0, 0.8 (125)	2.0 (66)
vm86029b	40, 80	19	3.1, 0.9 (97)	2.2 (65)
vm86029c	60, 120	22	3.6, 1.1 (60)	2.4 (49)
vm86029d	80, 160	25	3.9, 1.4 (68)	2.4 (58)
vm86029e	100, 200	27	4.3, 1.6 (66)	2.4 (57)
vm86029f	120, 240	30	3.7, 1.4 (53)	2.5 (48)

Table 4.5. T_2 as a function of pulse length for a-Si:H at 30 K. $\pi/2 = 20$ ns was repeated to check precision. The relatively constant values obtained for T_2 indicate little contribution from spectral diffusion. Curves were fit to all 256 points.

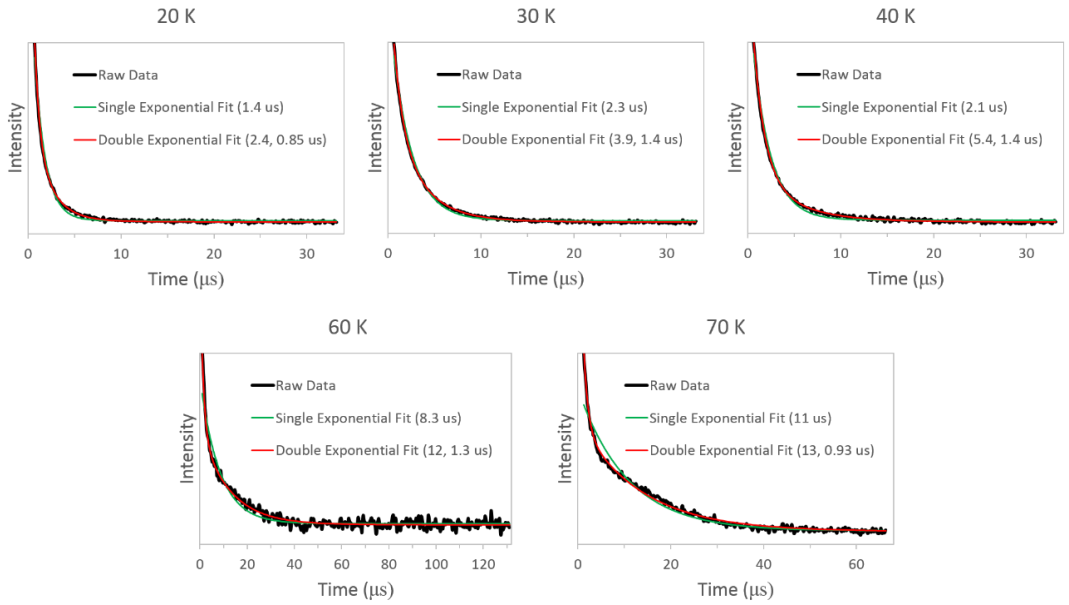

Figure 4.14. Spin echo decay curves for a-Si:H at various temperatures. Although the raw data (black) appear to have a rapid initial decay at higher temperature (60 and 70 K), the curves fit reasonably well to single exponentials (green). Double exponentials are shown for comparison (red).

T_1 follows a predictable pattern from 40-70 K; double exponential fitting in Multifit is confirmed by UPEN, and the values obtained by both programs agree well (Figure 4.15). Two exponentials at 60 K could not be separated in UPEN, but Multifit shows a reasonable fit of the raw data to a single exponential, the value of which matches UPEN. Below 40 K, T_1 was clearly multiexponential, but precise characterization was difficult. 30 K spectra were analyzed in detail using three different time windows in an attempt to accurately determine values for different contributions to T_1 (Figure 4.16). Two exponentials are well-described for each time window in Multifit, but accurate values for these processes are difficult to assign. Multifit results do not match UPEN, which shows an additional component, except for the shortest time window. This short window (Figure 4.16C) had the best agreement between the two programs, but it is clear

from the longest time window (Figure 4.16A) that there are additional components present. A similar analysis follows for T_1 at 20 K; although UPEN suggests two values, only one matches Multifit. The second value corresponds to a broad peak, and it is probable that the relaxation has additional components that cannot be separated.

It is important to note that short time windows were used for T_1 measurements below 60 K. To accurately describe T_1, the window is typically set to at least 10 times the relaxation time. This was attempted for 30 K, but relaxation seemed to increase with the length of the window. This behavior was also true at 20 K. Although the T_1 values obtained using Multifit and UPEN are skewed by the short windows for these samples, a pattern is observed based roughly on these results. The double exponential values for T_1 seem to vary linearly with temperature, suggesting a direct process contribution which may be due to spin-spin interaction. An additional contribution, which appears to be quite long compared to the other processes, appears around 40 K and is clearly temperature dependent. More measurements are needed to accurately assign these processes, but the patterns are present.

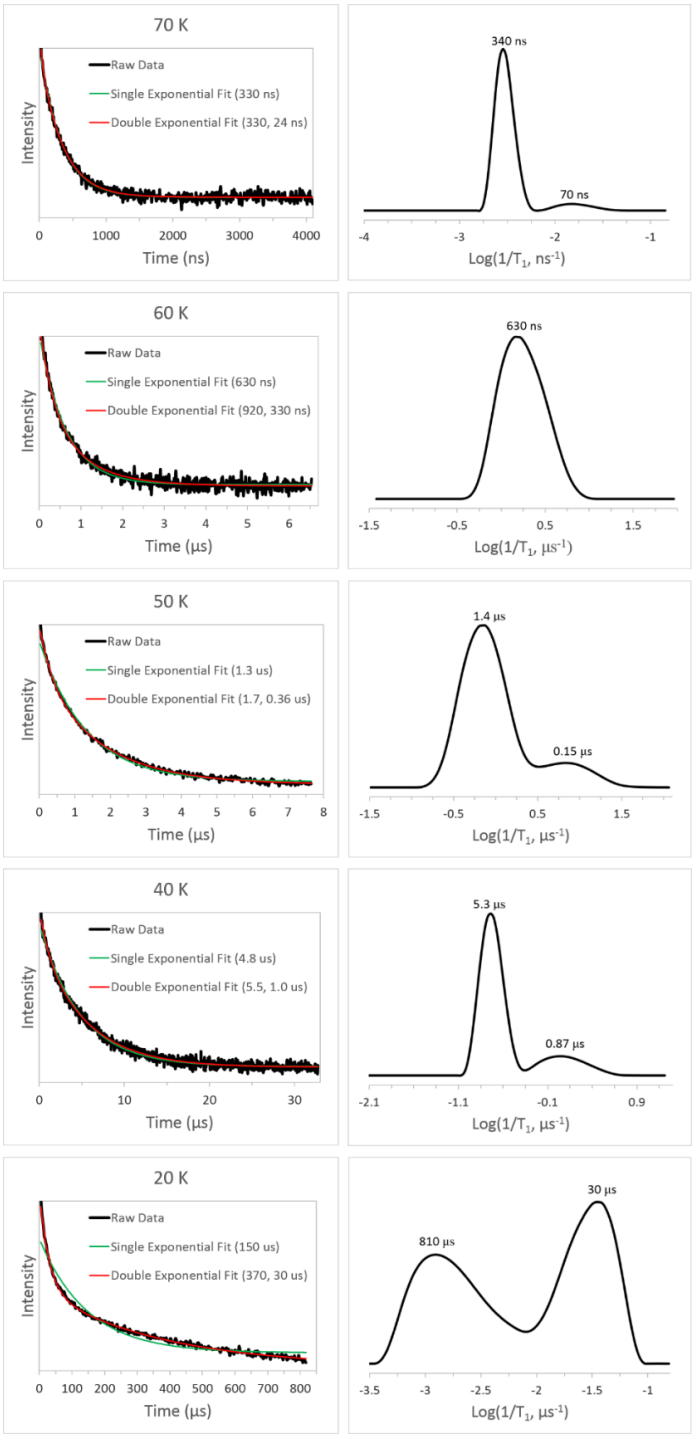

Figure 4.15. Comparison of Multifit to UPEN for T_1 data at varying temperatures of the a-Si:H sample. The two programs match well until 20 K, which requires a longer time window for accurate measurement of T_1.

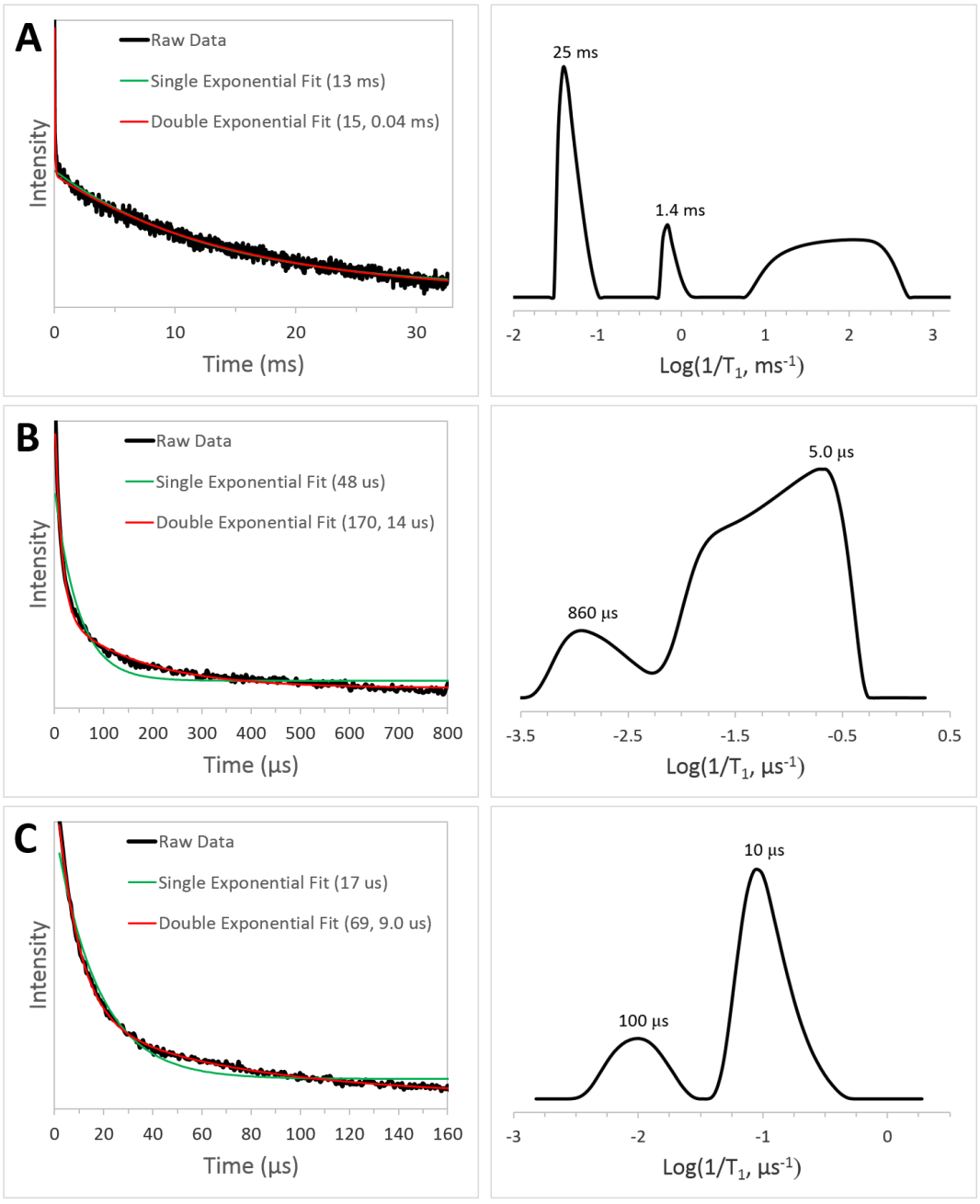

Figure 4.16. Comparison of Multifit to UPEN for T_1 data at 30 K of the a-Si:H sample. Relaxation was measured using time window lengths of 32 ms (A), 800 µs (B), and 160 µs (C). The short time window could not be correctly adjusted for measurements below 40 K; as a result, Multifit and UPEN values did not match and T_1 could not be defined.

4.2.4 Conclusions

The diamond samples emphasized the effect of concentration on relaxation, while the a-Si:H focused on the effect of temperature. At room temperature, data analysis was straightforward, and both T_2 and T_1 could be described by single exponential decay and recovery functions, respectively. At lower temperature, both T_2 and T_1 seemed to fit double exponential functions better, and at 20 and 30 K, relaxation appears to be triple exponential. Many studies have been performed using non-EPR techniques to determine accuracy of fitting multiple exponentials to a data set. Using NMR, Clayden and Hesler determined that a double exponential function could be fit with confidence if SNR $\geq$ 100, while a triple exponential fit required SNR $\geq$ 1000 [94]. On average, the SNR for T_1 between 20-70 K was 70, which is not high enough to justify a double-exponential fit. The triple exponential observed for 20 and 30 K is also difficult to verify based on these SNR requirements. For this reason, the triple exponential was not examined in detail. The trace closely follows the double exponential, and the two are difficult to distinguish. With low SNR, it has been reported that double and triple exponential functions both provide reasonable interpretations of data [95].

When taken together, accurate interpretation of T_2 and T_1 relaxation times for a-Si:H collected at low temperature as presented is challenging. At higher temperatures (60 and 70 K), T_2 appears to be longer than T_1, which is unexpected based on the nature of these relaxation times. This could be a result of the additional processes contributing to T_2 at these temperatures (see Figure 4.14), or from measurements of T_1 being skewed

by the length of the data collection time window, which was observed at lower temperature. Measurements at 30 K suggested a component of T_1 relaxation that was considerably longer than T_1 at 40 K, a trend that continued to lower temperature. These measurements were limited by the requirement of liquid He, and further measurements at additional temperatures using longer time windows would benefit comparison of T_2 and T_1 as a function of temperature for this sample.

The relatively low SNR that hindered collection of both CW and pulse measurements can be overcome using rapid scan. With rapid scan, the SNR improved over two orders of magnitude when collected in the same time as CW [42]. The diamond sample had a similar improvement in SNR using rapid scan. Like the diamond samples, a-Si:H provided an excellent example of long relaxation times that are difficult to analyze using conventional EPR techniques.

Chapter 5: Solid Organic Radicals

The solid organic radicals studied were BDPA and DPPH (Figure 5.1). Crystalline BDPA was examined, and DPPH was dissolved in polystyrene. Studies of BDPA are reported in reference [41], and studies of DPPH are reported in reference [96].

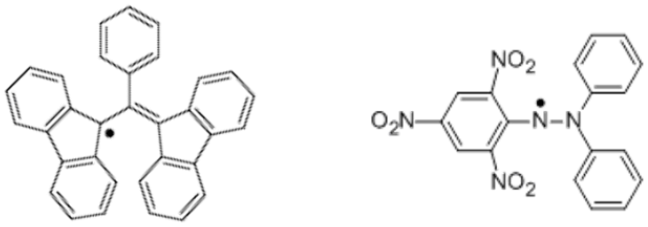

Figure 5.1. Structures of BDPA and DPPH.

5.1 BDPA

5.1.1 Introduction

BDPA (1,3-bisdiphenylene-2-phenylallyl) is a solid stable radical used for a variety of chemically-relevant applications. The most widespread application of BDPA is in NMR for dynamic nuclear polarization (DNP) experiments [97-101] in which spin polarization is transferred from electron to nuclear spins resulting in NMR signal enhancement. BDPA has been used for many other applications, including radical scavenging for kinetic studies of flavonoids [102], peroxides [103], and sulfonyl radicals [104]. The unique stability of BDPA can be utilized for charge storage in

batteries [105] and characterization of single molecules on a nanoparticle film, useful for data storage, spintronics, or quantum computing [106]. Lastly, BDPA has been used as a standard to assess high-frequency spectrometer performance [9] and has been well-characterized by EPR.

A beneficial quality of the magnetically concentrated solid BDPA is the strong CW EPR signal, which has been utilized for the development of new EPR techniques [107-109]. The initial aim of this project was to demonstrate the utility of rapid scan for extraction of T_2 from the simulation spectra at very fast rates. Solid BDPA at room temperature has a relatively short relaxation time (T_2 ~120 ns) that is difficult to measure using pulse methods but can be determined by rapid scan through simulation of the wiggle decay. T_2 values found in this manner were compared to the conventional technique of calculation using the CW linewidth and electron gyromagnetic ratio in Equation 1.6. Preliminary results performed by Deborah Mitchell showed that simulations of rapid scan data for bulk BDPA could not be fit to the spectra using a single value of T_2. About 400 different samples were then analyzed as single BDPA particles by CW. Once it was determined that different particles had different T_2 values, particles were analyzed by rapid scan, simulated, and compared to T_2 values from CW linewidth. The rapid scan spectra were also deconvolved and pseudomodulated to obtain derivative spectra, whose lineshapes were compared directly to CW. The comparisons were extended to include differences in simulation fitting and deconvolution for different scan rates, varying both scan frequency and amplitude.

5.1.2 Materials and Methods

The smallest-possible individual particles of 1:1 BDPA:benzene (Sigma Aldrich) were transferred into 0.8 mm i.d. Pyrex capillaries. These were placed inside a 4 mm quartz tube for measurement of EPR spectra. CW spectra were recorded without further manipulation of the sample. For rapid scan measurements, resonator *Q* was lowered to around 200 through addition of a 3:1 ethanol:water mixture to the 4 mm tube in the area surrounding the Pyrex capillary. Resonator *Q* was measured prior to each EPR measurement using the relationship in Equation 2.4. The calculated value of *Q* was used for rapid scan simulation to determine T_2.

5.1.3 Results and Discussion

Initial examination of heterogeneous relaxation times for solid BDPA suggested morphological variation, the extent of which depended on the size of the particle examined, as confirmed by scanning electron microscopy. CW-determined T_2 ranged from 80-160 ns for the much smaller particles required to obtain a single value. These values matched well to those determined by simulation of rapid scan spectra (Figure 5.2). Simulation was performed in MATLAB by finding T_2 values that gave the best fit to experimental data. The resulting value of T_2 is displayed in the figure. The rate is calculated from the experimental parameters by Equation 2.1. The value for resonator *Q* used in the simulation and deconvolution was that calculated prior to each measurement.

Deconvolution of the rapid scan spectra also matched well to the conventional CW spectra (Figure 5.3). The method of deconvolution was described in Section 2.3.3.

Neither T_2 nor spectral feature comparison between CW and rapid scan was successful for larger BDPA particles, which provided insight into the nature of the crystal as a heterogeneous aggregate of small particles. Additionally, the magnetic field gradient required for echo formation is not achieved over such small samples, so pulse measurements could not be compared in this study.

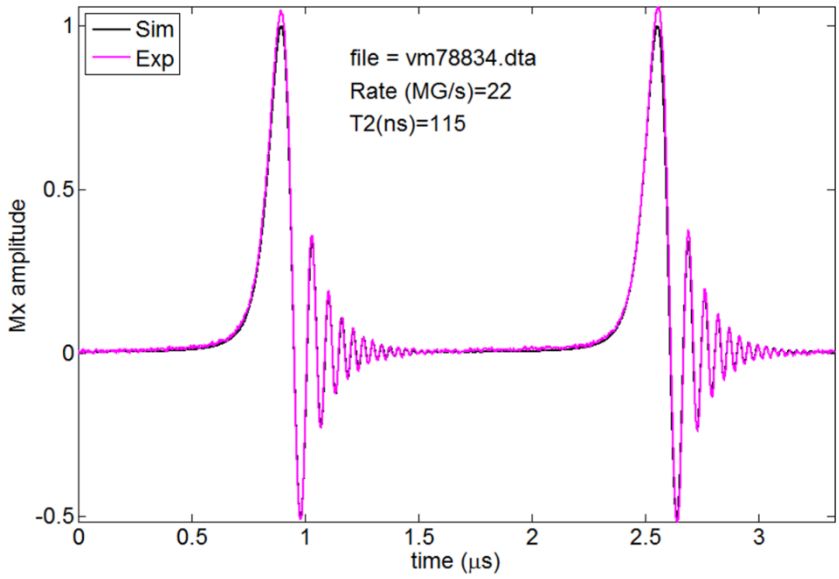

Figure 5.2. Rapid scan simulation of data for a single BDPA particle. Simulation parameters are altered to give the best fit (black) to the original rapid scan data (pink).

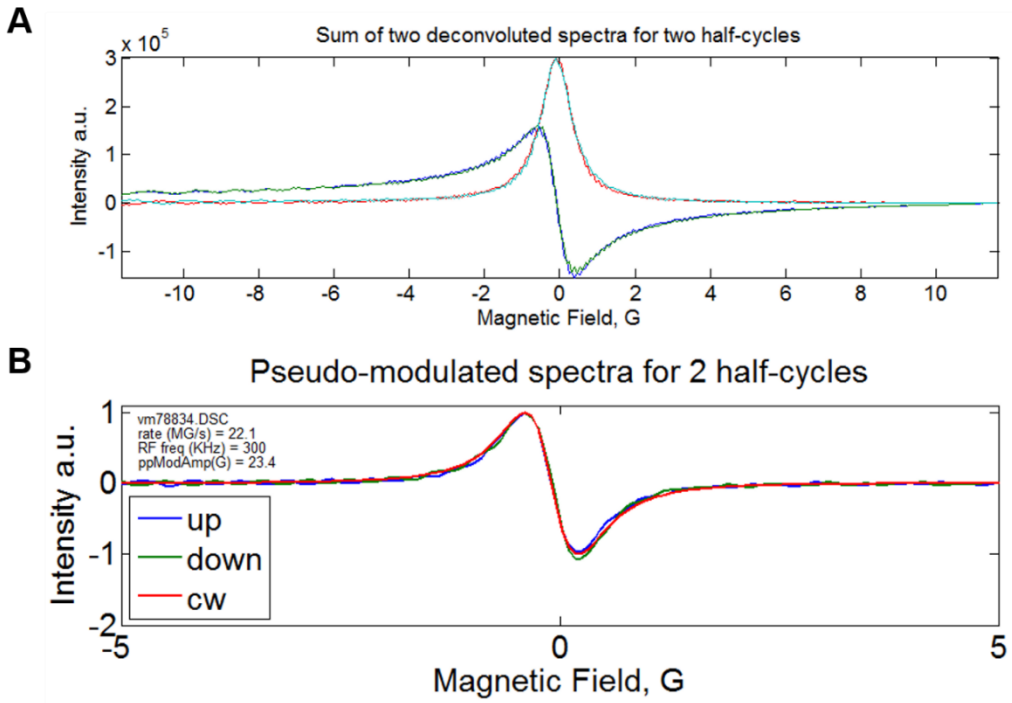

Figure 5.3. Deconvolution (A) of rapid scan signal of a single BDPA particle with comparison to CW (B). The deconvolution program converts the rapid scan signal (see Figure 5.2) to absorption ((A), red and cyan) and dispersion ((A), blue and green). The derivative of the absorption is then directly compared to the CW signal ((B), red).

5.1.4 Conclusions

BDPA has a well-characterized exchange-narrowed Lorentzian lineshape, which permits the use of Equation 1.6 to determine T_2 from the CW spectrum. Indeed, when this was attempted for bulk samples of BDPA, lineshape simulations were in good agreement with experimental data. When the same bulk samples were analyzed by rapid scan, spectra simulated using the CW-determined T_2 values fit poorly with experimental data. Rapid scan revealed that BDPA particles, so widely used in magnetic resonance, exhibited a property that had not previously been described. BDPA must now be considered a heterogeneous sample with a distribution of spin packets and numerous

overlapping Lorentzian lines. Relaxation properties of the bulk material will be especially important for future use of BDPA as a standard.

5.2 DPPH

5.2.1 Introduction

DPPH (2,2-diphenyl-1-picrylhydrazyl) is a solid stable radical that shares many properties and applications with BDPA [102, 106, 110]. In solution, DPPH has been widely used for radical scavenging, especially in food science and natural product investigation [111-114]. Like BDPA, DPPH has been used for DNP enhancement [101, 115, 116]. The well-characterized spectrum of crystalline DPPH has been used as a standard for g-factor determination [117] and for spectrometer performance evaluation [11, 118]. Although it is one of the most extensively studied radicals in EPR, questions remain regarding characteristic relaxation times of DPPH.

The electron spin relaxation times of DPPH have been studied predominantly for samples with high concentrations, in the range of 3 to 140 mM, which is typical for DNP experiments. T_1 for DPPH doped into solid matrices is concentration dependent [119-121], and the relaxation rate has been reported to be inversely proportional to the square of the concentration [122]. Prior measurements of T_1 for DPPH dissolved in polymers were performed using saturation recovery [121] and progressive saturation methods [119, 120, 122, 123], and it was observed that $1/T_1$ increased linearly with temperature up to 300 K for concentrated samples. The linear dependence of relaxation rate on temperature is characteristic of a direct process, but Bowman and Kevan pointed out that this dependence could also be described by an Orbach-Aminov process with

energy gap less than 1 K [92]. The aim of this project was to examine relaxation with decreased dopant concentration and to determine the dependence of relaxation processes on concentration and microwave frequency.

5.2.2 Materials and Methods

Preparation of samples. Two concentrations of DPPH in polystyrene were prepared: 5% (140 mM) and 0.01% (340 μM) by weight. DPPH and polystyrene beads (both Sigma Aldrich) were dissolved separately in dried toluene (Acros Organics) and then combined in the appropriate ratios. This solution was poured onto a large glass plate to form a thin film which was loosely covered with foil and allowed to dry. The sample was scraped from the glass with a razor and transferred to 4 and 1.6 mm o.d. tubes. Samples were evacuated for at least three hours (pressure < 5 mTorr) to remove oxygen and then flame sealed. The photosensitivity of DPPH was found to affect relaxation rates, so samples were covered to partially exclude light during most of the preparation. Even with storage in the dark at -20 °C, signal intensity decreased with time (Figure 5.4). Most measurements were performed on samples that had been stored for less than a week.

Figure 5.4. DPPH in polystyrene Q-band samples: 140 mM (left) and 340 μM (right). The low concentration sample is a very light purple color that turns brown after exposure to light. Degradation of the high concentration sample is less obvious.

EPR spectroscopy. Pulse measurements were carried out on the Bruker E580 spectrometer using the ER4118X-MD5-W1 (X-band) and ER5107D2 (Q-band) dielectric resonators. The magnetic field for the relaxation time measurements was set for resonance on the center of the central line of the spectrum, which was approximately the maximum intensity of the absorption spectrum, except for the high concentration sample at Q-band (Figure 5.5). T_1 measurements were recorded by inversion recovery (IR), and T_2 measurements were recorded by two-pulse echo decay. Microwave powers were adjusted to give the maximum echo at each temperature, using either 40 or 80 ns π pulse lengths. Spin lattice relaxation rates did not depend on pulse lengths. Spin echo decay times for the high concentration sample were pulse-length dependent. The SRT was always significantly longer than T_1.

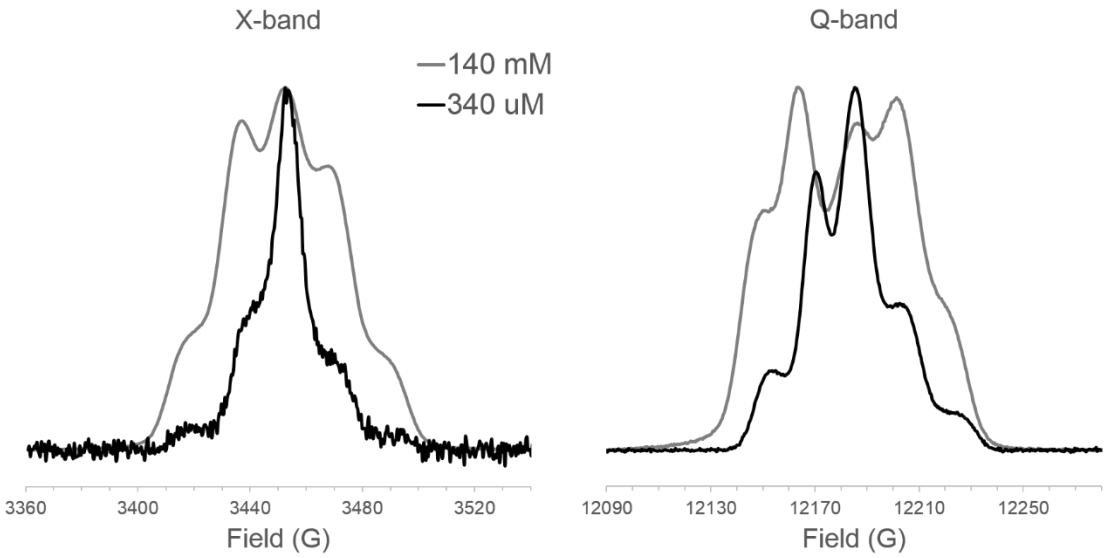

Figure 5.5. Field-swept echo-detected spectra for both concentrations of DPPH in polystyrene at X- and Q-bands. Spectra were recorded at room temperature. The high concentration sample shows signs of spectral broadening as a result of close proximity spin interactions. From X- to Q-band, the Boltzmann population is enhanced to give improved SNR at Q-band. The X- and Q-band samples were prepared independently.

For the 140 mM sample, variations in T_1 were observed that are attributed to nonuniformity in concentration through the sample. X-band measurements at 295 K for the high concentration sample were repeated at different sample positions by rotating the sample and changing the vertical position in the resonator. Eighteen measurements were recorded on five different days, giving an average T_1 value of 6.7 ± 2.0 μs and a range of values from 3.5 to 10 μs. This broad range and deviation demonstrates sample heterogeneity and the importance of sample positioning on reproducibility. The values in Figure 5.7 for the temperature dependence of T_1 were collected at the same position, except for the need to reposition when transitioning from liquid He to liquid N_2 at 80 K.

CW EPR was used to examine the half-field transition of the 140 mM sample at X-band. Spectra were collected around g-values of 2.0036 and 4.0072 on the EMX with

an ER4122-SHQ resonator at room-temperature. Parameters for both measurements were: 150 G sweep width, 100 kHz modulation frequency, 1.0 G modulation amplitude, and 0.6 mW power. Only the instrument gain and number of scans were modified to obtain the most accurate comparison between the two lines.

Data analysis. The experimental IR curves were not single exponentials. To characterize the distributions, outputs from Multifit were compared to those from UPEN. IR data for solid samples may include contributions from spectral diffusion, as well as T_1 [18], so for data sets that were fit better with two components, the shorter component was attributed to spectral diffusion and the longer component to T_1. Conversely, spin echo decay curves fit well to single exponential functions. T_2 values were determined using Multifit with a single exponential. At 140 mM, T_2 is dominated by spin diffusion, causing enhanced relaxation rates. Therefore, analysis of T_2 data focused on the 340 μM sample, which is sufficiently dilute to decrease contributions from spin diffusion.

The processes contributing to T_1 were modeled using the Mathcad program that fits the temperature dependence of $1/T_1$ as a sum of individual contributions. Modeling of the 340 μM data was based on Equation 5.2,

$$\frac{1}{T_1} = A_{dir}T + A_{Ram}\left[\left(\frac{T}{\theta_D}\right)^9 J_8\left(\frac{\theta_D}{T}\right)\right] + A_{loc}\left[\frac{e^{\Delta_{loc}/T}}{\left(e^{\Delta_{loc}/T} - 1\right)^2}\right] \qquad (5.2)$$

where contributions to T_1 relaxation include direct, Raman, and local mode vibrations. In Equation 5.2, A_x refers to the coefficient for a given contribution and T is temperature

in Kelvin. The Debye temperature is given by θ_D, while J_8 is the transport integral (Equation 5.3). The energy separation for the local mode process is represented by Δ_{loc}.

$$J_8\left(\frac{\theta_D}{T}\right) = \int_0^{\frac{\theta_D}{T}} x^8 \frac{e^x}{(e^x - 1)^2}\, dx \qquad (5.3)$$

The fits to experimental data for the 340 μM sample were accomplished through iterations of contributions from the various processes, to minimize the sum of the squares of the residuals (Figure 5.7). Since there is no known low-lying excited state, an Orbach process was not included in the analysis for the low concentration samples.

5.2.3 Results and Discussion

Analysis of T_1 for 340 μM DPPH in polystyrene. The distributions of relaxation times as a function of temperature obtained with UPEN for 340 μM DPPH in polystyrene are shown in Figure 5.6. At X-band, the IR data at most temperatures fit well to a single exponential function (Figure 5.6A), and the analysis showed predominantly a single peak in the distributions. The single component fits were used for the analysis of temperature dependence (Figure 5.7A). At Q-band, the analysis of the IR curves indicated two components at all temperatures (Figure 5.6B). The characteristic time for the slower process as calculated with a two component fit in Multifit was attributed to T_1. The relaxation rates at X- and Q-band are similar, which indicates that the dominant contributions are frequency independent. Figure 5.7 shows the contributions from each of the processes to T_1 for 340 μM DPPH in polystyrene. The values of the coefficients (s^{-1}) in Equation 5.2 that gave the best fits to the experimental data were: (X-band) A_{dir}= 0.2, A_{Ram} = 6.0x10^3, and A_{loc}= 2.1x10^4; (Q-

band) A_{dir}= 0.3, A_{Ram}= 2.6x10^3, and A_{loc} = 1.9x10^4. Values θ_D = 110 K and Δ_{loc} = 500 K were the same at both frequencies. The Raman process dominates relaxation at low temperatures, along with a small direct process contribution. A local mode becomes significant at high temperatures. The set of processes are similar at the two frequencies, with slightly increased direct process contribution at Q-band.

The model in Equation 5.2 for the temperature dependence of T_1 for the 340 μM sample fit the experimental data very well (solid black lines in Figure 5.7). The relaxation rates for DPPH at 100 K and 298 K are compared with those for other organic radicals in dilute glassy matrices in Table 5.1. The overall trend at both temperatures is toward shorter relaxation times for larger deviation of g-values from 2.0023. The dominant contributions to relaxation are the Raman process at 100 K and the local mode at 298 K, which also are the primary contributions to relaxation for other organic radicals in sucrose octaacetate at these temperatures [14]. The similar trends in relaxation rates at the two temperatures indicate that A_{loc} and A_{Ram} are correlated, which suggests that both processes modulate spin-orbit coupling.

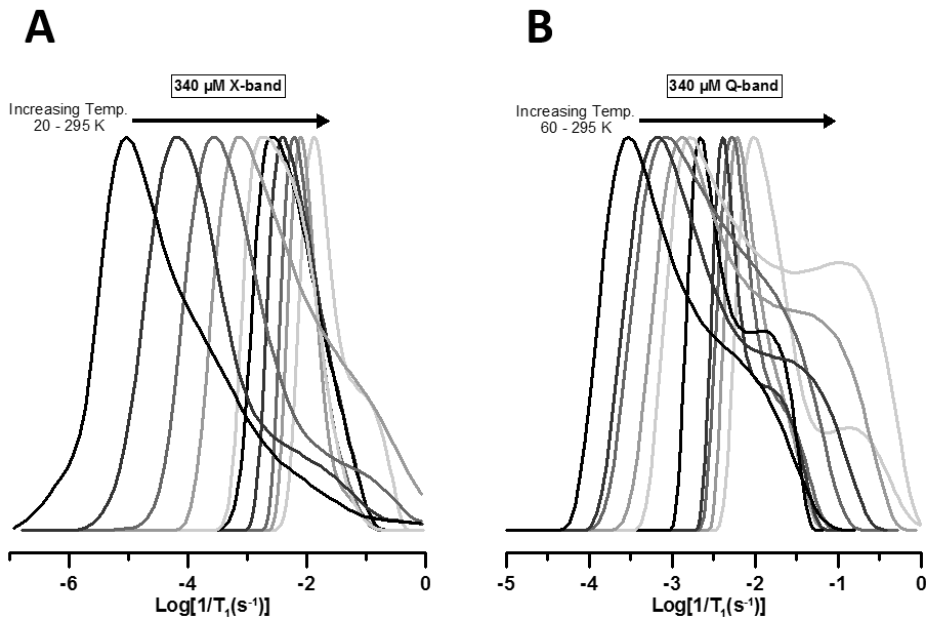

Figure 5.6. X-band (A) and Q-band (B) UPEN analyses for 340 µM DPPH in polystyrene. Different temperature ranges were used for clarity. Figure from reference [96].

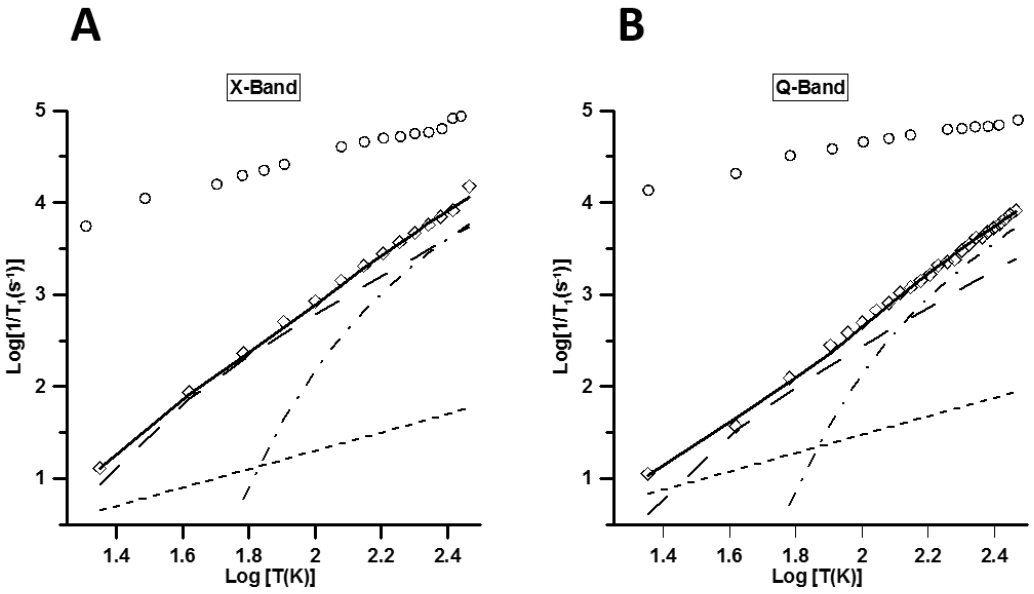

Figure 5.7. X-band (A) and Q-band (B) log-log plots of $1/T_1$ vs. temperature for 340 µM (◊) and 140 mM (O) DPPH in polystyrene. The contributions to T_1 (fit in solid black) for the 340 µM sample are the Raman process (large dash), a local mode (dot dash), and the direct process (small dash). The magnitude of each contribution is similar for the two frequencies. Figure from reference [96].

Radical	Matrix	Conc. (mM)	g_{iso}	T_1 at 100 K	T_1 at ~298K	Reference
BDPA[a]	Sucrose octaacetate	< 3	2.0026	10 ms	1 ms	[14]
BDPA[a]	Polystyrene	0.2	2.0026	47 ms[c]	90 µs	Unpublished
DPPH	Sucrose octaacetate	< 3	2.0036	1 ms	100 µs	[14]
DPPH	Polystyrene	0.34	2.0036	1.2 ms	65 µs	[96]
Galvinoxyl	Sucrose octaacetate	< 3	2.0044	300 µs	8 µs	[14]
TPHIO[b]	Sucrose octaacetate	< 3	2.0059	300 µs	40 µs	[14]
Tempone	1:1 water:glycerol	1	2.0059	150 µs	N/A	[124]
Tempone	Sucrose octaacetate	< 3	2.0060	80 µs	4 µs	[14]

[a] 1,3-bisdiphenylene-2-phenylallyl
[b] 1,1,3,3-tetraphenylisoindolin-2-yloxyl
[c] T_1 at 80 K

Table 5.1. T_1 values for organic radicals in glassy matrices at X-band. Table from reference [96].

The temperature dependence of T_2 for the 340 µM sample is shown in Figure 5.8. $1/T_2$ is faster at about 140 K than at higher and lower temperatures. A similar enhancement in spin echo dephasing has been reported for a spin-labeled polystyrene [125]. The enhancement with maximum impact at about 140 K was attributed to a wagging motion of the phenyl groups of the polystyrene, which is likely to also apply to the DPPH in polystyrene sample. The increase in relaxation rates above about 200 K is attributed to softening of the polystyrene matrix.

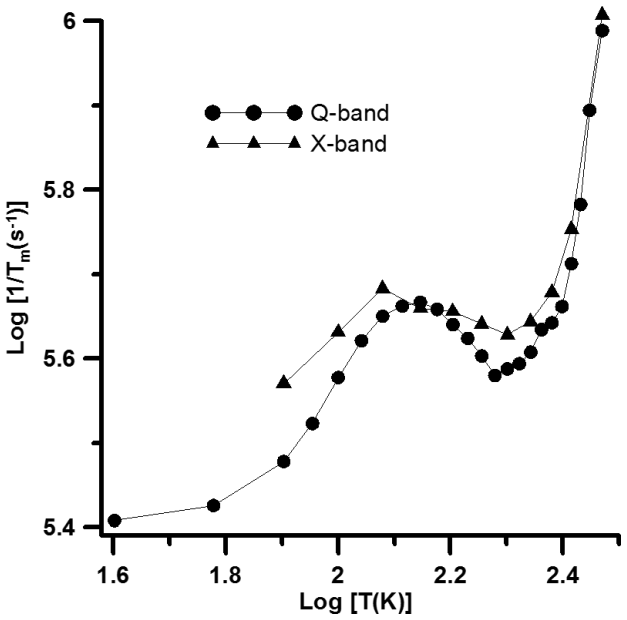

Figure 5.8. X-band (▲) and Q-band (●) log-log plots of $1/T_2$ vs. temperature for 340 μM DPPH in polystyrene. The enhancement around log T = 2.1 is attributed to a phenyl group wagging motion. Figure from reference [96].

Analysis of T_1 for 140 mM DPPH in polystyrene. As reported by others, T_1 for DPPH doped in solid matrices is strongly concentration dependent [119-122], and relaxation rates for the 140 mM sample are orders of magnitude faster than at lower concentrations (Figure 5.7). The strong electron-electron interactions in the 140 mM sample are confirmed by the observation of a half-field transition (Figure 5.9), from which an average electron-electron distance (r) of about 9 Å was calculated (Equation 5.4 [126]), which is similar to the 13 Å expected if this concentration were uniformly distributed [127].

$$\text{relative intensity} = \frac{A}{r^6}\left(\frac{9.1}{\nu}\right)^2 \qquad (5.4)$$

Relative intensity is the comparison of CW spectral integration in CWLV, and ν is the operating frequency of the instrument. The coefficient A is equal to 19.5 for organic biradicals close to the free-electron g-value.

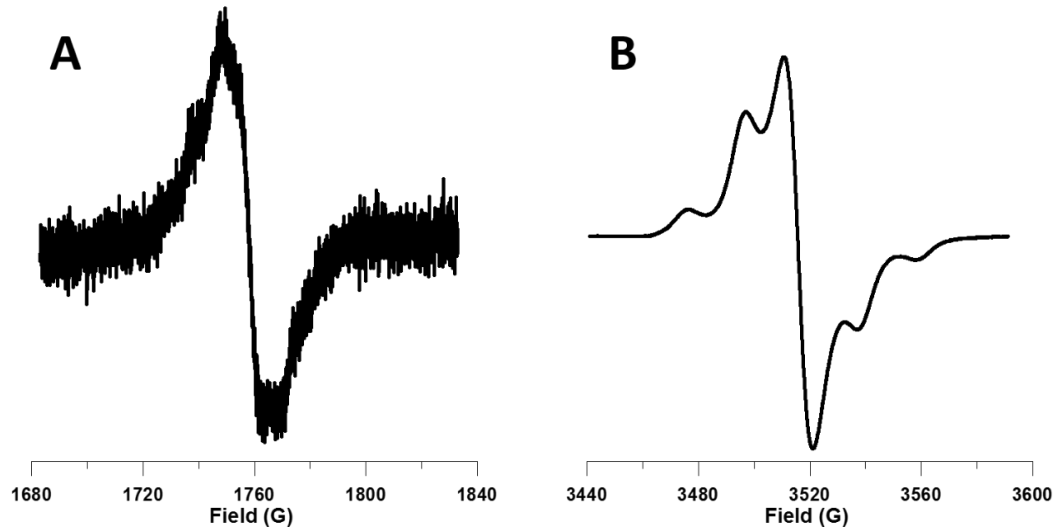

Figure 5.9. Half field spectrum (A) and g = 2.0036 spectrum (B) of 140 mM DPPH in polystyrene. Both spectra were recorded with 0.6 mW power and 1.0 G modulation amplitude at 100 kHz modulation frequency. The half-field transition is the average of 1280 scans, and the g = 2.0036 signal was recorded in a single scan. Figure from reference [96].

At this high concentration of DPPH, analysis of IR curves becomes difficult due to the wide distribution of T_1 values that is attributed to localized concentration variations in the sample. Analysis of the data with UPEN showed broad and poorly defined distributions. The values in Figure 5.7 are the longer components obtained by fits with two exponentials. At 140 mM, the relaxation rates at X- and Q-band are similar and vary approximately inversely with temperature as reported previously [119-123]. The contributions from the Raman and local mode process that dominated for the low concentration sample are very small relative to the experimental relaxation rates for the high concentration sample. The absence of significant frequency dependence of T_1 rules

out contributions from thermally-activated processes [128]. These rates (Figure 5.7) are still significantly slower than the temperature-independent value of 0.2 μs reported for magnetically concentrated DPPH at 28 MHz [129].

Strong electron-electron interactions dominate relaxation processes at X- and Q-band for 140 mM DPPH in polystyrene and make the relaxation much faster than at lower concentrations. The relaxation times at 77 K at X- and Q-band are 3.9×10^{-5} and 2.7×10^{-5} s, respectively. These values are similar to the previously reported values at 77 K at X-band (read from plots) of 8×10^{-6} s [120] and 2.5×10^{-5} s [123] for 140 mM DPPH in polystyrene. For 44 mM BDPA in sucrose octaacetate between 90 and 290 K at Q-band, $1/T_1$ was approximately linearly dependent on temperature, although at lower concentrations its relaxation was dominated by Raman and local mode processes [130]. This dependence of $1/T_1$ on T is similar for the high concentration samples of both DPPH and BDPA. It has been proposed that the dependence of $1/T_1$ on T for DPPH is due to the direct process [123] or to an Orbach process with energy less than 1 K [92]. Frequency dependence is predicted for the direct process [131], so the similarity in relaxation rates for the high concentration DPPH sample at X-band and Q-band (Figure 5.7) is not consistent with assignment of a direct process.

5.2.4 Conclusions

IR measurements of T_1 for 140 mM DPPH in polystyrene confirm the results obtained in prior studies using CW power saturation that T_1 varies approximately linearly with 1/T. The similarity in relaxation rates at X- and Q-band suggests that the primary contribution to T_1 relaxation at this high concentration may not be the direct

process. At lower concentrations (340 μM), the temperature dependence of $1/T_1$ is similar to that of other organic radicals in glassy solvents, and is dominated by the Raman process and a local mode. A local minimum in T_2 at about 140 K is consistent with prior assignment of phenyl motion within the polystyrene matrix.

5.3 Summary

This chapter dealt with samples that were studied for very different purposes. The BDPA project began as a means to show the utility of rapid scan as a new EPR technique. This evolved into an elegant example of rapid scan revealing spectral features that cannot be seen with CW. The DPPH project was motivated by prior papers reporting relaxation for very high concentrations of DPPH in polystyrene. Using more advanced techniques, results showed that these concentrations did not allow accurate description of relaxation mechanisms. By preparing a lower concentration of DPPH in polystyrene, the processes contributing to T_1 could be identified.

Chapter 6: Radicals in Solution

The EPR properties associated with paramagnetism in solids arising from lattice defects, partially filled atomic orbitals, or free radicals, can be vastly transformed for compounds studied in solution. Orientation dependence is replaced with motional averaging, and different processes contribute to relaxation, hyperfine interactions, concentration effects, and other properties. BDPA and DPPH were the only radicals to be studied both as solids and in solution in this project. Comparison of different states of these compounds provides less insight into their relaxation properties than comparison to other dissolved radicals. For this reason, a variety of dissolved compounds are introduced in this section for a more complete survey of radicals in solution.

6.1 BDPA, DPPH, Galvinoxyl, and Thianthrene

6.1.1 Introduction

BDPA and DPPH. Applications of solid BDPA and DPPH were discussed in the previous chapter. BDPA is a unique carbon-centered radical containing no heteroatoms, which can significantly impact electron spin relaxation. Relaxation times of dissolved BDPA were compared to other organic radicals, providing insight into the effects of molecular structure and heteroatoms on electron spin relaxation.

Galvinoxyl. Similar to BDPA and DPPH, galvinoxyl (Figure 6.1) is used for a variety of different applications, including DNP [132, 133]. Like DPPH, galvinoxyl has

been used to assess antioxidant activity of many different food products [134-136], including spices [137], teas [138], and oils [139]. Galvinoxyl has also been used for synthesis of unusual compounds [140], particularly with multiplet ground states [141-143]; stabilization and interaction of multiplet states with galvinoxyl have been studied extensively by EPR [144-146].

Relaxation properties of galvinoxyl were analyzed for comparison to other organic radicals in solution. The primary aim was to examine the influence of structural features (heteroatoms, charge, and size) on relaxation times of tumbling radicals. Compounds involved in this study include BDPA, DPPH, PDT, mHCTPO, thianthrene, and Triarylmethyl radicals OX63 and Trityl-CH_3.

Figure 6.1. Structures of galvinoxyl and the thianthrene cation radical.

Thianthrene cation radical. Like galvinoxyl, thianthrene was used for comparison of relaxation to other organic radicals in solution. Thianthrene belongs to a unique class of ion-radicals in which both the charge and electron density are fully delocalized (Figure 6.1). Thianthrene itself is a neutral compound, but the cation radical forms via several routes, notably exposure to strong acid. The majority of EPR using the thianthrene radical was performed in the 1950s and 1960s where studies focused on structure elucidation and identification of coupling species [147]. A lag in EPR studies of thianthrene followed, ending briefly in the early 1990s. EPR was used to identify the

thianthrene cation radical created spontaneously through adsorption of the neutral precursor to acid zeolites [148] or clay [149], via photoinduced electron transfer. More recent studies involving the cation radical focus on applications to organic chemistry [150] or use of thianthrene derivatives as EPR-active oxidation probes [151]. Although EPR studies have dwindled, the thianthrene cation radical contributed to the furthering of EPR as a powerful spectroscopic technique in the early years of the field.

6.1.2 Materials and Methods

BDPA. To study BDPA in solution, an individual particle was dissolved in toluene, and oxygen was removed by N_2 purge. The concentration was measured by UV-vis absorbance at 488 nm [41]. Solutions were prepared from single BDPA particles for comparison of CW to rapid scan EPR, but samples of known concentration in toluene (0.7, 1.4, 2.8, 5.5, and 12.5 μM) were also prepared to characterize concentration effects on relaxation times.

DPPH. For characterization in solution, DPPH was dissolved in toluene to a concentration of 12.0 μM. This value was confirmed by UV-vis absorbance at 515 nm using an extinction coefficient of 12000 $M^{-1}cm^{-1}$ [110]. The solution was degassed by FPT and sealed.

Galvinoxyl and thianthrene. Galvinoxyl in toluene (2.8 μM, confirmed by UV-vis absorbance at 428 nm with extinction coefficient 175000 $M^{-1}cm^{-1}$ [152]) was prepared for comparison of relaxation to BDPA and DPPH in toluene. Solid thianthrene, also for comparison to BDPA and DPPH, was prepared [153] by Ashley McDaniel in the laboratory of Prof. Matthew Shores at Colorado State University. Due

to limited solubility, thianthrene was dissolved in trifluoroacetic acid (TFA) instead of toluene. Thianthrene is extremely water-sensitive, so samples were run immediately following preparation and maintained under continuous N_2 purge. Several concentrations were prepared (90-700 μM). Degradation was monitored over several days by measuring decreasing UV-Vis absorbance. FPT preparation was attempted, but sample degradation was too rapid for practicality.

EPR spectroscopy. CW spectra were collected on the Bruker EMX and EMX Plus systems. Pulse measurements were performed on the Homebuilt pulse system at X-band. T_2 was collected by spin echo decay and T_1 by inversion recovery (IR). Rapid scan was collected on the Bruker E500T with the FlexLine ER4118X–MD5 dielectric resonator. Magnetic field scans were formed using a Tektronix AWG2021 arbitrary waveform generator operating with around 1% duty cycle.

6.1.3 Results and Discussion

Comparison of rapid scan to CW for BDPA. Rapid scan of BDPA in solution was compared to CW as an offshoot of the analogous comparison study on solid BDPA particles. BDPA is soluble in many organic solvents excluding water [10], so toluene was used to dissolve a single BDPA particle. The very narrow linewidth of solid BDPA is largely caused by exchange interactions that average hyperfine interaction. In solution, hyperfine splitting becomes increasingly defined with oxygen removal. Oxygen was removed for CW measurement by N_2 purge. For rapid scan, *Q* is usually lowered using a water/ethanol mixture, but purging rapidly evaporates the ethanol. The rapid scan spectrum was therefore obtained by removing the purge line, adding the

water/ethanol and quickly collecting the spectrum before considerable oxygen could be absorbed. An initial comparison of rapid scan and CW was completed, with some discrepancy in the amount of degassing between the two experiments (Figure 6.2). Considering the large effect of oxygen concentration on hyperfine resolution, the two spectra matched very well.

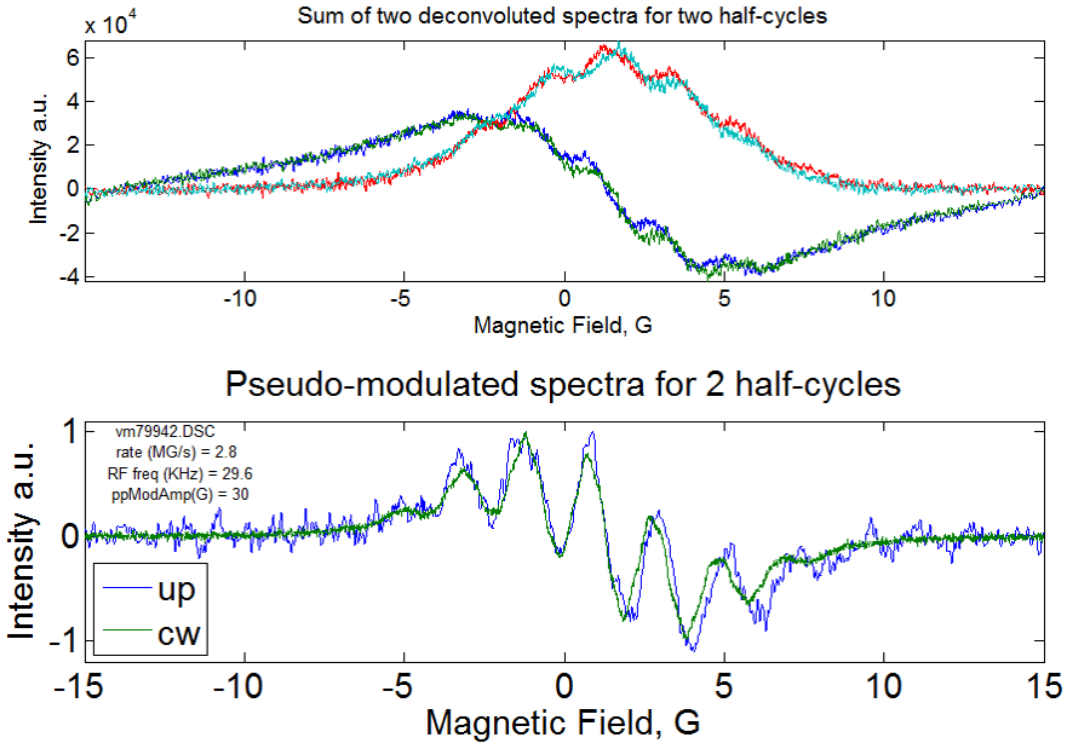

Figure 6.2. Deconvolution (green) of dissolved BDPA compared to CW (blue). Traces in the top panel correspond to the rapid scan signal (absorption, red and cyan and dispersion, blue and green) for a single cycle of up and down scans collected with 204800 averages. The sample had been purged for three hours prior to measurement. Additional rapid scan parameters are listed in the bottom panel. CW was collected with 4096 points in 16 scans after purging for one hour. Modulation frequency and amplitude were 30 kHz and 0.08 G.

Broadening of the rapid scan spectrum was attributed to mathematical signal filtering in the deconvolution program. Additional splittings were apparent in the CW spectrum, which does not appear to be fully degassed. Another experiment was

therefore performed to determine the amount of purging necessary for complete hyperfine resolution. It became evident that purging the dissolved BDPA samples would take too long to be practical (Figure 6.3). Therefore, a sample was prepared via freeze-pump-thaw to remove the oxygen, and this sample was used for CW and pulse measurements. Rapid scan could not be collected on this sample as the solvent (toluene) was not lossy enough to decrease resonator *Q* an appropriate amount. Recent synthesis of a water-soluble adduct [10] may allow for this comparison in the future.

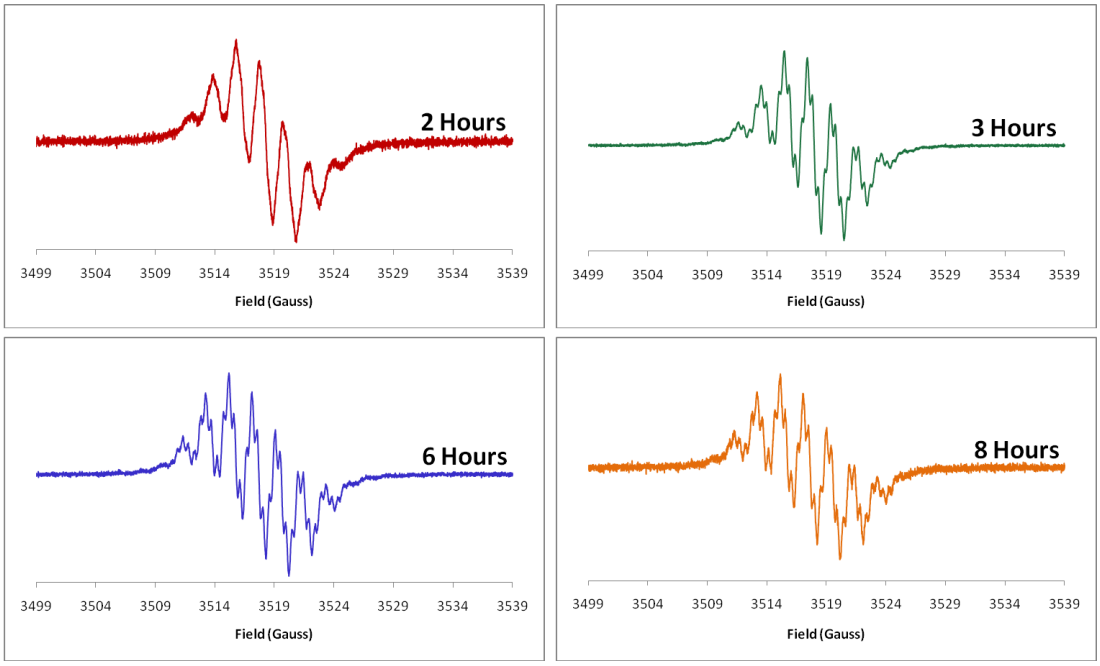

Figure 6.3. Resolution of hyperfine lines with increased N_2 purge times. CW spectra were collected with 4096 points, averaging 25 scans using 10 kHz modulation frequency and 0.01 G amplitude.

Comparison of BDPA relaxation to that of other organic radicals. Table 6.1 provides a summary of the radicals presented in this section. The radicals studied have molecular masses between 170-1340 g/mol and are dissolved in low viscosity solvents. Tumbling correlation times are short enough to be at or near the fast tumbling regime

where T_1~T_2 and both T_1 and T_2 may become shorter as the tumbling correlation time decreases, depending on the relaxation mechanism. The concentrations were selected to be in the range in which collisions do not dominate relaxation.

Structure	Compound	Solvent	Concentration	T_2 (μs)	T_1 (μs)
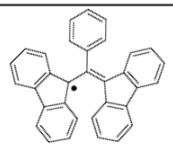	**BDPA (496 g/mol)**	**Toluene**	**0.70 μM**	**9.8**	**12**
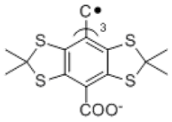	**Trityl-CH_3 (975 g/mol)**	**Water**	**0.20 mM**	**9.1**	**16**
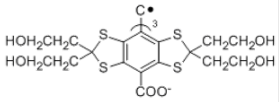	**OX63 (1340 g/mol)**	**Water**	**0.20 mM**	**6.4**	**15**
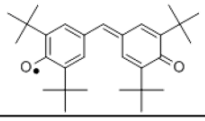	**Galvinoxyl (422 g/mol)**	**Toluene**	**2.8 μM**	**2.1**	**2.8**
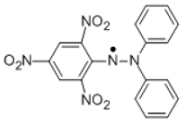	**DPPH (394 g/mol)**	**Toluene**	**12 μM**	**1.3**	**2.0**
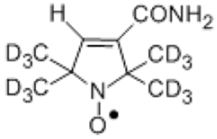	**mHCTPO (195 g/mol)**	**Toluene**	**0.40 mM**	**0.52**	**0.55**
		Water	**0.25 mM**	**0.53**	**0.64**
		Water	**60 μM**	**0.65**	**0.76**
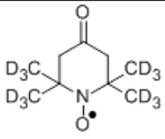	**PDT (170 g/mol)**	**Water**	**0.25 mM**	**0.56**	**0.59**
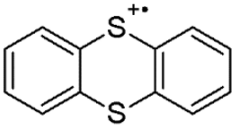	**Thianthrene (216 g/mol)**	**TFA**	**Unknown (degraded)**	**0.1 - 0.4**	**0.4 - 1**

Table 6.1. Molecular properties that contribute to relaxation for the radicals in solution. Size, shape, tumbling correlation times, and concentration affect molecular collisions in a predictable manner for these compounds. The trityl-CH_3 and OX63 measurements were described in [154]. The 60 μM mHCTPO measurements were collected by Joshua Biller and Hanan Elajaili.

Initial relaxation measurements were performed on a single particle of BDPA dissolved in toluene and sealed following FPT. The T_2 measured for the BDPA sample was 15 μs, which is quite long compared to other organic radicals in solution. After 24 hours, the T_2 had increased to just under 20 μs, indicating sample degradation leading to lower radical concentration. A new sample was made at a known concentration of 12.5 μM. The T_2 of this sample was initially 1.2 μs, but rose to 8.2 μs after 48 hours. The rapid changes in T_2 with sample degradation prompted an examination of the impact of concentration on relaxation times of BDPA. Figure 6.4 shows the strong concentration dependence of relaxation for this radical, which is attributed to π-stacking and molecular collisions. T_2 and T_1 values for various concentrations were monitored over several days, along with dissolved galvinoxyl and DPPH (Table 6.2). Galvinoxyl displayed slight concentration dependence and degradation, while DPPH relaxation stayed constant. Unlike BDPA, the unpaired electrons of galvinoxyl and DPPH have substantial spin density on oxygen and nitrogen atoms, respectively. Spin-orbit coupling with the heteroatoms shifts the g-values away from 2.0026 and enhances spin lattice relaxation, decreasing both T_1 and T_2.

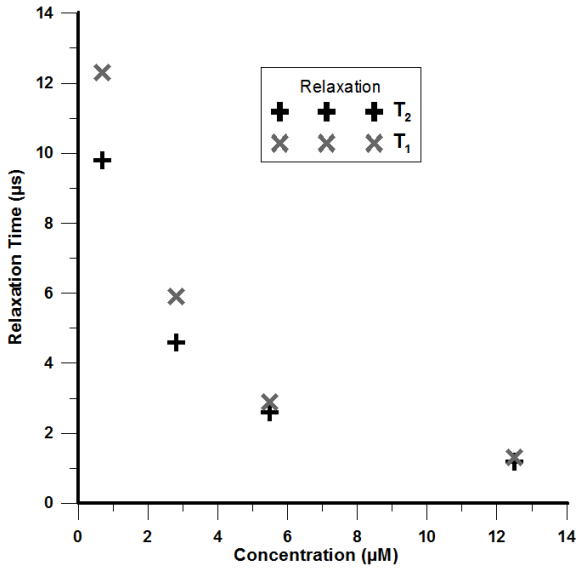

Figure 6.4. Relaxation times for BDPA in toluene as a function of concentration. The strong concentration dependence is attributed to π-stacking and radical-radical collisions. Pulse parameters: π/2 = 40 ns, SRT = 200-400 µs, 256 steps, 512 points/step, d_1 = 300 ns, 9.4 GHz. Power was adjusted to maximum echo height, and gate was FWHM on oscilloscope.

T_2 (µs)	conc (µM)	initial	24 hours	72 hours		T_1 (µs)	conc (µM)	initial	24 hours	72 hours
	12.5	1.2		8.2			**12.5**	1.3		18
	5.5	2.6	11	12			**5.5**	2.9	21	30
	2.8	4.6	14	14			**2.8**	5.9	28	29
	1.4	2.0	15	14			**1.4**	2.1	30	31
	0.7	9.8	27	21			**0.7**	12	65	55
	galv 2.8	2.1	2.8				**galv 2.8**	2.1	3.8	
	DPPH 12.0	1.3	1.3				**DPPH 12.0**	2.0	2.0	

Table 6.2. Degradation and relaxation concentration dependence of BDPA in toluene compared to galvinoxyl and DPPH. The difference in relaxation times comparing 24 to 72 hours is likely not a concentration effect but rather a consequence of the very poor SNR for the degraded samples.

The degradation of BDPA caused much larger changes in relaxation than the other radicals studied, so additional samples were prepared to better understand this

system. Regardless of the initial concentration of BDPA, T_2 and T_1 increased to around 14 and 30 μs, respectively, for all samples except the lowest concentration prepared. Following initial degradation, these values were stable for at least two weeks. Possible conversion of the paramagnetic BDPA radical to the diamagnetic form was investigated by dissolving a single crystal in carbon tetrachloride and recording an NMR spectrum after the sample sat for two days. There was a small peak in the aromatic region, but not enough to account for a large change in concentration. Ultimately, the degradation mechanism was not elucidated for BDPA in toluene, although it is possible that the carbon-centered radical reacts at a phenyl ring position, a phenomenon seen for the triphenylmethyl Gomberg radical [155, 156].

The structure of BDPA parallels other triarylmethyl (trityl) radicals, and this class of compounds share many magnetic properties. BDPA and other trityls are carbon-centered radicals with g-values close to 2.0026 and small unresolved proton hyperfine splittings. At low concentrations, the relaxation times for these radicals are longer than for radicals with larger nuclear hyperfine interactions. Unlike other radicals studied, BDPA does not contain heteroatoms which tend to increase relaxation times. Additionally, relaxation times for other trityls studied are less concentration dependent than for BDPA because of the negatively charged carboxy groups which decrease π stacking and make collisions less probable.

The nitroxide radicals are the smallest of the radicals studied; the molecules are tumbling more rapidly, and the g-values are further from 2.0026. In addition, the large anisotropic nitrogen hyperfine coupling provides a highly effective mechanism of

electron spin relaxation [157]. These factors lead to much shorter relaxation times for nitroxides compared to BDPA. A variety of complex factors contribute to nitroxide radical relaxation, and these are discussed in detail in Section 6.2.

The final radical compared to BDPA is the thianthrene radical cation, in which the spin density is fully delocalized. Like DPPH and galvinoxyl, the heteroatoms cause a shift to a higher g-value of 2.0084 [13, 149]. The five-line spectrum, first reported in 1955 [21], is attributed to the four para hydrogen atoms on the neighboring rings [149]. It became clear that the dissolved sample degrades rapidly in the first 24 hours following preparation, but then degradation slows (Figure 6.5A). Repeatability of relaxation measurements was attempted on samples that were newly prepared each day. There was wide variation in the field-swept echo-detected spectrum appearance (Figure 6.6) each day that could not be explained by sample positioning, or even positioning of a wrench in the field used to decrease FID interference. Adjustment of the acquisition gate and phase altered the echo appearance, but not in a repeatable or predictable manner. This variability carried over into relaxation measurements, which were too unreliable for accurate determination of T_2 and T_1. A final experiment aimed to describe the impact of oxygen concentration on the hyperfine resolution of the CW spectrum, similar to the experiment performed on solid BDPA. The highest concentration sample (700 μM) was purged for four hours with N_2 and CW spectra collected immediately after removing the purge line, 15 minutes, and then 30 minutes later (Figure 6.5B). Interactions with oxygen broaden the line to almost complete signal loss, a characteristic also observed for semiquinone radicals (Hanan Elajaili). The impact of oxygen

concentration is more substantial for the thianthrene cation radical than the other dissolved radicals studied here. The source of variability seen for pulse measurements of this sample was not determined.

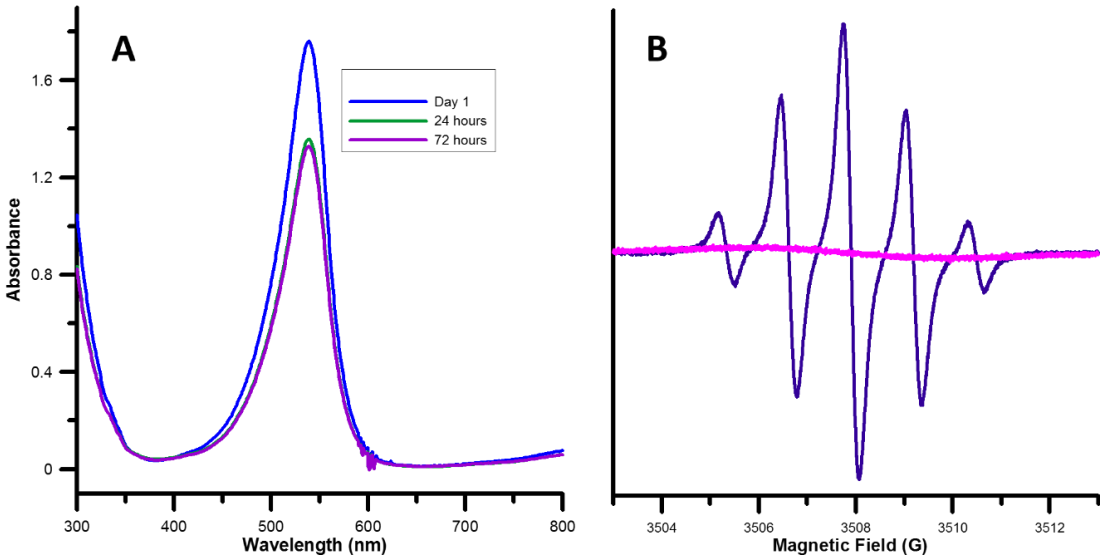

Figure 6.5. Degradation (A) and oxygen concentration dependence (B) of thianthrene. The solution was monitored by UV-Vis to assess the presence of the radical cation after several days (A). The CW spectrum (B) is extremely sensitive to oxygen concentration. Hyperfine lines are well-defined with four hours of N_2 purge (purple trace). 30 minutes after the purge line is removed, the signal is diminished (pink trace). CW were collected with 4096 points averaged for 4 scans with modulation frequency and amplitude of 100 kHz and 0.02 G.

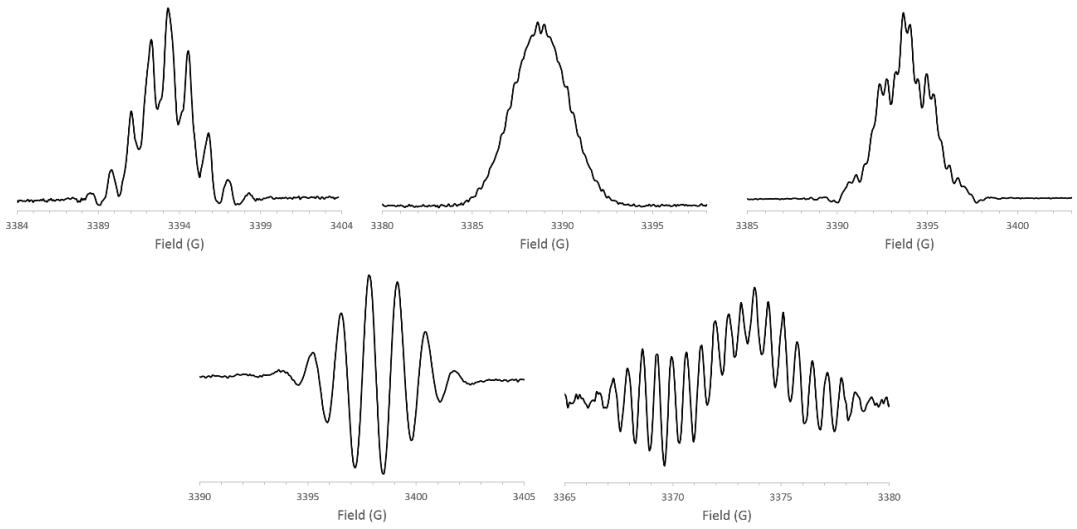

Figure 6.6. Variations seen in the field-swept echo-detected spectra of thianthrene in solution at room temperature. Consistent shapes could not be achieved through resonator retuning or N_2 purge. Relaxation measurements were attempted for different echoes. T_2 values ranged from 110 – 380 ns and T_1 from 390 – 980 ns. Pulse parameters: $\pi/2$ = 40 ns, SRT = 100 μs, 256 steps, 512-2048 shots/step, d_1 = 300-500 ns, 25 scans, 9.5 GHz. Power was adjusted to maximum echo height, and the gate was FWHM on oscilloscope.

6.1.4 Conclusions

Comparison of relaxation times for a variety of radicals in solution provides an excellent opportunity to understand the factors affecting relaxation. These factors differ greatly from the solid radicals presented in Chapters 3-5. The largest contributors to relaxation for the molecules studied in this section are tumbling in solution, collisions with molecular oxygen, orbital angular momentum due to heteroatoms within the molecule, anisotropic hyperfine coupling, and delocalization of spin density. Taking these factors into account, it is not surprising that molecules with similar size, and in turn similar tumbling correlation times, do not necessarily have the same relaxation times. The next section focuses solely on nitroxide radicals, and the effect of tumbling correlation time is examined in greater detail.

6.2 Nitroxide Radicals

6.2.1 Introduction

Nitroxide radicals are remarkably stable compounds in which the free electron is centered on a nitrogen-oxygen bond. Nitroxide radicals may be the most ubiquitous class of compounds studied by EPR. Stability is augmented by steric bulk of substituent groups on the carbons adjacent to the N-O moiety [158]. This stability makes nitroxide radicals attractive for a variety of applications in EPR, from spin trapping to protein labeling [159]. This project focused on nitroxides designed for use as spin probes in biological imaging. The structure of this class of compounds can be tuned for a variety of *in vivo* probe functions. Changes in hyperfine splitting can be used to monitor pH, and a range of nitroxide radicals have been synthesized to span the pH spectrum [160]. Successful *in vivo* measurements have been performed in rat stomach [161] and on human skin [162]. Nitroxides are also tunable for studies of redox environment *in vivo*. Reduction of nitroxides to hydroxylamines occurs *in vivo* through interaction with either ascorbic acid or thiols, notably glutathione, and redox studies often center on the rate of this conversion [163, 164]. The impact of oxygen concentration on spectral linewidth is also utilized to examine hypoxic environments *in vivo* [165]. Nitroxides have proven to be powerful probes for the study of tumors, which are characterized by decreased pH and oxygen concentration, and an increased amount of reducing agent.

Multifunctional spin probes have been developed for the specific study of tumor environments [166, 167], but additional considerations are necessary to image tumors using EPR. Many prior studies have focused on T_2 relaxation alone, but T_1 is gaining

in importance and applicability to the field [168]. An ideal candidate for imaging would have long T_1 for collection of maximum signal. Signal to noise is also a relevant consideration, and many factors contribute to shortening of T_1 and decreasing SNR. The focus of this project is to gain a better understanding of these factors and to characterize, in depth, the relaxation properties of a number of unique nitroxide radicals for application to EPR imaging. By recognizing the influence of different structural features on molecular tumbling, hyperfine interactions, and g anisotropy, novel nitroxides can be designed to be structurally tuned for imaging. Additionally, a thorough study of nitroxide relaxation times at varying frequency, concentration, and viscosity is of general interest to the field, as nitroxides are used for a multitude of *ex vivo* applications. This work was published in references [157, 169, 170].

6.2.2 Materials and Methods

Sample preparation. To undertake a thorough characterization of nitroxide radicals in solution, a number of compounds were studied, including several with large structural variations. Compounds 1, 3, and 4 (Figure 6.7) were prepared [157, 171] by Prof. Gerald Rosen at the University of Maryland Center for Biomedical Engineering and Technology. Compound 2 was provided [172] by Prof. Howard Halpern at the University of Chicago, compound 5 by Prof. Andre Rassat [173], and compound 6 from Prof. Steven Bottle, [14] currently at the Queensland University of Technology. Compound 1 was also purchased commercially from CDN isotopes and was experimentally indistinguishable from Rosen's preparation. Solutions were prepared as described in Table 6.3. Compound 6 was dissolved in toluene due to low solubility in

water. Oxygen was removed via N_2 purge for all samples, except 2A in toluene which was flame sealed following FPT.

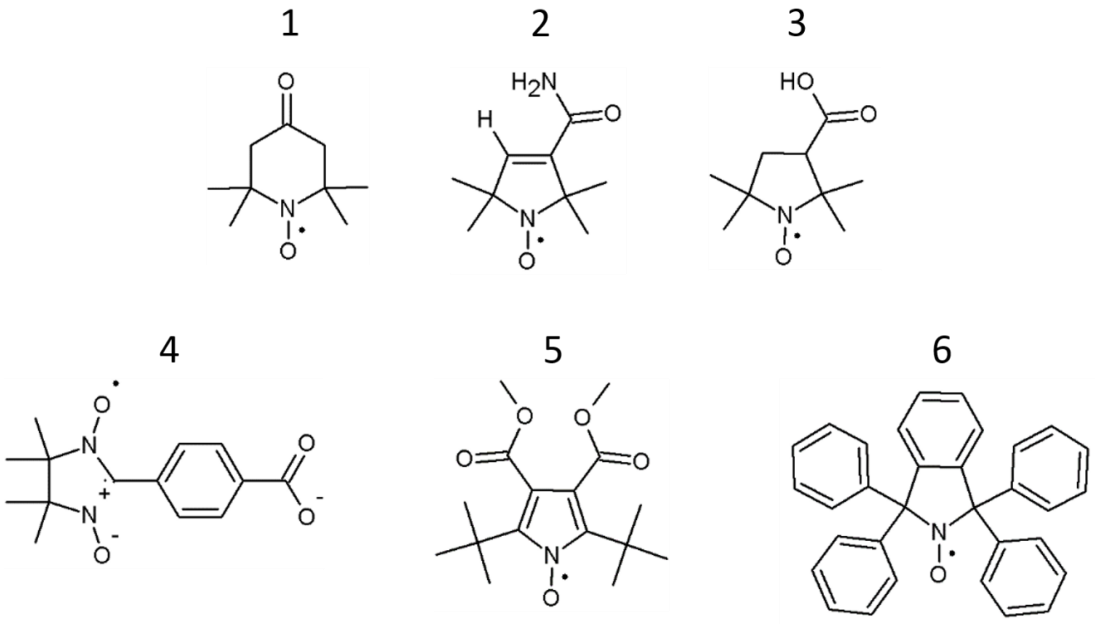

Figure 6.7. Structures of the nitroxide radicals studied in this section. Shorthand:
1 - PDT (4-oxo-2,2,6,6-tetra-perdeuteromethyl-piperidinyl-oxyl-d_{16})
2 - mHCTPO (4-hydro-3-carbamoyl-2,2,5,5-tetra-perdeuteromethyl-pyrrolin-1-oxyl-d_{12})
3 - proxyl (3-carboxy-2,2,5,5-tetramethyl-1-pyrrolidinyloxyl)
4 - nitronyl (2-(4-carboxy-phenyl)-4,4,5,5-tetramethylimidazoline-3-oxide-1-oxyl)
5 - Rassat radical (2,5-di-tert-butyl-3,4-bis(methoxycarbonyl)-1H-pyrrole-1-oxyl)
6 - TPHIO (1,1,3,3-tetraphenylisoindolin-2-yloxyl)

Compound	Solvent	Concentration(s) (μM)
1A, 1B	Water	62.5, 125, 250, 500
1A	24% glycerol in water	180
1A	44% glycerol in water	180
2A, 2B	Water	62.5, 125, 250, 500
2A	Toluene	400
3A, 3B	Water	62.5, 125, 250, 500
4	Water	250, 500
5	Water	500
6	Toluene	180

Table 6.3. Solutions of nitroxides from Figure 6.7 were prepared in different solvents at varying concentrations. 1A-3A refer to the ^{14}N derivative of the compound, and 1B-3B refer to the ^{15}N derivative. Compounds 4, 5, and 6 were studied as ^{14}N isotopes only.

Reproducibility of relaxation time measurements. Initial measurements were performed on evacuated and sealed samples of 0.27 mM 1A in water and 0.4 mM 2A in toluene. T_2 and T_1 values were collected almost every day for each sample, totaling approximately 30 data points for each line of both nitroxides (low, center, and high field). Relaxation times were initially collected on the Bruker E580 system and later on the Homebuilt pulse system for comparison. Relaxation times obtained by different instrument operators were also compared.

Following initial repeatability experiments, different concentrations of both ^{14}N and ^{15}N derivatives of 1, 2, and 3 in water were examined. T_2 and T_1 data were recorded in triplicate (to assign error bars) for each nitroxide at 250μM, 125μM, 63μM, 32μM. This aspect of the project was performed primarily on the Homebuilt pulse with help from Hanan Elajaili and Joshua Biller.

In addition to finding T_1 values by inversion recovery (IR), the 250 μM concentrations of each nitroxide were analyzed for T_1 by saturation recovery (SR). These measurements were initially recorded on the Homebuilt SR system, but final results were reported from the E580. Collection of a number of data points allowed assessment of reproducibility for the SR measurements and to again compare the two different instruments. The T_1 values collected by SR were compared to results from IR.

Variable frequency measurements. All of the nitroxide radicals in Figure 6.7 were studied at VHF, L-band, S-band, X-band, and Q-band (Section 2.1). Nitroxide 4 is a 5-line spectrum ($2nI + 1$, where $n = 2$ and $I = 1$) and relaxation of only the central three lines are reported. Measurements below X-band were performed by Joshua Biller on homebuilt systems. X-band data were collected on the E580 and the Homebuilt pulse instrument. All Q-band measurements were performed on the E580.

6.2.3 Results and Discussion

Repeatability of relaxation measurements. Prior to this study, T_2 and T_1 measurements were thought to be repeatable to around ±10%. Taking the confidence interval into account, the data varied by less than 5% from day to day. This value was consistent regardless of instrument or operator, allowing for a large number of data points to be collected in a short period of time. The extensive and precise data collected were used to assign a dependence of T_1 on m_I, a property that had not previously been acknowledged for this class of rapidly-tumbling nitroxides. Prior studies describe m_I dependence as being within experimental error [174]. By decreasing uncertainty with

thorough repeated measurements, this dependence could be confidently and accurately described.

Contribution to relaxation from spectral diffusion. In contrast to solid organic radicals summarized in previous chapters, the nitroxides in solution showed no contribution from spectral diffusion. For T_2, this was tested with variable pulse length measurements. T_1 was checked through comparison between IR and SR. There was almost no difference between values obtained by the two methods, implying that the contribution from spectral diffusion is minimal. However, because SR gives inherently lower SNR by using CW detection, T_1 by IR was a more attractive method for the nitroxides. Data calculated for SR measurements also showed repeatability well within 10% of the average. Little difference was found between operators, but instrument variance was significant. Comparison between the E580 and the Homebuilt SR systems showed baseline disparities that were partially attributed to the age of the klystron on the Homebuilt. Because of these differences, SR results were reported from the E580, and the microwave source from a Bruker ER042 microwave bridge is now used on the Homebuilt SR.

Exponential fitting of spin lattice relaxation at Q-band. Variable frequency measurements on all of the nitroxide radicals in Figure 6.7 revealed trends in contributions to T_2 and T_1. For all compounds studied, both T_2 and T_1 measured by SR fit well to single-exponential functions. Below 34 GHz, T_1 measured by IR could also be described by a single exponential fit function. Detailed analysis using Multifit and UPEN showed that IR at 34 GHz for all compounds required a double exponential fit to

T_1. This trend applied to both ^{14}N (Figure 6.8) and ^{15}N (Figure 6.9) variants. The figures show that UPEN gives two well-separated peaks. The values are similar to the double-exponential values from Multifit (Tables 6.4-6.6). In Multifit, the standard deviations of the single exponential fit and the short component of the double exponential fit are comparable. Additionally, the SNR in Multifit was significantly improved for the double exponential fit over that of the single. These observations differ from those at X-band, where the single exponential fit provided a reasonable estimation of T_1.

Nitroxide 4 (nitronyl) shows slight deviation from the double exponential fitting seen for the other nitroxides at Q-band. The compound was received as a crude product for initial measurements, and UPEN clearly shows a shoulder, but not a well-defined peak for all but one triplicate. Once the purified nitronyl arrived, the shoulder became resolved, and relaxation times grew longer.

At X-band, T_{1e} is close to T_{1n}, giving an observed T_1 that fits well with a single exponential. At Q-band, T_{1e} and T_{1n} are separated enough that the observed T_1 is the result of these two processes working independently [175, 176]. In this case, the double exponential at Q-band is as reproducible as the single exponential at X-band, which was observed. Separation of these components can be observed at lower frequencies if the nitroxide is tumbling slow enough [175]. The nitroxides studied here are in a very fast motional regime, where tumbling occurs on a ps time scale.

Altering T_1 relaxation of PDT by changing solvent viscosity. The most common way to study the impact of motion on radicals in EPR is to vary the temperature. In addition to varying frequency, the study presented here includes characterization

through variation of solvent viscosity. Compound 1 (PDT) was prepared in toluene, mineral oil, water, 24% glycerol, 44% glycerol, and 69% glycerol. Measurements below Q-band, as well as PDT in toluene, mineral oil, and 69% glycerol, were performed by Joshua Biller. Q-band relaxation times for the remaining nitroxides are shown in Table 6.7. In contrast to PDT in water or 44% glycerol, T_1 in 24% glycerol fit best to single exponential functions. This could be due to a shift in dominant relaxation processes from decreased motion, intermediate between rapid tumbling (water, τ_c = 9 ps) and slower tumbling (44% glycerol τ_c = 19 ps).

Rassat radical relaxation. The final nitroxide examined, 5, was slightly unstable in water, but more stable in toluene. Few replicates were collected at Q-band in water (Table 6.7), and additional measurements were performed in toluene by Joshua Biller for publication. Although the SNR was relatively poor for this sample, T_1 fit well to single exponentials, in contrast to most of the other nitroxides studied.

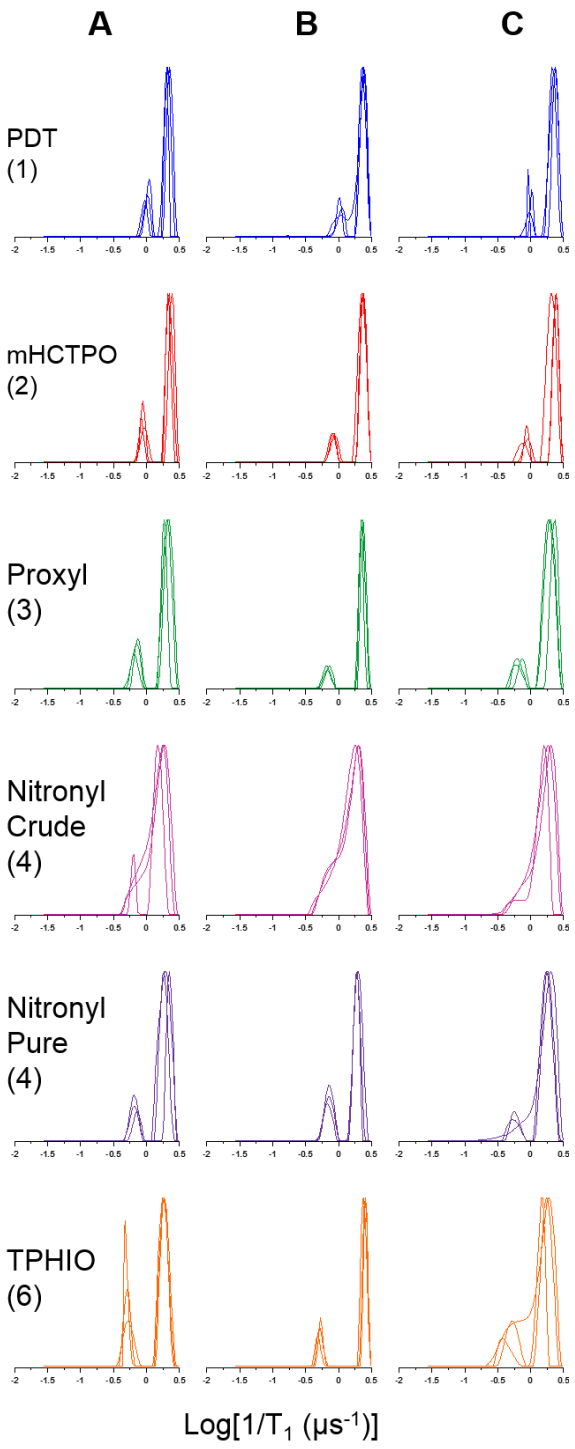

Figure 6.8. UPEN analysis of ^{14}N nitroxides at Q-band showing two processes involved in relaxation for the low (A), center (B) and high (C) field lines. Each trace is a single EPR measurement. These results differ from X-band in which only a single peak is present.

	Multifit Long	Multifit Short	Multifit Single	UPEN Long	UPEN Short
^{14}N PDT					
Low Field	1.01 ± 0.01	0.46 ± 0.01	0.76 ± 0.01	1.06 ± 0.03	0.52 ± 0.01
Center Field	1.06 ± 0.01	0.46 ± 0.00	0.72 ± 0.00	1.01 ± 0.06	0.46 ± 0.02
High Field	1.04 ± 0.06	0.44 ± 0.02	0.68 ± 0.00	1.13 ± 0.08	0.49 ± 0.02
^{14}N mHCTPO					
Low Field	1.30 ± 0.08	0.48 ± 0.03	0.96 ± 0.04	1.31 ± 0.09	0.52 ± 0.04
Center Field	1.38 ± 0.05	0.46 ± 0.01	0.93 ± 0.03	1.39 ± 0.10	0.49 ± 0.02
High Field	1.29 ± 0.04	0.45 ± 0.03	0.86 ± 0.03	1.37 ± 0.14	0.49 ± 0.05
^{14}N Proxyl					
Low Field	1.69 ± 0.11	0.55 ± 0.04	1.17 ± 0.04	1.72 ± 0.16	0.58 ± 0.06
Center Field	1.71 ± 0.05	0.46 ± 0.01	1.16 ± 0.02	1.70 ± 0.07	0.50 ± 0.00
High Field	1.69 ± 0.15	0.52 ± 0.06	1.03 ± 0.01	1.82 ± 0.22	0.54 ± 0.05

Table 6.4. Comparison of results from fitting programs for ^{14}N nitroxide T_1 relaxation at Q-band (compounds 1, 2, and 3 from Figure 6.7). Values obtained in UPEN match double exponential values from Multifit. At X-band and lower frequencies, the value from UPEN matched the single exponential value from Multifit.

	Multifit Long	Multifit Short	Multifit Single	UPEN Long	UPEN Short
^{14}N Nitronyl (Crude)					
Low Field	1.82 ± 0.10	0.73 ± 0.03	1.17 ± 0.01	1.90 ± 0.40	0.74 ± 0.09
Center Field	1.93 ± 0.08	0.73 ± 0.02	1.28 ± 0.03	1.98 ± 0.52	0.64 ± 0.02
High Field	1.85 ± 0.17	0.70 ± 0.06	1.10 ± 0.01	1.88 ± 0.40	0.68 ± 0.09
^{14}N Nitronyl (Pure)					
Low Field	2.07 ± 0.06	0.66 ± 0.01	1.32 ± 0.02	2.08 ± 0.22	0.66 ± 0.08
Center Field	2.08 ± 0.03	0.68 ± 0.02	1.49 ± 0.02	2.05 ± 0.11	0.70 ± 0.02
High Field	2.09 ± 0.16	0.64 ± 0.04	1.15 ± 0.01	2.21 ± 0.08	0.66 ± 0.05
^{14}N TPHIO					
Low Field	4.20 ± 0.08	0.91 ± 0.02	3.09 ± 0.07	4.29 ± 0.29	0.95 ± 0.00
Center Field	4.27 ± 0.13	0.57 ± 0.04	3.83 ± 0.09	4.51 ± 0.11	0.64 ± 0.06
High Field	4.21 ± 0.13	0.90 ± 0.14	2.82 ± 0.08	4.00 ± 0.61	0.88 ± 0.11

Table 6.5. Comparison of results from fitting programs for ^{14}N nitroxide T_1 relaxation at Q-band (compounds 4, 5, and 6 from Figure 6.7). UPEN values match the double exponential fit in Multifit.

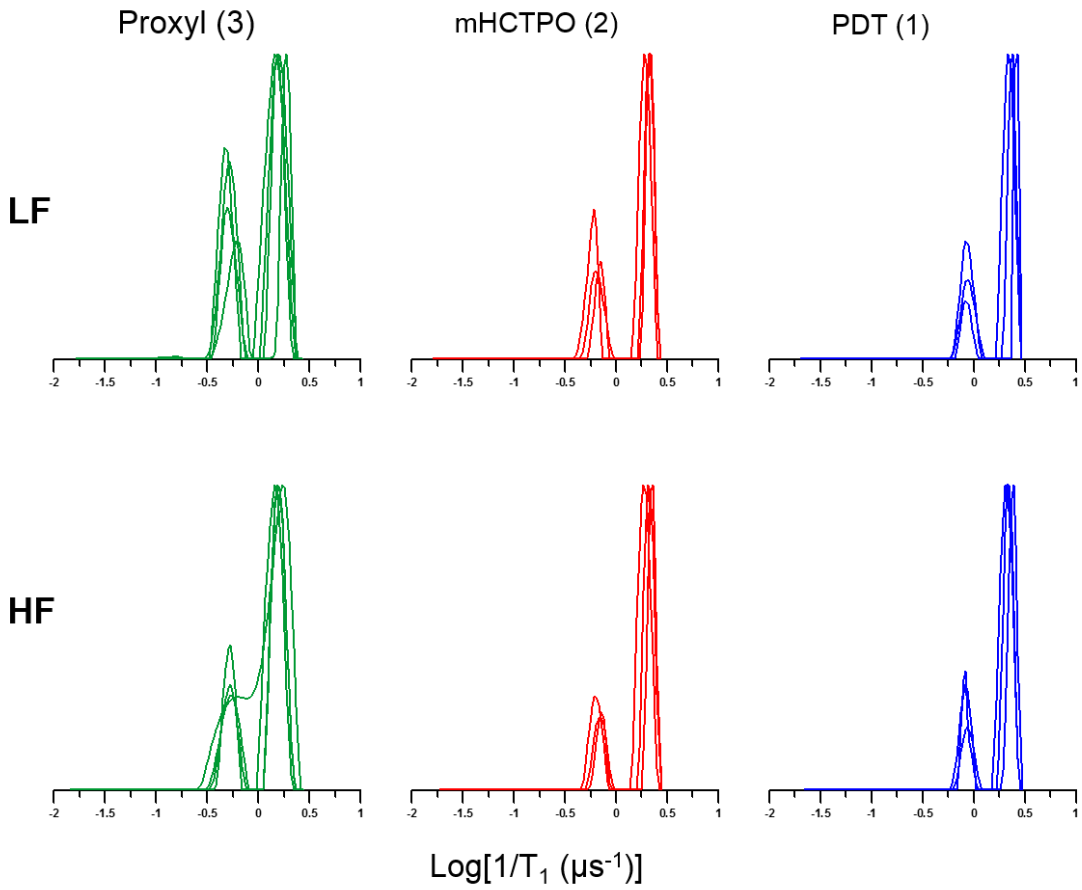

Figure 6.9. UPEN analysis of ^{15}N nitroxides at Q-band (compounds 1, 2, and 3). As with ^{14}N, the contribution from two components to T_1 is observed for this isotope. Each trace is a single relaxation measurement.

	Multifit Long	Multifit Short	Multifit Single	UPEN Long	UPEN Short
^{15}N PDT					
Low Field	1.13 ± 0.09	0.43 ± 0.06	0.95 ± 0.05	1.15 ± 0.07	0.48 ± 0.04
High Field	1.16 ± 0.10	0.45 ± 0.05	0.89 ± 0.04	1.20 ± 0.12	0.47 ± 0.04
^{15}N mHCTPO					
Low Field	1.42 ± 0.03	0.47 ± 0.01	1.19 ± 0.03	1.42 ± 0.06	0.49 ± 0.01
High Field	1.43 ± 0.07	0.47 ± 0.04	1.11 ± 0.02	1.44 ± 0.05	0.51 ± 0.04
^{15}N Proxyl					
Low Field	1.88 ± 0.08	0.66 ± 0.03	1.51 ± 0.06	1.84 ± 0.11	0.61 ± 0.05
High Field	1.92 ± 0.12	0.66 ± 0.04	1.40 ± 0.06	1.81 ± 0.11	0.66 ± 0.05

Table 6.6. Comparison of results from fitting programs for ^{15}N nitroxide T_1 relaxation at Q-band (compounds 1, 2, and 3). UPEN values match the double exponential fit in Multifit.

	T_1 Long	T_1 Short	T_1 Single	T_2 Single	# of Replicates
^{14}N PDT 24% Glycerol					
Low Field	N/A	N/A	1.26 ± 0.05	0.93 ± 0.01	2, 2
Center Field	N/A	N/A	1.06 ± 0.02	0.55 ± 0.00	2, 2
High Field	N/A	N/A	1.06 ± 0.04	0.31 ± 0.01	2, 2
^{14}N PDT 44% Glycerol					
Low Field	2.01 ± 0.24	0.83 ± 0.21	1.59 ± 0.11	0.81 ± 0.03	5, 4
Center Field	1.97 ± 0.16	0.56 ± 0.06	1.32 ± 0.11	0.39 ± 0.02	5, 4
High Field	1.77 ± 0.26	0.71 ± 0.20	1.31 ± 0.05	0.19 ± 0.01	4, 3
^{14}N Rassat					
Low Field	N/A	N/A	1.26 ± 0.04	0.52 ± 0.01	3, 2
Center Field	N/A	N/A	1.22	0.38	1, 1
High Field	N/A	N/A	N/A	0.31	0, 1

Table 6.7. T_1 and T_2 values for additional ^{14}N nitroxides studied. Compound 1 (PDT) was studied at different viscosities, which altered the exponential fitting to T_1. The number of replicates is reported. Instability of the Rassat radical in water and the limited amount of sample available made collection of additional replicates difficult.

6.2.4 Conclusions

Relaxation properties of nitroxides at X-band. The first paper published [157] examined only the smallest nitroxides, 1, 2, and 3 at X-band. Compound 1 was fully deuterated, 2 was deuterated at all but one hydrogen, and compound 3 was studied with both natural abundance and fully deuterated. Joshua Biller performed in-depth analysis

of the contributions to relaxation for both T_1 and T_2. Prior studies found contributions to T_1 from spin rotation, modulation of g and A anisotropy (tumbling), and generalized spin diffusion. Spin diffusion was not a significant contribution for these samples due to rapid tumbling and the extent of deuteration in each compound. T_1 was accurately calculated through contributions from spin rotation (Equation 6.1) and modulation of hyperfine anisotropy (Equation 6.2):

$$\frac{1}{T_1^{SR}} = \frac{\sum_{i=1}^{3}\left(g_i - g_e\right)^2}{9\tau_c} \tag{6.1}$$

$$\frac{1}{T_1^{A}} = \frac{2}{9} I(I+1) \sum_i (A_i - \bar{A})^2 J(\omega) \tag{6.2}$$

In Equation 6.1, τ_c is the tumbling correlation time, g_e is the free electron g-value, and i = x, y, and z. In Equation 6.2, I is the nitrogen nuclear spin (1 and ½ for ^{14}N and ^{15}N, respectively), A_i corresponds to the nitrogen nuclear hyperfine, and $\bar{A}$ is the average nitrogen hyperfine. $J(\omega)$ is the spectral density function [20]:

$$J(\omega) = \frac{\tau_R}{1 + (\omega\tau_R)^2} \tag{6.3}$$

The dependence of T_1 on m_I for slowly-tumbling radicals was reported in an early manuscript [177], but has not been noted in more recent papers [124, 178]. This study uncovered m_I dependence for rapidly-tumbling nitroxides, and Equation 6.4 was proposed as a model, using Equation 6.2 as a reference for the anisotropy term:

$$\frac{1}{T_1^{m}} = \left[c' \sum_i \left| (A_i - \bar{A})\left(g_i - \bar{g}\right) \right| \right] \frac{\mu_B B}{\hbar} m_I \tag{6.4}$$

Here, μ_B is the Bohr magneton, B is the magnetic field, $\hbar$ is Planck's constant over 2π, and m_I describes lines in the EPR spectrum (± 1 and 0 for ^{14}N and $\pm ½$ for ^{15}N). The c' constant refers to the slip coefficient, which varies by nitroxide. This equation contrasts with earlier models in which the $1/T_1$ varies depending on m_I^2, which was not consistent with experimental values of T_1. The results presented here suggest that the m_I dependence is large enough to be demonstrated experimentally.

This study examined relaxation only at X-band, but this was extended to other frequencies in later papers [169, 170]. The dependence of T_1 on m_I is maintained at frequencies below X-band but is significantly smaller at Q-band, regardless of analysis with Multifit or UPEN. There is slight m_I dependence in the single exponent fit from Multifit, but no other m_I dependence is apparent within experimental error. As with X-band, the lowest standard deviation is for the single exponent fit from the Multifit program. The results (Tables 6.4 to 6.6) clearly show that this dependence is diminished at Q-band, which is not consistent with Equation 6.4.

The structures of the nitroxides studied here provide a basis for interpretation of the effect of concentration on relaxation. Concentration dependence is primarily caused by variation in the probability of collisions between molecules, which provides an additional means of relaxation. In solution, compound 3 is negatively charged, which decreases the probability of collision with another anion. The large hyperfine splitting of compound 2 increases the effect of collision with a radical in a different spin state on relaxation as concentration increases. As a result, compound 2 has the highest concentration dependence of relaxation. Compound 3 has very little concentration

dependence, and compound 1 is intermediate between the two. The linewidth of compound 1, caused by small couplings to the ring methyls, is decreased due to conformational flexibility and by virtue of being a 6-membered ring. The very narrow linewidth leads to a decrease in concentration dependence for this compound.

The insights gained from this study concerning contributions to relaxation, m_I dependence, and concentration effects guided the development of the following papers.

Frequency dependence of nitronyl nitroxide and PDT relaxation. The second study [169] examined relaxation at varying frequencies in the fast motional regime (~9 ps tumbling correlation times). Prior studies presented a trend to faster relaxation rates at low frequency [179]. Rapidly decreasing relaxation times at low frequencies pose a potential problem for *in vivo* imaging using nitroxide spin probes. *In vivo* imaging studies are performed between 250 MHz and 1 GHz, frequencies at which the dielectric losses are less. The lower Boltzmann populations at lower frequency are offset by large sample size and filling factor [180, 181]. If T_1 becomes extremely short at these frequencies, nitroxide spin probes could not be used for imaging. Compound 4 (nitronyl) was chosen for this study due to a relatively long T_1, which is due to smaller nitrogen hyperfine couplings compared to other nitroxides. The small couplings are attributed to delocalization of spin density over the two nitrogen atoms [182]. The primary aim of this work was to demonstrate that T_1 does not diminish at low frequency, but also to determine the extent of T_1 augmentation due to the spin density delocalization of the nitronyl. For this aim, compound 1 (PDT) was used for comparison. Relaxation times for PDT between 2.5 GHz (S-band) and 34 GHz (Q-band, Table 6.4) matched

literature values well [179]. T_1 values at 250 MHz were more similar to those at X-band for PDT and S-band for the nitronyl, demonstrating that relaxation does not decrease below 2 GHz. The longer T_1 at L-band (1.5 GHz) than at 250 MHz was modelled as a contribution from a frequency-dependent thermally-activated process, described by Equation 6.5:

$$\frac{1}{T_1^{therm}} = C_{therm}\left(\frac{\nu}{\nu_{ref}}\right)\frac{\tau_{therm}}{1+(\nu\tau_{therm})^2} \tag{6.5}$$

C_{therm} describes the magnitude of the contribution from this thermal process, ν is the microwave frequency, and ν_{ref} is X-band, 9.5 GHz. τ_{therm} is described by Equation 6.6:

$$\tau_{therm} = \tau_c^0 e^{\left(E_a/RT\right)} \tag{6.6}$$

where τ_c^0 is the pre-exponential factor, E_a the activation energy of the process, T is temperature and R is the gas constant. The source of this thermal process is examined in more detail in the third nitroxide paper.

Hyde and coworkers studied nitroxide relaxation over a wide range of frequencies from 2.5-95 GHz [179, 183]. The present study extended those measurements to lower frequency, characterizing a number of relaxation mechanisms in the process. In the rapid tumbling regime, T_1 is the dominant contribution to T_2, and the values are roughly equivalent. This is true up to Q-band, at which point the g anisotropy is no longer fully averaged by the rapid motion and therefore becomes a larger contribution to T_2. At X-band, PDT T_1 relaxation could be modelled using spin rotation (Equation 6.1) and modulation of A anisotropy (Equation 6.2). Below Q-band, the contribution from modulation of g anisotropy (equation not shown, see Equation 4

in [169]) is dwarfed by that of A anisotropy. These insights were carried over into relaxation analysis of additional nitroxides at variable frequencies.

T_1 relaxation mechanisms of additional nitroxide radicals. The third paper [170] extends the findings from the nitronyl nitroxide to the other nitroxide radicals in Figure 6.7. One of the main goals was to define the thermally activated process that was introduced in the prior paper (Equation 6.5). Examination of PDT in solvents with varying viscosities revealed contribution to relaxation from the same thermal process seen through variation of frequency. The magnitude of the contribution is viscosity-dependent, but does not require a hydrogen-bonding protic solvent, which precludes involvement of solvent spin diffusion to relaxation. The viscosity dependence can likewise be interpreted as a dependence on radical size and tumbling. The ring structures in 1, 2, and 3 are more flexible than 4, 5, and 6 as a consequence of the large substituents. It is likely that the thermal process is modulation of nitrogen isotropic A and/or anisotropic g via changes in ring conformation. This is a reasonable assignment based on prior studies reporting large temperature dependence of g and A values for nitroxides that explain this phenomena by rapid switching between different ring conformations [184]. Despite problems with stability, compound 6 (Rassat radical) provided useful insight into assignment of the thermal process. The tumbling correlation time is similar to smaller radicals 1 and 2, but the contribution from modulation of A anisotropy, as modelled, was much smaller. Although size (and hence tumbling correlation time) was found to be a telling contribution to the thermal process,

the contribution to spin rotation for the Rassat radical decreased the thermal process contribution, as expected for a radical this size.

These in-depth studies of a variety of nitroxides at varying frequencies have provided new insights, including guiding synthesis of novel spin probes for *in vivo* imaging. Repeating relaxation measurements improved the understanding of experiment error in reported values. Relaxation times varied by less than 5% over a number of measurements. The m_I dependence on relaxation has resurfaced and been concretely documented. These studies provided not only a lesson in relaxation measurements and interpretation, but have contributed innovative concepts to a field with a rich history.

Chapter 7: EPR of Tau

Following the advent of site-directed spin labeling in 1990 [185], EPR has been used for the study of a multitude of unique biological systems. Information regarding kinetics, structure, binding, and more, is accessible via CW EPR or pulse methods. An example of a distance measurement using CW was shown in Figure 5.9 and described by Equation 5.4. Long-distance measurements in proteins require pulsed EPR, and the most commonly employed technique for the study of proteins is DEER [56].

7.1 Introduction

7.1.1 DEER of Protein Systems

DEER is emerging as a powerful technique for the study of protein systems. Many studies have elucidated structural changes within proteins in solution upon ligand binding or activation [186-188]. DEER is especially useful for the study of membrane proteins [189, 190] and proteins with multiple subunits [191]. When combined with complimentary techniques, DEER has proven beneficial to the understanding of protein structure and function [192, 193]. In this chapter, DEER is used to study structural variations within tau fibrils, which are associated with Alzheimer's disease and other neurodegenerative disorders. Utilizing additional available techniques, novel characteristics of these fibrils have been discovered [194, 195].

7.1.2 Tau

Tau protein has been implicated in over 20 phenotypically distinct neurodegenerative disorders, termed "tauopathies," including Alzheimer's disease [196, 197]. Tau is currently gaining attention for its link to chronic traumatic encephalopathy, a disease associated with repeated concussions sustained by athletes participating in a variety of high-impact sports [198, 199]. Humans express six isoforms of tau in the central nervous system that differ structurally in two regions (Figure 7.1). The N-terminus contains either 0, 1, or 2 amino acid insert regions (Figure 7.1, green) which are created by alternative mRNA splicing. The more important structural difference is in a series of amino acid repeat regions near the C-terminus (Figure 7.1, purple). Half of the isoforms contain four of these repeat regions (4R) and the other half contain three (3R), lacking the 2nd repeat. Tau was isolated in 1975 and shown to play an important role in microtubule stabilization and assembly [200]. Microtubules are involved in many cellular functions, pertaining primarily to structure and movement and are essential to the growth of axons in the brain [201]. Tau binds to microtubules via the repeat regions. It was shown that 4R tau binds microtubules more effectively than 3R tau due to the presence of the additional repeat region in 4R tau [202]. When tau becomes dissociated from microtubules, the interactions between the repeat regions [203] on different tau monomers can lead to aggregation. Tau monomers are natively unstructured [204], but tau fibrils are highly ordered. In the brain, these fibrils compose large structures termed "neurofibrillary tangles," (NFTs) which are the pathological hallmark of neurodegenerative tauopathies.

The tau isoforms found within fibrils comprising NFTs vary depending on the disease with which they are associated. Some diseases contain fibrils of only 4R tau, including progressive supranuclear palsy (PSP) and corticobasal degeneration (CBD), while others, primarily Pick's disease, are caused by fibrils composed of only 3R tau [205]. Several other diseases, including Alzheimer's disease, involve fibrils containing both 3R and 4R tau. In a normal brain, the ratio of 4R to 3R tau isoforms is ~1 [202], and it has been shown that this ratio is not altered in Pick's diseased brain [206], suggesting that development of this 3R tauopathy is not caused by decreased expression of 4R tau in the brain. However, studies have reported an increase in the 4R:3R ratio for the 4R tauopathies PSP and CBD [207, 208] but not for Alzheimer's disease [206]. The cause of preferential deposition of isoforms based on the number of repeat regions in different tauopathies is currently unknown. However, different seeding barriers of conformationally distinct fibrils could be a plausible explanation [209]. The observed seeding properties served as motivation for studying tau fibril structure using DEER, with the aim of finding a link between structure and disease pathology.

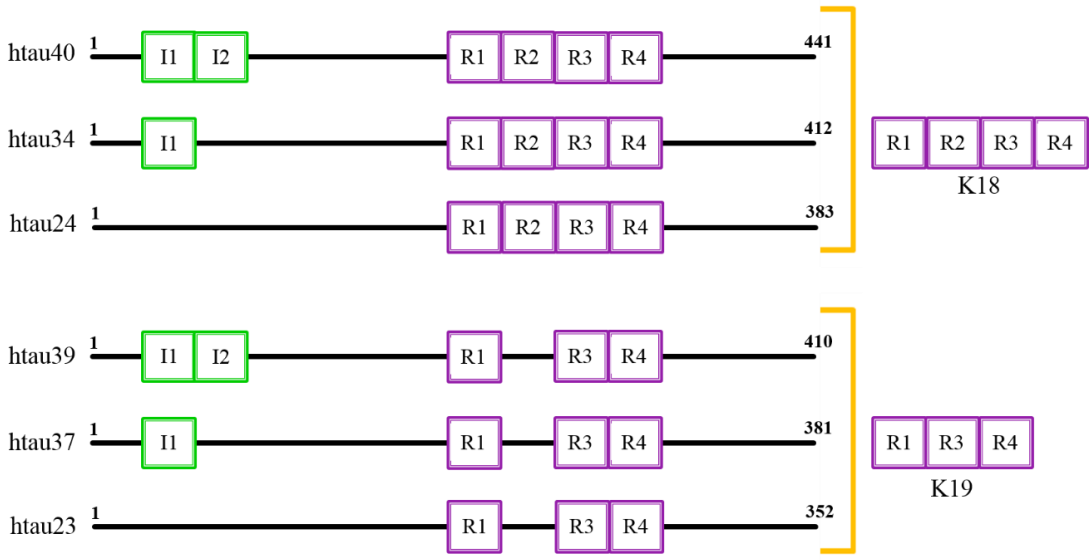

Figure 7.1. Six isoforms of tau. The primary sequence contains either 0, 1, or 2 insert regions (green) that are 29 amino acids in length. 4-repeat (4R) tau has all four repeat regions (purple) while 3-repeat (3R) tau lacks the second repeat region (R2). The repeat regions are composed of 31 or 32 amino acids. Truncated forms of tau contain only the repeat regions: K18 is 4R and K19 is 3R.

Characterizing tau fibril structure has been a long-standing goal that may lead to understanding variation in tauopathy phenotypes. For over 40 years, morphological differences have been recognized for fibrils extracted from patients presenting different diseases [196]. PSP and CBD offer an interesting comparison of 4R tauopathies, as they are often misdiagnosed due to the same presentation of symptoms. It was suggested that the mechanism of disease initiation and progression is in fact the same for PSP and CBD, and that the overlap of symptoms and pathology can be interpreted as equivalency of the two diseases [196]. In fact, it was later shown that fibrils from PSP are distinct from CBD in both shape and location of deposition in the brain [210]. Whether morphologically distinct fibrils represent alternate ways of packing protofilaments or whether they reflect fundamentally different conformations is

unknown. Structural studies could play an important role in distinguishing between tauopathies and may provide insight into the molecular mechanisms of disease propagation.

Some known structural variation is characteristic of different tau isoforms, including paired helical filaments (PHF) seen for 3R tau and straight filaments (SF) seen for 4R tau extracted from brain tissue [211]. Like other amyloid proteins, aggregated tau adopts β-sheet structure in the brain, which is also seen for fibrils formed *in vitro* [212]. Further, fibrils isolated from brain tissue are competent to seed recombinant tau *in vitro* [213]. Many recent efforts regarding tau have focused on mechanisms of inhibition and promotion of aggregation through molecular chaperones or small molecules [214-217]. Structural studies of tau are an excellent complement to this research and are important to better understand aggregation properties and help guide the development of therapeutic strategies. Many techniques have been employed to study tau structure, including NMR [203, 218, 219], FRET (fluorescence resonance energy transfer) [220], X-ray diffraction [221, 222], electron microscopy, CD (circular dichroism) [223], and atomic force microscopy [224]. These studies provide valuable information on higher order structure, but high resolution molecular level information remains scarce in the field. The structures of tau fibrils are challenging to study because, while monomeric tau is soluble and unstructured, fibrils are insoluble and cannot be crystallized. EPR has been utilized in the study of many amyloid proteins [225], and DEER in particular has proven highly effective in elucidating amyloid fibril structure [226-228]. DEER was used for this project to obtain molecular-level information

inaccessible using other techniques with the aim of gaining insight into the link between tau fibril structure and disease.

7.2 Materials

7.2.1 Chemical Supplies and Abbreviated Names

- BCA: bicinchoninic acid (Pierce).
- DTT: dithiothreitol (Gold Biotechnology)
- *E. coli*: *Escherichia coli* (Agilent)
- EDTA: ethylenediaminetetraacetic acid (J. T. Baker)
- Guanidine HCl (Thermo)
- Heparin (Celsus, average MW = 5000)
- HEPES: 4-(2-hydroxyethyl)-1-piperazineethanesulfonic acid (J. T. Baker)
- IPTG: isopropyl-β-D-thiogalactopyranoside (Gold Biotechnology)
- Kanamycin (Gold Biotechnology)
- LB: lysogeny broth/Luria-Bertani, Miller (BD)
- MTSL:(1-oxyl-2,2,5,5-tetramethyl-Δ3-pyrroline-3-methyl)methane-thiosulfonate (Toronto Research Chemicals)
- PIPES: piperazine-*N*,*N*'-bis(2-ethanesulfonic acid) (J. T. Baker)
- SDS-PAGE: sodium dodecyl sulfate-polyacrylamide gel electrophoresis (J. T. Baker)
- Tris: 2-amino-2-hydroxymethyl-propane-1,3-diol (Sigma)

7.2.2 Buffers

- Buffer EB (QIAGEN)

- Tau extraction buffer: 20 mM PIPES pH 6.5, 500 mM NaCl, 1 mM EDTA, 50 mM β-mercaptoethanol (MP Biomedicals)
- Ion exchange buffer: 10 mM PIPES pH 6.5, 50 – 1000 mM NaCl, 1 mM EDTA, 2 mM DTT
- Gel filtration buffer: 20 mM Tris pH 7.4, 100 mM NaCl, 1 mM EDTA, 2 mM DTT
- Protein buffer: 10 mM HEPES pH 7.4, 100 mM NaCl, 1 mM NaN_3

7.2.3 Equipment

- Midiprep kit (QIAGEN)
- Mono-S column (GE Healthcare)
- PD-10 column (GE Healthcare)
- Quickchange kit (Agilent)
- Superdex 200 column (GE Healthcare)
- Tip sonicator, D100 series (Fisher Scientific)

7.3 Methods

Truncated tau (K18 and K19, Figure 7.1) were used to prepare DEER samples. The truncated forms contain only the microtubule-binding repeat regions: K18 is 4R and K19 is 3R [229]. In addition to enhanced fibril growth kinetics, the shortened constructs could be centrifuged into the narrow Q-band EPR tubes. The flanking regions of full-length constructs (htau23 and htau40) did not allow compression of the fibrils into the narrow EPR tube. Compression can be achieved by shortening of full-length fibrils through sonication. An early experiment using K18 showed that fibril

structure was maintained following sonication (Figure 7.2), implying this may be a plausible method for future measurement of full-length tau using DEER.

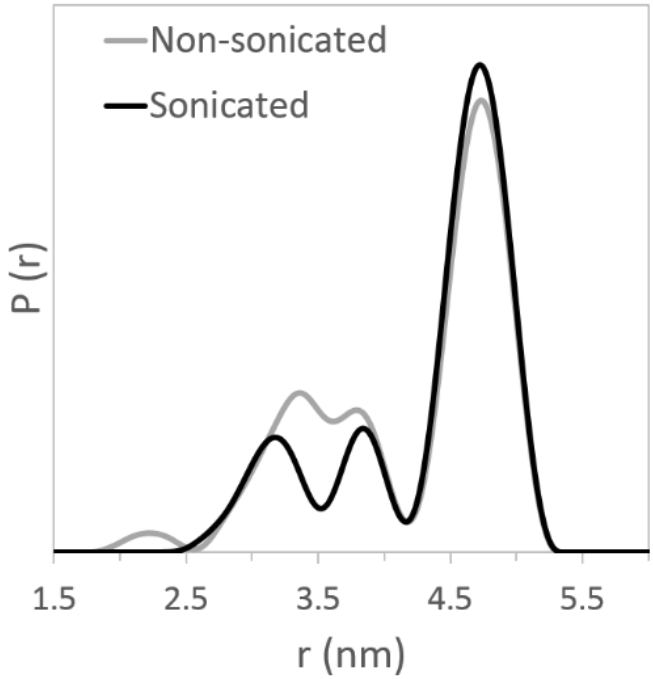

Figure 7.2. Comparison of distance distributions for fibrils before (gray) and after (black) sonication. Although the fibrils have been sheered in the process, the primary distances are preserved.

It is important to note that tau is hyperphosphorylated in disease [201]. Phosphorylation occurs predominantly outside of the microtubule binding domains, in the regions flanking the repeat sections [196]. Because these sections are lacking in K18 and K19, hyperphosphorylation is unlikely to impact the results presented here. Additionally, although studies link destabilization from microtubules to this phenomenon [201], the role of hyperphosphorylation in tau aggregation is not well understood.

The following procedures hold for the majority of tau DEER samples studied. Deviations were implemented for seeding and fibril assembly (Sections 7.3.6 and 7.2.7)

to examine effects of different growth environments on fibril structure. Details of these changes are described in the results and discussion section.

7.3.1 Plasmid Constructs and Mutagenesis

The following plasmids were cloned into pET28b and provided by Ayisha Siddiqua: K18 WT, K19 WT, K18 K311C, K18 I328C, K18 K311C/C322C, K18 K311C/G326C, K18 K311C/I328C, K19 K311C, K19 K311C/C322C, K19 K311C/G326C, and K19 K311C/I328C. The spin label used, MTSL [230], attaches to cysteine residues (Figure 7.6), so the naturally-occurring cysteines, two in K18 located in the 2nd and 3rd repeat regions and one in K19 located in the 3rd repeat region, were mutated to serines. The wild-type (WT) designation above refers to the cysteine-less constructs that have not been further mutated. Mutation of the other constructs listed above are defined in the following manner: original amino acid, position of mutation in the peptide sequence, new amino acid. For example, K311C means that a lysine residue at position 311 was mutated to a cysteine. This convention is used in the remainder of this dissertation, except for mutations that have already been listed. In the following sections, K18 K311C/I328C is shortened to K18 311/328. The above mutations are all located in the third repeat region, which is conserved for K18 and K19.

New mutagenic tau primers were received as lyophilized powders and dissolved in autoclaved water to 100 pM and were stored long-term at -20 °C. Mutations added to the K18 311/328 double cysteine construct were inserted via site-directed mutagenesis using the QuikChange method (Appendix A). The following mutations were introduced: ΔK280 (deletion at position 280), P301S, I308M, P312I, D314I,

S320F, G323I, G326I, and Q336R (Figure 7.3). The correctness of all constructs was confirmed by DNA sequencing.

7.3.2 Transformation

A Midiprep (Appendix B) was performed to amplify the previously described plasmid DNA, which was transformed into XL1-Blue supercompetent *E. coli* cells and streaked onto a kanamycin-containing agar plate. The plasmids (pET28b) used in this dissertation mediate kanamycin resistance, so only those bacteria that have taken up the plasmid will grow on this type of plate. Colonies grew overnight at 37 °C, after which single colonies were picked and grown in 50 mL LB broth at 37 °C for 17 hours. Following Midiprep, amplified DNA were quantified via absorbance at 260 nm. To visualize the DNA on an agarose gel, the plasmids were digested with restriction enzymes Xho1 and Nco1 that cleave the tau insert from the vector. The insert and vector are separated by number of base pairs (or molecular weight, MW) via the agarose matrix and stained using ethidium bromide which is visible under UV light. Multiple Midipreps were performed using the same plasmid to maximize the probability of correct DNA uptake. Figure 7.3 shows agarose gels for K18 following mutagenesis in which all but one inset (mutation at position 305) have the correct number of base pairs. Following confirmation of DNA correctness based on MW (~400 base pairs for K18) and/or sequencing, the plasmid DNA was transformed into BL21 (DE3) *E. coli*. The plates were incubated overnight at 37 °C and stored at 4 °C until needed for expression.

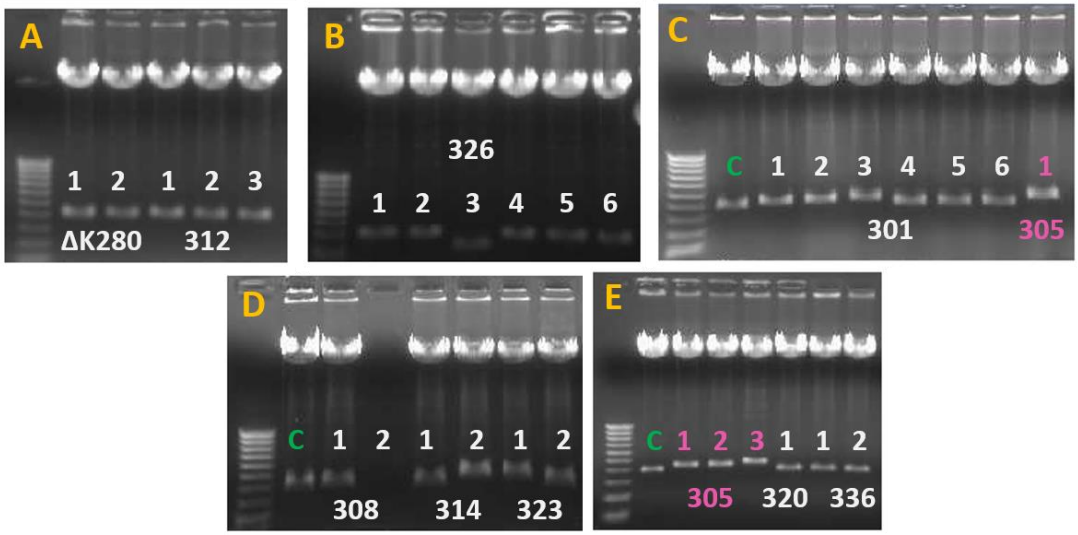

Figure 7.3. Agarose gels showing mutants introduced into K18 311/328. The lower bands are the plasmid insert (~400 base-pair) and the upper bands are the remaining vector. The 100 base-pair ladder is shown to the left of each panel, followed by a control of correct molecular weight (green) in panels C, D, and E. Multiple Midipreps (numbered 1, 2, 3, etc.) were performed for each construct, all of which yielded usable DNA for mutants at positions 280, 312, 320, and 336. At least one Midiprep produced usable DNA for mutants 301, 308, 314, 323, and 326. Panel D shows that no DNA was recovered from the second prep of 308, and panels C and E show that the MWs of all 305 inserts are incorrect (pink). Only those plasmids with inserts of correct molecular weight were sent for sequencing.

7.3.3 Expression

A single colony was picked from the transformation plate and incubated with agitation for 16-17 hours at 37 °C in 50 mL LB broth with 20 μg/mL kanamycin. Overnight cultures were diluted 1:100 with LB medium and incubated with agitation at 37 °C until the optical density reached ~0.8 at 600 nm. Protein expression was induced by addition of 1 mM IPTG and continued for at least 3.5 hours at 37 °C. The bacteria were then pelleted at 3,000 X g, resuspended in tau extraction buffer, and stored at -80 °C.

7.3.4 Purification

Purification of tau was performed in the same manner for both K18 and K19. Natively unfolded tau is highly charged and stable at elevated temperature, so cells were thawed at 80 °C for 30 minutes. At this temperature, most bacterial proteins precipitate, leaving tau in solution. Cells were cooled for five minutes on ice, sonicated for one minute, and centrifuged at 15,000 X g for 30 minutes to separate soluble protein from cellular debris. The supernatant was added to 55% w/v ammonium sulfate and mixed on a mechanical rocker at room temperature for one hour to precipitate tau protein. This was collected by centrifugation at 15,000 X g for 10 minutes. The pellet was resuspended in deionized water to which 2 mM DTT was added to maintain a reducing environment. This solution was sonicated using the tip sonicator at level 5 for 40 seconds and immediately filtered through a 0.45 μm syringe filter. This was run over a Mono S cation exchange column using ion exchange buffer to which a linear NaCl gradient was applied for protein elution (Figure 7.4A). Fractions containing the highest concentration of protein were found using SDS-PAGE (Figure 7.4B). Appropriate fractions were combined and run over a Superdex 200 gel filtration column to achieve further purification. Protein eluted over time with gel filtration buffer (Figure 7.5). Fractions containing pure tau were combined and precipitated overnight at 4 °C using a three-fold volumetric excess of acetone to which 5 mM DTT was added. Pellets were collected at 15,000 X g the following day and stored in 2 mM DTT acetone at -80 °C.

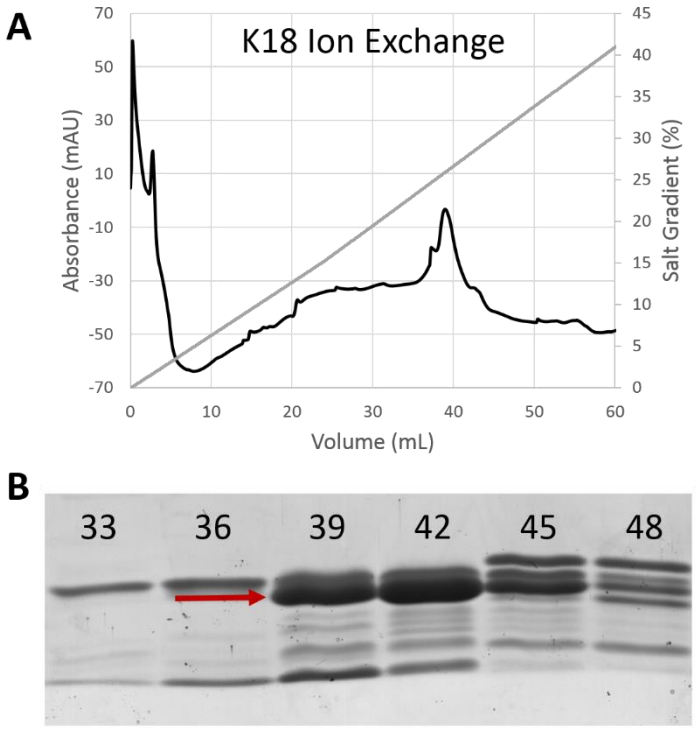

Figure 7.4. Ion exchange purification of K18. Panel A shows the UV absorbance trace at 254 nm (black) and the percentage of salt that has run for a given volume (gray). Panel B shows the fractions that were run on SDS-PAGE with numbers corresponding to the volume from panel A. The red arrow shows the molecular weight of the desired protein. For this sample, the fractions corresponding to 39-45 mL were collected, matching the peak location in panel A.

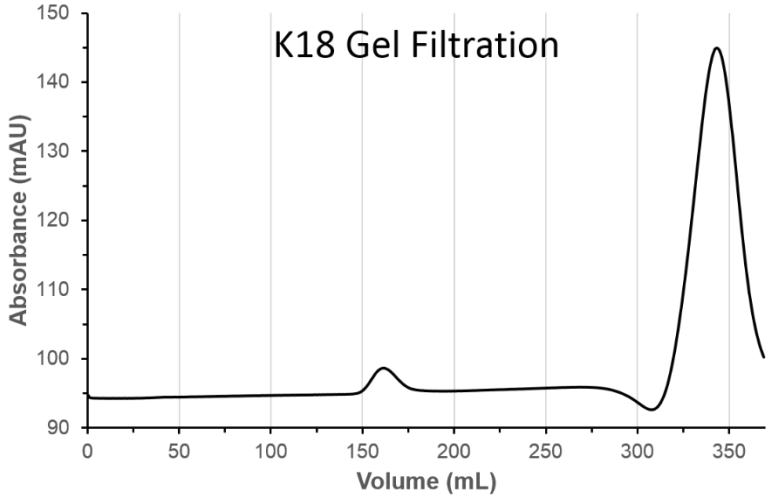

Figure 7.5. Gel filtration purification of K18. The peak around 340 mL contains tau protein.

7.3.5 Protein Labeling and Monomerization

Purified protein pellets were dissolved in 200 μL 8 M guanidine HCl. Double- and single-cysteine mutants were labeled by addition of a 10-fold molar excess of the MTSL spin label (Figure 7.6) and incubated at 25 °C for one hour. The mutants, along with wild-type (WT) tau, were passed over PD-10 columns to remove excess label and guanidine HCl. Protein eluted with protein buffer, and concentrations were determined by BCA assay (Appendix C).

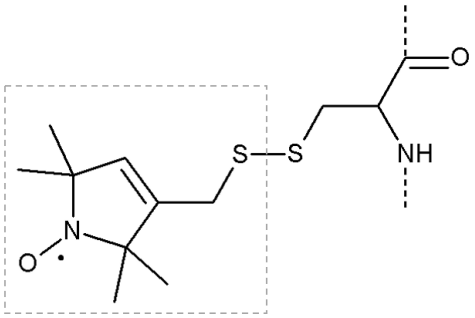

Figure 7.6. The MTSL moiety (boxed) attached to a cysteine residue in the protein backbone.

The K18 311/328 samples to which additional mutations were introduced were analyzed by CW EPR to ensure these mutations did not alter labeling efficiency. CW spectra are shown in Figure 7.7A; the integrated signal intensity was $(3.2 \pm 0.1) \times 10^{11}$ for mutant monomers diluted to 10 μM (concentration confirmed on SDS-PAGE, Figure 7.7B). The similarity in integrated intensities indicates that the labeling efficiency is equivalent for K18 311/328 variants prepared in parallel. Although not measured, labeling is likely similar for every sample prepared by this method as all cysteines are highly accessible.

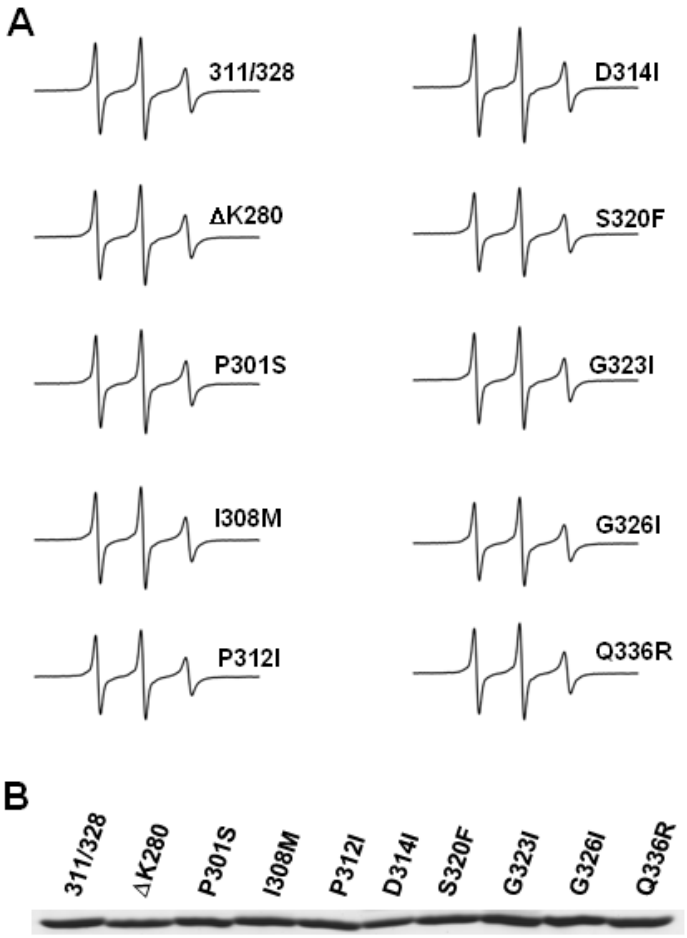

Figure 7.7. Labeling efficiencies of K18 monomers. CW EPR spectra of K18 311/328 and variants (A). Staining of spin-labeled K18 monomers after SDS-PAGE (B). The gel verifies that equal protein concentrations were applied. The EPR data indicate that all mutants were labeled with similar efficiencies. Scan width was 150 G, modulation frequency and amplitude were 100 kHz and 1.0 G, respectively. Spectra were collected using 2048 points averaging for 20 scans at 10 dB power attenuation (20 mW). The y-axis, in arbitrary units, is the same for all mutants. Figure from reference [195].

7.3.6 Multistep Seed Preparation

To form tau fibrils, it is convenient to use seeds to overcome the initial lag phase associated with nucleation [213, 231]. Populations of conformers may be influenced by growth conditions of the initial seeds, leading to slight variations in peak height of DEER distance distributions. For this reason, the same seed batch was used for experiments that required direct comparison of samples, such as the impact of mutations

on fibril structure. For most experiments, seeds were prepared analogously as outlined in this section. Initial fibrils were formed by stirring a mixture of 25 μM WT (K18 or K19) monomer and 12.5 μM heparin, a highly sulfated glycosaminoglycan that was used as a cofactor to facilitate fibril growth [211], in protein buffer for three days at room temperature. These fibrils were sonicated using the tip sonicator at level 1.5 for 20 seconds on ice, breaking them into small fragments used as seeds. 10% of these seeds were added to 25 μM fresh WT monomer and 50 μM heparin in protein buffer, and fibrils grew for one hour at 37 °C. The new fibrils were sonicated in the same manner to create new seeds. This series of sonication and incubation was performed five times, and the final cycle corresponded to preparation of the DEER sample.

The conformational template provided by the seeds is amplified through recruitment of monomer onto the ends of the fibrils. It was therefore necessary to ensure that the template being propagated is representative of the fully formed fibril conformations. The DEER distance distributions for fully formed fibrils were compared to the same fibrils subjected to sonication. The distances were conserved following sonication, establishing that the conformations of the seeds are indeed representative of the conformations of the fibrils (Figure 7.2).

7.3.7 Fibril Assembly and DEER Preparation

Tau fibrils for DEER were formed from combination of 2% spin-labeled monomer with 98% WT to a total protein concentration of 50 μM, along with 12.5 μM heparin cofactor and 10% seeds. With expected differences in SNR, 1% and 4% label could also be used, and the raw DEER data are affected as shown in Figure 7.8. Fibrils

grew overnight during 37 °C incubation. Following centrifugation (100,000 X g) and washing, pellets were resuspended in 10 - 30 μL protein buffer and transferred into 1.6 mm o.d. EPR tubes. Excess buffer was removed after centrifugation (1000 X g) of the samples. CW EPR was performed at room temperature to probe for short distance spin interactions that can interfere with analysis of DEER data. CW was measured at X-band with the Q-band sample tube supported inside the larger X-band tube. Figure 7.9 shows representative spectra for the fibrils. The characteristic peak broadening caused by spin label immobilization indicates that the labeled monomers are incorporated into the fibrils. The spectra also show that the labeled monomer does not preferentially stack onto itself, which would result in narrowing of the spectrum to a single line. After this check, samples were immediately frozen in liquid N_2 and stored for no longer than one month at -80 °C to await DEER analysis.

7.3.8 DEER Measurements

DEER measurements were performed at Q-band (34 GHz) on the Bruker E580 pulse spectrometer at 80 K, unless otherwise noted. Dipolar evolution curves were formed via four-pulse DEER (see Figure 1.5 for the pulse sequence). The $\pi/2$ observer pulse at ν_1 was adjusted for each experiment to give the maximum echo height and ranged from 36 – 42 ns. The π pump pulse at ν_2 was 40 ns, and 8-step phase cycling was used to remove unwanted echoes. τ_1 and τ_2 were held constant for each experiment at 200 and 2500 ns, respectively. The pump pulse started at T = 100 ns and was stepped in 8 ns increments. A field-swept echo-detected spectrum was recorded before each DEER experiment to find the field position of the echo maximum. The pump frequency

(ν_2) was set to the center of the resonator dip, corresponding to the center of the field-swept spectrum. The observer frequency (ν_1) was adjusted 37 MHz below the pump frequency, corresponding to the position of highest intensity in the field-swept spectrum. The SRT was set to 1.2 times the T_1 measured by inversion recovery. Spectra were averaged for 48-120 hours, depending on signal strength.

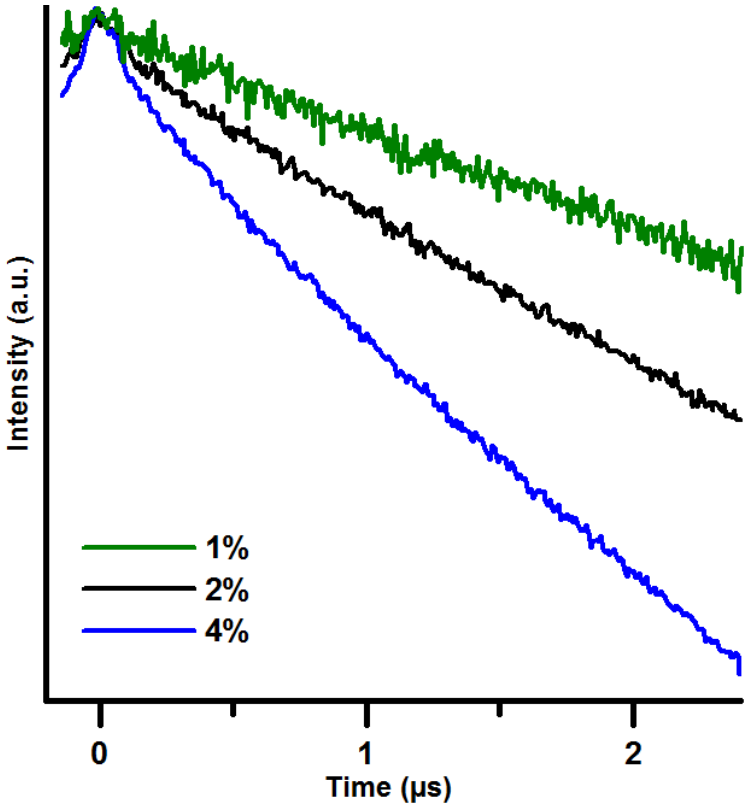

Figure 7.8. Effect of using different concentrations of spin-labeled tau monomer on raw DEER data for singly-labeled K18 311. The number of averages collected for each trace were: 469 (1%), 254 (2%), and 177 (4%). Interfering exchange interactions were not seen up to 4% label. Additionally, the 2% label trace was used to determine the background function for analysis of the double mutants; this trace is best fit to a 3D homogenous background function in the DEERAnalysis program.

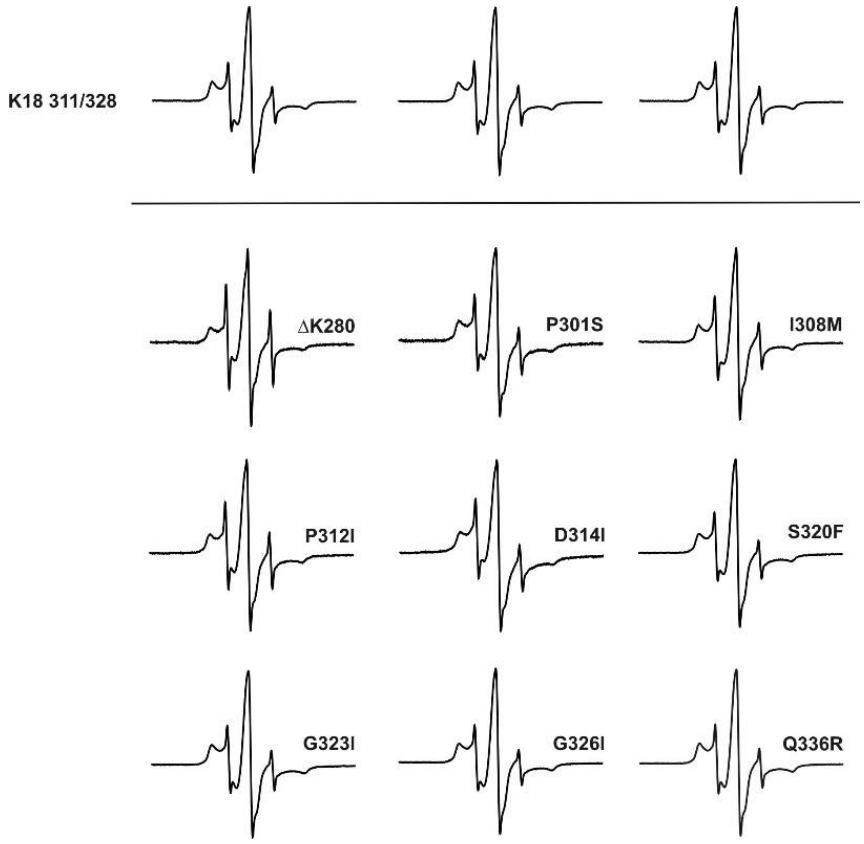

Figure 7.9. CW spectra of tau fibrils at room temperature. Traces are the average of 20 scans collected at 12 dB power attenuation (12.6 mW) with 100 kHz modulation frequency and 3.0 G modulation amplitude. Spectra were collected with 2048 points and 150 G scan width. Figure from reference [195].

7.3.9 Analysis of DEER Data

Raw DEER data were analyzed with DEERAnalysis2009 and 2011 [69]. It was important to use a fit function that would display the most detailed distance distributions in order to detect variation in fibril conformations. For this purpose, Tikhonov regularization was used because it does not constrain the resulting distances to a set number of Gaussians, single, double, or triple. The background caused by spins on neighboring monomers was decreased by diluting the spin-labeled monomers with an excess of WT tau. However, the background remained significant and was subtracted using a 3D homogenous model, as determined by the best fit to DEER data from fibrils

grown using singly labeled monomers (either 311 or 328, Figure 7.8). The starting point of background subtraction was selected to give the best fit to a well-separated Pake doublet. The Pake pattern (Figure 7.10B) represents the background-subtracted signal in the frequency domain. Altering the starting position varies the distance distribution only slightly; extremes in background fit for K18 311/328 are shown in Figure 7.10.

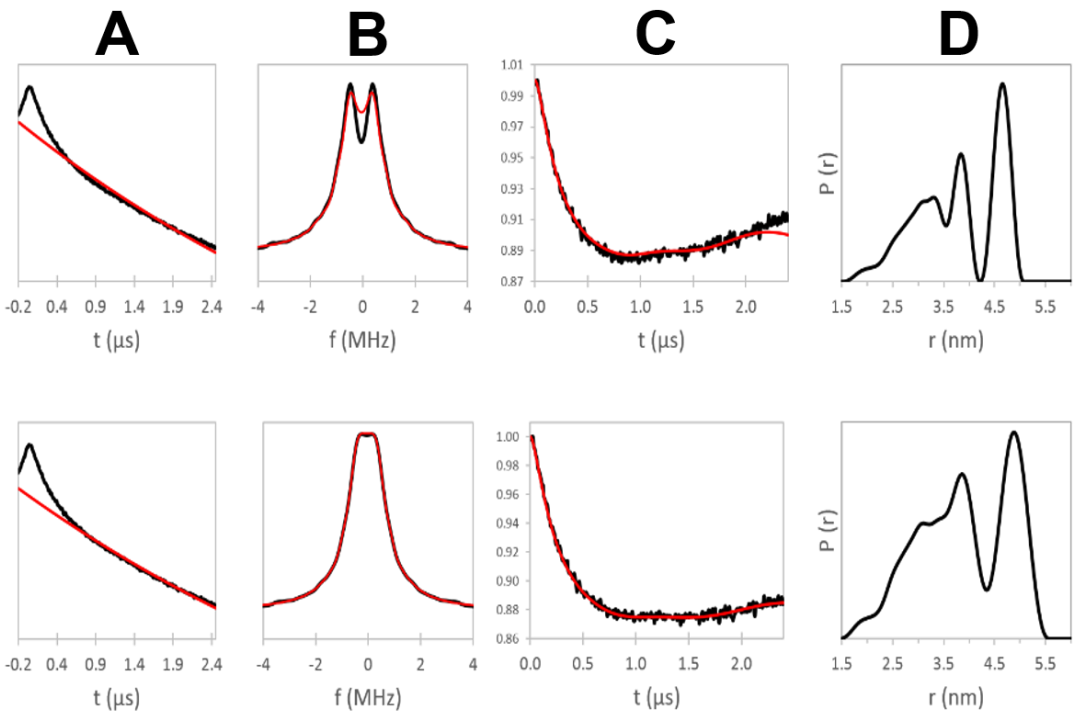

Figure 7.10. Effect of background fitting on distance distributions. Background fits (A), Pake patterns (B), background-subtracted DEER data (C), and distance distributions (D). Fit lines are in red. The top and bottom rows represent two extremes in background fit. If background subtraction is positioned too early in the trace (top row, A), the Pake doublet is well separated, but the fit is poor (top row, B). If positioned too late (bottom row, A), the Pake splitting is diminished (bottom row, B), although the fit is improved. Throughout this dissertation, background subtraction parameters were chosen that gave the best fit to a well-resolved Pake doublet, and were consistent for all samples. Importantly, the two extremes in background fit do not alter the peak positions, only the peak heights (D). Figure from reference [195].

The regularization parameter (α) of 100 was typically selected as the intersection point on the L-curves, giving the best compromise between peak resolution

and smoothness. The L-curves are very similar for all tau samples, and the choice of α = 100 was kept constant for comparison between different samples and experiments. Figure 7.11A shows L-curves for K18 311/328 prepared in triplicate, and Figures 7.12A and 7.13A show L-curves for the mutations added to the K18 311/328 monomer. The points corresponding to α = 100 are highlighted in green.

It is important to note that the SNR varies slightly in the background-subtracted data for the different mutations in Figures 7.12D and 7.13D. To ensure that SNR was not impacting the calculated distance distributions, the highly repeatable K18 311/328 double cysteine-mutant was analyzed with varying degrees of noise in the spectrum. Figure 7.14 shows that the distance distribution does not change significantly as the SNR decreases. The noisiest spectrum from Figure 7.13, ΔK280, is included for reference.

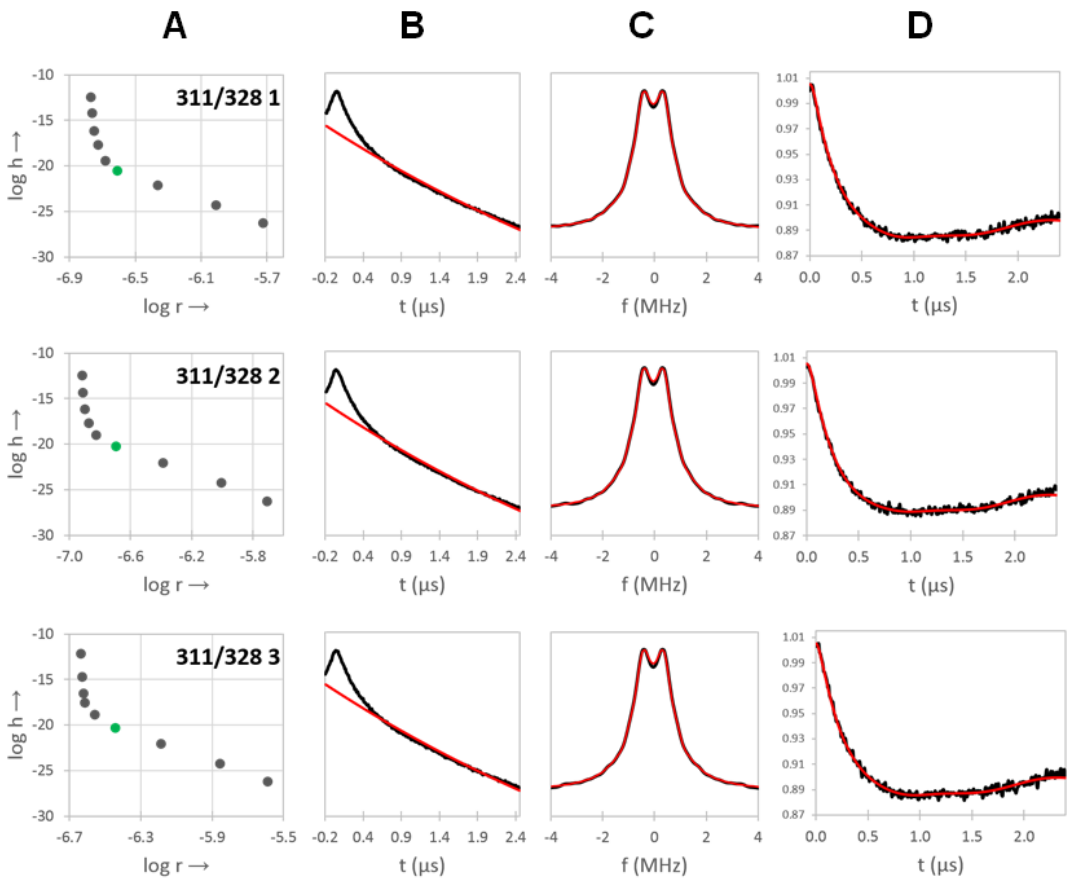

Figure 7.11. DEER data analysis of K18 fibrils labeled at positions 311/328. L-curves (A), background fitting (B), Pake patterns (C), and background subtracted DEER data (D). Fit lines are in red, and α = 100 is in green on the L-curve. The different rows represent independent experiments. Figure from reference [195].

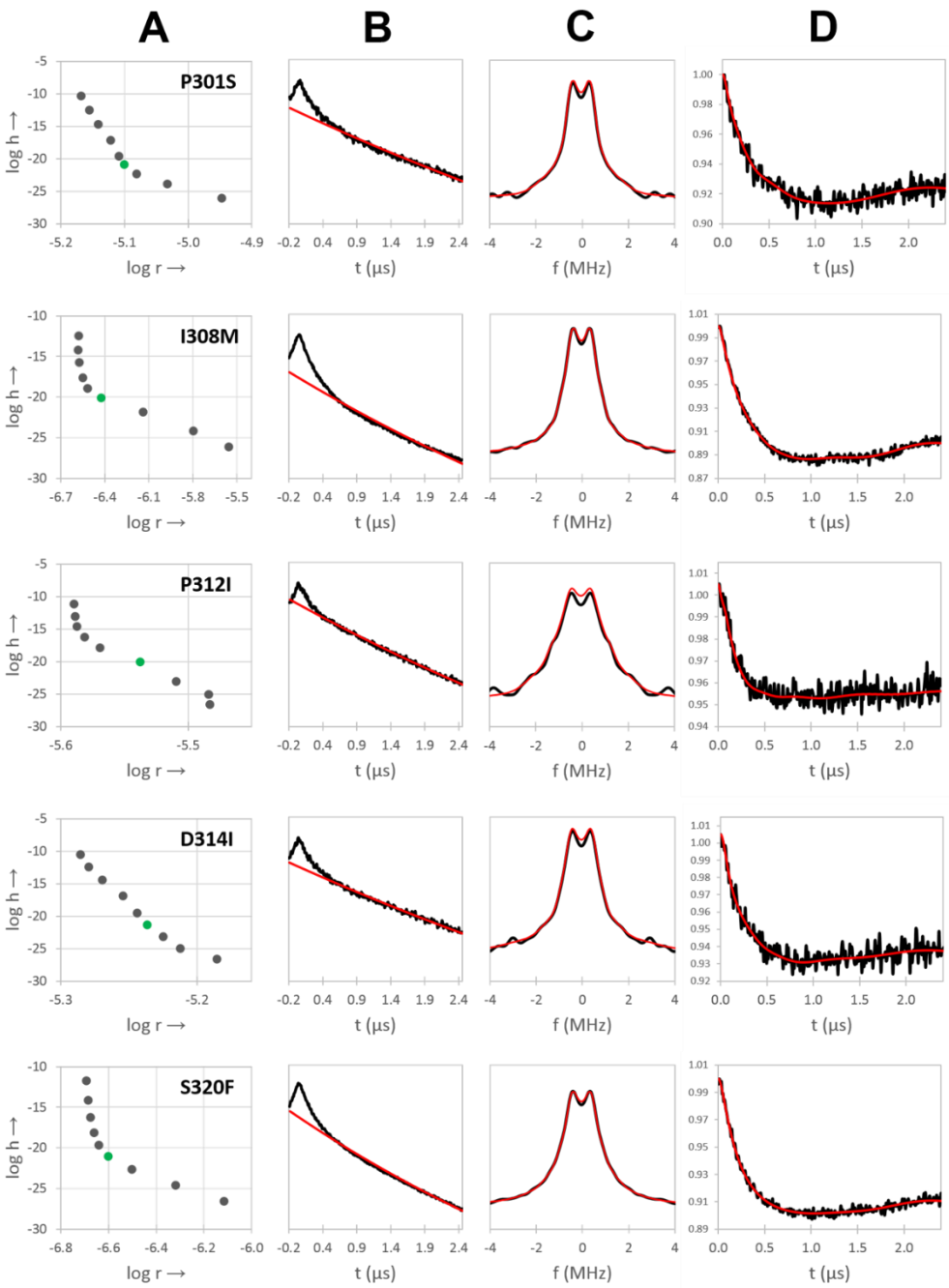

Figure 7.12. DEER data analysis of some K18 variants. All proteins are spin-labeled at positions 311/328. L-curves (A), background fits (B), Pake patterns (C), and background subtracted DEER data (D). Fit lines are in red, and α = 100 is in green on the L-curve. The different rows represent different tau variants. Figure from reference [195].

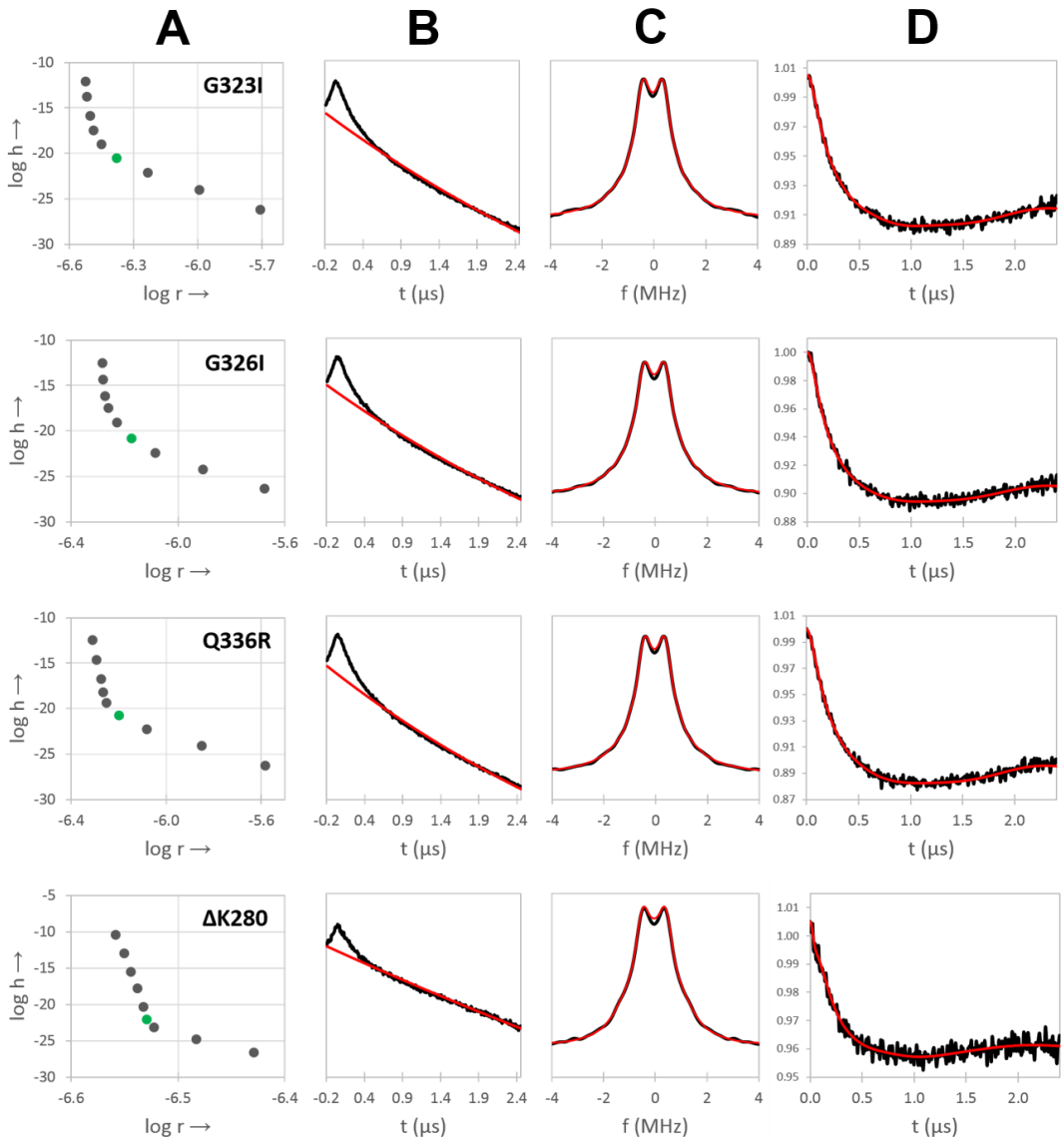

Figure 7.13. DEER data analysis of additional K18 variants. All proteins are spin-labeled at positions 311/328. L-curves (A), background fits (B), Pake patterns (C), and background subtracted DEER data (D). Fit lines are in red, and α = 100 is in green on the L-curve. The different rows represent different tau variants. Figure from reference [195].

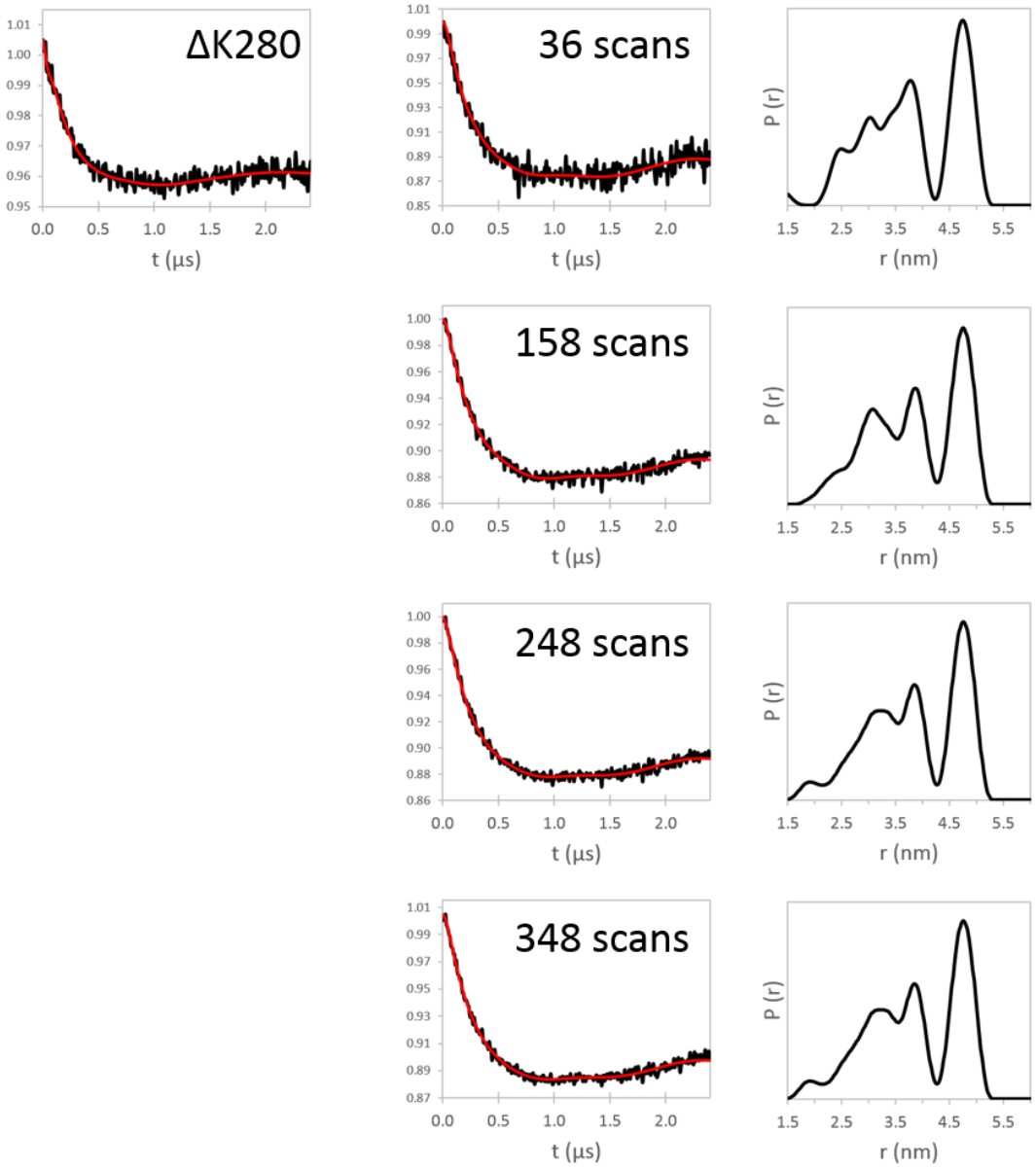

Figure 7.14. The effect of SNR on distance distributions of K18 311/328 fibrils. Corresponding distance distributions are shown next to the background subtracted DEER data. The overall peak positions are unaffected by changes in SNR. The relatively noisy spectrum of K18 311/328 ΔK280 is shown for reference. Figure from reference [195].

The DEER fit program GLADD was used for comparison of the main structural features of K18 311/328 that were repeatedly obtained with DEERAnalysis. The K18

311/328 double cysteine mutant was used as both the basis and a control for most tau DEER experiments, so accurate determination of the distance distribution for this sample was important. While the double Gaussian distance distribution obtained using GLADD shows features that are similar to the Tikhonov fit in DEERAnalysis, the sharpness of the peak around 4.8 nm was a concern. Data were collected for K18 311/328 at 60 K with τ_2 of 3500 ns, an increased window size, and GLADD analysis showed broadening of the sharp peak (Figure 7.15). These analyses indicate that the peak at 4.8 nm is needed to fit the data. However, the limitation to only two Gaussians does not provide a way to model the multiple components at shorter distances that are obtained by Tikhonov regularization. Although GLADD provided an excellent check of spectral analysis, it was not feasible to study the ensemble of fibril conformers for additional samples.

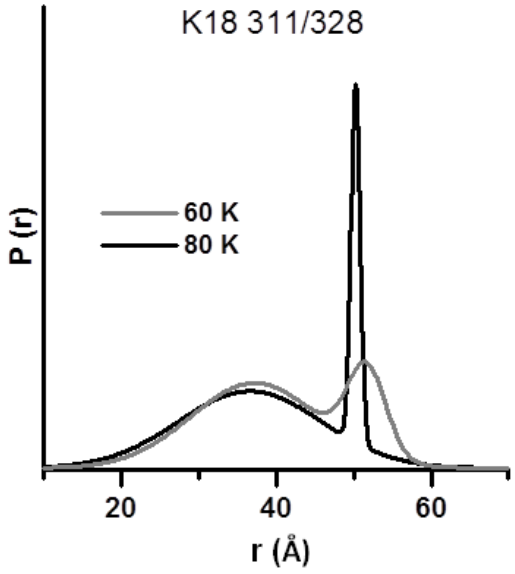

Figure 7.15. Comparison of distance distributions obtained using GLADD for fits to two Gaussian distributions of distances based on analysis of raw data obtained with time windows of 2.4 μs (80 K) and 3.4 μs (60 K). The sharp peak at 4.8 nm broadens as the length of the time window is increased, which provides better definition of the spin-spin interactions. Figure from reference [195].

7.3.10 Negative Stain Transmission Electron Microscopy

Tau fibrils were often visualized with transmission electron microscopy (TEM). The fibrils were stained with 2% uranyl acetate and adsorbed onto 200 mesh carbon-coated copper grids. Images were taken with a Philips/FEI Tecnai-12 transmission electron microscope at 80 keV that was equipped with a Gatan CCD camera.

7.4 Results and Discussion

7.4.1 Fibril Conformations of K18 and K19 Monomers

The aim of the first tau study, in collaboration with Ayisha Siddiqua, was to determine structural differences between 3R and 4R fibrils. Both K18 and K19 were doubly spin-labeled at three pairs of positions: 311/322, 311/326, and 311/328. It was previously shown that K18 can grow onto K19 seeds, but not the converse [209]. Therefore, distances were measured for K18 monomer grown onto K18 and K19 seeds, while K19 monomer was grown only onto K19 seeds. It is understood that the seeds provide the templates onto which the tau monomers grow, and if the same template is used, the same fibril conformations emerge. This phenomenon was seen for K18 and K19 monomers grown onto K19 seeds, in which the distance distributions for 311/322 were very similar (Figure 7.16). The dipolar oscillation traces for this spin pair clearly superimpose, further indicating the conversion of K18 monomers to K19-like fibril conformation. This work was published in reference [194].

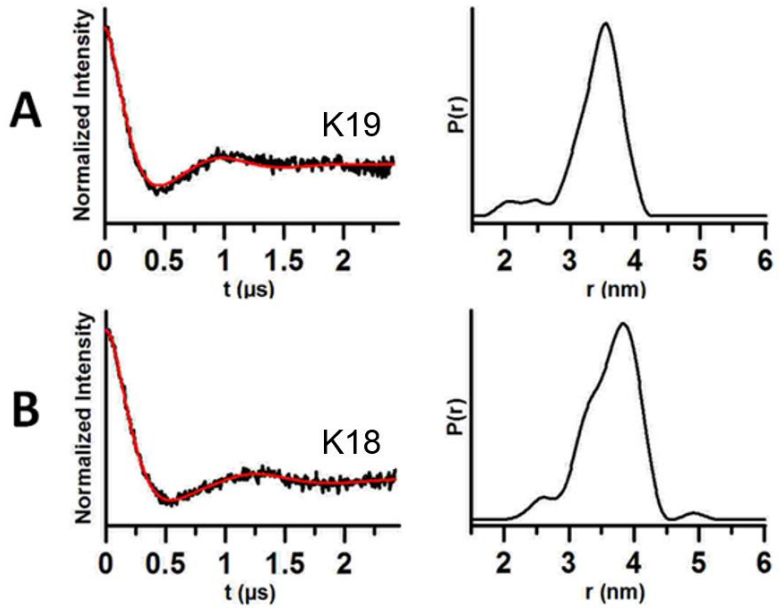

Figure 7.16. K19 (A) and K18 (B) monomer grown onto K19 seeds. When presented the same seed conformations (K19), both types of monomer adopt the same conformations, with a distance of ~3.5 nm between spin labels at positions 311 and 322. Figure from reference [194].

The K19-seeded traces diverge slightly for spin pairs 311/326 and 311/328, although both fibril types have very weak dipolar interaction, suggesting extended conformations in which the spin labels are separated by long distances (Figure 7.17). An extended conformation is modelled by the green trace for 311/326, which is the result obtained for singly-labeled monomer. In K19, 311 is too far from positions 326 and 328 to obtain a distance distribution. In contrast, distances could be obtained for K18 monomers grown onto K18 seeds, revealing a mixture of fibril conformations for each spin pair studied (Figure 7.18). The dipolar oscillations show strong spin interactions and vary significantly from the traces for K19-seeded fibrils.

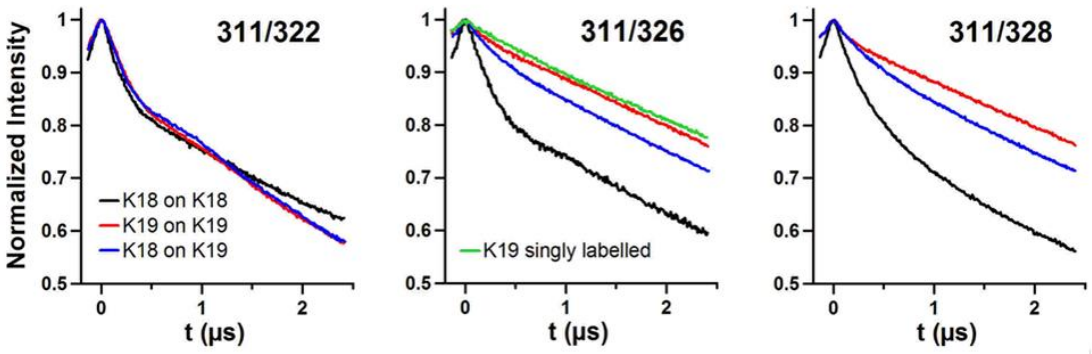

Figure 7.17. Dipolar oscillation curves for all samples studied. Spin labels at positions 311/322 using K19 seeds overlap, but diverge slightly for positions 311/326 and 311/328. Distance distributions were not obtained for K19 on K19 seeds, as the spin labels are thought to be out of range for dipolar interaction (~5 nm). The K18 grown onto K18 seeds gave measureable distance distributions for all spin label pairs. Figure from reference [194].

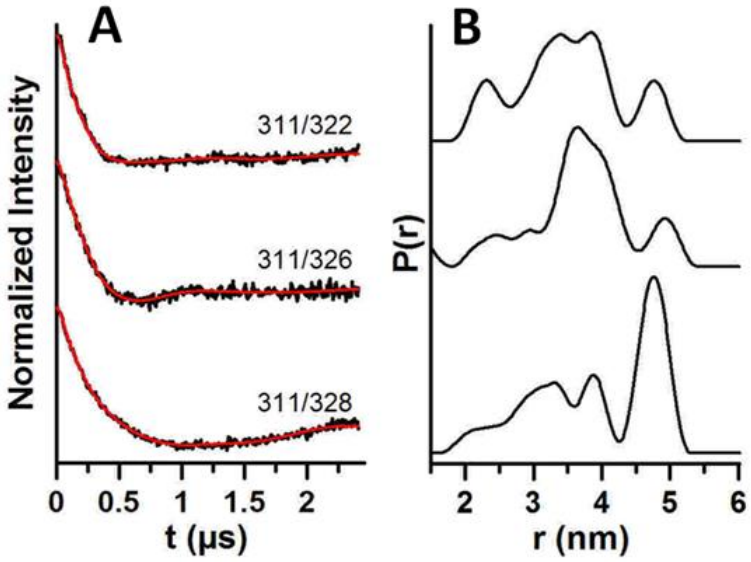

Figure 7.18. Background-subtracted raw data (A) and distance distributions (B) for K18 on K18 seeds, spin-labeled at different positions. All positions had distributions containing a mixture of distances, implying the presence of a mixture of fibril conformations. Figure from reference [194].

Whereas other protein analysis techniques provide averaged structural characteristics for a mixture of distinct protein assemblies, DEER is capable of qualitatively describing the relative populations of fibrils in a heterogeneous mixture.

Data from the first tau structural study using DEER showed that K19 adopts a single, extended monomer conformation within fibrils. Conversely, K18 is more versatile and can adopt a mixture of different conformations when grown onto K18 seeds, or adjust to the specific conformation of K19 seeds. Once the utility of DEER for analysis of fibril mixtures was demonstrated, the question arose whether conformer populations could be varied by addition of mutations to tau monomer.

7.4.2 Mutations Alter Seed Selection of Tau

It has been previously shown that mutations to tau are sufficient to trigger disease [196]. In general, the mechanisms by which mutations can induce neurodegeneration is unknown: mutations can alter the natural ratio of 4R:3R within the brain or the stability of the interaction between tau and microtubules. It was reported that several mutations destabilize this interaction [232, 233], in addition to stimulating fibril formation (heparin cofactor required) [234]. The aim of this study was to determine if the effects seen by some of the mutations to tau have a structural basis. Known disease-related mutations ΔK280 [232], P301S [233], S320F [235], and Q336R [236] were studied, as well as additional mutations I308M, P312I, D314I, G323I, G326I. This work was published in reference [195].

The representative K18 double mutant 311/328 with a heterogeneous distance distribution was chosen to examine differences in seed selection initiated by mutated monomers. The mutations listed above were incorporated into K18 311/328. The mutated monomers grew onto the templates provided by WT K18 seeds. Resultant DEER data were analyzed analogously for all samples to detect whether the mutants

grew preferentially onto specific fibril conformations present in the mixture. Variations in seed selection were determined through comparison to the distance distribution of non-mutated K18 311/328.

Before analysis of mutation effects, it was important to demonstrate that the K18 311/328 system was robust for use as an indicator of conformational variation. The sample was prepared and analyzed in triplicate and the distribution shown to be repeatable (Figure 7.19A). The relative populations of fibrils adopting these conformations are also well-conserved. When prepared with different seed batches, three distances for this system at 3.2, 3.8, and 4.8 nm that vary only in peak height or width were consistently observed. We therefore concluded that K18 311/328 is an appropriate starting point to examine variation in conformation selection of mutated monomer grown onto seeds.

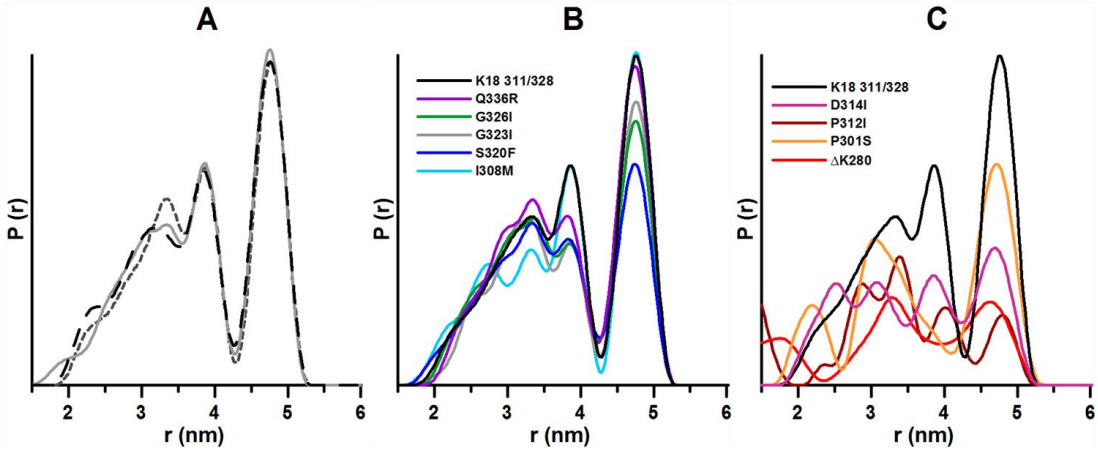

Figure 7.19. Distance distributions of K18 311/328: repeatability (A), mutations with distance distributions similar to non-mutated K18 311/328 (B), mutations with very different distributions compared to non-mutated K18 311/328 (C). Figure from reference [195].

The distance distributions for the mutant-bearing fibrils were examined next, and several of the mutations gave distributions similar to that of non-mutated K18 311/328 (Figure 7.19B). Conversely, some of the mutations at significant positions in the protein (ΔK280, P301S, P312I, and D314I) clearly change the distribution of fibril conformers following template-assisted growth (Figure 7.19C). To ensure that these dramatic changes to seed selection were not in fact a result of amorphous monomer aggregation, fibril formation was confirmed by EM (Figure 7.20).

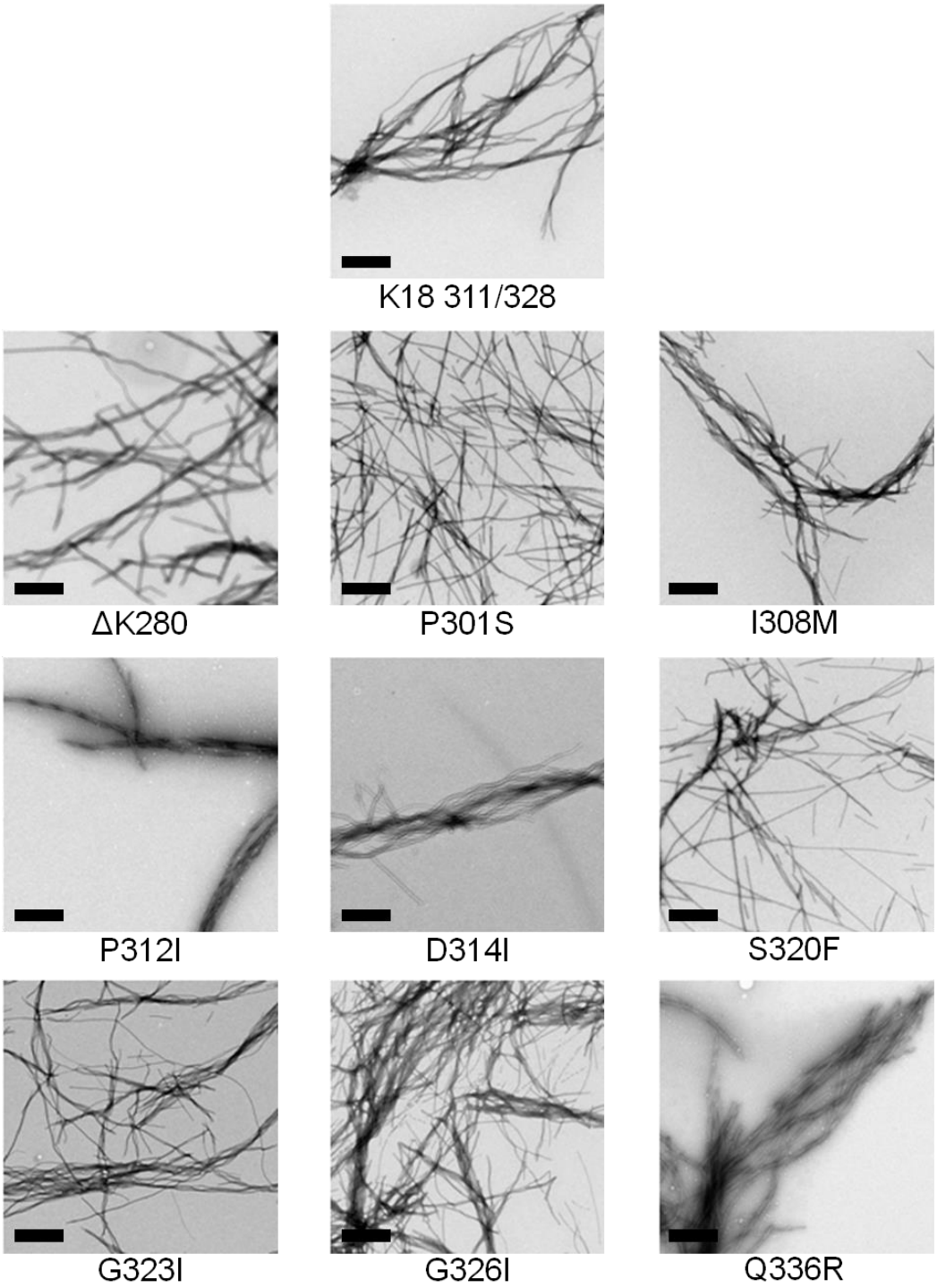

Figure 7.20. Electron micrographs of spin-labeled K18 fibrils (labeled at positions 311 and 328). The additional mutations are noted. All monomers formed elongated fibrils, indicating that differences in DEER data are not caused by amorphous aggregates. Bar = 500 nm. Figure from reference [195].

The DEER distance distributions suggested that key mutations play a role in seed selection during fibril growth, while mutations with similar distributions have little or no conformational effect. In addition to variation in distance distributions, comparisons can be made from examination of the raw DEER data to support these conclusions. When grouped according to degree of similarity to non-mutated K18 311/328, the traces and fit functions for the background-subtracted data align with the grouping of similar and dissimilar distance distributions (Figure 7.21). The initial drop in signal of the raw data before background subtraction provides a qualitative measure of the interaction between the spin labels; in this area of the spectrum, similar mutants trace together and different mutants trace separately, with ΔK280 the furthest outlier. A shallow initial drop in the raw data corresponds to weak spin-spin interactions. This suggests that the mutations with very different population distributions may contain conformers with interspin distances longer than 5 nm, which was previously shown for K19 fibrils. Adoption of extended-monomer conformations may account for the asymmetric seeding barrier demonstrated for tau, for which K18 can grow onto K19 fibrils, but K19 cannot grow onto K18. Since K18 ΔK280 may also adopt a more extended conformation, it was logical to test whether K19 could be grown onto K18 ΔK280 seeds. Additionally, the ΔK280 mutant corresponds to removal of a positively-charged lysine residue at position 280, which is in the 2nd tau repeat region, and K19 does not contain this region. An experiment performed by Paul Dinkel using an intrinsic acrylodan fluorescence assay as well as sedimentation [195] demonstrated that K18 ΔK280 is competent to seed K19 monomer.

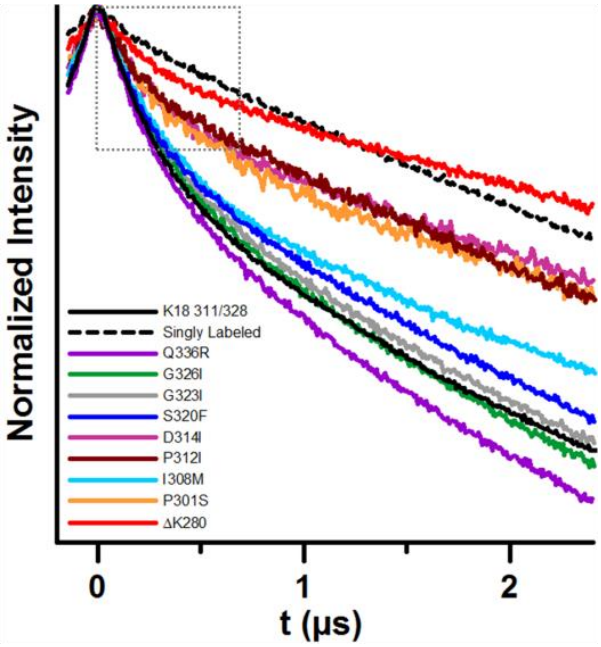

Figure 7.21. Overlay of raw DEER data for all mutants studied, including the K18 311/328 core and singly labeled monomer. The largest difference is apparent from the initial drop region (boxed). Figure from reference [195].

The development of DEER spectroscopy has provided a unique tool with which variation in protein conformation can be studied. This tool was utilized to investigate the effect of a single mutation on the seed conformations that monomers select for growth. Figure 7.22 illustrates an overview of the concepts presented here. There are three distinct fibril conformations consistently observed for non-mutated K18 311/328 (Figure 7.22A). Non-mutated fibrils are used to create seeds which contain the same populations of conformations as the fibrils (Figure 7.22C). When these seeds are added to monomers containing mutations at various positions in the sequence, the populations of these conformations will vary depending on seed selection of the monomers. As demonstrated, some mutations assume populations consistent with non-mutated monomer, while other mutations significantly alter the populations of conformers

(Figure 7.22D). Seeing that mutations could have a dramatic effect on seed selection, the effect of variations in fibril growth conditions was investigated next.

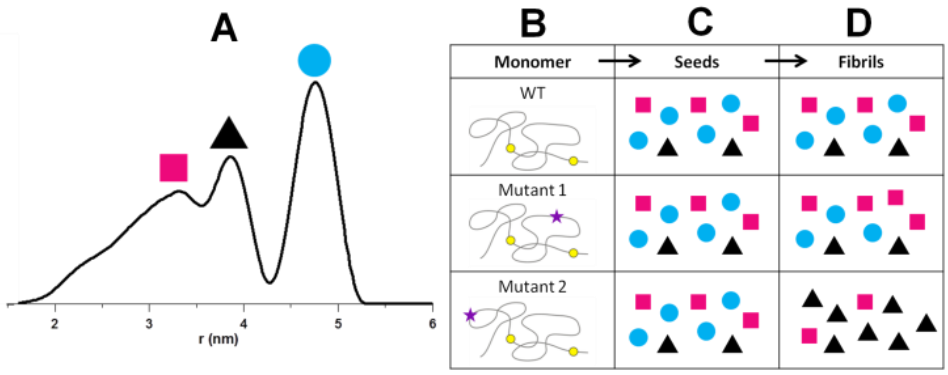

Figure 7.22. Fibril populations in the heterogeneous mixture of conformations show sequence dependence. From the distance distribution, there are three distinct fibril conformations (A). Different monomers (B) are added to the same populations of seeds (C). The populations of conformers for the resulting fibrils (D) can be similar to the wild-type populations (Mutant 1) or can differ (Mutant 2).

7.4.3 Growth Conditions Vary Tau Fibril Structure

Insertion of mutations to K18 311/328 proved insightful and indicated the presence of different accessible conformations within the seeds. Fibrils studied up to this point were formed through seeding over multiple cycles (see Section 7.3.6). In this study, changes in fibril structure brought about by varying seeding conditions, temperature, and stirring during fibril growth were examined. The K18 311/328 double mutant was again used as a standard by which to measure changes to the DEER distance distributions.

Variation in number of seeding steps. Typically, five seeding steps are used to prepare samples, and conformations repeatedly consist of three peaks (Figure 7.19A). Here, fibrils were sonicated and used for seeds directly following three days of stirring (for initial fibril growth). These seeds corresponded to step 0, as no additional cycles

of sonication and incubation were performed. Additionally, fibrils were grown following 10 and 15 seeding steps. Fibrils grown following 5 seeding steps were prepared as a control. Figure 7.23 shows the distance distributions for fibrils grown from different seeding steps.

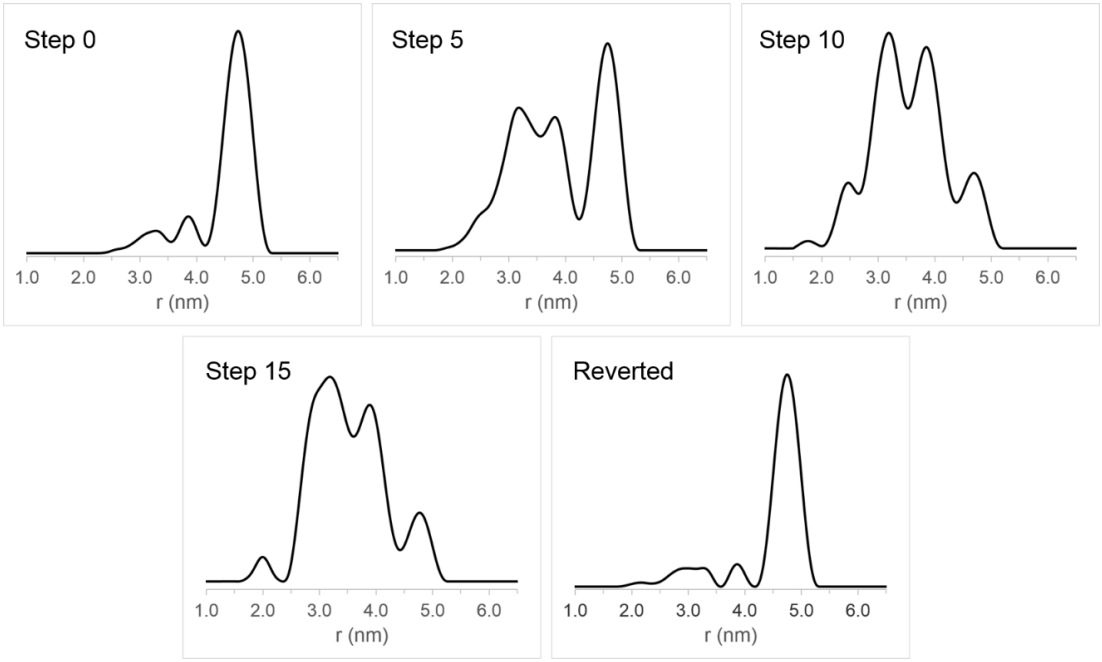

Figure 7.23. Distance distributions for K18 311/328 grown using different numbers of seeding steps. Step 5 is the control, showing the reproducible peaks at 3.2, 3.8, and 4.8 nm. The reverted sample refers to fibrils grown stirring overnight at 37 °C made from seeds of step 15 sonicated. No post-processing normalization was implemented.

The largest variation is seen in the peaks at 3.2 and 3.8 nm, which are almost fully suppressed in step 0 and gradually enrich in population with additional seeding steps. Step 5 is equivalent to prior measurements of this control, while the difference between step 10 and step 15 is negligible. This may indicate that by step 10, the fibril conformations have reached a population equilibrium, and seed selection beyond this point does not change enough to be evident in the distance distribution.

The primary difference between step 0 and step 15 lies in stirring of the fibrils used for seeds. Step 0 is prepared from fibrils that have stirred for three days, while the seeds used for step 15 were not stirred during any of the seeding cycles. To check whether the short distance peaks, once enriched, could then be suppressed, fibrils from step 15 were used to seed new fibrils grown overnight under stirring conditions. The distance distribution for the reverted fibrils is also shown in Figure 7.23. The conformation populations of these fibrils match almost perfectly with fibrils grown using stirred seeds (step 0). The raw DEER data traces confirm that the reverted fibrils are similar to step 0, and also that steps 10 and 15 are equivalent (Figure 7.24).

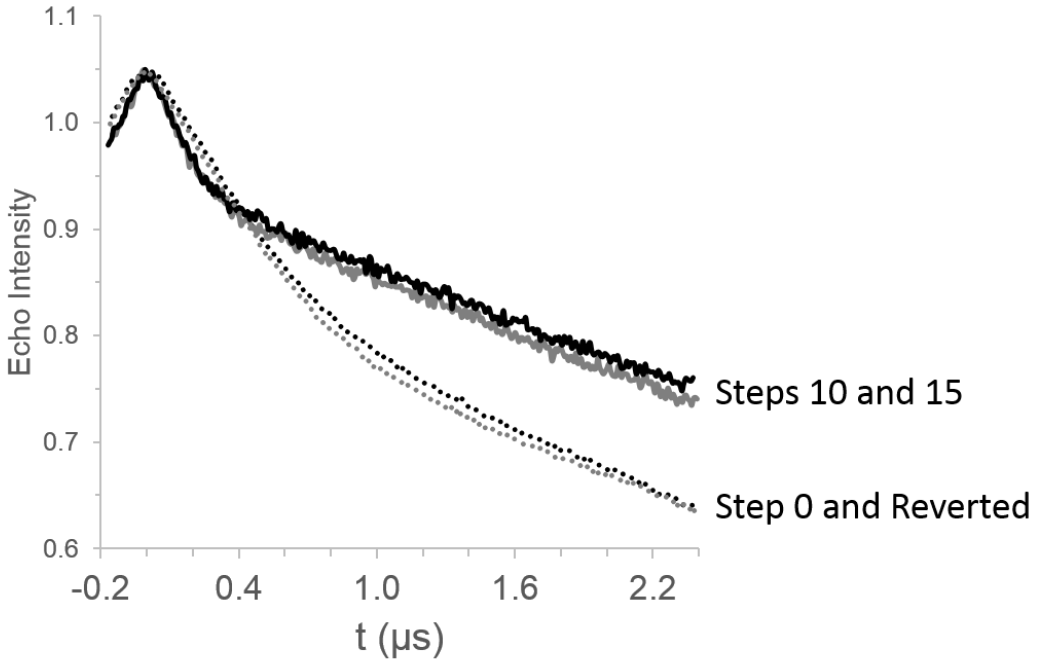

Figure 7.24. Raw DEER data showing the similarities in steps 10 and 15 (solid) and step 0 and the reverted sample (dotted). The decreased SNR of steps 10 and 15 caused by poor compression into the EPR tube is evident.

It was observed that fibrils from different seeding steps centrifuged into the Q-band EPR tubes differently. Steps 10 and 15 did not compress very much, and the

SNR was lower for these samples than step 0 and the reverted fibrils (Figure 7.24), which compressed much more. Step 5, the control, compressed intermediately and behaved similarly to previous preparations. It was thought that fibrils from steps 10 and 15 were longer than those from step 0 and the reverted sample. In this case, the extended fibrils may hinder centrifugal compression, similar to full-length tau. Slight differences in SNR can be seen from the room-temperature CW spectra (Figure 7.25). Longer fibrils were consistently seen in electron micrographs of step 10 compared to step 0 (Figure 7.26). In addition to differences in compressibility, fibrils from steps 10 and 15 were more transparent following centrifugation than step 0 and reverted, which were an opaque white.

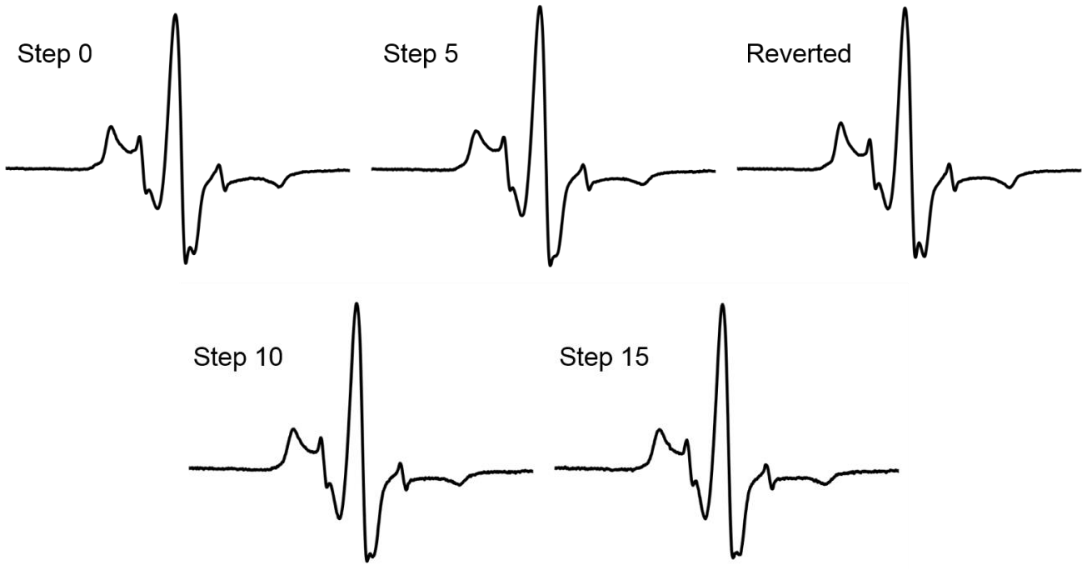

Figure 7.25. Normalized X-band CW spectra for the fibrils grown with different seeding steps. Traces are the average of 20 scans using 2048 points, 100 kHz modulation frequency, 3.0 G modulation amplitude and 150 G scan width at 20 mW power.

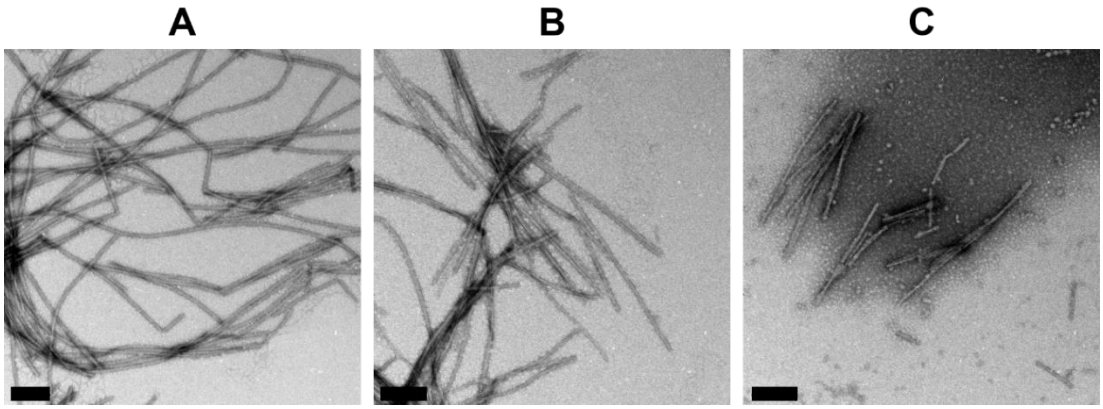

Figure 7.26. EM of fibrils formed from 10 seeding cycles (A), 0 seeding cycles (B), and 15 cycles stirred overnight (C). Fibrils in (A) are longer than those in (B). Panel (C) shows that stirring breaks the fibrils into smaller fractions. Bar = 200 nm.

Stirring fibrils causes breakage. After observing that the populations of shorter distance fibril conformations were suppressed for seeds that had been stirred, a direct comparison of fibrils formed under stirring and non-stirring conditions followed. Fibrils are typically not stirred during the incubation steps of multistep seeding. The first comparison, therefore, was to fibrils that were stirred during incubation (Figure 7.27A). As expected, the peaks at 3.2 and 3.8 nm are suppressed for the stirred sample. This analysis was then repeated for fibrils that grew without addition of seeds. For the stirred fibrils, this type of preparation corresponds to the fibrils formed over three days of stirring, which are usually used for the first seeding step. Here, the fibrils were analyzed directly. Stirring speeds fibril growth, so the non-stirring, non-seeded fibrils were allowed to grow for seven days total. Completion of fibril growth was assessed by the observation of visible, opaque filaments in the reaction tube. Figure 7.27B shows the effect of stirring on the distance distribution of non-seeded fibrils. Again, the populations corresponding to shorter distance peaks, which are less well defined for the fibrils grown under quiescent conditions, are decreased. The resolution of the peaks in

the non-seeded quiescent distribution is likely poor due to decreased SNR from non-ideal fibril growth conditions. Distance distributions in Figure 7.27 have been normalized to the peak at 4.8 nm for straightforward comparison of the lower-probability peaks.

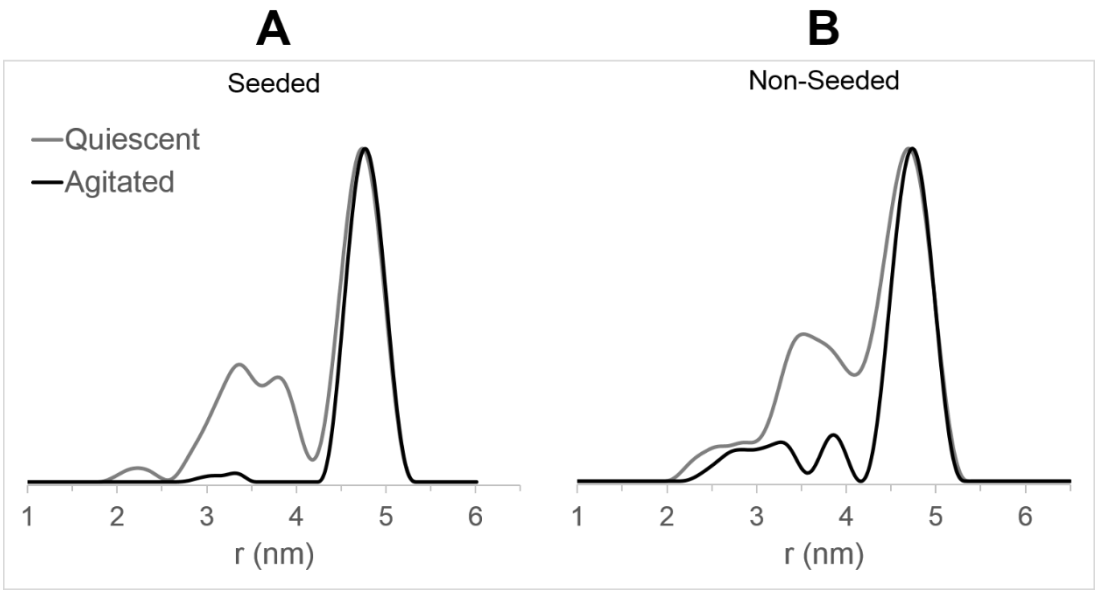

Figure 7.27. Effect of stirring (agitation) on conformer populations for seeded (A) and non-seeded (B) fibrils. Distributions were normalized to the 4.8 nm peak amplitude for comparison of shorter distance peaks.

As mentioned, SNR was decreased for the non-seeded quiescent sample, but it was also less for the seeded quiescent sample. The stirred samples compressed more into the EPR tube, resulting in greater signal within the resonator. The increase in SNR with stirring is not significant enough to affect the room-temperature CW spectra (Figure 7.28). It is clear from the distance distributions, as well as differences in compressibility, appearance, and SNR, that structural properties of fibrils are influenced by the environments in which they are grown.

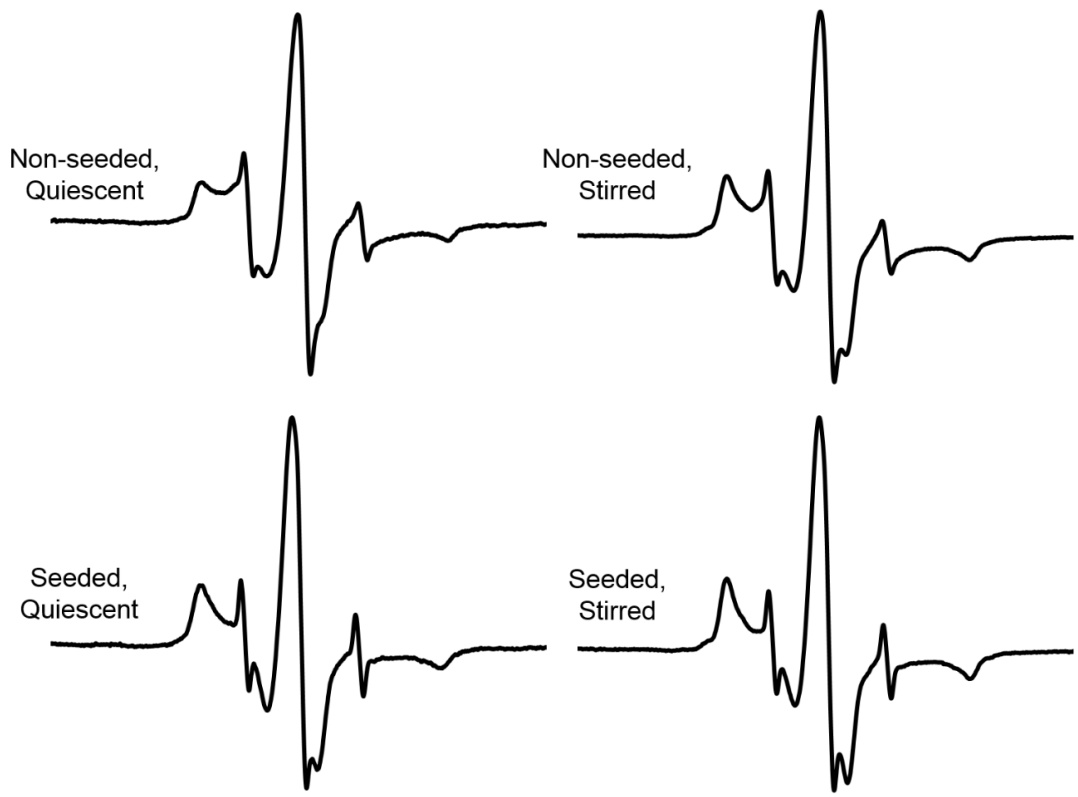

Figure 7.28. Normalized X-band CW spectra for the fibrils grown under stirring and quiescent conditions. Traces are the average of 20 scans using 2048 points, 100 kHz modulation frequency, 3.0 G modulation amplitude and 150 G scan width at 20 mW power.

Effect of growth temperature on fibril conformations. It became clear that the environment of the fibrils during growth was essential to the conformations that emerged. The simplest environmental change to make was variation in temperature. Using K18 311/328 as a control, a sample was prepared in triplicate under normal conditions. This included five seeding steps and overnight incubation at 37 °C for the final cycle in which the fibrils include 2% spin-labeled monomer for DEER (Figure 7.29A). Samples were then compared using overnight incubation temperatures of 25 °C and 4 °C for final DEER fibril growth. Figure 7.29B shows that the differences in

distance distributions from altering final incubation temperatures is not as substantial as the differences seen from using additional seeding steps. Interestingly, however, the peak that is altered is only that at 3.2 nm. Previously, changes were only seen in a combination of this peak and the peak at 3.8 nm. Distance distributions in Figure 7.29 were again normalized to the peak at 4.8 nm. Although the differences in populations are not as sizeable as seen for the other altered growth conditions, it is clear that temperature plays some role in monomer seed selection.

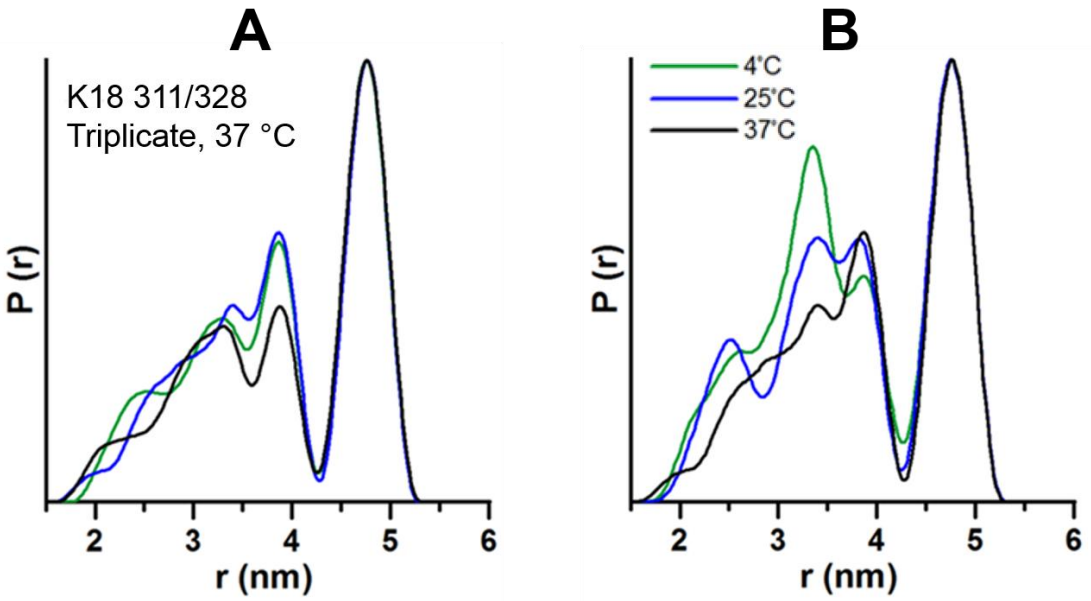

Figure 7.29. Effect of temperature on populations of fibril conformers. K18 311/328 prepared in triplicate under normal conditions (A) and the same conditions but different temperatures of final overnight incubation (B). Distributions were normalized to the 4.8 nm peak amplitude for comparison of shorter distance peaks.

Interpretation of variation in fibril conformations. This section introduced large variations in tau fibril structure. To explain some of these changes, it is necessary to look at trends in the individual peaks. Fibril populations corresponding to the short distance peaks at 3.2 and 3.8 nm are enriched at increased seeding steps, while the peak

at 4.8 nm is dominant whenever the fibrils are formed while stirring. From EM, it appears that the fibrils with 4.8 nm between spin labels are shorter than fibrils with 3.2 and 3.8 nm between spin labels. It follows that 4.8 nm populations are increased during stirring through continual breakage of these fibrils, increasing the number of ends onto which monomer can attach. This suggests that the 4.8 nm fibrils are more fragile than the other conformations. To test this, fibrils from step 10 and step 0 were sonicated in parallel and resultant fibril length compared by EM. Figure 7.30 shows that sonication breaks step 0 fibrils to a greater extent than step 10 fibrils. This supports the postulate that the conformation corresponding to 4.8 nm is enriched by stirring due to enhanced breakage.

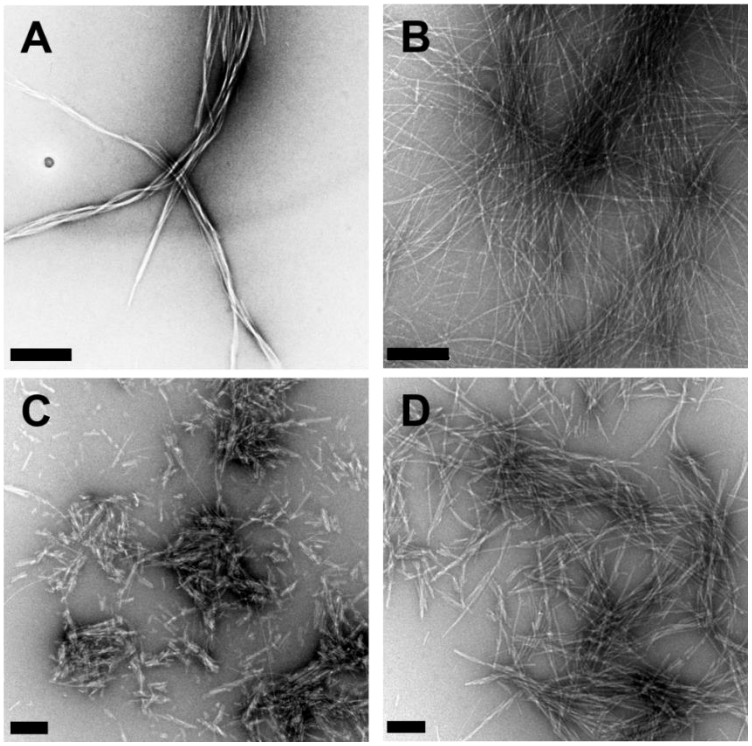

Figure 7.30. EM of step 0 pre-sonication (A) and post-sonication (C) and step 10 pre-sonication (B) and post-sonication (D). The bar in A and B is 0.5 μm and in C and D is 0.2 μm. Fibrils appeared to be similarly elongated pre-sonication (A vs. B) but step 0 broke into smaller pieces than step 10 post-sonication (C vs. D).

Similarly, the 4.8 nm peak is suppressed over multiple cycles. Without stirring, the selective pressure toward the 4.8 nm conformation is lost. Additionally, the fibrils are given only one hour between seeding steps to elongate. This suggests that the fibril conformation corresponding to the 4.8 nm peak grows more slowly than the conformations with shorter distance peaks. Early kinetic studies by Michael Holden showed that fibrils enriched with the 4.8 nm conformation and fibrils enriched in the shorter distance conformations all grew to completion within the one hour incubation time. Current studies are focused on studying differences in the rates of fibril growth for the different conformations.

Fibril breakage may also explain the minimal sample obtained through non-seeded, non-stirring fibril formation. While stirring, the fibrils are constantly forming and breaking. Without this breakage, individual, long fibrils will form, and the amount of fibrils will be reduced based on the number of ends onto which monomer can grow. Stirring is not necessary for seeded samples because nucleation is circumvented and fibril growth occurs quickly onto the introduced seeds. The above findings suggest that preference for specific conformations can be modulated by selective pressures.

7.5 Conclusions

Although natively unstructured in solution, binding of tau to microtubules [237] and small enzymes [238] induces distinct conformational changes. With this level of conformational flexibility, it is reasonable to assume that tau can adopt different structures depending on the substance to which it is bound. Using DEER, the Margittai lab has demonstrated that there are indeed variations in tau structure that depend not only on the seed structures, but also the monomer sequence. It is possible that these

structural variations play a role in disease development and propagation though specific genetic and environmental factors, some of which have been specificially linked to disease [239] and others that have not yet.

Following observation of unique structures for different isoforms (3R compared to 4R fibrils), the studies presented here focused on variation of 4R tau structures based on mutations and growth conditions. The effect of modified seed selection for certain mutations can be explained by the conformational compatibilities of individual mutants. Mutants that do not interfere with any of the original conformers will be recruited akin to the WT monomer. Mutants that are incompatible with some of the original conformers will change the overall composition of the ensemble. While these selection processes could be modulated by additional factors in the complex cellular environment of the human brain, the findings presented here provide an important general model of how new fibril ensembles might emerge. It is plausible that the conformational composition of tau fibrils could vary for different forms of inherited frontotemporal dementia, where dominant mutations in the tau gene (*MAPT*) are linked to disease. Also important in the context of the herein presented studies, at least in some cases somatic mutations in tau could define the initial ensemble of conformers in sporadic forms of tauopathies and hence influence the selective processes as fibrils spread throughout the brain. Specifically, if different fibril ensembles composed of mutant tau transferred to connected neurons (free of tau mutations) the recruitment of WT tau would vary in a conformation dependent manner. The presented model shows similarities to current models of strain mutation and selection in prions [240]. Remarkably, a single amino acid difference at position 226 in the prion proteins of elk and deer, combined with

conformational selection of compatible seeds, determines strain mutation in chronic wasting disease [241]. Although transmissibility of tau is confined to neurons within a single human brain, the overall conformational selection processes appear to be governed by the same underlying structural principles. It is likely that other pathological amyloid fibrils share similar selection properties. The recent finding that structural variations in fibrils of the β-amyloid peptide may contribute to variations in Alzheimer's disease [242] underscores the biological relevance of fibril conformation. Changes in fibril conformation through seed selection could be an important molecular mechanism of diversifying disease phenotype. The existence of different fibril ensembles and their emergence upon spreading must be taken into account when designing new therapeutic strategies for interfering with amyloid diseases.

It was shown here that changing the environmetal conditions under which fibrils are grown can have a very large effect on the structures that emerge. When seeds were formed under normal conditions (stirring three days at room temperature followed by five seeding cycles at 37 °C), fibril fragility and breakage dictated the conformation of the dominant species. Altering these conditions through the number of seeding cycles, stirring, or temperature imparted selective pressures on the system that changed the dominant fibril structure. It is understood that the spread of disease in the brain depends on cell-to-cell transfer of fibrilar units. Changes to the cellular environment may preferentially enhance certain fibril conformations, which are then spread and can be further enhanced or alternatively modified. Additionally, fibril breakage may facilitate propagation of diease-relevant fibril structures. This concept is utilized for amplification of tau fibrils in Chapter 9.

Tau belongs to a class of proteins that aggregate to form insoluble amyloids. Amyloids can be either beneficial or disease-inducing, and some have yet unknown function. Amyloid proteins share many features, both structural and mechanistic. In addition to the studies presented in this dissertation on tau, structural polymorphism has been reported for Aβ protein [242], implicated in Alzheimer's disease, and Sup35 [243], a yeast prion whose structural variation results in different strains. Studies continue to focus on revealing the link between structural variation and disease [244] , and gaining a better understanding of this phenomenon for tau benefits the study of other amyloidogenic proteins as well.

Chapter 8: DEER Analysis and Acquisition Improvement

8.1 Experimental Requirements and Limitations of DEER

The previous chapter demonstrated the advantages of DEER for the study of protein structure. Although DEER overcomes the inherent shortcomings of structural techniques like X-ray crystallography and NMR, it is not free from its own unique limitations. Data are typically collected at liquid N_2 or colder temperatures for several reasons, primarily for improved SNR relating to the Boltzmann distribution (Equation 1.4). At colder temperatures, there are fewer spins in the excited state, leading to enhancement of the signal. The population ratio of the upper to lower energy levels decreases from 0.9985 at room temperature (298 K) to 0.9943 at 80 K. This difference of only 0.4% is significant enough to improve SNR. Cold temperature also aids in spin immobilization, which is required to obtain a DEER signal. The necessary dipolar interaction is averaged if two spins are rotating freely in solution, so the net interaction becomes zero. The stacking of monomers in tau fibrils generally immobilizes the spin labels at room temperature. Further immobilization occurs once the sample is frozen, decreasing the dipolar averaging. Many labs perform DEER using liquid N_2, which is a modest cost requirement compared to a cryogen-free system or liquid He. For a large startup cost, a cryogen-free system can be purchased which does not require liquid He for cooling. This saves money in the long run, but is often not feasible as a replacement for liquid N_2.

In general, T_2 does not change much with temperature, but it is important to consider the limitation T_2 places on a DEER experiment. The echo that is being probed is technically a T_2 echo and will decay accordingly. The dipolar evolution occurs in the time between the second and fourth pulses, and the echo must still be present by the fourth pulse to collect a signal. The T_2 for the most commonly-used nitroxide spin label, MTSL, is around 1.5 μs at 80 K in tau fibrils. The distance between pulses is of the same order, so by the end of the sequence, the echo signal is extremely weak. For this reason, SNR must be increased as much as possible. A shorter distance between the second and fourth pulses could be used. This would reduce the evolution time, and in turn the number of echo modulation cycles, decreasing the distance information obtained. The best, albeit most difficult, way to improve SNR is to design a spin label with long T_2, so that the signal remains strong even after refocussing of the third pulse.

There are inherent upper and lower limitations on distances that can be measured with DEER. Below 2.0 nm, the radicals are close enough for exchange-coupling interactions which can be further complicated by pulse overlap (due to excitation bandwidth requirements, Equation 1.13). The upper limit is mainly determined by T_2 and is currently around 8 nm at 15 K for nitroxide spin labels. T_1 at 15 K is quite long; for spin-labeled hemoglobin, T_1 was predicted to be around 30 ms [245] at this temperature. These data are not only very costly to collect, but would also take a very long time. Practically, the experiments presented for tau have assumed an upper limit of around 5 nm.

8.2 Improvements to DEER

8.2.1 Recent Developments

A predominant theme in the discussion of DEER requirements is enhancement in SNR. Most of the improvements presented here involve increasing SNR. One of the most straightforward means to accomplish this goal is to decrease T_1, which decreases the repetition rate (SRT) of the experiment. This, in turn, increases the number of scans collected per unit time, and SNR increases proportional to √# of scans. In the following sections, this improvement is demonstrated through several different methods.

Although somewhat related to improved SNR, measurement of distances longer than 6 nm is another common goal for DEER spectroscopists. Advancements have been made in this field through use of lower temperatures, non-nitroxide spin labels, alternative pulse sequences [246], and deuterated proteins [247]. Prof. Daniella Goldfarb has used Gd-nitroxide spin pairs, reaching distances up to 10 nm [248]. She has also used the Mn-Mn interaction to achieve time windows of 5 μs [249], more than twice as long as the available window for tau in Chapter 7. These studies are typically performed at W-band (94 GHz), which also leads to an increase in SNR based on the Boltzmann population shift, but bears the added complexity of orientation selection of the spin labels.

Several variations to the technique itself have emerged recently to combat poor SNR. Five-pulse DEER was developed to improve echo focusing, decreasing signal decay due to spin diffusion. T_2 is in turn longer for this method, and distances up to 12 nm are theoretically possible [250]. In a similar manner, DEER-stitch was developed to combine the high sensitivity of three-pulse DEER with the dead-time free feature of

four-pulse DEER [251]. The dead-time section at the beginning of a data set of a three-pulse DEER experiment is very distorted because the echo decays in the same time as the length of the pulses, roughly. This portion of the data is therefore inserted from the four-pulse experiment, and the long time window can then be achieved from the higher SNR three-pulse experiment. Measured distances with this method have increased up to 8 nm.

These are just several examples of improvements that have been made to DEER as of late. Additional efforts have been put forth for suppression of ghost peaks in distance distributions [252], improving sensitivity through alternative pulse sequences [246], and development of new analysis programs [71], including GLADD [70], which was used for analysis of tau. Employment of DEER for novel applications will undoubtedly contribute to development of continuing improvements to the method, including those presented in this chapter.

8.2.2 Proposed Improvements

As previously mentioned, decreasing T_1 is a fundamental goal in SNR improvement for DEER. The focus of one of the projects presented here was to decrease T_1 using the cross-relaxation pathway that arises when a paramagnetic metal is brought into proximity with the spin labels attached to a protein. The impact of different concentrations of a variety of possible metals was determined through initial measurements using free nitroxide. These experiments were performed by Priyanka Aggarwal. Based on the changes to T_2 and T_1, an appropriate metal was chosen to add to protein for DEER measurements. The SNR for measurements collected in the same acquisition time for the protein with and without added metal were then compared.

Another advantage to SNR can be achieved by increasing T_2 of the spin label. A second project with this aim utilized a new nitroxide spin label. The spirocyclohexyl (Figure 8.1) differs from the commonly used MTSL in lacking methyl groups, which dominate T_2 relaxation at temperatures commonly used for DEER measurement [253]. Relaxation enhancement compared to MTSL has already been described for this nitroxide [16], so utilization for DEER was a logical next step.

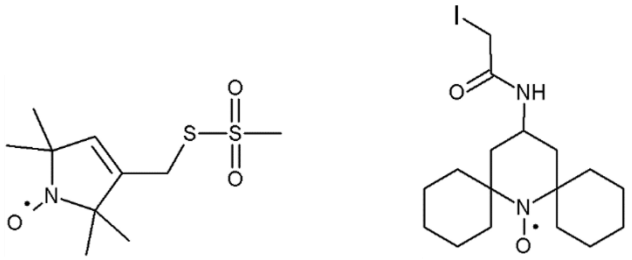

Figure 8.1. Structure of the spirocyclohexyl spin label compared to MTSL. The spirocyclohexyl, synthesized by Prof. Andrei Rajca, lacks the geminal methyl groups of MTSL, leading to greatly enhanced T_2.

The final project presented here involves understanding better the distance distributions obtained using Tikhonov regularization in DEERAnalysis. Many of the studies on tau have centered on the heterogeneous mixture of conformations that could be examined using DEER but were invisible using other biochemical and analytical techniques. This project was inspired following numerous discussions with colleagues and reviewers regarding peak artifacts and the ability to confidently separate distinct distances using DEER. Mixing spin-labeled proteins with more than one known distance helped determine whether these different peaks correspond to distinct conformations, in addition to showing that the distances can be deconvolved in

DEERAnalysis. This experiment also provided information on interpretation of peak heights and areas in the distance distributions.

These projects required the use of well-defined protein systems. The Habc domain of Syntaxin was used for the paramagnetic metal project and the DEERAnalysis peak separation. T4 Lysozyme was used with the spirocyclohexyl spin label. The remainder of the chapter is organized by protein involved.

8.3 Habc Domain of Syntaxin 1A

8.3.1 Introduction

Syntaxin 1A is a member of the SNARE protein superfamily and facilitates fusion of the synaptic vesicle membrane with the plasma membrane, resulting in the release of neurotransmitters into the synaptic cleft. The SNARE domain (Figure 8.2) of syntaxin 1A forms a helical bundle with partner proteins SNAP-25 and synaptobrevin, while the transmembrane domain anchors the protein to the neuronal cell membrane. The SNARE motif only assumes helical conformation upon complex formation, but the N-terminus of syntaxin forms a highly stable three-helix bundle [254, 255], commonly known as Habc domain. It is thought that this domain plays some regulatory role in SNARE complex formation as it is able to fold back onto the SNARE motif [256, 257] aided by the flexible linker [258] connecting the two segments. The structure of the Habc domain has been extensively studied and high resolution data are available from X-ray crystallography (PDB 1EZ3 [255]) and NMR (PDB 1BR0 [254]). Importantly, the central helix in the Habc domain expands over 5 nm and hence is ideally suited for DEER-based distance measurements. Additionally, the Habc α-helices are highly stable (melting temperature ~80 °C [254]) even when detached from

the remainder of the protein. For these reasons, only this domain is used in the following studies.

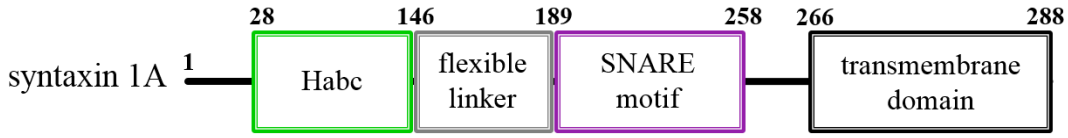

Figure 8.2. Structure of syntaxin 1A showing the transmembrane domain (black), and SNARE motif section (purple) which is connected to the Habc domain (green) by a flexible linker (gray). Only the Habc domain, composed of three α-helices, was used for experiments presented in this dissertation.

8.3.2 Materials and Methods

Transformation and expression. The codon-optimized constructs of the Habc domain of syntaxin 1A were purchased from Biomatik, cloned into the pET28b vector similarly to tau (section 7.3.1). Double cysteine mutations were coded in the vector of the Habc domain to be positioned at amino acid pairs 73/102, 77/102, 80/102, 84/102, and 87/102 in the protein. Midipreps (Appendix B) were performed to amplify the DNA. The inserts coding Habc were cleaved from the remaining vector using Xho1 and Nco1 restriction enzymes, and these were then visualized on an agarose gel (Figure 8.3A). Inserts from each Midiprep showed the correct molecular weight (~450 base pairs) compared to the 100 base pair ladder. Expression followed the tau protocol (section 7.3.3), however several constructs required 5-7 hours of agitated incubation until OD_{600} ~ 0.8. Figure 8.3B shows an SDS-PAGE gel from solutions collected prior to induction and during expression, demonstrating that the large amount of protein (Habc domain is ~15 kDa) expressed is relatively pure. Cells were stored in a slightly different buffer than tau (100 mM Tris pH 7.4, 500 mM NaCl, and 0.8 mM imidazole), without β-mercaptoethanol, which can interfere with nickel column purification.

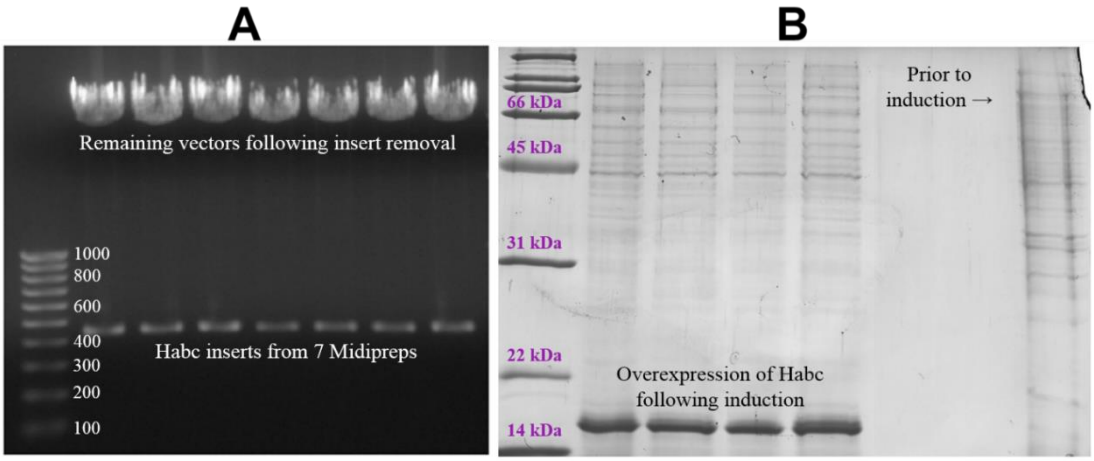

Figure 8.3. Agarose gel following Midiprep (A) and SDS-PAGE gel following expression (B) of the Habc domain of syntaxin 1A. Both gels were prepared from the 80/102 double cysteine mutant. The first column of each gel is a molecular weight ruler: 100 base pairs (A) and protein MW in kiloDaltons (kDa, B) as labeled. The DNA inserts containing the Habc sequence are ~450 base pairs, and all migrated to the correct position in (A). The SDS-PAGE shows overexpression of the protein of interest (~15 kDa) in the four wells following the ruler (B). The last well of this gel was collected prior to induction to emphasize the overexpression of Habc in the other wells.

Purification. Because the three dimensional structure of syntaxin's Habc domain has been characterized using several techniques [254, 255, 258, 259], purification followed prior papers as closely as possible. Frozen cells were thawed slowly in a room-temperature water bath. Small spatulas of lysozyme and DNAse (both Sigma) were introduced to aid in cell lysis and to reduce viscosity. 80 μL of 1% Triton X-100 (VWR) was also added. Initial purification was via affinity chromatography using a histidine tag attached to the N-terminus of the Habc domain (coded in the pET28b vector) with affinity for nickel beads. Samples were sonicated for one minute, followed by centrifugation at 15,000 X g. The supernatant was mixed with 1-2 mL Ni beads (QIAGEN) and rocked at 4 °C for at least one hour. This mixture was applied to an empty PD-10 column and washed with 10 mL buffer (10 mM HEPES, 100 mM NaCl,

1 mM NaN_3 at pH 7.4). 2 mL of 50 mM imidazole, which replaces the binding site on the Ni to the histidine tag, was applied to the column twice as an initial wash, followed by 2 mL of 800 mM imidazole, repeated up to eight times to ensure full elution. The 2 mL fractions were analyzed by SDS-PAGE for concentration and purity to determine which fractions should be pooled (Figure 8.4). Often, the wash fractions contained considerable amounts of desired protein; if these fractions were relatively clean, they were combined with the 800 mM imidazole elution fractions for a total sample collection of 8 mL. This volume was dialyzed for two hours with 4 mg thrombin (BD), which cleaves off the histidine tag when Ni purification is completed, in 20 mM Tris pH 7.4, 10 mM NaCl, 1 mM DTT, 1 mM EDTA buffer. The dialysis bag (Spectrumlabs, MWCO 6-8 kDa) was then transferred to fresh buffer lacking EDTA, and dialysis continued overnight. Both dialyses were performed at 4 °C. The following morning, an additional 1 mg thrombin was added to the dialysis bag to ensure full tag removal, and dialysis continued in fresh buffer at room temperature for 1-2 hours.

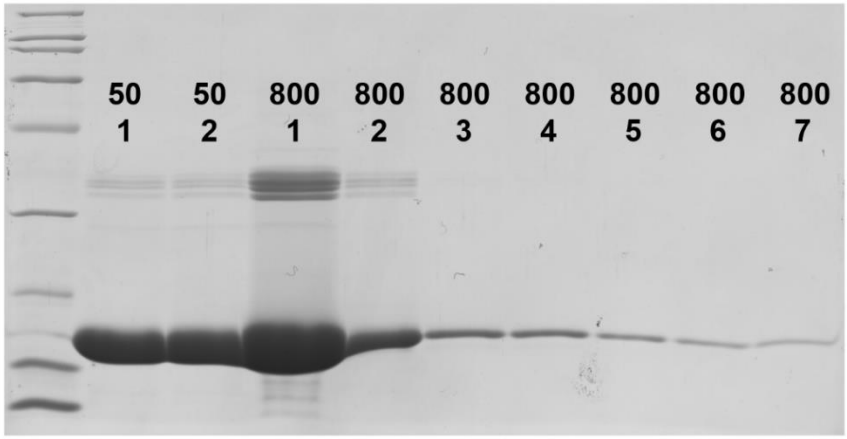

Figure 8.4. SDS-PAGE gel (15%) showing fractions collected from the nickel column purification of the Habc domain for double mutant 73/102. Fractions 1 and 2 were washes, using only 50 mM imidazole. These fractions often contained a large amount of relatively pure protein, and were thus included for collection.

The sample was filtered through a 0.45 μm syringe filter and run over a Mono S cation exchange column with a linear NaCl gradient (50 – 1000 mM NaCl, 20 mM HEPES pH 7.4, 2 mM DTT). The theoretical pI of the Habc domain of syntaxin is 5, suggesting that the protein will bind to an anion exchange column with buffer at pH above 7. This was attempted several times using a Mono Q column, and protein eluted each time almost exclusively in the flow-through. A small amount of protein came in the flow-through of the Mono S column, but the majority eluted in several fractions. These were combined and stored at 4 °C.

The final purification step was via gel filtration using the same buffer as for tau. Although the Habc domain is larger than K18 tau, it elutes in later fractions because tau is natively unfolded and Habc is a tightly-packed bundle of α-helices. Five fractions were pooled (Figure 8.5) for a total volume of 25 mL, which was concentrated down to around 2.5 mL using Vivaspin 20 concentrators (Sartorius, MWCO 5 kDa). 500 μL aliquots with 5 mM DTT were flash frozen and stored at -80 °C until EPR sample preparation.

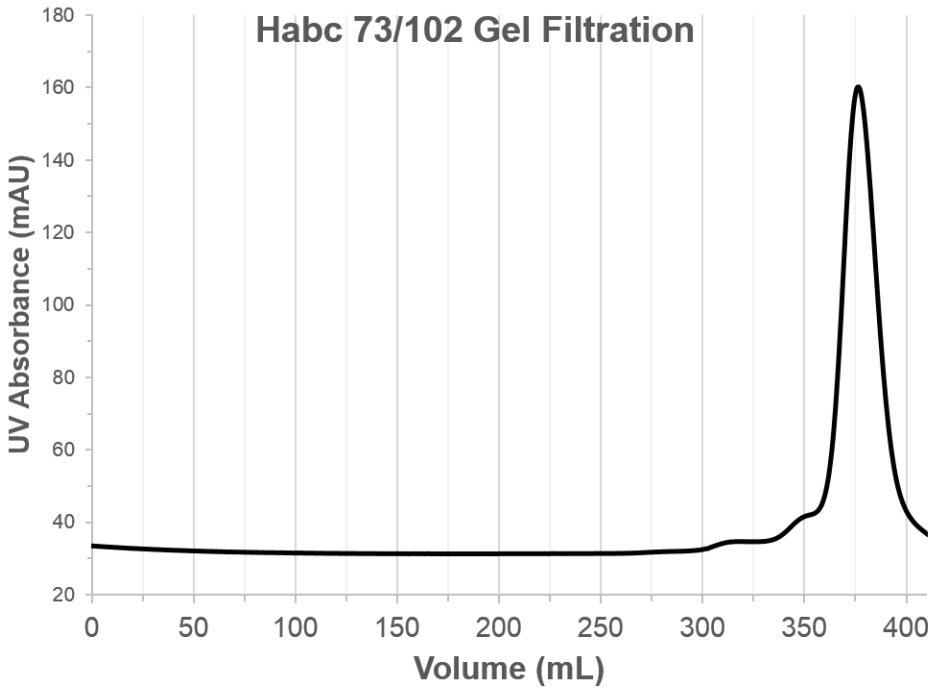

Figure 8.5. Elution profile for gel filtration of the Habc domain. Habc eluted around 375 mL, and the small bump around 350 mL was present for all constructs. The signal corresponds to absorbance at 280 nm.

DEER sample preparation, acquisition, and analysis. A 500 μL aliquot of purified Habc was thawed slowly in a room temperature water bath and concentrated to 200 μL using Amicon Ultra-0.5 centrifugal filters (Millipore) with 3 kDa MWCO. The sample was kept at 4 °C during this process. Residual DTT from purification was removed by washing sample with 200 μL fresh buffer five times during concentration. The final concentration was found by BCA assay. The sample was labeled with five-fold molar excess MTSL, since significant precipitation occurred at 10-fold excess. Labeling proceeded for two hours. The sample was then loaded onto a PD-10 column to remove excess label, collecting 2 mL of eluate. This was concentrated down to around 200 μL, and the concentration again determined by BCA assay. Several samples

required decreased pH to prevent added metal from precipitating. In these cases, buffer (10 mM HEPES pH 7.4, 100 mM NaCl, 1 mM NaN_3) was exchanged from pH 7.2 to 6.1 prior to concentration measurement. Final concentration was to be around 100 μM, so 200 μM sample, combined in the appropriate ratio with buffer, was added 1:1 with 60% sucrose or 48% glycerol. If metal was added to the protein, it was present in the cryoprotectant. Syntaxin samples were also mixed in varying amounts to examine separation of distances in DEERAnalysis. In different experiments, 73/102 and 77/102 were mixed with 84/102 at 0, 25, 50, 75, and 100% total concentration. Samples were pipetted into a Q-band EPR tube which was held in an X-band tube for room temperature CW measurement. Unlike tau fibrils, syntaxin is soluble and the CW spectra are representative of a more slowly-tumbling but not immobilized nitroxide radical attached to a protein (Figure 8.6). Following CW collection, samples were frozen in liquid N_2 for DEER measurement, which was performed analogously to tau (Section 7.3.8).

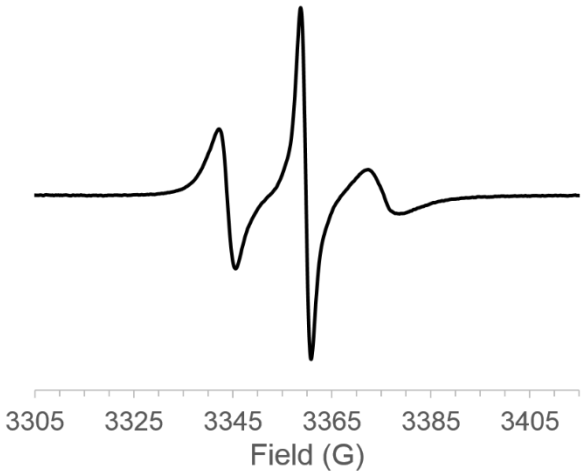

Figure 8.6. Room temperature CW spectrum for spin-labeled Habc 77/102. Spectrum was collected in 20 scans with modulation frequency and amplitude 100 kHz and 0.5 G.

8.3.3 Results and Discussion

DEER enhancement using paramagnetic metal. As a proof of concept for the project, Er-DTPA was added to tau fibrils that had previously been measured by DEER. Originally, only 32 μM Er^{3+} (pH 6.1) was added to K18 311/328 G323I fibrils composed of 2% spin-labeled tau monomer and 98% wild-type monomer. This concentration of metal had a strong effect on relaxation at 80 K; T_1 was decreased from 500 μs without metal to 4 μs with the metal. This difference would theoretically shorten the acquisition time over two orders of magnitude. However, the T_2 was also decreased from 1.4 μs without metal to 450 ns. This rapid echo decay shortened the usable time window to a size at which no echo modulation could be observed. The amount of metal was then decreased to 0.5 μM. T_1 and T_2 decreased only to 200 μs and 1.3 μs, respectively. DEER was collected, and this sample was compared to the original DEER results recorded in the absence of metal. The raw data and distance distributions show that the structure of the tau fibrils may have been altered by the addition of metal (Figure 8.7). This is not wholly surprising, as tau monomer is positively charged, and there is a negatively charged cofactor present. The metal may have attached preferentially to a specific position in the protein. Additionally, the sample had been stored for several months at -80 °C and was thawed and refrozen to conduct this experiment. Lastly, it was shown that tau is heterogeneous (Section 7.4.1), and it may be difficult to interpret results of method improvement on this type of sample. It was clear, therefore, that a different protein (the Habc domain of syntaxin 1A) would be better suited for this experiment.

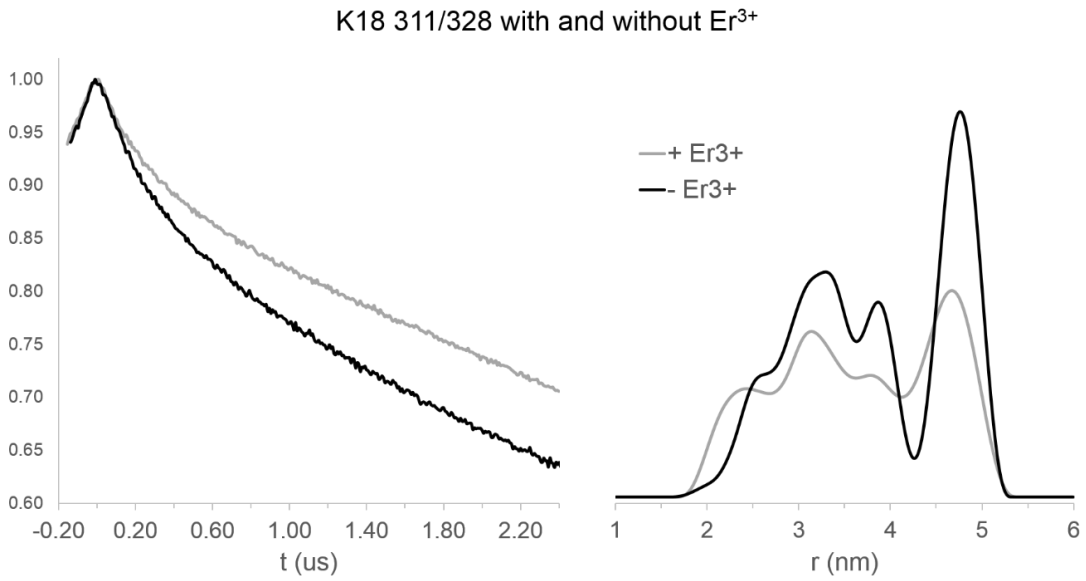

Figure 8.7. DEER of tau (K18 311/328) with and without Er^{3+}. Addition of the metal (gray) altered the distance distribution (right), suggesting a structural change to the tau fibrils. This was instinctually attributed to preferential binding of the charged metal to either the charged protein or cofactor. The difference is evident from the raw data as well (left).

Syntaxin was chosen to test the effect of an added lanthanide for several reasons: in addition to structural characterization of the Habc domain by X-ray crystallography and NMR, the α-helical structure provided several possible spin label locations up to ~5 nm distance (Figure 8.8). Additionally, the protein structure is very robust. All Habc mutants shown in Figure 8.8 were successfully expressed and purified. Distance distributions obtained by DEER were similar to the expected distances based on spin label location (Table 8.1). The distances measured by DEER are from the radical position instead of the C_α, which contributes to the slight variation in Table 8.1. Additional differences are attributed to conformational isomerism of the spin label.

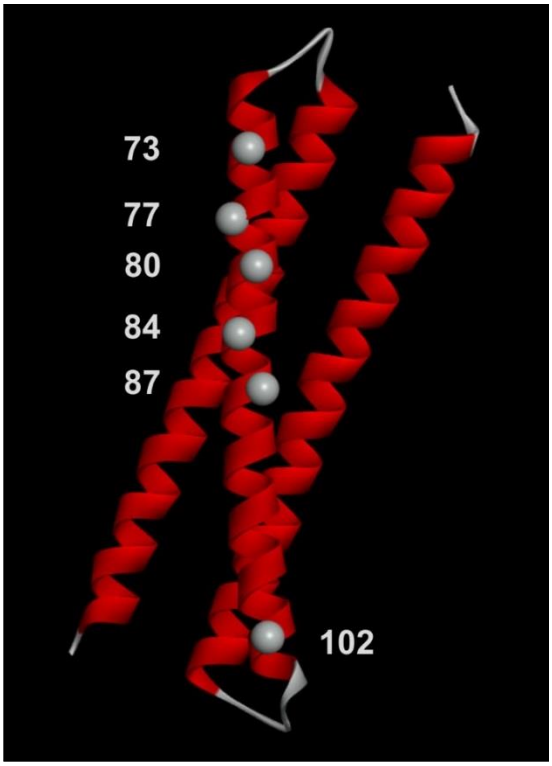

Figure 8.8. Structure of the Habc domain of syntaxin based on PDB 1EZ3 (Rattus norvegicus) with locations of cysteine mutations for attachment of spin labels. Position 102 was constant for all double mutants. Locations were chosen to be on the surface of the helix.

Double Mutant	C_α/C_α Distance	DEER Distance
73/102	4.4 nm	4.7 nm
77/102	3.8 nm	4.0 nm
80/102	3.3 nm	3.3 nm
84/102	2.7 nm	3.2 nm
87/102	2.2 nm	2.8 nm

Table 8.1. Comparison of experimental distances determined by DEER with theoretical distances from crystal structure (PDB 1EZ3). Small variations from spin label positioning are expected, including rotamer conformation and bond lengths from the Cα carbon to the radical position.

The distance distributions obtained through Tikhonov regularization with parameter α = 100 are shown in Figure 8.9. The additional peaks in 73, 80, and 87/102, and the shoulders in 77 and 84/102 are attributed to rotamers due to the small distance separation from the main peak. The small peak in 84/102 is likely an artifact of data analysis, however the size of the peak at similar distance in 87/102 is more difficult to assign. It is possible that addition of spin label to position 87 alters the structural properties of Habc, however it is unclear from DEER data alone.

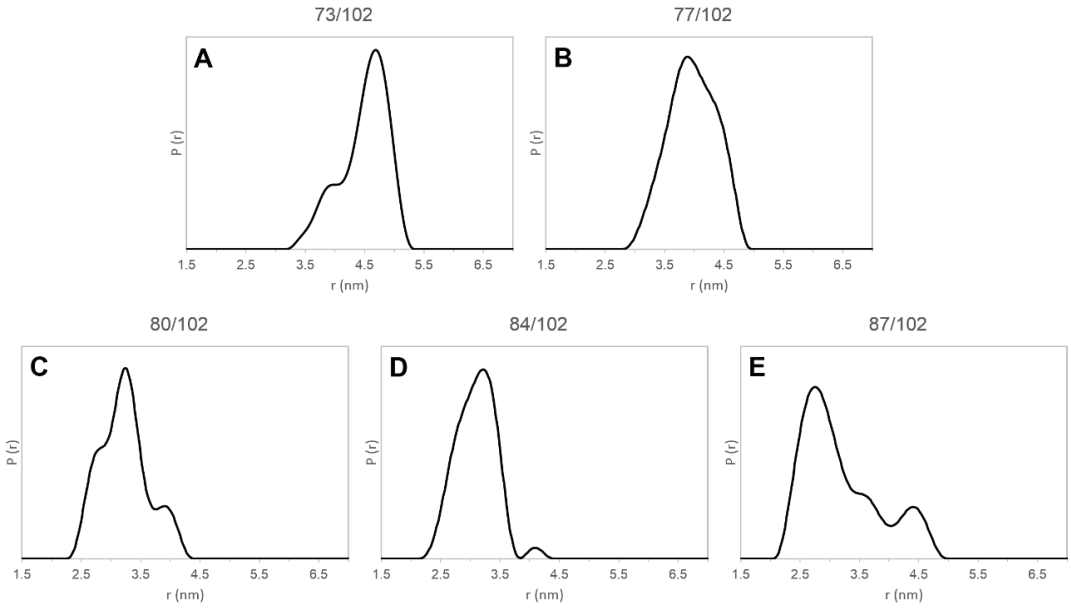

Figure 8.9. Distance distributions for all Habc double mutants. Additional peaks and shoulders are most likely due to nitroxide rotamers.

Following confirmation of individual distances, DEER was performed on the Habc domain with addition of paramagnetic metal. To decrease the probability of preferential interaction between metal and protein, Er^{3+} was complexed with DTPA. The metal complexes used for this project were prepared by Priyanka Aggarwal. An initial experiment using Habc 80/102 with different concentrations of Er-DTPA showed

that addition of a high concentration (30 mM) of complex decreases the SNR of the raw data. However, unlike in the case of tau, the distance distributions were not altered by addition of the metal (Figure 8.10). The differences in relaxation are reported in Table 8.2. As shown in the table, this experiment was repeated for 10 mM Er-DTPA with a different sample preparation of Habc 80/102. The results were nearly identical to those in Figure 8.10.

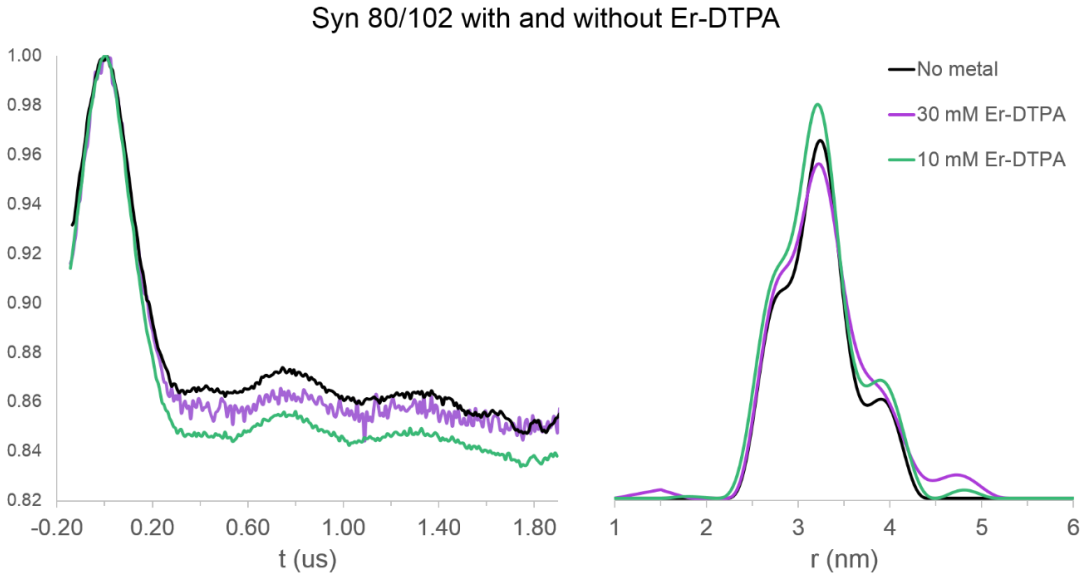

Figure 8.10. Habc (Syn) 80/102 with and without addition of Er-DTPA using sucrose as a cryoprotectant. Addition of high concentrations of the complex decreases the SNR due to shortening of T_2 that cannot be compensated with the decrease in T_1. Importantly, the metal complex did not alter the distance distribution as the free metal had for tau.

Decreasing T_1 significantly with a modest change in T_2 should improve SNR via acquisition of additional scans in the same amount of time. For all data presented here, the DEER acquisition time was held constant for comparison of SNR with and without metal. Only minimal improvement was seen for Habc 80/102. To exclude the possibility of interference from the sucrose cryoprotectant, Habc 87/102 was also prepared using 24% glycerol. Some protein precipitated during sample preparation,

which excluded use of glycerol for future samples. The raw data showed similar SNR with and without metal, but the peaks in the distance distributions did not perfectly match as they had for 80/102 (Figure 8.11). This may have been caused by the presence of some precipitated protein in the sample.

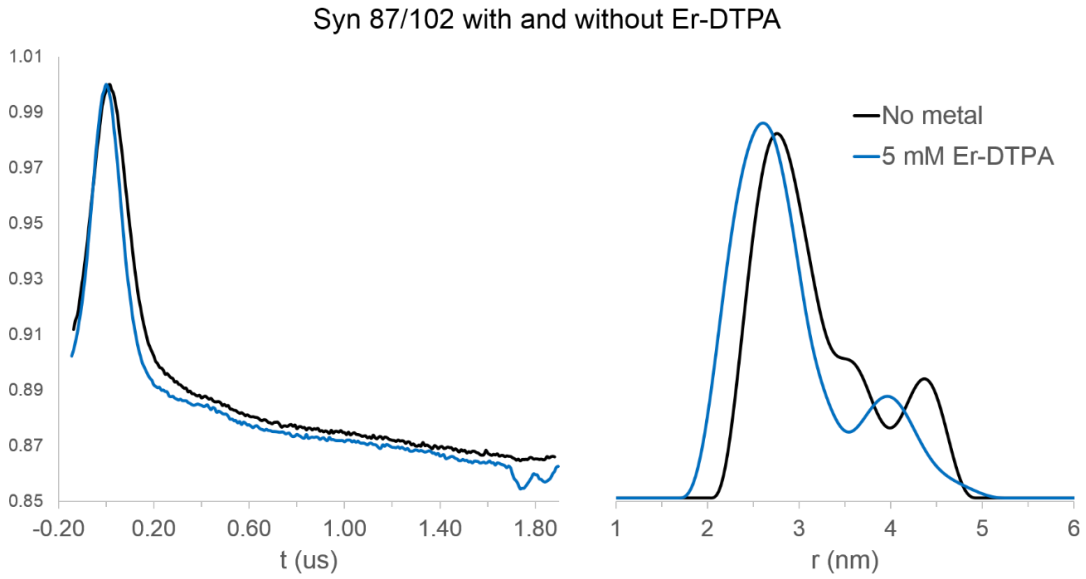

Figure 8.11. Habc (Syn) 87/102 with and without addition of Er-DTPA using glycerol as a cryoprotectant. The same additional peaks shown in Figure 8.9 were again seen. The SNR was unchanged with addition of the metal, despite decreased T_1, and the distance distributions were not well-matched.

Both 80 and 87/102 had additional peaks present in the distance distributions (Figure 8.9C and E). The next sample studied was Habc 77/102, which had only a small shoulder in the distance distribution (Figure 8.9B). In relaxation experiments performed by Priyanka Aggarwal, Dy^{3+} showed promise as the paramagnetic source in addition to Er^{3+}, so this experiment examined addition of Dy-DTPA to the protein. A definite improvement in SNR is seen in Figure 8.12 for 1 mM Dy-DTPA, but little improvement with 5 mM Dy-DTPA. The distance distributions generally matched well for all samples.

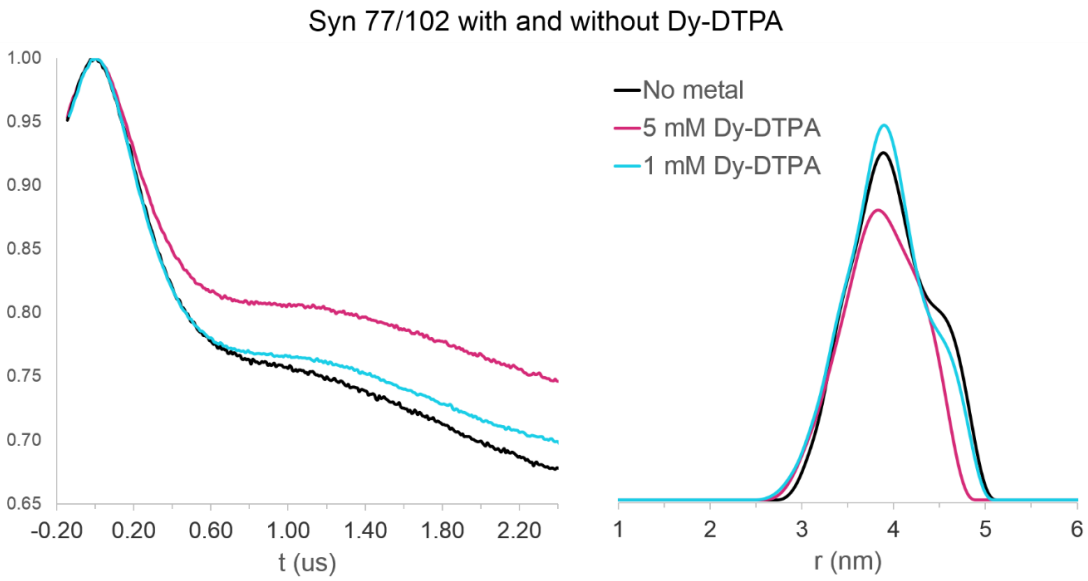

Figure 8.12. Habc (Syn) 77/102 with and without addition of Dy-DTPA. SNR is visibly improved with addition of 1 mM Dy-DTPA (blue), but again decreases with higher concentration (fuchsia). The distance distributions indicate that the complex did not alter the protein structure.

Table 8.2 shows the changes in relaxation and SNR for the Habc samples studied to this point. The SNR was calculated from a modified MATLAB program written by Deborah Mitchell, originally used for testing SNR of DEER data for fabrication of an improved X-band DEER resonator.

	Cryo-protectant	T_1 (µs)	T_2 (µs)	SNR
Habc 87/102				
No metal	24% glycerol	940	2.2	120
5 mM Er-DTPA	24% glycerol	350	1.9	80
Habc 80/102				
No metal	30% sucrose	910	2.7	130
10 mM Er-DTPA	30% sucrose	120	2.2	130
No metal	30% sucrose	940	2.8	180
10 mM Er-DTPA	30% sucrose	120	2.3	190
30 mM Er-DTPA	30% sucrose	20	1.6	60
Habc 77/102				
No metal	30% sucrose	760	2.4	200
1 mM Dy-DTPA	30% sucrose	440	2.3	330
5 mM Dy DTPA	30% sucrose	100	1.8	240

Table 8.2. Relaxation and DEER SNR data at 80 K for the spin-labeled Habc domain with and without addition of metal complexes. Improvement in the DEER SNR is a balance between maintaining T_2 and decreasing T_1. Results show that addition of a high concentration of complex actually decreases SNR. SNR is compared for samples run in the same amount of time.

Habc 77/102 with 1 mM Dy-DTPA had the best improvement in SNR. Based on the amount of change in T_1 (~1.7X decrease) and the unchanged T_2, the expected SNR is calculated to ~1.7 x 200 = 340. The SNR improvement, therefore, is as estimated based on T_1. However, a discrepancy exists between the SNR improvements seen for DEER data compared to the predicted improvement from initial measurements by Priyanka Aggarwal. Nitroxide relaxation was measured varying metal, metal concentration, and temperature to determine parameters necessary from optimum SNR enhancement. Equation 8.1, which compares the improvement in T_1 to the decline in T_2, was used as an indicator of the magnitude of SNR improvement:

$$\frac{T_2 \text{ intensity (with metal)}}{T_2 \text{ intensity (without metal)}} \text{ X } \sqrt{\frac{T_1 \text{ (without metal)}}{T_1 \text{(with metal)}}} \qquad (8.1)$$

These experiments concluded that Er-DTPA would give the best improvement, as well as Dy-DTPA, but to a lesser extent. Equation 8.1 predicts a greater improvement than was seen for the DEER experiments.

In an attempt to understand this discrepancy, a final set of experiments were performed. The Habc 77/102 was prepared with 0.5, 1, and 2 mM Er-DTPA and 1, 2, and 5 mM Dy-DTPA. CW spectra were recorded prior to DEER acquisition; the integrated intensities (Table 8.3) predict modest improvement in SNR of the Dy-DTPA samples, but decrease in SNR for the Er-DTPA. Variable temperature measurements of free nitroxide with and without metal suggested optimal improvement at 50 K for Er-DTPA and 60 K for Dy-DTPA. As shown in the table, the actual improvements in SNR are quite small. The 2 mM Er-DTPA sample was not analyzed due to the trend toward decreased SNR with increased metal concentration shown in the table.

Sample (Habc 77/102)	Temp	SRT (us)	# of Scans	Acquisition Time	T_2 2.5 (mm)	T_2 3.5 (mm)	SNR	CW Intensity
No metal	60 K	2500	2	1 hr, 51 min	49	34	190	1.33
1 mM Dy-DTPA	60 K	900	6	1 hr, 55 min	45	30	210	1.36
2 mM Dy-DTPA	60 K	530	10	1 hr, 58 min	39	25	190	1.36
5 mM Dy-DTPA	60 K	195	25	1 hr, 56 min	28	18	140	1.36
No metal	50 K	4200	1.25	2 hr, 3 min	47	33	140	1.33
0.5 mM Er-DTPA	50 K	600	9	2 hr, 0 min	24	16	110	1.27
1 mM Er-DTPA	50 K	240	21	2 hr, 2 min	21	13	60	1.19
1 mM Dy-DTPA	50 K	1500	4	2 hr, 8 min	40	27	200	1.36
No metal	80 K	930	6	2 hr	36	23	200	2.51
1 mM Dy-DTPA	80 K	530	11	2 hr, 10 min	34	21	330	2.39
5 mM Dy-DTPA	80 K	135	36	2 hr	25	14	230	2.50
1 mM Dy^{3+}	80 K	20	228	2 hr	4	1	4	2.15

Table 8.3. Detailed results from experiments to improve SNR through relaxation enhancement. Comparisons can be made between samples run under the same conditions, which are separated by the gray bars. T_2 in mm refers to the echo height as physically measured in mm at 2.5 and 3.5 μs in the echo decay. The impact of 1 mM Dy^{3+} on relaxation is also shown; T_1 becomes incredibly short, but SNR is poor due to extreme decrease in echo intensity (T_2 in mm). A single scan consists of 8-step phase cycling, so 1.25 scans refers to a second scan that has only completed two of the eight phase cycles.

Separation of multiple distances. After determining that the expected DEER distances could be obtained for all the Habc domain double mutants (Table 8.1 and Figure 8.9), the ability of this technique to accurately separate different distances within the same protein was examined. Two different double mutants were mixed in varying quantities and analyzed by the same method as the individual double mutants. This was executed for mixtures of both 73 and 77 with 84/102. These mutations were chosen based on the sharpness of the peak in Figure 8.9 and the relative absence of additional rotamer peaks, which were more obtrusive in 80 and 87/102. Mutants were mixed 25:75, 50:50, 75:25 by concentration as determined by BCA and were compared to the distributions of the pure double mutants.

Figure 8.13 shows a clear trend in peak height correlating to the amount of protein present. Interestingly, comparison of peak heights for samples containing 100% of a single protein do not align exactly. The area under the peaks provides a better estimation of sample composition than amplitude. With the exception of the mixture of 75% 77/102 with 84/102 (Figure 8.13B, light blue), there is clear separation between the peaks within the mixtures. At this ratio of concentrations, the shoulder indicates that the peaks could not be well-separated because 77/102 was the dominant frequency in the DEER signal. The background-subtracted DEER data for each mixture are shown in Figure 8.14. It is clear that the ability of Tikhonov regularization to distinguish between more than one frequency is crucial to separation of peaks within the distance distribution. This issue is resolved for the 50% mixture of 77/102 with 84/102, where the frequencies are equally represented in the raw data, and the peak resolution in the distance distribution is improved (Figure 8.13B, light gray). The progression of frequencies can be clearly seen from the background-subtracted raw data with Tikhonov fitting (Figure 8.14).

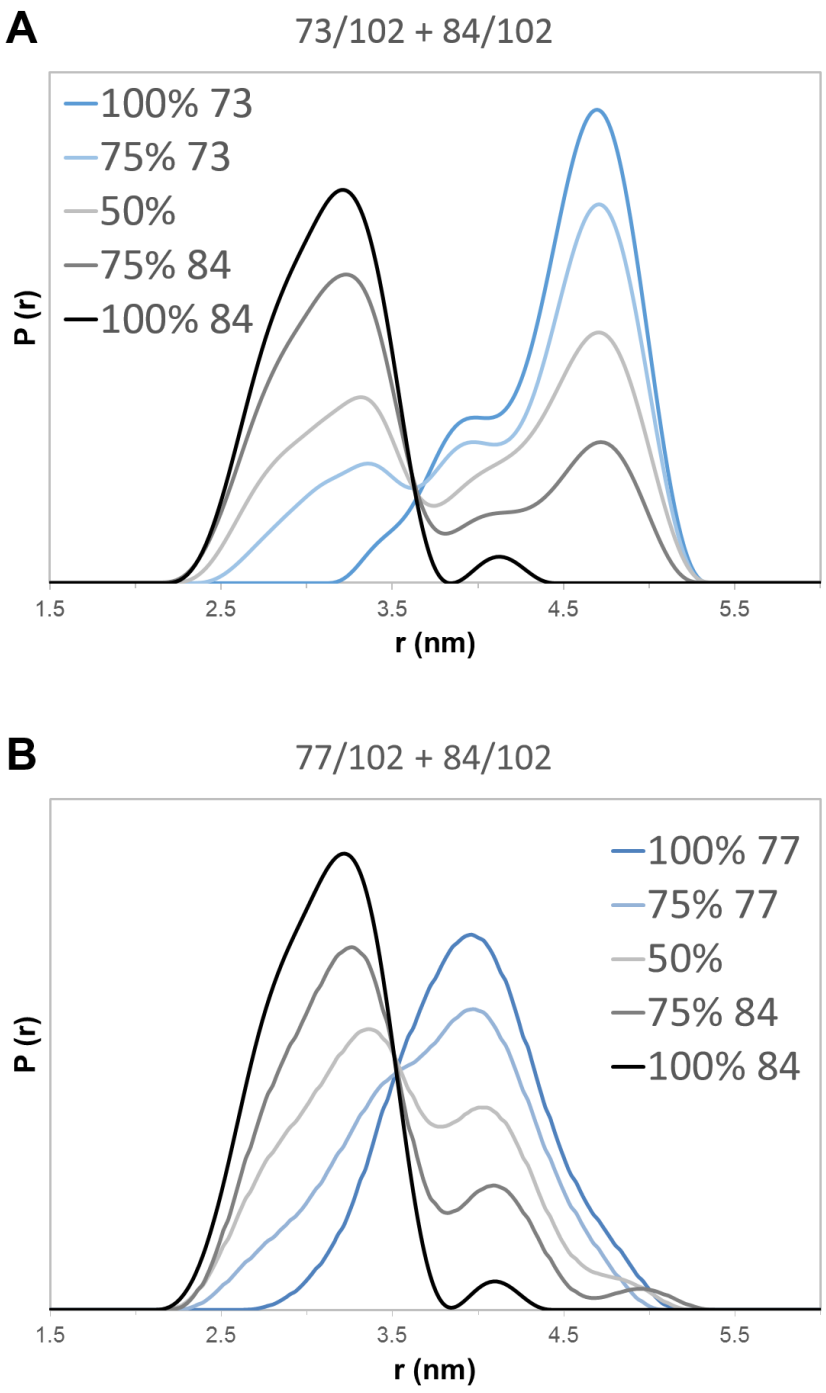

Figure 8.13. Distance distributions for mixtures of Habc double mutants, 73 with 84/102 (A), and 77 with 84/102 (B). All peaks were well-separated, except for the mixture of 75% 77/102 with 25% 84/102 (B, light blue). Additional peaks could be artifacts or rotamers.

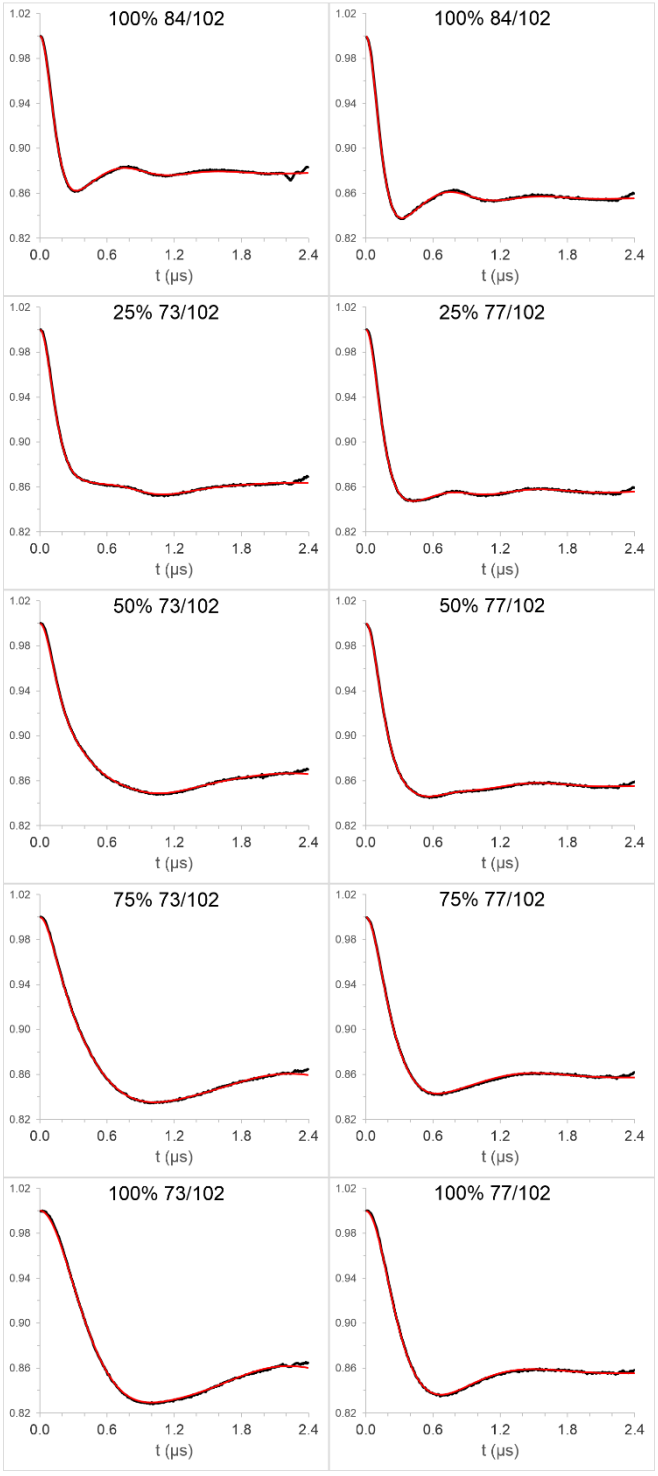

Figure 8.14. Background-subtracted raw data for Habc mixtures. The evolution of oscillation is clearly seen from top (100% 84/102) to bottom (0% 84/102). Importantly, the traces for both 100% 84/102 are nearly identical, although prepared separately.

This experiment sheds some light on the presence of artifacts or "ghost peaks" for this sample. While it is unwise to discount the presence of artifacts when applying DEER to a new protein system, it may also be ill-advised to write off a small peak as an artifact. Habc 84/102 has a small peak around 4 nm, which seems to be ubiquitous for this double mutant (Figure 8.9D and 8.13A and B). This peak falls at the same distance as Habc 77/102 (Figure 8.13B), and undoubtedly contributes to the area under the 77/102 peak. If one were examining any single distribution from Figure 8.13B without seeing the other traces, it would not be surprising for the data to be misinterpreted. This peak in the black trace could be designated 77/102, or could be considered an artifact in the dark gray trace. The proximity of these distances could also be interpreted as rotamers, especially for 75% 77/102 with 25% 84/102 (light blue), as the peaks are not fully resolved. The 73/102 with 84/102 mixture also reveals difficulty with peak interpretation. The small peak in 84/102 does not overlap the main peak in the 73/102 and 84/102 mixture (Figure 8.13A), but it does overlap a conserved shoulder on 73/102 (see Figure 8.9A). This shoulder was designated a rotamer, but could also be an artifact. Because the main peaks are so dominant for these mixtures, interference from additional smaller peaks does not hinder data interpretation. It is extremely important, however, to carefully distinguish rotamers and artifacts. The additional peak around 4 nm in Figure 8.13A may in fact be a real feature, as it is conserved for all samples containing either 73 or 84/102.

This project provided some additional insight into interpretation of tau DEER data which was not originally anticipated. Many comments from colleagues at research conferences indicated concern at peak assignments in the distance distributions of tau.

The background subtracted raw data (Figure 8.15A and B) shows that the echo modulation does not complete a full cycle within the acquisition window used. Longer frequency oscillations correspond to longer distances, and the longest distance within the distribution is around 4.8 nm. In Chapter 7, stirring was shown to enrich the long-distance populations, the background-subtracted raw data for which is shown in Figure 8.15A (zero seeding steps). Five seeding steps corresponds to conditions under which the peak at 4.8 nm is present, along with shorter distance peaks, and the Tikhonov fitting clearly shows a mixture of frequencies compared to zero seeding steps. The tau peak at 4.8 nm is similar to the distance measured for syntaxin 73/102 (4.7 nm), which matched well to the expected distance of 4.4 nm. The background subtracted raw data causing this peak for both tau and syntaxin are compared in Figure 8.15B. The Tikhonov fitting in red is very similar, and the incomplete frequency oscillation has very similar relative amplitude. Using syntaxin as a standard for this type of data interpretation provides evidence that the 4.8 nm peak in tau presented throughout Chapter 7 is not an artifact, and that information on conformational changes involving this peak can be accurately assigned with confidence. It remains important to not over interpret DEER data from a non-ideal protein, but the use of syntaxin as a model system has contributed to accurate interpretation of the tau data presented in this dissertation.

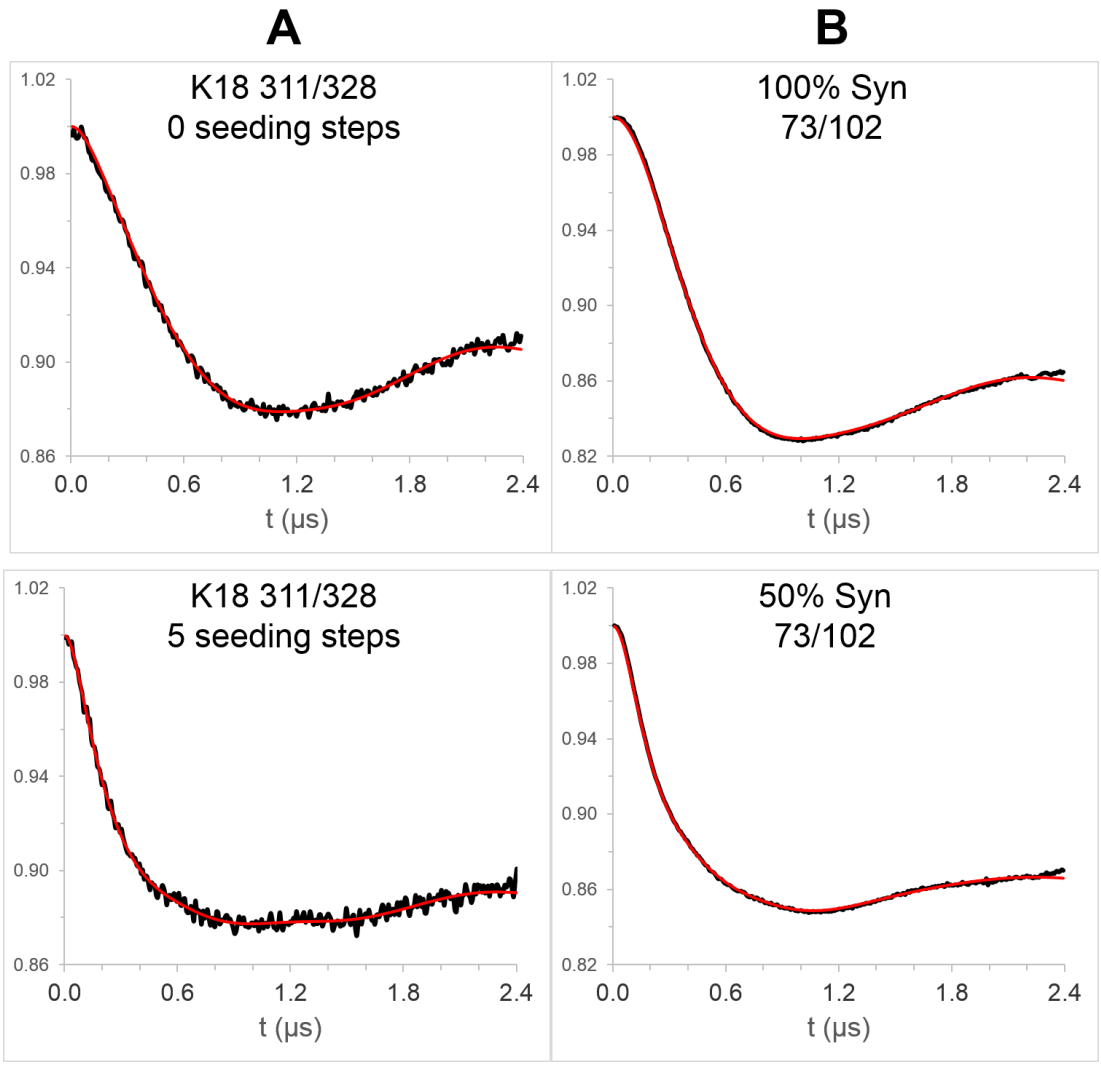

Figure 8.15. Comparison of background-subtracted DEER data (black) for tau (A) and Habc (Syn, B) with Tikhonov fit function in red. Tau formed with 0 seeding steps gives a single distance at 4.8 nm and 100% Habc (Syn) 73/102 gives a single distance at 4.7 nm. Tau with five seeding steps gives roughly three distances at 3.2, 3.7, and 4.8 nm, and 50:50 Habc 73:84 includes 3.2 and 4.7 nm. The red traces are very similar for tau compared to the Habc domain of syntaxin.

8.3.4 Conclusions

DEER enhancement using paramagnetic metal. The SNR of DEER has been a fundamental concern for EPR spectroscopists. The nature of the method requires collection of data at the limit of the spin echo signal. A number of techniques have been

developed with the aim of improving SNR, but almost all of them require additional instrument capabilities or application of new analysis software. The aim of this project was to develop an improvement that could be implemented for any protein system and would not require upgrades to hardware, software, or analysis programs. Addition of a paramagnetic metal decreased acquisition time by shortening T_1 and, when complexed, did not alter protein structure. However, optimization of both the metal used and the concentration was challenging.

Many experiments were performed by Priyanka Aggarwal on the impact of various metals and metal complexes on nitroxide T_1. Weighing the beneficial decrease in T_1 with the detrimental decrease in T_2, it was concluded that 5-10 mM Er-DTPA would provide the best improvement in SNR. This concentration range did not improve SNR of the DEER experiment, however. The initial experiments using Dy-DTPA showed similar promise, so DEER was repeated using this metal complex, and some improvement in SNR was seen. The predicted improvement was ~4X SNR without metal, and only ~2X better SNR was observed. After a number of additional experiments, Er-DTPA was found to be a weak choice for DEER, although it showed the most promise for free nitroxide. Dy-DTPA consistently gave improved or similar SNR to protein without metal added. The discrepancy could be caused by preferential binding of the partially-complexed metal to a section of the Habc domain of syntaxin. It was obvious that the free metal attached to tau, changing the conformation, but when partially attached to Habc on the surface, the distance distribution is not disrupted (see Figures 8.10-8.12). Additional experiments are required to prove interaction between the protein and the metal complex. In general, however, SNR was improved slightly

using this method. Data could be collected in around half the time as the protein without metal to achieve the same spectrum. This method has the potential of shortening acquisition time from as long as one week down to four days.

Separation of multiple distances. Utilization of DEER to examine differences in tau fibril structure have demonstrated the value of this technique for examining mixtures of fibrils, a quality unmatched by other methods. A degree of hesitation concerning the validity of these findings is anticipated when studying a new protein system by a relatively new technique. It was important to reiterate the findings, therefore, using a model system like the Habc domain of syntaxin. This study showed that DEER is capable of separating mixed distances as little as 0.8 nm apart. This distance may be decreased further for a system in which the spin label is more immobilized or has fewer rotamers populated. The broadness of peaks for Habc compared to tau is probably due to the increased mobility of spin labels on the surface of a protein in solution compared to spin labels buried within solid tau fibrils. Even at 80 K, molecular motions are large enough to contribute to peak broadening. Proper peak separation depends on SNR of the raw data, and the algorithm involved in Tikhonov regularization must be able to distinguish between different frequencies in the raw data. For the Habc domain, SNR is quite high, and the differences in frequency can be seen visually (see Figure 8.14). For samples with lower SNR, a model system like the Habc domain of syntaxin can help visualize the presence of multiple peaks. For some samples, it may be possible to prepare a model with the distances commonly found in the unknown. Both the distance distributions and the trace of the Tikhonov fitting could then be compared for the standard and unknown, as in Figure 8.15. Performing

this type of check lends additional validity to DEER results and maintains confidence in the accuracy of the method.

8.4 T4 Lysozyme

8.4.1 Introduction

T4 Lysozyme (T4L) is an enzyme that degrades bacterial cell walls, allowing a bacterial virus (bacteriophage T4) to inject genetic material into the cell. T4L shares several characteristics with the better known lysozyme extracted from hen egg white, including relatively small size and ability to cleave β (1-4) glycosidic bonds. Structurally, they are similar enough to have convergent evolutionary roots, but the primary sequences are extremely different [260]. Brian Matthews studied the structure of T4L extensively by X-ray crystallography, contributing hundreds of structures to the PDB [261-263]. Because the structure has been thoroughly characterized, T4L has been utilized as a standard protein for evaluating enhancement of EPR techniques [250, 264, 265] and has provided an excellent tool for studying protein dynamics and interactions using EPR [266-268]. For similar reasons, T4L was chosen for this study, in which DEER is performed using a spirocyclohexyl spin label with increased T_2. The purpose of this study was to investigate the effect of increasing T_2 of the spin label on the acquisition window to use DEER for longer distances and at higher temperature.

8.4.2 Materials and Methods

Sample preparation. DEER measurements were performed on T4L spin-labeled at positions 61/135 (72 μM), 65/135 (85 μM), and 65/80 (130 μM). These samples were provided by Prof. Hassane Mchaourab at Vanderbilt University, where they were spin-labeled by incubating the protein at room temperature for two hours with a five-fold

molar excess of the spirocyclohexyl spin label (Figure 8.1) synthesized by Prof. Andrej Rajca at the University of Nebraska, Lincoln. For measurements at liquid N_2 temperatures, the samples were in a 24% glycerol solution with buffer (9 mM 3-(N-morpholino)propanesulfonic acid (MOPS), 6 mM tris(hydroxymethyl)aminomethane (Tris), 50 mM NaCl, 0.02 % azide, and 0.1 mM EDTA at pH 7.2). Samples were contained in 1.6 mm o.d. quartz EPR tubes.

To perform DEER at room temperature, the spin-labeled protein had to be immobilized. This was achieved through drying. To separate spins and avoid interfering dipolar contacts, a 10-fold excess by weight of hen egg white lysozyme (Sigma) was added to the 65/80 T4L in buffer. The structural similarities mentioned previously ensured there would not be detrimental interactions between the two proteins. The mixture was combined with 0.2 M trehalose (Tokyo Chemical) and left to dry in the dark on a watchglass. As the sample dried, trehalose replaced the hydrogen bonds that the protein lost with water [269, 270]. The resulting crystalline residue was scraped into an EPR tube and was further dried by evacuation for ~48 hours.

EPR spectroscopy. EPR data were collected at Q-band (34 GHz) on the Bruker E580 system between 80-160 K and also at room temperature (~298 K). T_2 and T_1 were determined by spin echo decay and inversion recovery, respectively. T_2 provides a quantitative measure of the available DEER acquisition window. The SRT used for DEER measurements was calculated as 1.2 X T_1. The long component of T_1 fit to a double exponential function was used for this calculation. Prior to each DEER measurement, a field-swept echo-detected spectrum was recorded to determine the position of the maximum echo height. Several parameters for 80-160 K measurements

differed from those used for DEER of tau at 80 K. The observer pulse was varied to maximize echo intensity, and was typically set to $\pi/2 \sim 40$ ns. The pump pulse was constant at $\pi = 40$ ns. The echo was monitored using a gate equal to the echo width at FWHM centered on the echo. Other parameters were constant for all low-temperature DEER measurements: $d_1 = 200$ ns, $d_2 = 4000$ ns, $d_3 = 100$ ns, dx = 8 ns, 507 points, 500 shots/point. 8-step phase cycling was used to remove unwanted echoes.

Room temperature DEER was performed on the T4L labeled at 65/80. Spectrometer settings were similar to those used at lower temperatures. The shape of the echo decay at room temperature is different from that at 80 K; whereas a single exponential function fits well at 298 K, a stretched exponential fits best at 80 K. With these fitting parameters, the T_2 for the dried sample decreased from 3.6 μs at 80 K to 920 ns at 298 K. As a consequence, the acquisition window (set by d_2) was decreased from 4 μs to 1.5 μs. T_1 was also dramatically shorter at room temperature, allowing the SRT to be reduced from 1500 μs at 80 K to 50 μs at 298 K. Bruker SpecJet II was used to achieve this rapid repetition rate. In addition to adjustments to parameters based on relaxation, the maximum DEER echo was achieved at $\pi/2$ observer pulse of 52 ns. The step size, dx, was decreased to 4 ns to allow collection of 390 points. All other parameters are the same as above.

Data analysis. Data were evaluated using DEERAnalysis2011. The background was subtracted using 3D homogenous background subtraction. The starting point for subtraction was chosen based on the shape of the Pake pattern (Figure 8.16B and D). Dipolar evolution curves were fit using Tikhonov regularization, with $\alpha = 1000$ for all samples except T4L 65/80 studied at low temperature. For DEER measurements

at 80 and 160 K for T4L 65/80, the L-curve intersection was best described by $\alpha = 100$, so this value was used instead of 1000. The background subtractions and Pake patterns were similar for 61/135 and 65/135 at 80 and 160 K (Figure 8.16). For 65/80 at 80 and 160 K, the Pake pattern suggests the presence of additional background in the spectrum, probably caused by use of an unnecessarily long time window. Changes to the background model did not significantly alter the Pake pattern for T4L 65/80.

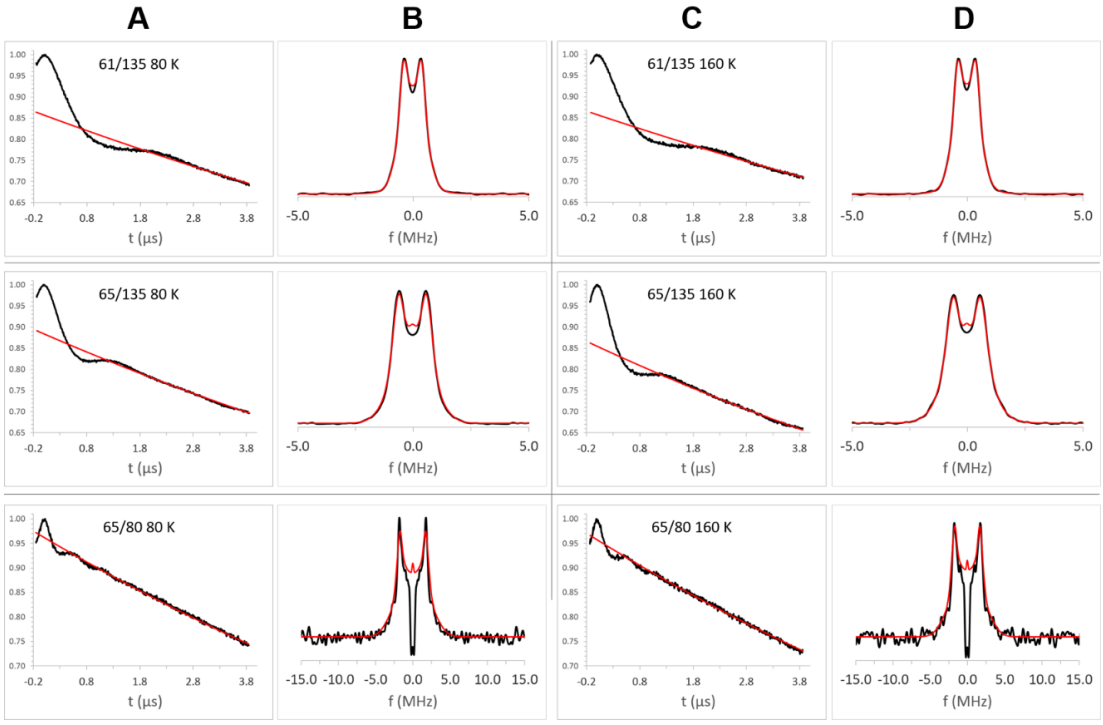

Figure 8.16. Background subtraction and Pake patterns for T4L spin-labeled at positions 61/135, 65/135, and 65/80. DEER was performed at both 80 and 160 K. The backgrounds of the raw data (black, A and C) were fit using 3D homogeneous subtraction (red, A and C). The shape of the Pake pattern (black, B and D) served as a guide for the start of background subtraction. The fit line on the Pake pattern (red, B and D) corresponds to the Tikhonov fit to the background-subtracted data.

8.4.3 Results and Discussion

Increased acquisition window. Variable-temperature relaxation measurements were conducted from 80-160 K to compare the relative decrease in T_2 with that of T_1 (Table 8.4).

	61/135		65/135		65/80	
Temp (K)	T_2 (μs)	T_1 (μs)	T_2 (μs)	T_1 (μs)	T_2 (μs)	T_1 (μs)
80	4.0 (1.8)	1700	4.1 (2.0)	1600	4.1 (2.1)	1600
100	4.0 (1.9)	900	4.0 (1.9)	950	4.0 (2.0)	1000
120	3.7 (1.7)	620	3.8 (1.8)	520	3.9 (1.9)	570
140	3.4 (1.5)	400	3.7 (1.7)	330	3.7 (1.8)	400
160	3.1 (1.4)	260	3.5 (1.7)	190	3.3 (1.7)	280

Table 8.4. Values of T_2 and T_1 for the T4L samples studied at low temperature. T_2 spectra were fit to stretched exponential functions, and the stretch factor is shown in parentheses. T_1 values are reported as the long component of fitting to double exponential functions.

The preservation of T_2 and decrease in T_1 allowed faster repetition rates (SRT) at higher temperature with minimal impact on echo intensity for DEER. The DEER experiments were repeated at 160 K and compared to 80 K DEER. Total acquisition time was kept constant at both temperatures: 70 hours for T4L 61/135, 40 hours for 65/135, and 44 hours for 65/80. The number of averages collected in these acquisition times are shown in Figure 8.17. The slight difference in SNR of the raw data is attributed to the tradeoff between averaging more scans at 160 K than 80 K with the decrease in Boltzmann distribution, which is approximately a factor of two from 80-160 K. Even with

nominally decreased SNR, the same baseline was achieved at higher temperature resulting in an equivalent distance distribution for all three samples (Figure 8.17). It is important to note that the distances measured in the Eaton lab are similar to the previously reported distances measured in the Mchaourab lab (4.7 nm for 61/135, 4.6 nm for 65/135, and 3.0 nm for 65/80) [271]. 65/135 was slightly short, around 4.1 nm (Figure 8.17C), but this did not interfere with evaluation of the improvement in T_2 via the spirocyclohexyl spin label. The 4 μs window is beneficial to studying longer distances, which is the case for T4L 61/135 and 65/135. For T4L 65/80, the spin labels are close enough that a shorter time window can be used. The proximity of the spin labels provides well-defined oscillations in the 4 μs window.

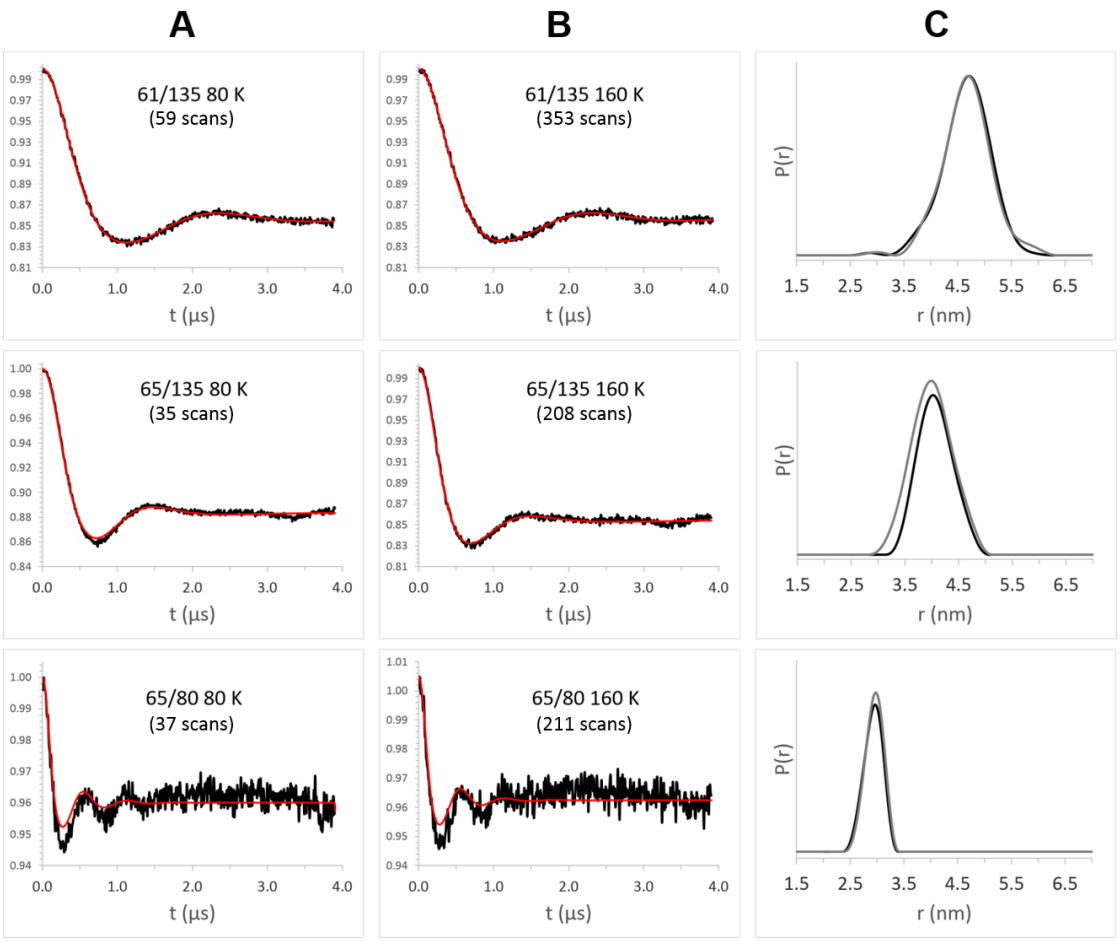

Figure 8.17. Background-subtracted DEER data (black, A and B) with Tikhonov fitting (red) for T4L spin-labeled at different positions. For 61/135 and 65/135, a Tikhonov parameter of $\alpha = 1000$ was used, and for 65/80, $\alpha = 100$ was used. For all samples, the distance distributions at 80 K (black, C) were the same.

DEER at room temperature. A central limitation to performing room-temperature DEER is the very rapid T_2 relaxation that consequently shortens the available acquisition window with which to collect dipolar evolution. A spin label designed without strongly-coupled methyl groups removes a large contribution to T_2 relaxation. Using the spirocyclohexyl spin label, T_2 increased such that the echo remained present at a reasonable window with which to collect DEER data. The spectrum was collected in 3 days. The fast repetition rate allowed acquisition of 2900

scans during this time period. The background subtraction and Pake pattern (Figure 8.18) are comparable to DEER collected at low temperature (Figure 8.16). The calculated distance matched well with the frozen solution spectrum obtained at 80 K.

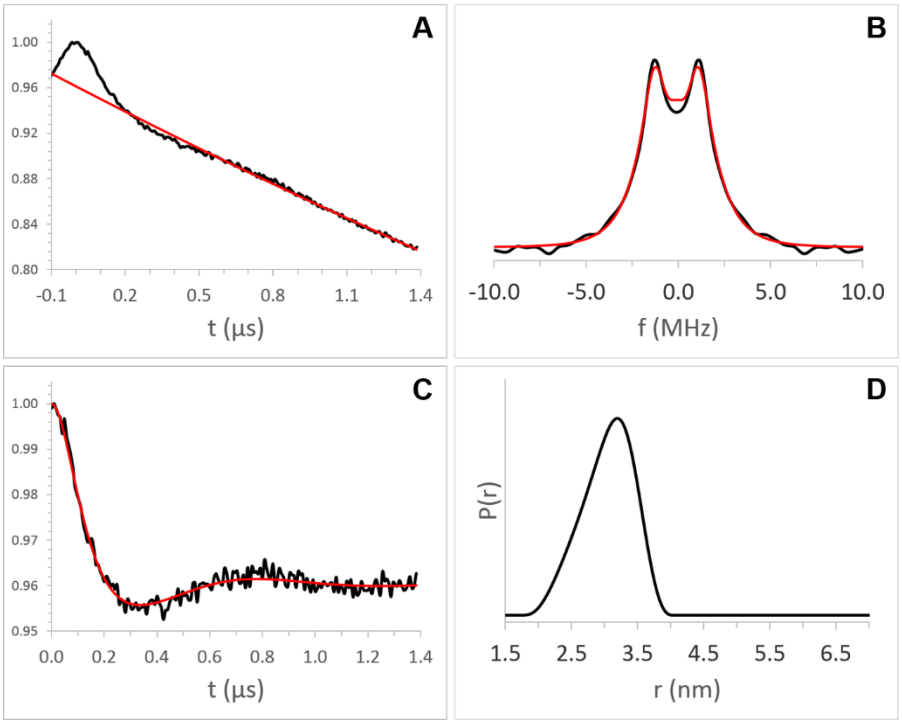

Figure 8.18. Raw data (A, black) with background subtraction (A, red) for T4L measured by DEER at room temperature. The Pake pattern (B, black) is similar to the other samples studied. The background subtracted raw data (C, black) was fit with Tikhonov regularization (B and C, red) using $\alpha = 1000$. The distance distribution (D) matches the protein in frozen solution (Figure 8.17C for 65/80).

Improved SNR. Creating a spin label with increased T_2 provides an excellent tool for studying distances longer than 5 nm using DEER. As shown for T4L, the ability to measure distances this long is not always necessary. For this kind of sample, using the spirocyclohexyl spin label is still beneficial because the echo amplitude at the required time window is greatly enhanced over MTSL. Figure 8.19 shows the SNR for the T4L 65/80 in 24% glycerol collected at 80 K. The time window was $d_2 = 1.5$ µs

instead of 4 μs, which was used for Figure 8.17. The dipolar evolution curve was collected with excellent SNR in only 3.5 hours.

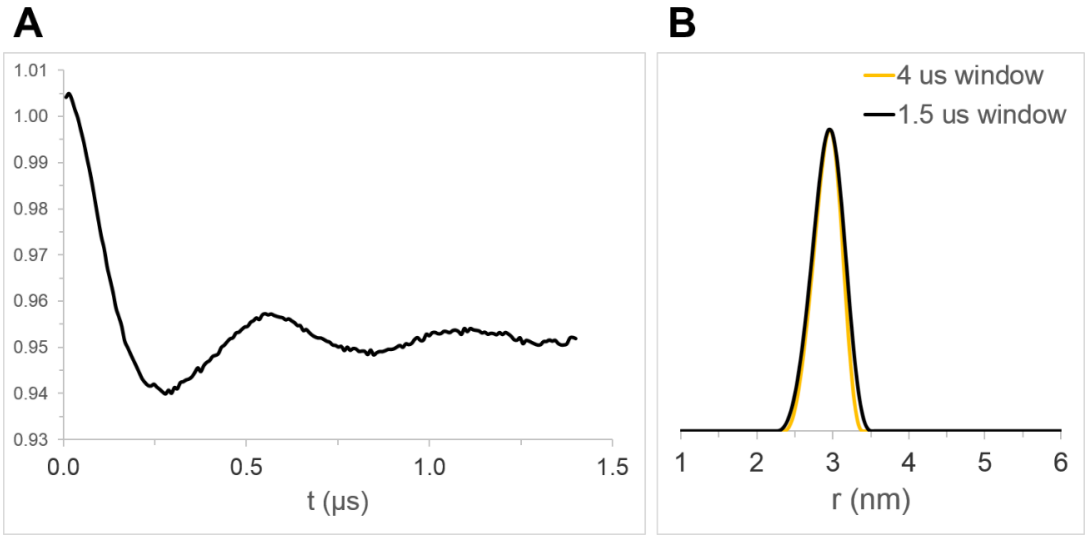

Figure 8.19. Background-subtracted raw data for T4L 65/80 in 24% glycerol at 80 K (A) and distance distributions obtained at two different acquisition windows (B). The spectrum in (A) was collected in only 4 scans with total acquisition time ~ 3.5 hours. The distance distribution from this signal (B, black) matched perfectly to the longer time window (B, yellow) for which the SNR is considerably worse (see Figure 8.17A, last row).

8.4.4 Conclusions

The initial goal of this project was to show that utilization of a known nitroxide synthesized to have long T_2 would benefit DEER measurements in the areas of SNR and probing longer distances. The achievable time window, which corresponds to a reasonable echo signal, was 4 μs, 1.6 μs longer than that used for tau in Chapter 7. A time window of 5 μs was also achieved (data not shown), but required extensive signal averaging.

It became evident after initial measurements that performing DEER higher than 80 K with little detriment to SNR was easily achievable (160 K) with the

spirocyclohexyl spin label. DEER measurements at 160 K using methyl-containing nitroxide spin labels is not possible due to greatly decreased T_2 from methyl rotation [16]. At even higher temperature, molecular motions begin to average out the DEER signal. Several techniques were attempted to dry the protein sample for immobilized spin labels. The ability to immobilize the spin labels was monitored by room temperature CW EPR (Figure 8.20). Using 100% spin-labeled protein without addition of unlabeled counterpart brought neighboring spins too close, diminishing the DEER interaction. Following sample preparation using only 10% labeled protein, the lineshape of the CW spectrum looked similar but with decreased amplitude, as expected.

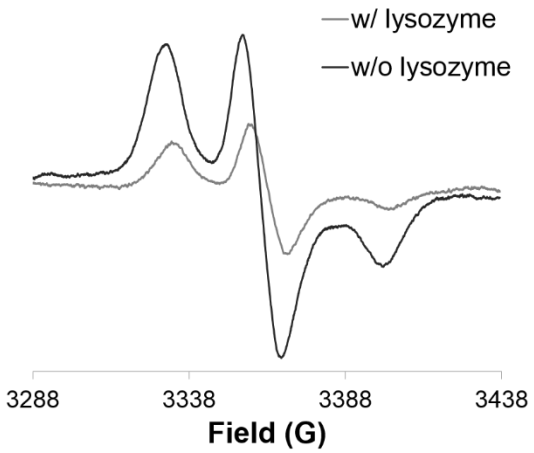

Figure 8.20. CW spectra of T4L with and without 10-fold dilution by hen egg white lysozyme. The undiluted sample (black) has strong dipolar contacts, although peak shapes are similar. Traces are the average of 20 scans using 2048 points, 100 kHz modulation frequency, 0.5 G modulation amplitude, and 20 mW power.

This example may be the first recorded DEER measurement on a protein at room temperature. Prior studies have found distances by CW EPR at room temperature [272], and DEER is easily performed at room temperature for rigid bi- or triradicals [273]. The method by which T4L was dried for this study used trehalose to replace hydrogen

bonding with water, but lyophilization may also be performed to dry a protein sample without disturbing structural contacts. The DEER provided a test to see whether the distance obtained for the dried sample matched the protein in solution collected at 80 K, which was true for this sample. The spirocyclohexyl spin label provides not only a means to room temperature DEER measurement, but also DEER at 160 K, which relinquished little in SNR but consumed significantly less liquid N_2 than measurements at 80 K. Widespread use of a spin label with these characteristics would greatly impact the quality of DEER data in the future.

Chapter 9: Cyclic Amplification of Tau Fibrils

All of the projects presented up to this point have involved analysis using EPR. The Margittai lab has been instrumental in describing seeding properties of tau fibrils, including the ability of 3R and 4R tau to form both independent and mixed fibrils [274], the asymmetric seeding barrier between 3R and 4R tau [209] and the variation in accessible conformations for 3R and 4R fibrils [194]. This chapter is a continuation of the study of tau seeding properties, with an emphasis on the mechanism of fibril propagation and spreading. The unique seeding properties of tau were exploited for the development of a refined assay for sensitive detection of tau fibrils.

9.1 Introduction

Tau fibrils spread through a self-propagating, prion-like mechanism [275, 276]; the natively-unfolded monomer is recruited onto fibril templates forming highly-ordered aggregates. The unique mechanism of prion proliferation stimulated the development of protein misfolding cyclic amplification (PMCA) [277], a technique used to amplify small amounts of misfolded prion to measureable quantities. PMCA is similar to the polymerase chain reaction (PCR) for DNA, cycling between different environments to achieve maximal amplification of misfolded protein aggregates. The first step in PMCA involves mixing a minimal amount of preformed aggregate (fibrils) with monomer. The mixture is sonicated to break the fibrils into multiple fragments/seeds. During a period of incubation at 37 °C, monomer grows onto the ends

of the seeds, elongating the fibrils. Fibrils are again sonicated for breakage. This process is summarized in Figure 9.1. Alternating between periods of sonication and incubation continues over many cycles until the desired protein amplification is achieved. This technique has been successfully utilized for a variety of applications to prion proteins, including *in vitro* generation of infectious prions [278-280], transmissibility [281] and species barrier studies [282, 283], and diagnostic screening of prions from blood [284]. Motivated by the similarities between prions and tau, PMCA was adapted for amplification of tau fibrils in a manner similar to that of misfolded prion strains.

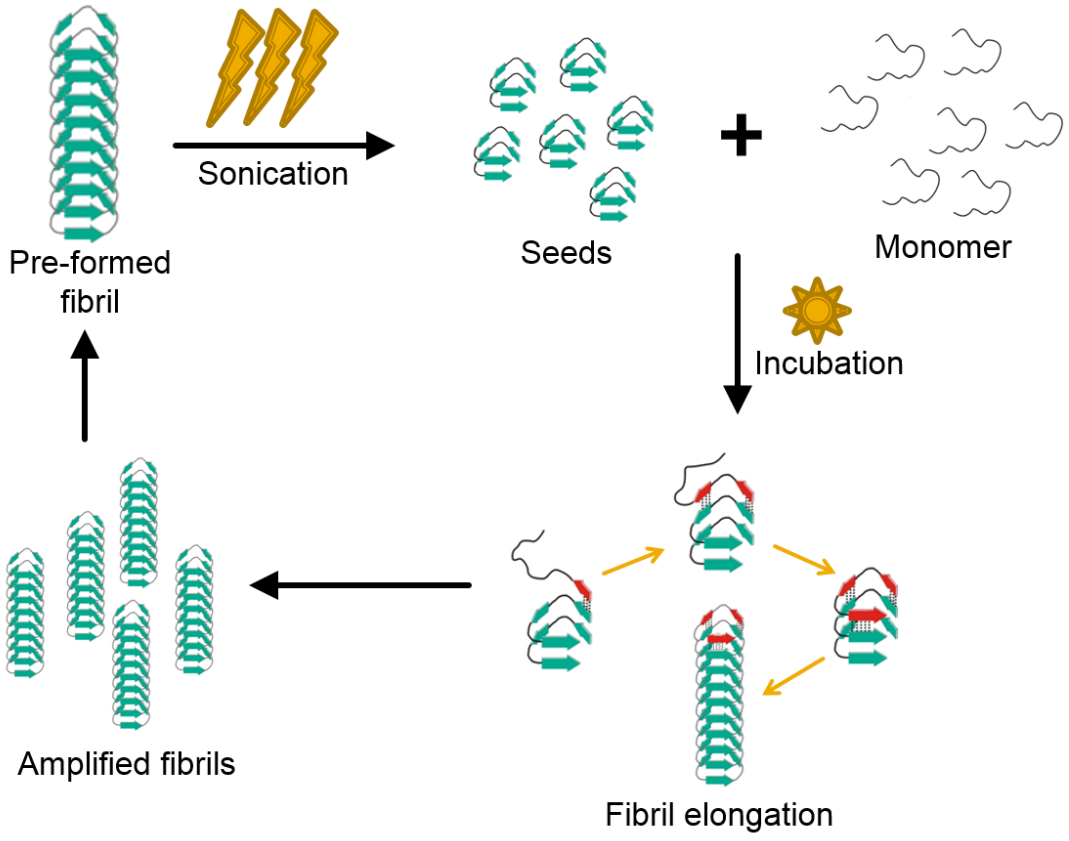

Figure 9.1. Schematic showing the cycling between sonication and incubation in PMCA. Fibrils are introduced as seeds to tau monomer. Monomer is given time to grow onto the seeds, elongating the fibrils, which are again broken, restarting the cycle.

9.2 Methods

9.2.1 Protein Preparation

Four types of tau were used in this study; truncated forms K18 and K19 were described in Section 7.3. Full-length constructs htau40 and htau23 were similarly cloned into pET28b at NcoI/XhoI cleavage sites, and native cysteines replaced by serines (Ayisha Siddiqua). For application to DEER, removal of cysteines prevented unwanted spin labeling. Removal of cysteines here prevents intermolecular disulfide bonds, which have been postulated as the first step in aggregation [285]. Expression and purification were carried out in the same manner as K18 and K19, with the exception of final precipitation in a two-fold volumetric excess of methanol instead of a three-fold volumetric excess of acetone.

9.2.2 Equipment and Experimental Design for PMCA

Sonication cycles were achieved using a bath sonicator in which a water-filled microplate horn (#431MPX, QSonica) was coupled to an ultrasonic processor (Q700, QSonica). A single PMCA cycle consisted of five second sonication pulses at 5% total power. Sonication using 10% total power initiated spontaneous fibril growth in earlier cycles than 5% total power. The water temperature was held constant at 37 °C using a recirculating chiller for the incubation cycles which were 30 minutes. Incubation at 37 °C for one hour did not significantly alter fibril growth but required twice as much time for a single experiment. Various methods of sample containment were attempted; experiments with floating 1.5 mL Eppendorf vials showed that the samples sustained a heavy sonication force, resulting in spontaneous monomer nucleation without addition of seeds. For straightforward fluorescence measurement, the samples were instead

contained within Nunclon 96-well plates (Thermo Scientific) which were covered with BioDot Microplate sealing tape (Dot Scientific). Thioflavin T (ThT, Sigma, Figure 9.2 insert), which binds strongly to tau fibrils but not to tau monomer, was used as the fluorescent indicator of fibril growth. Each well in the microplate corresponded to an individual experiment. The following were added to each well: 10 μM tau monomer (htau40 or htau23), 40 μM heparin, 5 μM ThT, appropriate concentration of seeds, and additional buffer (100 mM NaCl, 10 mM HEPES, pH 7.4) to make the total sample volume 200 μL.

Control wells were run alongside each experiment; a monomer control contained all components except seeds to show that aggregation of the reaction wells occurred through PMCA, not through spontaneous nucleation. A ThT-only control was also run to determine the background fluorescent signal of the dye. This background was then subtracted from the experimental signal. A 4:1 protein:heparin ratio was used, as it was found that 2:1 is not as efficient, and 10:1 actually suppresses aggregation in all wells. Seeds were formed from K18 and K19 by stirring 25 μM monomer with 12.5 μM heparin for three days at room temperature. Htau40 and htau23 were formed analogously, but stirred for six days, as fibril growth is slower for full-length tau. All microplate experiments involved diluting the initial seeds, which was done using buffer and 40 μM heparin to ensure fibrils remained intact. Seeds were added to reactions prior to incubation or PMCA sequence and are present according to the molar percentage of seed per monomeric tau, which is 10 μM for all experiments.

Buoyant bulbs were attached to either side of the microplates to prevent sinking into the sonicator bath. Heating to 37 °C caused condensation droplets on the sealing

tape, so following PMCA cycling, the plate was inverted and then centrifuged at 1,650 X g for two minutes. Fluorescence was immediately measured using a Tecan Infinite M1000 microplate reader. ThT was excited at 440 nm and spectra were collected by scanning emission from 450 – 530 nm in 5 nm steps. For accurate comparison, the gain and z-position of the plate within the reader were kept constant. The degree of tau aggregation was monitored by the emission maximum for ThT at 480 nm. In the bar graphs that follow, error bars were calculated using standard error of the mean (SEM) from multiple wells prepared to test the same experimental parameters.

In addition to ThT as a fluorescent readout, fibrils were sedimented and analyzed on an SDS-PAGE gel with Coomassie staining. Experiments were performed in multiplet by preparing several microplate wells with the same components. These wells were then pooled and centrifuged at 100,000 X g for 30 minutes at 10 °C and washed with 1 ml fresh buffer. Pellets were dissolved in SDS and visualized on the gel.

Using the techniques outlined here, htau40 could undergo ~60 cycles before spontaneous aggregation, as indicated by control experiments in which fibril seeds were excluded. Htau23, which grew less efficiently than htau40, could undergo ~80 cycles before spontaneous aggregation. Unique experiments will be described alongside the results.

9.2.3 Negative Stain Transmission Electron Microscopy

Fibrils of htau40 seeded onto K18 and htau40, and htau23 seeded onto K19 and htau23 were amplified over 40 PMCA cycles. These were transferred onto EM grids and analyzed as described in Section 7.3.10.

9.3 Results and Discussion

9.3.1 PMCA Amplifies Tau Fibrils

The advantage of PMCA lies in amplification of minute quantities of initial aggregates. It was likewise important to demonstrate that the degree of tau fibril growth correlates to the initial seed concentration. Truncated tau (K18 and K19) was used to seed full-length tau (htau40 and htau23). Tau monomer was mixed with varying seed concentrations, along with heparin cofactor, and incubated at 37 °C. Fibril elongation continued for six hours (htau40) or 10 hours (htau23) without additional sonication. ThT displayed decreasing fluorescence consistent with the decrease in seed concentration for both htau40 on K18 (data not shown; collected by Paul Dinkel) and htau23 on K19 (Figure 9.2). Importantly, incubation of monomer without addition of seeds showed no spontaneous fibril growth.

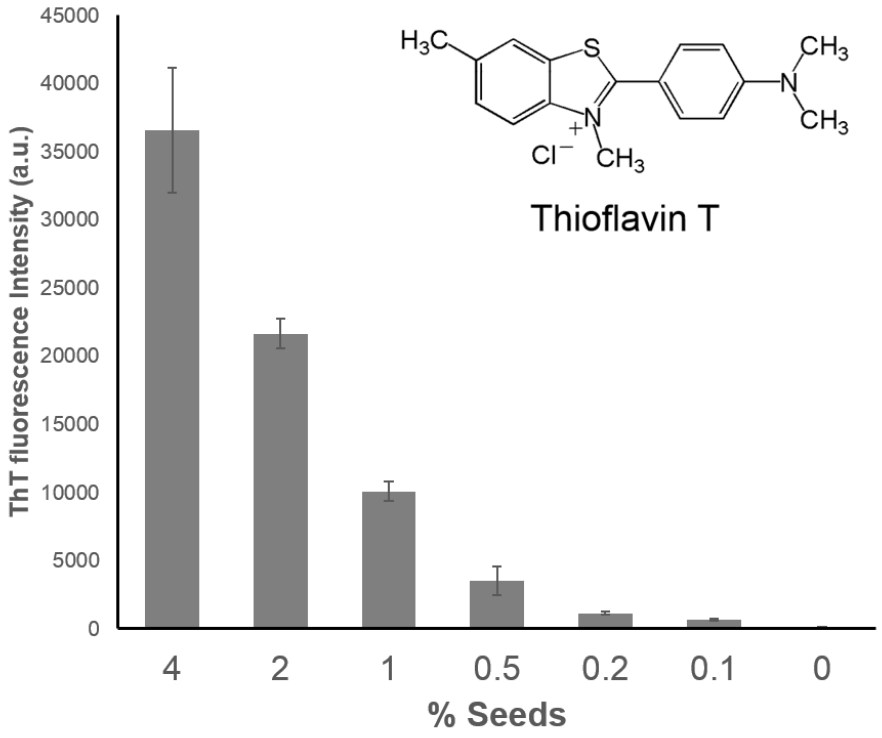

Figure 9.2. Degree of fibril growth with 10 hours of 37 °C incubation for htau23 grown onto varying amounts of K19 seeds. Fluorescence was monitored using ThT (insert), a dye that binds to β-sheet rich amyloids. 0% initial seeds refers to a control containing only tau monomer and heparin cofactor.

At the lowest seed concentration in Figure 9.2, 0.1%, fibril elongation is extremely inefficient. It was next examined whether inclusion of intermittent sonication steps during incubation would amplify fibrils at this seed concentration. PMCA was monitored by ThT fluorescence over 10 cycles for htau40 on K18 seeds and over 16 cycles for htau23 on K19 seeds. Amplification was monitored every two and four cycles for htau40 and htau23, respectively. ThT fluorescence steadily increased with additional PMCA cycles (Figures 9.3A and B). The amplified fibrils were sedimented by ultracentrifugation and visualized on an SDS-PAGE gel (Figures 9.3C and D). The gel corroborates the ThT results showing consistent amplification with increasing

cycles. For htau23, the total eight hour incubation time for 16 PMCA cycles demonstrated fibril amplification onto 0.1% seeds compared to 10 hour incubation following a single sonication step from Figure 9.2. Similar results were seen for amplification of htau40 over five hours from 10 PMCA cycles compared to six hours of incubation only.

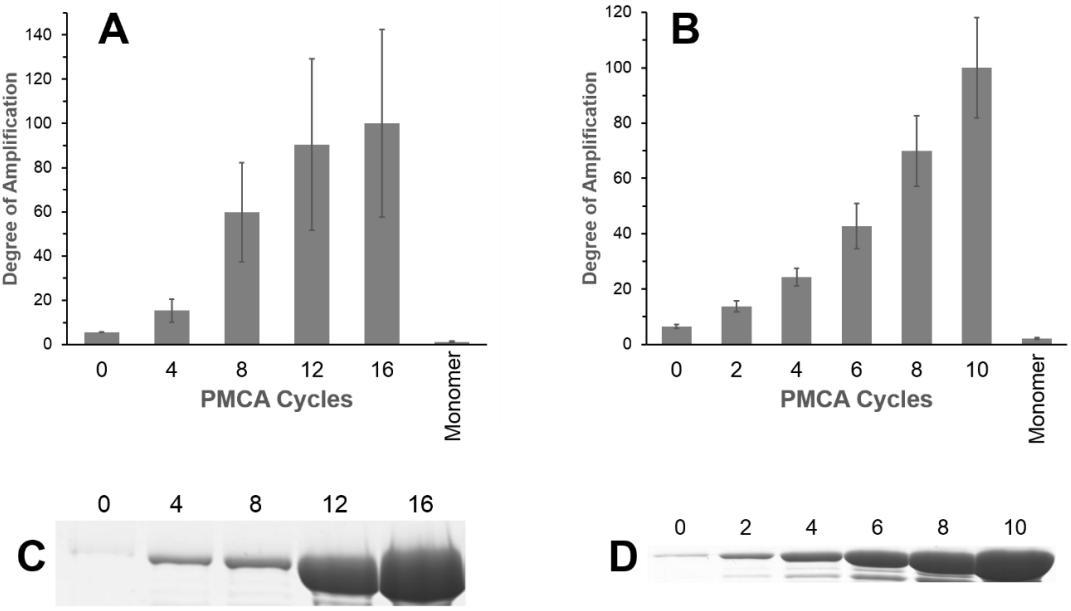

Figure 9.3. PMCA monitored over several cycles for htau23 on K19 seeds (A, C) and htau40 on K18 seeds (B, D). ThT fluorescence shows a steady increase in the degree of amplification for both constructs (A, B). Fibril growth was confirmed by sedimentation and a subsequent SDS-PAGE gel (C, D). Subtraction of the background ThT signal shows no amplification of the monomer alone, although there is a small signal from cycle 0, corresponding to binding of ThT to the initial seeds.

Results to this point show that PMCA successfully amplifies 0.1% initial fibrils for both htau23 and htau40, whereas incubation alone is insufficient to promote fibril elongation at this concentration. It was consistently observed that htau23 requires additional PMCA cycles to achieve the ThT fluorescence intensities seen for htau40 fibrils. Decreased efficiency of htau23 fibril growth is expected based on prior studies

[214, 229]. Additionally, the variability seen for htau23 was greater than that of htau40, resulting in larger error bars for this construct (Figure 9.3A). In both Figure 9.3A and B, a small signal is seen for the zero cycles sample, which is attributed to initial interaction between ThT and the added seeds. The gels show that the signal for zero cycles is negligible, and the slight staining is caused by sedimentation of the initial seeds in addition to attachment of tau monomer to the walls of the centrifuge tubes.

9.3.2 Detection of Minute Quantities of Initial Fibrils

PMCA shows significant enhancement in fibril concentration over incubation alone for 0.1% initial seeds. The seeds were further diluted to characterize the sensitivity of this technique. Monomer was added to seeds ranging from 0.1% to 0.00001% of the monomer concentration, and 40 cycles of PMCA were applied. Amplification using htau40 on K18 seeds decreases proportionally with seed concentration, as expected (experiment performed by Paul Dinkel). Importantly, neither monomer nor seeds alone gave increased ThT signal after 40 cycles. The degrees of amplification for different seed concentrations were almost identical for htau40 grown onto both K18 initial seeds and htau40 initial seeds, reiterating the similar seeding properties of the full length and truncated constructs. K19 and htau23 seeds could also be diluted, but not to the same extent. This is expected, as we have observed that seeding is not as efficient for htau23. The lowest seed concentration that resulted in amplification over 40 cycles using htau23 was 0.001% K19 (Figure 9.4). This was also the lowest amplifiable concentration of htau23 seeds (experiment performed by Paul Dinkel).

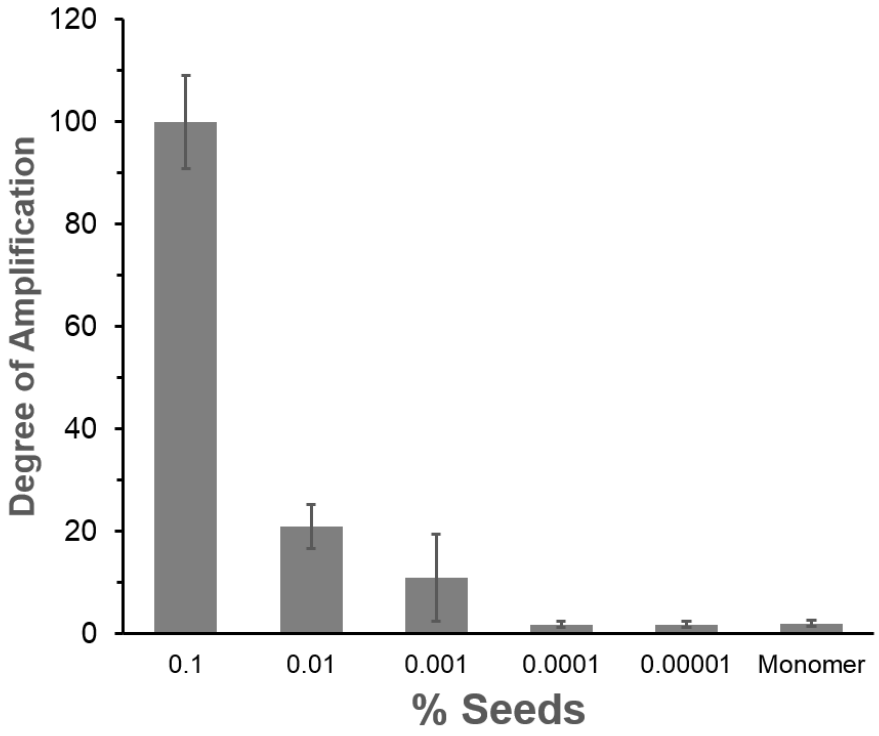

Figure 9.4. Amplification of minute quantities of K19 seeds with htau23 monomer. Seeds diluted 10,000-fold achieved amplification using PMCA. Seeds could be diluted more than 1,000,000-fold using htau40 (data not shown).

To ensure that fibrillar structure was the source of increased ThT fluorescence, fibrils grown from 0.1% seeds following 40 PMCA cycles were visualized by EM (Figure 9.5). Fibrillar structure was clear for all fibrils formed from PMCA.

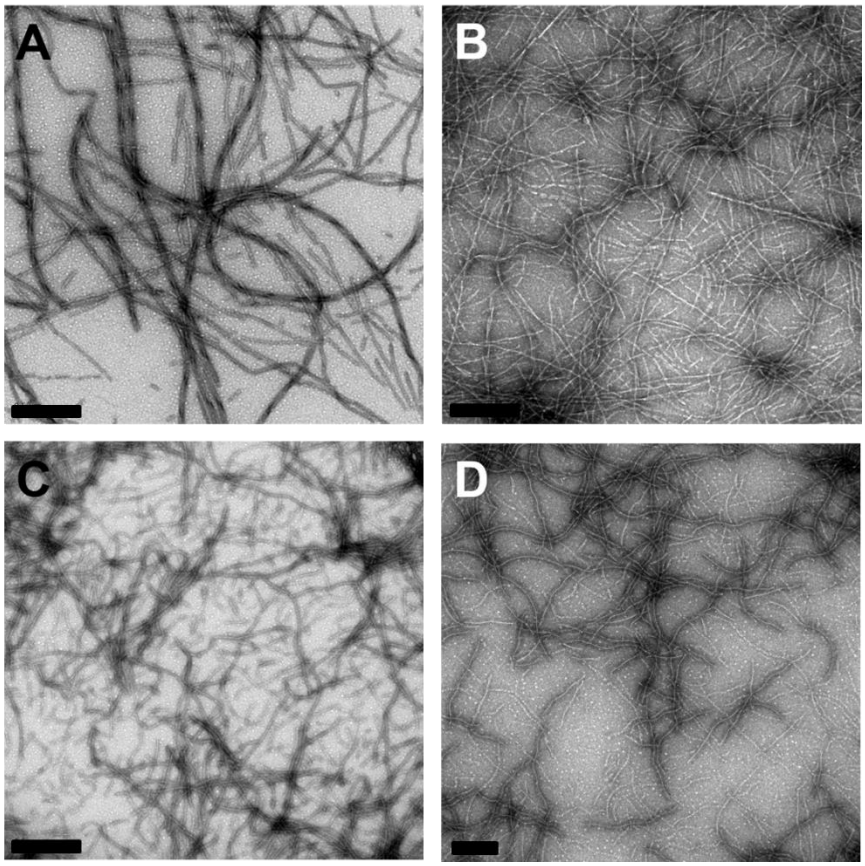

Figure 9.5. EM images of 0.1% initial seeds amplified over 40 PMCA cycles. Htau23 was grown onto K19 (A) and htau23 (B) seeds, and htau40 was grown onto K18 (C) and htau40 (D) seeds. Bar = 0.5 μm.

PMCA has been shown to be a highly sensitive technique for the amplification of prion protein, and the results presented here demonstrate that a high degree of sensitivity can also be achieved for amplification of tau fibrils. The lowest seed concentration amplified in Figure 9.6 corresponds to 1 pM tau monomer. The sensitivity of PMCA for prion detection has been reported in a variety of ways; the earliest paper claimed detection of ~10 pg infectious (aggregated) prion [277], while the number of monomers necessary to carry out PMCA has been predicted to be ~7 [279]. Detection of prions from the body are reported at 20 fg/mL in blood [284] and 5 fg/mL

in urine [286] compared to 1 fg/mL from brain tissue directly [287]. One of the difficulties in comparison of tau with prion sensitivities is variation in extraction protocol. Whereas many of the prion values are based on initial extraction of highly-stable infectious prion, the tau models presented here were performed from initial seeds formed *in vitro* from recombinant protein. Tau fibrils are at equilibrium with monomer in solution, and it is expected that dilution of these fibrils will shift the equilibrium toward monomer during experiment preparation. The method, therefore, may require additional optimization. These experiments are nonetheless the first reported successful application of PMCA to tau.

9.3.3 Impact of Experimental Parameters on Fibril Growth

A number of additional PMCA experiments were performed to better understand the parameters necessary for optimum fibril growth. In addition to heparin, polyglutamate and RNA have also been used as cofactors to grow tau fibrils [288]. PMCA was successful using polyglutamate as a cofactor, but RNA binds strongly to ThT, enhancing fluorescence beyond a level expected from binding to fibrils. As a result, RNA could be used as a cofactor for tau PMCA, but ThT could not be used to monitor fibril growth.

Monomer concentration was varied from as low as 0.5 μM up to 20 μM, and the extent of fibril amplification varied in accordance to the amount of monomer used. 0.5 μM monomer did not show significant fibril amplification, while 20 μM did not provide substantial advantage over 10 μM. 10 μM was therefore chosen as the final monomer concentration, as it also consistently showed no spontaneous aggregation following 40 PMCA cycles, and it did not require using a large amount of material.

PMCA performed on brain tissue would require addition of detergent, such as Triton X-100, for cell lysis, and would be performed in the presence of other cellular components. Both 1% Triton X-100 and bacterial extract were added to wells, and neither the detergent nor the extract interfered with fibril growth. Several additional considerations when optimizing PMCA included measuring ThT fluorescence with and without the plate film intact, addition of ThT immediately before fluorescence measurements, and varying the time and intensity of sonication and incubation. Fluorescence readings taken with the film still attached decreased the intensity slightly, but it was determined to be very important to assure no sample leakage from neighboring wells. Adding ThT after PMCA as opposed to during the process resulted in decreased intensity. While not published, the experiments presented in this section were fundamental to development of the method.

9.4 Conclusions

Current efforts in the Margittai lab toward further development of PMCA for tau fibrils have focused on amplification of fibrils from diseased brain tissue. PMCA has already shown promise as a diagnostic tool for early detection of various prion diseases [289, 290]. The ability to amplify tau from brain tissue is the first step toward a similar application of PMCA for the detection of Alzheimer's disease, frontotemporal dementia, or a number of other tauopathies. Prior studies have demonstrated the difficulty in pre-mortem diagnosis of these disorders based on cognitive decline and physiological changes [242], and diagnosis based on the presence of tau fibrils in cerebrospinal fluid could lead to more accurate diagnosis. The combination of PMCA-assisted detection with a recent procedure describing the visualization of tau fibrils

through *in vivo* imaging [291] could provide a powerful strategy for early detection of neurodegenerative disease in the future.

References

1. Dalal, D. P.; Eaton, S. S.; Eaton, G. R., The effects of lossy solvents on quantitative electron paramagnetic resonance studies. *J. Magn. Reson.* **1981,** 44, 415-428.

2. Eaton, G. R.; Eaton, S. S.; Barr, D. P.; Weber, R. T., *Quantitative EPR*. Springer Wien: New York, NY, 2010.

3. Weil, J. A.; Bolton, J. R., *Electron Paramagnetic Resonance: Elementary Theory and Practical Applications*. 2nd ed.; John Wiley & Sons: Hoboken, NJ, 2007.

4. Housecroft, C. E.; Sharpe, A. G., *Inorganic Chemistry*. 3rd ed.; Pearson/Prentice Hall: Harlow, 2008.

5. Jani, M. G.; Bossoli, R. B.; Halliburton, L. E., Further characterization of the E1' center in crystalline SiO_2. *Phys. Rev. B.* **1983,** 27, 2285-2293.

6. Ikeya, M., *New Applications of Electron Spin Resonance: Dating, Dosimetry, and Microscopy*. World Scientific: Singapore, 1993.

7. Felton, S.; Edmonds, A. M.; Newton, M. E.; Martineau, P. M.; Fisher, D.; Twitchen, D. J.; Baker, J. M., Hyperfine interaction in the ground state of the negatively charged nitrogen vacancy center in diamond. *Phys. Rev. B.* **2009,** 79, 075203-1-075203-8.

8. Fehr, M.; Schnegg, A.; Rech, B.; Lips, K.; Astakhov, O.; Finger, F.; Freysoldt, C.; Bittl, R.; Teutloff, C., Dangling bonds in amorphous silicon investigated by multifrequency EPR. *J. Non-Cryst. Solids.* **2012,** 358, 2067-2070.

9. Bennati, M.; Farrar, C. T.; Bryant, J. A.; Inati, S. J.; Weis, V.; Gerfen, G. J.; Riggs-Gelasco, P.; Stubbe, J.; Griffin, R. G., Pulsed electron-nuclear double resonance (ENDOR) at 140 GHz. *J. Magn. Reson.* **1999,** 138, 232-243.

10. Dane, E. L.; Swager, T. M., Synthesis of a water-soluble 1,3-bis(diphenylene)2-phenylallyl radical. *J. Org. Chem.* **2010,** 75, 3533-3536.

11. Krzystek, J.; Sienkiewicz, A.; Pardi, L.; Brunel, L. C., DPPH as a standard for high-field EPR. *J. Magn. Reson.* **1997,** 125, 207-211.

12. Royaud, J., Solvent effect on g-factor of galvinoxyl radical. *C.R. Acad. Sc. Paris.* **1972,** 274, 1277-1279.

13. Marti, C.; Irurre, J.; Alvarezlarena, A.; Piniella, J. F.; Brillas, E.; Fajari, L.; Aleman, C.; Julia, L., Synthesis, properties, and x-ray structure of 6-aza-5,7,12,14-tetrathiapentacene as a novel polyheterocyclic electron donor, and related compounds. *J. Org. Chem.* **1994,** 59, 6200-6207.

14. Sato, H.; Kathirvelu, V.; Fielding, A.; Blinco, J. P.; Micallef, A. S.; Bottle, S. E.; Eaton, S. S.; Eaton, G. R., Impact of molecular size on electron spin relaxation rates of nitroxyl radicals in glassy solvents between 100 and 300K. *Mol. Phys.* **2007,** 105, 2137-2151.

15. Owenius, R.; Engstrom, M.; Lindgren, M.; Huber, M., Influence of solvent polarity and hydrogen bonding on the EPR parameters of a nitroxide spin label studied by 9 GHz and 95 GHz EPR spectroscopy and DFT calculations. *J. Phys. Chem. A.* **2001,** 105, 10967-10977.

16. Rajca, A.; Kathirvelu, V.; Roy, S. K.; Pink, M.; Rajca, S.; Sarkar, S.; Eaton, S. S.; Eaton, G. R., A spirocyclohexyl nitroxide amino acid spin label for pulsed EPR spectroscopy distance measurements. *Chem.-Eur. J.* **2010,** 16, 5778-5782.

17. Hyde, J. S., Saturation recovery methodology. In *Time Domain Electron Spin Resonance*, Kevan, L.; Schwartz, R. N., Eds. John Wiley & Sons: New York, NY, 1979; pp 1-30.

18. Eaton, S. S.; Eaton, G. R., Relaxation times of organic radicals and transition metal ions. In *Biological Magnetic Resonance: Distance Measurements in Biological Systems by EPR*, Berliner, L. J.; Eaton, S. S.; Eaton, G. R., Eds. Kluwer Academic/Plenum Publishers: New York, NY, 2000; Vol. 19, pp 29-154.

19. van Holde, K. E.; Johnson, W. C.; Ho, P. S., *Principles of Physical Biochemistry*. 2nd ed.; Pearson/Prentice Hall: Upper Saddle River, NJ, 2006.

20. Bloembergen, N.; Purcell, E. M.; Pound, R. V., Relaxation effects in nuclear magnetic resonance absorption. *Phys. Rev.* **1948,** 73, 679-712.

21. Wertz, J. E.; Vivo, J. L., Multiple thio-radicals in sulfuric acid solution. *J. Chem. Phys.* **1955,** 23, 2193-2194.

22. Standley, K. J.; Vaughan, R. A., *Electron Spin Relaxation Phenomena in Solids*. Plenum Press: New York, NY, 1969.

23. Bloch, F., Nuclear induction. *Phys. Rev.* **1946,** 70, (7-8), 460-474.

24. More, K. M.; Eaton, G. R.; Eaton, S. S., Determination of T_1 and T_2 by simulation of electron paramagnetic resonance power saturation curves and

saturated spectra: Application to spin-labeled iron porphyrins. *J. Magn. Reson.* **1984,** 60, 54-65.

25. Harbridge, J. R.; Eaton, G. R.; Eaton, S. S., Impact of spectral diffusion on apparent relaxation times for the stable radical in irradiated glycylglycine, *1st Asia-Pacific EPR/ESR Symposium: Modern Applications of EPR/ESR: From Biophysics to Materials Science*, 1998; pp 220-225.

26. Portis, A. M., Rapid passage effects in electron spin resonance. *Phys. Rev.* **1955,** 100, 1219-1221.

27. Hyde, J. S.; Dalton, L., Very slowly tumbling spin labels: Adiabatic rapid passage. *Chem. Phys. Lett.* **1972,** 16, 568-572.

28. Pake, G. E.; Estle, T. L., *The Physical Principles of Electron Paramagnetic Resonance*. 2nd ed.; Benjamin-Cummings Publishing Company: Reading, MA, 1973.

29. Weger, M., Passage effects in paramagnetic resonance. *Bell. Syst. Tech. J.* **1960,** 39, 1013-1112.

30. DeRose, V. J.; Hoffman, B. M., Protein structure and mechanism studied by electron nuclear double resonance spectroscopy. In *Methods in Enzymology: Biochemical Spectroscopy*, Sauer, K., Ed. Academic Press, Inc.: San Diego, CA, 1995; Vol. 246, pp 554-589.

31. Galtsev, V. E.; Galtseva, E. V.; Grinberg, O. Y.; Lebedev, Y. S., Human tooth EPR dosimetry with enhanced sensitivity. *J. Radioanal. Nucl. Chem. Lett.* **1994,** 186, 35-45.

32. Fedin, M.; Gromov, I.; Schweiger, A., Sensitivity optimization in amplitude-modulated CW-EPR experiment. *J. Magn. Reson.* **2006,** 182, 293-297.

33. Harbridge, J. R.; Rinard, G. A.; Quine, R. W.; Eaton, S. S.; Eaton, G. R., Enhanced signal intensities obtained by out-of-phase rapid-passage EPR for samples with long electron spin relaxation times. *J. Magn. Reson.* **2002,** 156, 41-51.

34. Tseitlin, M.; Rinard, G. A.; Quine, R. W.; Eaton, S. S.; Eaton, G. R., Rapid frequency scan EPR. *J. Magn. Reson.* **2011,** 211, 156-161.

35. Tseitlin, M.; Rinard, G. A.; Quine, R. W.; Eaton, S. S.; Eaton, G. R., Deconvolution of sinusoidal rapid EPR scans. *J. Magn. Reson.* **2011,** 208, 279-283.

36. Dadok, J.; Sprecher, R. F., Correlation NMR spectroscopy. *J. Magn. Reson.* **1974,** 13, 243-248.

37. Jacobsohn, B. A.; Wangsness, R. K., Shapes of nuclear induction signals. *Phys. Rev.* **1948,** 73, 942-946.

38. Beeler, R.; Roux, D.; Bene, G.; Extermann, R., Rapid-passage effects in electron spin resonance. *Phys. Rev.* **1956,** 102, 295-295.

39. Joshi, J. P.; Ballard, J. R.; Rinard, G. A.; Quine, R. W.; Eaton, S. S.; Eaton, G. R., Rapid-scan EPR with triangular scans and fourier deconvolution to recover the slow-scan spectrum. *J. Magn. Reson.* **2005,** 175, 44-51.

40. Mitchell, D. G.; Quine, R. W.; Tseitlin, M.; Meyer, V.; Eaton, S. S.; Eaton, G. R., Comparison of continuous wave, spin echo, and rapid scan EPR of irradiated fused quartz. *Radiat. Meas.* **2011,** 46, 993-996.

41. Mitchell, D. G.; Quine, R. W.; Tseitlin, M.; Weber, R. T.; Meyer, V.; Avery, A.; Eaton, S. S.; Eaton, G. R., Electron spin relaxation and heterogeneity of the 1:1 alpha,gamma-bisdiphenylene-beta-phenylallyl (BDPA)/benzene complex. *J. Phys. Chem. B.* **2011,** 115, 7986-7990.

42. Mitchell, D. G.; Tseitlin, M.; Quine, R. W.; Meyer, V.; Newton, M. E.; Schnegg, A.; George, B.; Eaton, S. S.; Eaton, G. R., X-band rapid-scan EPR of samples with long electron spin relaxation times: a comparison of continuous wave, pulse and rapid-scan EPR. *Mol. Phys.* **2013,** 111, 2664-2673.

43. Hyde, J. S.; Jesmanowicz, A.; Ratke, J. J.; Antholine, W. E., Pseudomodulation: A computer-based strategy for resolution enhancement. *J. Magn. Reson.* **1992,** 96, 1-13.

44. Schweiger, A.; Jeschke, G., *Principles of Pulse Electron Paramagnetic Resonance*. Oxford University Press: New York, NY, 2001.

45. Mitchell, D. G.; Rosen, G. M.; Tseitlin, M.; Symmes, B.; Eaton, S. S.; Eaton, G. R., Use of rapid-scan EPR to improve detection sensitivity for spin-trapped radicals. *Biophys. J.* **2013,** 105, 338-342.

46. Biller, J. R.; Tseitlin, M.; Quine, R. W.; Rinard, G. A.; Weismiller, H. A.; Elajaili, H.; Rosen, G. M.; Kao, J. P. Y.; Eaton, S. S.; Eaton, G. R., Imaging of nitroxides at 250 MHz using rapid-scan electron paramagnetic resonance. *J. Magn. Reson.* **2014,** 242, 162-168.

47. Hahn, E. L., Spin echoes. *Phys. Rev.* **1950,** 80, 580-594.

48. Blume, R. J., Electron spin relaxation times in sodium-ammonia solutions. *Phys. Rev.* **1958,** 109, 1867-1873.

49. Mims, W. B., Electric field effects in spin echoes. *Phys. Rev. A-Gen. Phys.* **1964,** 133, A835-A840.

50. Bowman, M. K., Pulsed electron paramagnetic resonance. In *Electron Paramagnetic Resonance: A Practitioner's Toolkit*, Brustolon, M.; Giamello, E., Eds. John Wiley & Sons: Hoboken, NJ, 2009; pp 159-194.

51. Gemperle, C.; Aebli, G.; Schweiger, A.; Ernst, R. R., Phase cycling in pulse EPR. *J. Magn. Reson.* **1990,** 88, 241-256.

52. Mims, W. B.; Nassau, K.; McGee, J. D., Spectral diffusion in electron resonance lines. *Phys. Rev.* **1961,** 123, 2059-2069.

53. Yu, H. T., Extending the size limit of protein nuclear magnetic resonance. *Proc. Natl. Acad. Sci. U.S.A.* **1999,** 96, 332-334.

54. Milov, A. D.; Salikhov, K. M.; Schirov, M. D., Application of ENDOR in electron spin-echo for paramagnetic center space distribution in solids. *Fiz. Tverd. Tela.* **1981,** 23, 975-982.

55. Milov, A. D.; Ponomarev, A. B.; Tsvetkov, Y. D., Electron-electron double resonance in electron spin-echo: Model biradical systems and the sensitized photolysis of decalin. *Chem. Phys. Lett.* **1984,** 110, 67-72.

56. Jeschke, G., DEER distance measurements on proteins. *Annu. Rev. Phys. Chem.* **2012,** 63, 419-446.

57. Milov, A. D.; Maryasov, A. G.; Tsvetkov, Y. D., Pulsed electron double resonance (PELDOR) and its applications in free-radicals research. *Appl. Magn. Reson.* **1998,** 15, 107-143.

58. Jeschke, G.; Pannier, M.; Spiess, H. W., Double electron-electron resonance. In *Biological Magnetic Resonance: Distance Measurements in Biological Systems by EPR*, Berliner, L. J.; Eaton, S. S.; Eaton, G. R., Eds. Kluwer Academic/Plenum Publishers: New York, NY, 2000; Vol. 19, pp 493-512.

59. Rinard, G. A.; Quine, R. W.; Ghim, B. T.; Eaton, S. S.; Eaton, G. R., Easily tunable crossed-loop (bimodal) EPR resonator. *J. Magn. Reson. Ser. A.* **1996,** 122, 50-57.

60. Ezhevskaya, M.; Bordignon, E.; Polyhach, Y.; Moens, L.; Dewilde, S.; Jeschke, G.; Van Doorslaer, S., Distance determination between low-spin ferric haem and

nitroxide spin label using DEER: The neuroglobin case. *Mol. Phys.* **2013,** 111, 2855-2864.

61. Quine, R. W.; Mitchell, D. G.; Tseitlin, M.; Eaton, S. S.; Eaton, G. R., A resonated coil driver for rapid scan EPR. *Concept. Magn. Reso. B.* **2012,** 41, 95-110.

62. Quine, R. W.; Mitchell, D. G.; Eaton, G. R., A general purpose Q-measuring circuit using pulse ring-down. *Concept. Magn. Reso. B.* **2011,** 39, 43-46.

63. Quine, R. W.; Eaton, G. R.; Eaton, S. S., Pulsed electron paramagnetic resonance spectrometer. *Rev. Sci. Instrum.* **1987,** 58, 1709-1723.

64. Quine, R. W.; Eaton, S. S.; Eaton, G. R., Saturation recovery electron paramagnetic resonance spectrometer. *Rev. Sci. Instrum.* **1992,** 63, 4251-4262.

65. Rinard, G. A.; Quine, R. W.; Eaton, S. S.; Eaton, G. R.; Froncisz, W., Relative benefits of overcoupled resonators vs. inherently low-Q resonators for pulsed magnetic resonance. *J. Magn. Reson. A.* **1994,** 108, 71-81.

66. Kivelson, D., Theory of ESR linewidths of free radicals. *J. Chem. Phys.* **1960,** 33, 1094-1106.

67. Provencher, S. W., Eigenfunction expansion method for analysis of exponential decay curves. *J. Chem. Phys.* **1976,** 64, 2773-2777.

68. Borgia, G. C.; Brown, R. J. S.; Fantazzini, P., Uniform-penalty inversion of multiexponential decay data II: Data spacing, T_2 data, systematic data errors, and diagnostics. *J. Magn. Reson.* **2000,** 147, 273-285.

69. Jeschke, G.; Chechik, V.; Ionita, P.; Godt, A.; Zimmermann, H.; Banham, J.; Timmel, C. R.; Hilger, D.; Jung, H., DeerAnalysis2006: A comprehensive software package for analyzing pulsed ELDOR data. *Appl. Magn. Reson.* **2006,** 30, 473-498.

70. Brandon, S.; Beth, A. H.; Hustedt, E. J., The global analysis of DEER data. *J. Magn. Reson.* **2012,** 218, 93-104.

71. Sen, K. I.; Logan, T. M.; Fajer, P. G., Protein dynamics and monomer-monomer interactions in AntR activation by electron paramagnetic resonance and double electron-electron resonance. *Biochemistry.* **2007,** 46, 11639-11649.

72. Toyoda, S.; Rink, J. W.; Schwarcz, H. P.; Ikeya, M., Formation of E(1)' precursors in quartz: Applications to dosimetry and dating. *Appl. Radiat. Isotopes.* **1996,** 47, 1393-1398.

73. Eaton, S. S.; Eaton, G. R., Irradiated fused-quartz standard sample for time-domain EPR. *J. Magn. Reson. Ser. A.* **1993,** 102, 354-356.

74. Grun, R.; Invernati, C., Uranium accumulation in teeth and its effect on electron spin resonance dating: A detailed study of a mammoth tooth. *Nucl. Tracks Rad. Meas.* **1985,** 10, 869-877.

75. Cole, T.; Silver, A. H., Production of hydrogen atoms in teeth by x-irradiation. *Nature.* **1963,** 200, 700-701.

76. Cevc, P.; Schara, M.; Ravnik, C., Electron paramagnetic resonance study of irradiated tooth enamel. *Radiat. Res.* **1972,** 51, 581-589.

77. Fattibene, P.; Callens, F., EPR dosimetry with tooth enamel: A review. *Appl. Radiat. Isotopes.* **2010,** 68, 2033-2116.

78. Sato, H.; Filas, B. A.; Eaton, S. S.; Eaton, G. R.; Romanyukha, A. A.; Hayes, R.; Rossi, A. M., Electron spin relaxation of radicals in irradiated tooth enamel and synthetic hydroxyapatite. *Radiat. Meas.* **2007,** 42, 997-1004.

79. Trompier, F.; Romanyukha, A.; Kornak, L.; Calas, C.; LeBlanc, B.; Mitchell, C.; Swartz, H.; Clairand, I., Electron paramagnetic resonance radiation dosimetry in fingernails. *Radiat. Meas.* **2009,** 44, 6-10.

80. Weber, J. R.; Koehl, W. F.; Varley, J. B.; Janotti, A.; Buckley, B. B.; Van de Walle, C. G.; Awschalom, D. D., Quantum computing with defects. *Proc. Natl. Acad. Sci. U.S.A.* **2010,** 107, 8513-8518.

81. Shcherbyna, L.; Torchynska, T., Si quantum dot structures and their applications. *Physica E.* **2013,** 51, 65-70.

82. Hong, C. Y.; Yeh, Y. S.; Yang, S. Y.; Horng, H. E.; Yang, H. C., Ordered structures with point-like defects of various shapes in magnetic fluid films. *J. Magn. Magn. Mater.* **2004,** 283, 22-27.

83. Pierson, H. O., *Handbook of Carbon, Graphite, Diamond and Fullerenes - Properties, Processing and Applications*. Noyes Publications: Park Ridge, NJ, 1993.

84. Tallaire, A.; Collins, A. T.; Charles, D.; Achard, J.; Sussmann, R.; Gicquel, A.; Newton, M. E.; Edmonds, A. M.; Cruddace, R. J., Characterisation of high-quality thick single-crystal diamond grown by CVD with a low nitrogen addition. *Diam. Relat. Mater.* **2006,** 15, 1700-1707.

85. Griffiths, J. H. E.; Owen, J.; Ward, I. M., Paramagnetic resonance in neutron-irradiated diamond and smoky quartz. *Nature.* **1954,** 173, 439-440.

86. Mineeva, R. M.; Zudina, N. N.; Titkov, S. V.; Ryabchikov, I. D.; Speransky, A. V.; Zudin, N. G., EPR spectroscopy of cubic diamonds from placers in the north-east of the Siberian platform: New type of nitrogen centers. *Dokl. Earth Sci.* **2013,** 448, 243-247.

87. Braatz, A.; Ott, U.; Henning, T.; Jager, C.; Jeschke, G., Infrared, ultraviolet, and electron paramagnetic resonance measurements on presolar diamonds: Implications for optical features and origin. *Meteorit. Planet Sci.* **2000,** 35, 75-84.

88. Rakhmanova, M. I.; Nadolinny, V. A.; Yuryeva, O. P., Impurity centers in synthetic and natural diamonds with a system of electron-vibronic Lines at 418 nm in luminescence spectra. *Phys. Solid State.* **2013,** 55, 127-130.

89. Cox, A.; Newton, M. E.; Baker, J. M., C^{13}, N^{14}, and N^{15} ENDOR measurements on the single substitution nitrogen center (P1) in diamond. *J. Phys.-Condens. Mat.* **1994,** 6, 551-563.

90. Hoffmann, S. K.; Lijewski, S.; Goslar, J.; Ulanov, V. A., Electron spin relaxation of exchange coupled pairs of transition metal ions in solids. Ti^{2+}-Ti^{2+} pairs and single Ti^{2+} ions in SrF_2 crystals. *J. Magn. Reson.* **2010,** 202, 14-23.

91. Klauder, J. R.; Anderson, P. W., Spectral diffusion decay in spin resonance experiments. *Phys. Rev.* **1962,** 125, 912-932.

92. Bowman, M. K.; Kevan, L., Electron spin-lattice relaxation in nonionic solids. In *Time Domain Electron Spin Resonance*, Kevan, L.; Schwartz, R. N., Eds. John Wiley & Sons: New York, NY, 1979; pp 67-105.

93. Rech, B.; Wagner, H., Potential of amorphous silicon for solar cells. *Appl. Phys. A-Mater.* **1999,** 69, 155-167.

94. Clayden, N. J.; Hesler, B. D., Multiexponential analysis of relaxation decays. *J. Magn. Reson.* **1992,** 98, 271-282.

95. Laiken, S. L.; Printz, M. P., Kinetic Class Analysis of Hydrogen-exchange Data. *Biochemistry.* **1970,** 9, 1547-1553.

96. Meyer, V.; Eaton, S. S.; Eaton, G. R., Temperature dependence of electron spin relaxation of 2,2-diphenyl-1-picrylhydrazyl in polystyrene. *Appl. Magn. Reson.* **2013,** 44, 509-517.

97. Lumata, L.; Ratnakar, S. J.; Jindal, A.; Merritt, M.; Comment, A.; Malloy, C.; Sherry, A. D.; Kovacs, Z., BDPA: An efficient polarizing agent for fast dissolution dynamic nuclear polarization NMR spectroscopy. *Chem.-Eur. J.* **2011,** 17, 10825-10827.

98. Giraudeau, P.; Shrot, Y.; Frydman, L., Multiple ultrafast, broadband 2D NMR spectra of hyperpolarized natural products. *J. Am. Chem. Soc.* **2009,** 131, 13902-13903.

99. Haze, O.; Corzilius, B.; Smith, A. A.; Griffin, R. G.; Swager, T. M., Water-soluble narrow-line radicals for dynamic nuclear polarization. *J. Am. Chem. Soc.* **2012,** 134, 14287-14290.

100. Becerra, L. R.; Gerfen, G. J.; Bellew, B. F.; Bryant, J. A.; Hall, D. A.; Inati, S. J.; Weber, R. T.; Un, S.; Prisner, T. F.; McDermott, A. E.; Fishbein, K. W.; Kreischer, K. E.; Temkin, R. J.; Singel, D. J.; Griffin, R. G., A spectrometer for dynamic nuclear polarization and electron paramagnetic resonance at high frequencies. *J. Magn. Reson. Ser. A.* **1995,** 117, 28-40.

101. Hu, J. Z.; Zhou, J. W.; Yang, B. L.; Li, L. Y.; Qiu, J. Q.; Ye, C. H.; Solum, M. S.; Wind, R. A.; Pugmire, R. J.; Grant, D. M., Dynamic nuclear polarization of nitrogen-15 in benzamide. *Solid State Nucl. Mag.* **1997,** 8, 129-137.

102. Butkovic, V.; Klasinc, L.; Bors, W., Kinetic study of flavonoid reactions with stable radicals. *J. Agr. Food Chem.* **2004,** 52, 2816-2820.

103. Lamb, R. C.; Pacifici, J. G.; Ayers, P. W., Organic Peroxides IV: Kinetics and products of decompositions of cyclohexaneformyl and isobutyryl peroxides: BDPA as a free-radical scavenger. *J. Am. Chem. Soc.* **1965,** 87, 3928-3935.

104. Iino, M.; Yanagisawa, T.; Takahashi, Y.; Matsuda, M., Studies of sulfonyl radicals III: Solvent effects on the thermal decomposition of benzyl phenylazosulfone. *B. Chem. Soc. Jpn.* **1976,** 49, 2272-2274.

105. Dane, E. L.; Swager, T. M., Carbanionic route to electroactive carbon-centered anion and radical oligomers. *Org. Lett.* **2010,** 12, 4324-4327.

106. Gorini, L.; Fabrizioli, M.; Mannini, M.; Sorace, L.; Yakovenko, A., Addressing single molecules of a thin magnetic film. *Inorg. Chim. Acta.* **2008,** 361, 4089-4093.

107. Goldfarb, D.; Lipkin, Y.; Potapov, A.; Gorodetsky, Y.; Epel, B.; Raitsimring, A. M.; Radoul, M.; Kaminker, I., HYSCORE and DEER with an upgraded 95 GHz pulse EPR spectrometer. *J. Magn. Reson.* **2008,** 194, 8-15.

108. Durkan, C.; Welland, M. E., Electronic spin detection in molecules using scanning-tunneling-microscopy-assisted electron-spin resonance. *Appl. Phys. Lett.* **2002,** 80, 458-460.

109. Koksharov, Y. A.; Bykov, I. V.; Malakho, A. P.; Polyakov, S. N.; Khomutov, G. B.; Bohr, J., Radicals as EPR probes of magnetization of gadolinium stearate Langmuir-Blodgett film. *Mat. Sci. Eng. C-Bio. S.* **2002,** 22, 201-207.

110. Ewald, A. H., Hydrogen-atom transfer reactions at high pressures. Reaction between mercaptans and diphenylpicrylhydrazyl. *T. Faraday Soc.* **1959,** 55, 792-7.

111. Essaidi, I.; Brahmi, Z.; Snoussi, A.; Koubaier, H. B.; Casabianca, H.; Abe, N.; El Omri, A.; Chaabouni, M. M.; Bouzouita, N., Phytochemical investigation of Tunisian Salicornia herbacea L., antioxidant, antimicrobial and cytochrome P450 (CYPs) inhibitory activities of its methanol extract. *Food Control.* **2013,** 32, 125-133.

112. Zhao, C.; Liu, Z. Q., Diaryl-1,2,4-oxadiazole antioxidants: Synthesis and properties of inhibiting the oxidation of DNA and scavenging radicals. *Biochimie.* **2013,** 95, 842-849.

113. Kowalska, I.; Jedrejek, D.; Ciesla, L.; Pecio, L.; Masullo, M.; Piacente, S.; Oleszek, W.; Stochmal, A., Isolation, chemical and free radical scavenging characterization of phenolics from Trifolium scabrum L. Aerial parts. *J. Agr. Food Chem.* **2013,** 61, 4417-4423.

114. Kim, T. S.; Yeo, J.; Kim, J. Y.; Kim, M. J.; Lee, J., Determination of the degree of oxidation in highly-oxidised lipids using profile changes of fatty acids. *Food Chem.* **2013,** 138, 1792-1799.

115. Lumata, L.; Merritt, M.; Khemtong, C.; Ratnakar, S. J.; van Tol, J.; Yu, L.; Song, L. K.; Kovacs, Z., The efficiency of DPPH as a polarising agent for DNP-NMR spectroscopy. *RSC Adv.* **2012,** 2, 12812-12817.

116. Schacher, G. E., Variation of nuclear spin polarization time with excitation of electron resonances. *Phys. Rev.* **1964,** 135, A185-A190.

117. Kolaczkowski, S. V.; Cardin, J. T.; Budil, D. E., Some remarks on reported inconsistencies in the high-field EPR spectrum of DPPH. *Appl. Magn. Reson.* **1999,** 16, 293-298.

118. Jang, Z. H.; Suh, B. J.; Corti, M.; Cattaneo, L.; Hajny, D.; Borsa, F.; Luban, M., Broadband electron spin resonance at low frequency without resonant cavity. *Rev. Sci. Instrum.* **2008,** 79, 046101-1-046101-3.

119. Hocherl, G.; Wolf, H. C., Zur konzentrationsabhangigkeit der elektronenspin-relaxationszeiten von diphenyl-picryl-hydrazyl in fester phase. *Z. Phys.* **1965,** 183, 341-351.

120. Goldsborough, J. P.; Mandel, M.; Pake, G. E., Influence of exchange interaction on paramagnetic relaxation times. *Phys. Rev. Lett.* **1960,** 4, 13-15.

121. Swanenberg, T. J. B.; Poulis, N. J.; Drewes, G. W. J., Dynamic polarization of protons in polystyrene. *Physica.* **1963,** 29, 713-720.

122. Yoshida, H.; Hayashi, K.; Okamura, S., Saturation phenomena of electron spin resonance of free radicals in polymers. *Ark. Kemi.* **1964,** 23, 177-189.

123. Turkevich, J.; Soria, J.; Che, M., Localization of energy in organic molecules as revealed by dynamic nuclear polarization of diphenylpicrylhydrazyl in polystyrene. *J. Chem. Phys.* **1972,** 56, 1463-1466.

124. Sato, H.; Bottle, S. E.; Blinco, J. P.; Micallef, A. S.; Eaton, G. R.; Eaton, S. S., Electron spin-lattice relaxation of nitroxyl radicals in temperature ranges that span glassy solutions to low-viscosity liquids. *J. Magn. Reson.* **2008,** 191, 66-77.

125. Brown, I. M., Molecular oxygen effects on the electron spin relaxation in a spin-labeled polystyrene. *J. Chem. Phys.* **1976,** 65, 630-638.

126. Eaton, S. S.; More, K. M.; Sawant, B. M.; Eaton, G. R., Use of the ESR half-field transition to determine the interspin distance and the orientation of the interspin vector in systems with two unpaired electrons. *J. Am. Chem. Soc.* **1983,** 105, 6560-6567.

127. Chandrasekar, S., Stochastic problems in physics and astronomy. *Rev. Modern Phys.* **1943,** 15, 1-89.

128. Atsarkin, V. A.; Demidov, V. V.; Vasneva, G. A., Metal-insulator transition in RbC_{60} polymer fulleride studied by ESR and electron-spin relaxation. *Phys. Rev. B.* **1997,** 56, 9448-9453.

129. van Gerven, L.; van Itterbeek, A.; De Laet, L., In *Paramagnetic Resonance*, Low, W., Ed. Academic Press, Inc.: New York, NY, 1963; pp 905-918.

130. Sato, H.; Kathirvelu, V.; Spagnol, G.; Rajca, S.; Rajca, A.; Eaton, S. S.; Eaton, G. R., Impact of electron-electron spin interaction on electron spin relaxation of nitroxide diradicals and tetraradical in glassy solvents between 10 and 300 K. *J. Phys. Chem. B.* **2008,** 112, 2818-2828.

131. Davids, D. A.; Wagner, P. E., Magnetic field dependence of paramagnetic relaxation in Kramers salt. *Phys. Rev. Lett.* **1964,** 12, 141-142.

132. Lumata, L. L.; Merritt, M. E.; Malloy, C. R.; Sherry, A. D.; van Tol, J.; Song, L. K.; Kovacs, Z., Dissolution DNP-NMR spectroscopy using galvinoxyl as a polarizing agent. *J. Magn. Reson.* **2013,** 227, 14-19.

133. Kirimli, H. E.; Peksoz, A., A low field proton-electron double resonance study for paramagnetic solutions. *Mol. Phys.* **2011,** 109, 337-350.

134. McPhail, D. B.; Gardner, P. T.; Duthie, G. G.; Steele, G. M.; Reid, K., Assessment of the antioxidant potential of Scotch whiskeys by electron spin resonance spectroscopy: Relationship to hydroxyl-containing aromatic components. *J. Agr. Food Chem.* **1999,** 47, 1937-1941.

135. Espinoza, M.; Olea-Azar, C.; Speisky, H.; Rodriguez, J., Determination of reactions between free radicals and selected Chilean wines and transition metals by ESR and UV-vis technique. *Spectrochim. Acta A.* **2009,** 71, 1638-1643.

136. Yamamoto, S.; Nakashima, Y.; Yoshikawa, J.; Wada, N.; Matsugo, S., Radical scavenging activity of the Japanese traditional food, amazake. *Food Sci. Technol. Res.* **2011,** 17, 209-218.

137. Ramadan, M. F.; Kroh, L. W.; Morsel, J. T., Radical scavenging activity of black cumin (Nigella sativa L.), coriander (Coriandrum sativum L.), and niger (Guizotia abyssinica Cass.) crude seed oils and oil fractions. *J. Agr. Food Chem.* **2003,** 51, 6961-6969.

138. Gardner, P. T.; McPhail, D. B.; Duthie, C. G., Electron spin resonance spectroscopic assessment of the antioxidant potential of teas in aqueous and organic media. *J. Sci. Food Agr.* **1998,** 76, 257-262.

139. Papadimitriou, V.; Sotiroudis, T. G.; Xenakis, A.; Sofikiti, N.; Stavyiannoudaki, V.; Chaniotakis, N. A., Oxidative stability and radical scavenging activity of extra virgin olive oils: An electron paramagnetic resonance spectroscopy study. *Anal. Chim. Acta.* **2006,** 573, 453-458.

140. Masuda, H.; Iwamoto, T.; Kabuto, C.; Kira, M., Unusual reactions of isolable dialkylgermylene and -stannylene with galvinoxyl radical. *Russ. Chem. B.* **2004,** 53, 1105-1108.

141. Ingleson, M. J.; Pink, M.; Fan, H.; Caulton, K. G., Redox chemistry of the triplet complex (PNP)Co. *J. Am. Chem. Soc.* **2008,** 130, 4262-4276.

142. Fukuzaki, E.; Takahashi, N.; Imai, S.; Nishide, H.; Rajca, A., Synthesis of dendritic, non-Kekule-, and nondisjoint-type trophenylmethanes terminated with galvinoxyl radicals. *Polym. J.* **2005,** 37, 284-293.

143. Nishide, H.; Hozumi, Y.; Nii, T.; Tsuchida, E., Poly(1,2-phenylenevinylene)s bearing nitronyl nitroxide and galvinoxyl at the 4-position: pi-conjugated and non-Kekule-type polyradicals with a triplet ground state. *Macromolecules.* **1997,** 30, 3986-3991.

144. Blank, A.; Levanon, H., Triplet radical interaction. Direct measurement of triplet polarization transfer by Fourier transform electron paramagnetic resonance. *J. Phys. Chem. A.* **2000,** 104, 794-800.

145. Kawai, A.; Watanabe, Y.; Shibuya, K., Time resolved ESR study on energy difference of quartet and doublet states in radical-triplet encounter pairs. *Mol. Phys.* **2002,** 100, 1225-1234.

146. Terazono, H.; Kawai, A.; Tsuji, K.; Shibuya, K., Enhanced intersystem crossings of S-1-T-1 and T-1-S-0 in coronene- and pyrene-galvinoxyl systems as studied by a pulsed ESR method. *J. Photoch. Photobio. A.* **2006,** 183, 22-30.

147. Shine, H. J., EPR and the history of the thianthrene cation radical. In *Foundations of Modern EPR*, Eaton, G. R.; Eaton, S. S.; Salikhov, K. M., Eds. World Scientific: River Edge, NJ, 1998; pp 202-212.

148. Corma, A.; Fornes, V.; Garcia, H.; Marti, V.; Miranda, M. A., Acid zeolites as electron acceptors: Use of thianthrene radical-cation as a probe. *Chem. Mater.* **1995,** 7, 2136-2143.

149. Mao, Y.; Thomas, J. K., Photoinduced electron transfer and subsequent chemical reactions of adsorbed thianthrene on clay surfaces. *J. Org. Chem.* **1993,** 58, 6641-6649.

150. Park, H. J.; Park, M. S.; Lee, T. H.; Park, K. H., Synthesis of 2-styrylbenzoxazole derivatives by the reaction of styrylphenolic Schiff bases with thianthrene cation radical. *J. Heterocyclic Chem.* **2013,** 50, 663-667.

151. Goldberg, H.; Kaminker, I.; Goldfarb, D.; Neumann, R., Oxidation of carbon monoxide cocatalyzed by palladium(0) and the $H_5PV_2Mo_{10}O_{40}$ polyoxometalate probed by electron paramagnetic resonance and aerobic catalysis. *Inorg. Chem.* **2009,** 48, 7947-7952.

152. Lembke, R. R.; Natarajan, L. V.; Kuntz, R. R., The extinction coefficient for the para-aminophenylthiyl radical as determined by reaction with galvinoxyl. *J. Photochem.* **1983,** 21, 157-166.

153. Boduszek, B.; Shine, H. J., Preparation of solid thianthrene cation radical tetrafluoroborate. *J. Org. Chem.* **1988,** 53, 5142-5143.

154. Owenius, R.; Eaton, G. R.; Eaton, S. S., Frequency (250 MHz to 9.2 GHz) and viscosity dependence of electron spin relaxation of triarylmethyl radicals at room temperature. *J. Magn. Reson.* **2005,** 172, 168-175.

155. Gomberg, M., An instance of trivalent carbon triphenylmethyl. *J. Am. Chem. Soc.* **1900,** 22, 757-771.

156. Lankamp, H.; Nauta, W. T.; Maclean, C., A new interpretation of monomer-dimer equilibrium of triphenylmethyl and alkyl-substituted diphenylmethyl radicals in solution. *Tetrahedron Lett.* **1968**, 249-254.

157. Biller, J. R.; Meyer, V.; Elajaili, H.; Rosen, G. M.; Kao, J. P. Y.; Eaton, S. S.; Eaton, G. R., Relaxation times and line widths of isotopically-substituted nitroxides in aqueous solution at X-band. *J. Magn. Reson.* **2011,** 212, 370-377.

158. Likhtenshtein, G. I.; Yamauchi, J.; Nakatsuji, S.; Smirnov, A. I.; Tamura, R., *Nitroxides: Applications in Chemistry, Biomedicine, and Materials Science*. John Wiley & Sons: Weinheim, 2008.

159. Rozantsev, E. G., *Free Nitroxyl Radicals*. Plenum Press: New York, NY, 1970.

160. Balakirev, M. Y.; Khramtsov, V. V.; Berezina, T. A.; Martin, V. V.; Volodarsky, L. B., The synthesis of amidine derivatives of imidazoline nitroxides - a new series of pH-sensitive spin probes. *Synthesis.* **1992,** 12, 1223-1225.

161. Foster, M. A.; Grigor'ev, I. A.; Lurie, D. J.; Khramtsov, V. V.; McCallum, S.; Panagiotelis, I.; Hutchison, J. M. S.; Koptioug, A.; Nicholson, I., In vivo detection of a pH-sensitive nitroxide in the rat stomach by low-field ESR-based techniques. *Magn. Reson. Med.* **2003,** 49, 558-567.

162. Kroll, C.; Herrmann, W.; Stosser, R.; Borchert, H. H.; Mader, K., Influence of drug treatment on the microacidity in rat and human skin: An in vitro electron spin resonance imaging study. *Pharm. Res.* **2001,** 18, 525-530.

163. Ilangovan, G.; Li, H. Q.; Zweier, J. L.; Kuppusamy, P., In vivo measurement of tumor redox environment using EPR spectroscopy. *Mol. Cell. Biochem.* **2002,** 234, 393-398.

164. Kinoshita, Y.; Yamada, K.; Yamasaki, T.; Mito, F.; Yamato, M.; Kosem, N.; Deguchi, H.; Shirahama, C.; Ito, Y.; Kitagawa, K.; Okukado, N.; Sakai, K.;

Utsumi, H., In vivo evaluation of novel nitroxyl radicals with reduction stability. *Free Radical Bio. Med.* **2010,** 49, 1703-1709.

165. Shen, J. G.; Liu, S. M.; Miyake, M.; Liu, W. L.; Pritchard, A.; Kao, J. P. Y.; Rosen, G. M.; Tong, Y.; Liu, K. J., Use of 3-acetoxymethoxycarhonyl-2,2,5,5-tetramethyl-1-pyrrolidinyloxyl as an EPR oximetry probe: Potential for in vivo measurement of tissue oxygenation in mouse brain. *Magn. Reson. Med.* **2006,** 55, 1433-1440.

166. Bobko, A. A.; Eubank, T. D.; Voorhees, J. L.; Efimova, O. V.; Kirilyuk, I. A.; Petryakov, S.; Trofimiov, D. G.; Marsh, C. B.; Zweier, J. L.; Grigor'ev, I. A.; Samouilov, A.; Khramtsov, V. V., In vivo monitoring of pH, redox status, and glutathione using L-band EPR for assessment of therapeutic effectiveness in solid tumors. *Magn. Reson. Med.* **2012,** 67, 1827-1836.

167. Komarov, D. A.; Dhimitruka, I.; Kirilyuk, I. A.; Trofimiov, D. G.; Grigor'ev, I. A.; Zweier, J. L.; Khramtsov, V. V., Electron paramagnetic resonance monitoring of ischemia-induced myocardial oxygen depletion and acidosis in isolated rat hearts using soluble paramagnetic probes. *Magn. Reson. Med.* **2012,** 68, 649-655.

168. Epel, B.; Halpern, H. J., Comparison of transverse and spin-lattice relaxation-based electron paramagnetic resonance oxygen images, *2011 IEEE International Symposium on Biomedical Imaging: From Nano to Macro*, Chicago, IL, 2011; pp 754-757.

169. Biller, J. R.; Meyer, V.; Elajaili, H.; Rosen, G. M.; Eaton, S. S.; Eaton, G. R., Frequency dependence of electron spin relaxation times in aqueous solution for a nitronyl nitroxide radical and perdeuterated-tempone between 250 MHz and 34 GHz. *J. Magn. Reson.* **2012,** 225, 52-57.

170. Biller, J. R.; Elajaili, H.; Meyer, V.; Rosen, G. M.; Eaton, S. S.; Eaton, G. R., Electron spin-lattice relaxation mechanisms of rapidly-tumbling nitroxide radicals. *J. Magn. Reson.* **2013,** 236, 47-56.

171. Burks, S. R.; Bakhshai, J.; Makowsky, M. A.; Muralidharan, S.; Tsai, P.; Rosen, G. M.; Kao, J. P. Y., H-2,N-15-substituted nitroxides as sensitive probes for electron paramagnetic resonance imaging. *J. Org. Chem.* **2010,** 75, 6463-6467.

172. Halpern, H. J.; Peric, M.; Nguyen, T. D.; Spencer, D. P.; Teicher, B. A.; Lin, Y. J.; Bowman, M. K., Selective isotopic labeling of a nitroxide spin label to enhance sensitivity for T_2 oxymetry. *J. Magn. Reson.* **1990,** 90, 40-51.

173. Ramasseul, R.; Rassat, A., Nitroxides XXXIII. Hindered pyrrolic nitroxide radicals: A stable pyrryloxyl. *B. Soc. Chim. Fr.* **1970**, 4330-41.

174. Percival, P. W.; Hyde, J. S., Saturation recovery measurements of spin-lattice relaxation times of some nitroxides in solution. *J. Magn. Reson.* **1976,** 23, 249-257.

175. Robinson, B. H.; Reese, A. W.; Gibbons, E.; Mailer, C., A unified description of the spin-spin and spin-lattice relaxation rates applied to nitroxide spin labels in viscous liquids. *J. Phys. Chem. B.* **1999,** 103, 5881-5894.

176. Popp, C. A.; Hyde, J. S., Electron-electron double resonance and saturation recovery studies of nitroxide electron and nuclear spin-lattice relaxation times and Heisenberg exchange rates: Lateral diffusion in dimyristoyl phosphatidylcholine. *Proc. Natl. Acad. Sci. U.S.A.* **1982,** 79, 2559-2563.

177. Van der Drift, E.; Rousseeuw, B. A. C.; Smidt, J., EPR and ELDOR studies on spin relaxation in perdeuterated 2,2,6,6-tetramethyl-4-piperidone N-oxide in liquid solutions. The slowly relaxing local structure mechanism. *J. Phys. Chem.* **1984,** 88, 2275-2284.

178. Robinson, B. H.; Haas, D. A.; Mailer, C., Molecular dynamics in liquids: Spin-lattice relaxation of nitroxide spin labels. *Science.* **1994,** 263, 490-493.

179. Hyde, J. S.; Yin, J. J.; Subczynski, W. K.; Camenisch, T. G.; Ratke, J. J.; Froncisz, W., Spin-label EPR T_1 values using saturation recovery from 2 to 35 GHz. *J. Phys. Chem. B.* **2004,** 108, 9524-9529.

180. Stevens, A. D.; Brivati, J. A., A 250 MHz EPR spectrometer with rapid phase-error correction for imaging large biological specimens. *Meas. Sci. Technol.* **1994,** 5, 793-796.

181. Quine, R. W.; Rinard, G. A.; Eaton, S. S.; Eaton, G. R., A pulsed and continuous wave 250 MHz electron paramagnetic resonance spectrometer. *Concept. Magn. Reson.* **2002,** 15, 59-91.

182. Volodarsky, L. B., *Imidazoline Nitroxides, Synthesis and Properties*. CRC Press: Boca Raton, FL, 1988; Vol. I.

183. Froncisz, W.; Camenisch, T. G.; Ratke, J. J.; Anderson, J. R.; Subczynski, W. K.; Strangeway, R. A.; Sidabras, J. W.; Hyde, J. S., Saturation recovery EPR and ELDOR at W-band for spin labels. *J. Magn. Reson.* **2008,** 193, 297-304.

184. Siri, D.; Gaudel-Siri, A.; Tordo, P., Conformational analysis of five-membered rings by molecular mechanics: Application to nitroxides. *J. Mol. Struc.-Theochem.* **2002,** 582, 171-185.

185. Altenbach, C.; Marti, T.; Khorana, H. G.; Hubbell, W. L., Transmembrane protein structure: Spin labeling of bacteriorhodopsin mutants. *Science.* **1990,** 248, 1088-1092.

186. Myers, W. K.; Xu, X. Z.; Li, C. M.; Lagerstedt, J. O.; Budamagunta, M. S.; Voss, J. C.; Britt, R. D.; Ames, J. B., Double electron-electron resonance probes Ca^{2+}-induced conformational changes and dimerization of recoverin. *Biochemistry.* **2013,** 52, 5800-5808.

187. White, E. A.; Raghuraman, H.; Perozo, E.; Glotzer, M., Binding of the CYK-4 subunit of the centralspindlin complex induces a large scale conformational change in the kinesin subunit. *J. Biol. Chem.* **2013,** 288, 19785-19795.

188. Pliotas, C.; Ward, R.; Branigan, E.; Rasmussen, A.; Hagelueken, G.; Huang, H. X.; Black, S. S.; Booth, I. R.; Schiemann, O.; Naismith, J. H., Conformational state of the MscS mechanosensitive channel in solution revealed by pulsed electron-electron double resonance (PELDOR) spectroscopy. *Proc. Natl. Acad. Sci. U.S.A.* **2012,** 109, E2675-E2682.

189. Lorigan, G. A., Probing the structure of membrane proteins with ESEEM and DEER pulsed EPR techniques. *Biophys. J.* **2012,** 102, 423A.

190. Sahu, I. D.; McCarrick, R. M.; Troxel, K. R.; Zhang, R. F.; Smith, H. J.; Dunagan, M. M.; Swartz, M. S.; Rajan, P. V.; Kroncke, B. M.; Sanders, C. R.; Lorigan, G. A., DEER EPR measurements for membrane protein structures via bifunctional spin labels and lipodisq nanoparticles. *Biochemistry.* **2013,** 52, 6627-6632.

191. Matalon, E.; Faingold, O.; Eisenstein, M.; Shai, Y.; Goldfarb, D., The topology, in model membranes, of the core peptide derived from the T-cell receptor transmembrane domain. *Chembiochem.* **2013,** 14, 1867-1875.

192. Wu, K. Q.; Shi, C. W.; Li, J.; Wang, H. P.; Shi, P.; Chen, L.; Wu, F. M.; Xiong, Y.; Tian, C. L., Efficient long-distance NMR-PRE and EPR-DEER restraints for two-domain protein structure determination. *Protein Cell.* **2013,** 4, 893-896.

193. Grohmann, D.; Klose, D.; Klare, J. P.; Kay, C. W. M.; Steinhoff, H. J.; Werner, F., RNA-binding to archaeal RNA polymerase subunits F/E: A DEER and FRET study. *J. Am. Chem. Soc.* **2010,** 132, 5954-5955.

194. Siddiqua, A.; Luo, Y.; Meyer, V.; Swanson, M. A.; Yu, X.; Wei, G. H.; Zheng, J.; Eaton, G. R.; Ma, B. Y.; Nussinov, R.; Eaton, S. S.; Margittai, M., Conformational basis for asymmetric seeding barrier in filaments of three- and four-repeat tau. *J. Am. Chem. Soc.* **2012,** 134, 10271-10278.

195. Meyer, V.; Dinkel, P. D.; Luo, Y.; Yu, X.; Wei, G.; Zheng, J.; Eaton, G. R.; Ma, B.; Nussinov, R.; Eaton, S. S.; Margittai, M., Single mutations in tau modulate the populations of fibril conformers through seed selection. *Angew. Chem. Int. Edit.* **2014,** 53, 1590-1593.

196. Lee, V. M. Y.; Goedert, M.; Trojanowski, J. Q., Neurodegenerative tauopathies. *Annu. Rev. Neurosci.* **2001,** 24, 1121-1159.

197. Spillantini, M. G.; Goedert, M., Tau pathology and neurodegeneration. *Lancet Neurol.* **2013,** 12, 609-622.

198. McKee, A. C.; Cantu, R. C.; Nowinski, C. J.; Hedley-Whyte, E. T.; Gavett, B. E.; Budson, A. E.; Santini, V. E.; Lee, H. S.; Kubilus, C. A.; Stern, R. A., Chronic traumatic encephalopathy in athletes: Progressive tauopathy after repetitive head injury. *J. Neuropath. Exp. Neur.* **2009,** 68, 709-735.

199. McKee, A. C.; Stein, T. D.; Nowinski, C. J.; Stern, R. A.; Daneshvar, D. H.; Alvarez, V. E.; Lee, H. S.; Hall, G.; Wojtowicz, S. M.; Baugh, C. M.; Riley, D. O.; Kubilus, C. A.; Cormier, K. A.; Jacobs, M. A.; Martin, B. R.; Abraham, C. R.; Ikezu, T.; Reichard, R. R.; Wolozin, B. L.; Budson, A. E.; Goldstein, L. E.; Kowall, N. W.; Cantu, R. C., The spectrum of disease in chronic traumatic encephalopathy. *Brain.* **2013,** 136, 43-64.

200. Weingarten, M. D.; Lockwood, A. H.; Hwo, S. Y.; Kirschner, M. W., Protein factor essential for microtubule assembly. *Proc. Natl. Acad. Sci. U.S.A.* **1975,** 72, 1858-1862.

201. Drechsel, D. N.; Hyman, A. A.; Cobb, M. H.; Kirschner, M. W., Modulation of the dynamic instability of tubulin assembly by the microtubule-associated protein tau. *Mol. Biol. Cell.* **1992,** 3, 1141-1154.

202. Goedert, M.; Jakes, R., Expression of separate isoforms of human tau protein: Correlation with the tau pattern in brain and effects on tubulin polymerization. *EMBO J.* **1990,** 9, 4225-4230.

203. Andronesi, O. C.; von Bergen, M.; Biernat, J.; Seidel, K.; Griesinger, C.; Mandelkow, E.; Baldus, M., Characterization of Alzheimer's-like paired helical filaments from the core domain of tau protein using solid-state NMR spectroscopy. *J. Am. Chem. Soc.* **2008,** 130, 5922-5928.

204. Cleveland, D. W.; Hwo, S. Y.; Kirschner, M. W., Physical and chemical properties of purified tau factor and role of tau in microtubule assembly. *J. Mol. Biol.* **1977,** 116, 227-247.

205. Sergeant, N.; David, J. P.; Lefranc, D.; Vermersch, P.; Wattez, A.; Delacourte, A., Different distribution of phosphorylated tau protein isoforms in Alzheimer's and Pick's diseases. *FEBS Lett.* **1997,** 412, 578-582.

206. Connell, J. W.; Rodriguez-Martin, T.; Gibb, G. M.; Kahn, N. M.; Grierson, A. J.; Hanger, D. P.; Revesz, T.; Lantos, P. L.; Anderton, B. H.; Gallo, J. M., Quantitative analysis of tau isoform transcripts in sporadic tauopathies. *Mol. Brain Res.* **2005,** 137, 104-109.

207. Takanashi, M.; Mori, H.; Arima, K.; Mizuno, Y.; Hattori, N., Expression patterns of tau mRNA isoforms correlate with susceptible lesions in progressive supranuclear palsy and corticobasal degeneration. *Mol. Brain Res.* **2002,** 104, 210-219.

208. Sutherland, G. T.; Nowak, G.; Halliday, G. M.; Kril, J. J., Tau isoform expression in frontotemporal dementia without tau deposition. *J. Clin. Neurosci.* **2007,** 14, 1182-1185.

209. Dinkel, P. D.; Siddiqua, A.; Huynh, H.; Shah, M.; Margittai, M., Variations in filament conformation dictate seeding barrier between three- and four-repeat tau. *Biochemistry.* **2011,** 50, 4330-4336.

210. Hattori, M.; Hashizume, Y.; Yoshida, M.; Iwasaki, Y.; Hishikawa, N.; Ueda, R.; Ojika, K., Distribution of astrocytic plaques in the corticobasal degeneration brain and comparison with tuft-shaped astrocytes in the progressive supranuclear palsy brain. *Acta Neuropatho.* **2003,** 106, 143-149.

211. Goedert, M.; Jakes, R.; Spillantini, M. G.; Hasegawa, M.; Smith, M. J.; Crowther, R. A., Assembly of microtubule-associated protein tau into Alzheimer-like filaments induced by sulphated glycosaminoglycans. *Nature.* **1996,** 383, 550-553.

212. Berriman, J.; Serpell, L. C.; Oberg, K. A.; Fink, A. L.; Goedert, M.; Crowther, R. A., Tau filaments from human brain and from in vitro assembly of recombinant protein show cross-beta structure. *Proc. Natl. Acad. Sci. U.S.A.* **2003,** 100, 9034-9038.

213. Friedhoff, P.; von Bergen, M.; Mandelkow, E. M.; Davies, P.; Mandelkow, E., A nucleated assembly mechanism of Alzheimer paired helical filaments. *Proc. Natl. Acad. Sci. U.S.A.* **1998,** 95, 15712-15717.

214. Kuret, J.; Congdon, E. E.; Li, G. B.; Yin, H. H.; Yu, X.; Zhong, Q., Evaluating triggers and enhancers of tau fibrillization. *Micros. Res. Techniq.* **2005,** 67, 141-155.

215. Abisambra, J.; Jinwal, U. K.; Miyata, Y.; Rogers, J.; Blair, L.; Li, X.; Seguin, S. P.; Wang, L.; Jin, Y.; Bacon, J.; Brady, S.; Cockman, M.; Guidi, C.; Zhang, J.; Koren, J.; Young, Z. T.; Atkins, C. A.; Zhang, B.; Lawson, L. Y.; Weeber, E. J.; Brodsky, J. L.; Gestwicki, J. E.; Dickey, C. A., Allosteric heat shock protein 70 inhibitors rapidly rescue synaptic plasticity deficits by reducing aberrant tau. *Biol. Psychiat.* **2013,** 74, 367-374.

216. Carman, A.; Kishinevsky, S.; Koren, J.; Luo, W. J.; Chiosis, G., Regulatory chaperone complexes in neurodegenerative diseases: A perspective on therapeutic intervention. *Curr. Alzheimer Res.* **2014,** 11, 59-68.

217. Farid, M.; Corbo, C. P.; Alonso, A. D. C., Tau binds ATP and induces its aggregation. *Micros. Res. Techniq.* **2014,** 77, 133-137.

218. Daebel, V.; Chinnathambi, S.; Biernat, J.; Schwalbe, M.; Habenstein, B.; Loquet, A.; Akoury, E.; Tepper, K.; Muller, H.; Baldus, M.; Griesinger, C.; Zweckstetter, M.; Mandelkow, E.; Vijayan, V.; Lange, A., Beta-sheet core of tau paired helical filaments revealed by solid-state NMR. *J. Am. Chem. Soc.* **2012,** 134, 13982-13989.

219. Sibille, N.; Huvent, I.; Fauquant, C.; Verdegem, D.; Amniai, L.; Leroy, A.; Wieruszeski, J. M.; Lippens, G.; Landrieu, I., Structural characterization by nuclear magnetic resonance of the impact of phosphorylation in the proline-rich region of the disordered tau protein. *Proteins.* **2012,** 80, 454-462.

220. Jeganathan, S.; von Bergen, M.; Brutlach, H.; Steinhoff, H. J.; Mandelkow, E., Global hairpin folding of tau in solution. *Biochemistry.* **2006,** 45, 2283-2293.

221. Kirschner, D. A.; Abraham, C.; Selkoe, D. J., X-ray diffraction from intraneuronal paired helical filaments and extraneuronal amyloid fibers in Alzheimer-disease indicates cross-beta conformation. *Proc. Natl. Acad. Sci. U.S.A.* **1986,** 83, 503-507.

222. von Bergen, M.; Barghorn, S.; Biernat, J.; Mandelkow, E. M.; Mandelkow, E., Tau aggregation is driven by a transition from random coil to beta sheet structure. *BBA-Mol. Basis Dis.* **2005,** 1739, 158-166.

223. Uversky, V. N.; Winter, S.; Galzitskaya, O. V.; Kittler, L.; Lober, G., Hyperphosphorylation induces structural modification of tau protein. *FEBS Lett.* **1998,** 439, 21-25.

224. Pollanen, M. S.; Markiewicz, P.; Bergeron, C.; Goh, M. C., Twisted ribbon structure of paired helical filaments revealed by atomic-force microscopy. *Am. J. Pathol.* **1994,** 144, 869-873.

225. Margittai, M.; Langen, R., Fibrils with parallel in-register structure constitute a major class of amyloid fibrils: Molecular insights from electron paramagnetic resonance spectroscopy. *Q. Rev. Biophys.* **2008,** 41, 265-297.

226. Karyagina, I.; Becker, S.; Giller, K.; Riedel, D.; Jovin, T. M.; Griesinger, C.; Bennati, M., Electron paramagnetic resonance spectroscopy measures the distance between the external beta-strands of folded alpha-synuclein in amyloid fibrils. *Biophys. J.* **2011,** 101, L1-L3.

227. Pornsuwan, S.; Giller, K.; Riedel, D.; Becker, S.; Griesinger, C.; Bennati, M., Long-range distances in amyloid fibrils of alpha-synuclein from PELDOR spectroscopy. *Angew. Chem. Int. Edit.* **2013,** 52, 10290-10294.

228. Bedrood, S.; Li, Y. Y.; Isas, J. M.; Hegde, B. G.; Baxa, U.; Haworth, I. S.; Langen, R., Fibril structure of human islet amyloid polypeptide. *J. Biol. Chem.* **2012,** 287, 5235-5241.

229. Barghorn, S.; Mandelkow, E., Toward a unified scheme for the aggregation of tau into Alzheimer paired helical filaments. *Biochemistry.* **2002,** 41, 14885-14896.

230. Berliner, L. J.; Grunwald, J.; Hankovszky, H. O.; Hideg, K., A novel reversible thiol-specific spin label: Papain active-site labeling and inhibition. *Anal. Biochem.* **1982,** 119, 450-455.

231. Guo, J. L.; Lee, V. M., Seeding of normal tau by pathological tau conformers drives pathogenesis of Alzheimer-like tangles. *J. Biol. Chem.* **2011,** 286, 15317-15331.

232. Rizzu, P.; Van Swieten, J. C.; Joosse, M.; Hasegawa, M.; Stevens, M.; Tibben, A.; Niermeijer, M. F.; Hillebrand, M.; Ravid, R.; Oostra, B. A.; Goedert, M.; van Duijn, C. M.; Heutink, P., High prevalence of mutations in the microtubule-associated protein tau in a population study of frontotemporal dementia in the Netherlands. *Am. J. Hum. Genet.* **1999,** 64, 414-421.

233. Bugiani, O.; Murrell, J. R.; Giaccone, G.; Hasegawa, M.; Ghigo, G.; Tabaton, M.; Morbin, M.; Primavera, A.; Carella, F.; Solaro, C.; Grisoli, M.; Savoiardo, M.; Spillantini, M. G.; Tagliavini, F.; Goedert, M.; Ghetti, B., Frontotemporal dementia and corticobasal degeneration in a family with a P301S mutation in tau. *J. Neuropath. Exp. Neur.* **1999,** 58, 667-677.

234. Goedert, M.; Jakes, R.; Crowther, R. A., Effects of frontotemporal dementia FTDP-17 mutations on heparin-induced assembly of tau filaments. *FEBS Lett.* **1999,** 450, 306-311.

235. Rosso, S. M.; van Herpen, E.; Deelen, W.; Kamphorst, W.; Severijnen, L. A.; Willemsen, R.; Ravid, R.; Niermeijer, M. F.; Dooijes, D.; Smith, M. J.; Goedert, M.; Heutink, P.; van Swieten, J. C., A novel tau mutation, S320F, causes a tauopathy with inclusions similar to those in Pick's disease. *Ann. Neurol.* **2002,** 51, 373-376.

236. Pickering-Brown, S. M.; Baker, M.; Nonaka, T.; Ikeda, K.; Sharma, S.; Mackenzie, J.; Simpson, S. A.; Moore, J. W.; Snowden, J. S.; de Silva, R.; Revesz, T.; Hasegawa, M.; Hutton, M.; Mann, D. M. A., Frontotemporal dementia with Pick-type histology associated with Q336R mutation in the tau gene. *Brain.* **2004,** 127, 1415-1426.

237. Gustke, N.; Trinczek, B.; Biernat, J.; Mandelkow, E. M.; Mandelkow, E., Domains of tau protein and interactions with microtubules. *Biochemistry*. **1994,** 33, 9511-9522.

238. Wintjens, R.; Wieruszeski, J. M.; Drobecq, H.; Rousselot-Pailley, P.; Buee, L.; Lippens, G.; Landrieu, I., H-1 NMR study on the binding of Pin1 Trp-Trp domain with phosphothreonine peptides. *J. Biol. Chem.* **2001,** 276, 25150-25156.

239. Spillantini, M. G.; Van Swieten, J. C.; Goedert, M., Tau gene mutations in frontotemporal dementia and parkinsonism linked to chromosome 17 (FTDP-17). *Neurogenetics.* **2000,** 2, 193-205.

240. Collinge, J.; Clarke, A. R., A general model of prion strains and their pathogenicity. *Science.* **2007,** 318, 930-936.

241. Angers, R. C.; Kang, H. E.; Napier, D.; Browning, S.; Seward, T.; Mathiason, C.; Balachandran, A.; McKenzie, D.; Castilla, J.; Soto, C.; Jewell, J.; Graham, C.; Hoover, E. A.; Telling, G. C., Prion strain mutation determined by prion protein conformational compatibility and primary structure. *Science.* **2010,** 328, 1154-1158.

242. Lu, J. X.; Qiang, W.; Yau, W. M.; Schwieters, C. D.; Meredith, S. C.; Tycko, R., Molecular structure of beta-amyloid fibrils in Alzheimer's disease brain tissue. *Cell.* **2013,** 154, 1257-1268.

243. Tanaka, M.; Collins, S. R.; Toyama, B. H.; Weissman, J. S., The physical basis of how prion conformations determine strain phenotypes. *Nature.* **2006,** 442, 585-589.

244. Campioni, S.; Mannini, B.; Zampagni, M.; Pensalfini, A.; Parrini, C.; Evangelisti, E.; Relini, A.; Stefani, M.; Dobson, C. M.; Cecchi, C.; Chiti, F., A

causative link between the structure of aberrant protein oligomers and their toxicity. *Nat. Chem. Biol.* **2010,** 6, 140-147.

245. Du, J. L.; Eaton, G. R.; Eaton, S. S., Temperature, orientation, and solvent dependence of electron spin-lattice relaxation rates for nitroxyl radicals in glassy solvents and doped solids. *J. Magn. Reson. Ser. A.* **1995,** 115, 213-221.

246. Mentink-Vigier, F.; Collauto, A.; Feintuch, A.; Kaminker, I.; Le, V. T.; Goldfarb, D., Increasing sensitivity of pulse EPR experiments using echo train detection schemes. *J. Magn. Reson.* **2013,** 236, 117-125.

247. Richard, W.; Bowman, A.; Sozudogru, E.; El-Mkami, H.; Owen-Hughes, T.; Norman, D. G., EPR distance measurements in deuterated proteins. *J. Magn. Reson.* **2010,** 207, 164-167.

248. Raitsimring, A.; Astashkin, A. V.; Enemark, J. H.; Kaminker, I.; Goldfarb, D.; Walter, E. D.; Song, Y.; Meade, T. J., Optimization of pulsed-DEER measurements for Gd-based labels: Choice of operational frequencies, pulse durations and positions, and temperature. *Appl. Magn. Reson.* **2013,** 44, 649-670.

249. Banerjee, D.; Yagi, H.; Huber, T.; Otting, G.; Goldfarb, D., Nanometer-range distance measurement in a protein using Mn^{2+} tags. *J. Phys. Chem. Lett.* **2012,** 3, 157-160.

250. Borbat, P. P.; Georgieva, E. R.; Freed, J. H., Improved sensitivity for long-distance measurements in biomolecules: Five-pulse double electron-electron resonance. *J. Phys. Chem. Lett.* **2013,** 4, 170-175.

251. Lovett, J. E.; Lovett, B. W.; Harmer, J., DEER-Stitch: Combining three- and four-pulse DEER measurements for high sensitivity, deadtime free data. *J. Magn. Reson.* **2012,** 223, 98-106.

252. von Hagens, T.; Polyhach, Y.; Sajid, M.; Godt, A.; Jeschke, G., Suppression of ghost distances in multiple-spin double electron-electron resonance. *Phys. Chem. Chem. Phys.* **2013,** 15, 5854-5866.

253. Zecevic, A.; Eaton, G. R.; Eaton, S. S.; Lindgren, M., Dephasing of electron spin echoes for nitroxyl radicals in glassy solvents by non-methyl and methyl protons. *Mol. Phys.* **1998,** 95, 1255-1263.

254. Fernandez, I.; Ubach, J.; Dulubova, I.; Zhang, X.; Sudhof, T. C.; Rizo, J., Three-dimensional structure of an evolutionarily conserved N-terminal domain of syntaxin 1A. *Cell.* **1998,** 94, 841-849.

255. Lerman, J. C.; Robblee, J.; Fairman, R.; Hughson, F. M., Structural analysis of the neuronal SNARE protein syntaxin 1A. *Biochemistry.* **2000,** 39, 8470-8479.

256. Dulubova, I.; Sugita, S.; Hill, S.; Hosaka, M.; Fernandez, I.; Sudhof, T. C.; Rizo, J., A conformational switch in syntaxin during exocytosis: Role of munc18. *EMBO J.* **1999,** 18, 4372-4382.

257. Richmond, J. E.; Weimer, R. M.; Jorgensen, E. M., An open form of syntaxin bypasses the requirement for UNC-13 in vesicle priming. *Nature.* **2001,** 412, 338-341.

258. Margittai, M.; Fasshauer, D.; Jahn, R.; Langen, R., The Habc domain and the SNARE core complex are connected by a highly flexible linker. *Biochemistry.* **2003,** 42, 4009-4014.

259. Bracher, A.; Weissenhorn, W., Crystal structure of the Habc domain of neuronal syntaxin from the squid Loligo pealei reveals conformational plasticity at its C-terminus. *BMC Struct. Biol.* **2004,** 4, 6.

260. Matthews, B. W.; Remington, S. J.; Grutter, M. G.; Anderson, W. F., Relation between hen egg-white lysozyme and bacteriophage T4 lysozyme: Evolutionary implications. *J. Mol. Biol.* **1981,** 147, 545-558.

261. Matthews, B. W.; Dahlquis, F. W.; Maynard, A. Y., Crystallographic data for lysozyme from bacteriophage T4. *J. Mol. Biol.* **1973,** 78, 575-576.

262. Matthews, B. W.; Remington, S. J., 3-dimensional structure of lysozyme from bacteriophage T4. *Proc. Natl. Acad. Sci. U.S.A.* **1974,** 71, 4178-4182.

263. Matthews, B. W.; Remington, S. J., Structure of lysozyme from bacteriophage T4. *Acta Crystallogr. A.* **1975,** 31, S25.

264. Langen, R.; Oh, K. J.; Cascio, D.; Hubbell, W. L., Crystal structures of spin labeled T4 lysozyme mutants: Implications for the interpretation of EPR spectra in terms of structure. *Biochemistry.* **2000,** 39, 8396-8405.

265. Razzaghi, S.; Brooks, E. K.; Bordignon, E.; Hubbell, W. L.; Yulikov, M.; Jeschke, G., EPR relaxation-enhancement-based distance measurements on orthogonally spin-labeled T4 lysozyme. *Chembiochem.* **2013,** 14, 1883-1890.

266. Jacobsen, K.; Risse, T., Structural changes of T4 lysozyme upon adsorption to planar surfaces as monitored by EPR spectroscopy. *Biophys. J.* **2005,** 88, 158A.

267. Pyka, J.; Ilnicki, J.; Altenbach, C.; Hubbell, W. L.; Froncisz, W., Accessibility and dynamics of nitroxide side chains in T4 lysozyme measured by saturation recovery EPR. *Biophys. J.* **2005,** 89, 2059-2068.

268. Islam, S. M.; Stein, R. A.; McHaourab, H. S.; Roux, B., Structural refinement from restrained-ensemble simulations based on EPR/DEER data: Application to T4 lysozyme. *J. Phys. Chem. B.* **2013,** 117, 4740-4754.

269. Selva, C.; Malferrari, M.; Ballardini, R.; Ventola, A.; Francia, F.; Venturoli, G., Trehalose preserves the integrity of lyophilized phycoerythrin-antihuman CD8 antibody conjugates and enhances their thermal stability in flow cytometric assays. *J. Pharm. Sci.* **2013,** 102, 649-659.

270. Sundaramurthi, P.; Suryanarayanan, R., Influence of crystallizing and non-crystallizing cosolutes on trehalose crystallization during freeze-drying. *Pharm. Res.* **2010,** 27, 2384-2393.

271. Borbat, P. P.; McHaourab, H. S.; Freed, J. H., Protein structure determination using long-distance constraints from double-quantum coherence ESR: Study of T4 lysozyme. *J. Am. Chem. Soc.* **2002,** 124, 5304-5314.

272. Banham, J. E.; Jeschke, G.; Timmel, C. R., Evidence from EPR that nitroxide spin labels attached to human hemoglobin alter their conformation upon freezing. *Mol. Phys.* **2007,** 105, 2041-2047.

273. Jeschke, G.; Sajid, M.; Schulte, M.; Godt, A., Three-spin correlations in double electron-electron resonance. *Phys. Chem. Chem. Phys.* **2009,** 11, 6580-6591.

274. Siddiqua, A.; Margittai, M., Three- and four-repeat tau coassemble into heterogeneous filaments: An implication for Alzheimer's disease. *J. Biol. Chem.* **2010,** 285, 37920-37926.

275. Newby, G. A.; Lindquist, S., Blessings in disguise: Biological benefits of prion-like mechanisms. *Trends Cell Biol.* **2013,** 23, 251-259.

276. Costanzo, M.; Zurzolo, C., The cell biology of prion-like spread of protein aggregates: Mechanisms and implication in neurodegeneration. *Biochem. J.* **2013,** 452, 1-17.

277. Saborio, G. P.; Permanne, B.; Soto, C., Sensitive detection of pathological prion protein by cyclic amplification of protein misfolding. *Nature.* **2001,** 411, 810-813.

278. Morales, R.; Duran-Aniotz, C.; Diaz-Espinoza, R.; Camacho, M. V.; Soto, C., Protein misfolding cyclic amplification of infectious prions. *Nat. Protoc.* **2012,** 7, 1397-1409.

279. Deleault, N. R.; Harris, B. T.; Rees, J. R.; Supattapone, S., Formation of native prions from minimal components in vitro. *Proc. Natl. Acad. Sci. U.S.A.* **2007,** 104, 9741-9746.

280. Castilla, J.; Saa, P.; Hetz, C.; Soto, C., In vitro generation of infectious scrapie prions. *Cell.* **2005,** 121, 195-206.

281. Garza, M. C.; Fernandez-Borges, N.; Bolea, R.; Badiola, J. J.; Castilla, J.; Monleon, E., Detection of PrPres in genetically susceptible fetuses from sheep with natural scrapie. *Plos One.* **2011,** 6, 1-5.

282. Castilla, J.; Gonzalez-Romero, D.; Saa, P.; Morales, R.; De Castro, J.; Soto, C., Crossing the species barrier by PrP(Sc) replication in vitro generates unique infectious Prions. *Cell.* **2008,** 134, 757-768.

283. Chianini, F.; Fernandez-Borges, N.; Vidal, E.; Gibbard, L.; Pintadoe, B.; de Castro, J.; Priola, S. A.; Hamilton, S.; Eaton, S. L.; Finlayson, J.; Pang, Y.; Steele, P.; Reid, H. W.; Dagleish, M. P.; Castilla, J., Rabbits are not resistant to prion infection. *Proc. Natl. Acad. Sci. U.S.A.* **2012,** 109, 5080-5085.

284. Castilla, J.; Saa, P.; Soto, C., Detection of prions in blood. *Nat. Med.* **2005,** 11, 982-985.

285. Sugino, E.; Nishiura, C.; Minoura, K.; In, Y.; Sumida, M.; Taniguchi, T.; Tomoo, K.; Ishida, T., Three-/four-repeat-dependent aggregation profile of tau microtubule-binding domain clarified by dynamic light scattering analysis. *Biochem. Bioph. Res. Co.* **2009,** 385, 236-240.

286. Gonzalez-Romero, D.; Barria, M. A.; Leon, P.; Morales, R.; Soto, C., Detection of infectious prions in urine. *FEBS Lett.* **2008,** 582, 3161-3166.

287. Saa, P.; Castilla, J.; Soto, C., Ultra-efficient replication of infectious prions by automated protein misfolding cyclic amplification. *J. Biol. Chem.* **2006,** 281, 35245-35252.

288. Friedhoff, P.; Schneider, A.; Mandelkow, E. M.; Mandelkow, E., Rapid assembly of Alzheimer-like paired helical filaments from microtubule-associated protein tau monitored by fluorescence in solution. *Biochemistry.* **1998,** 37, 10223-10230.

289. Coste, J., An overview of the diagnostic tools. *Transfus. Clin. Biol.* **2013,** 20, 412-415.

290. Zhou, P.; Luo, Q. Y.; Lin, Y.; Chen, L.; Li, S.; Zhou, G. H.; Ji, X. H.; He, Z. K., Immunoassays with protein misfolding cycle amplification: A platform for ultrasensitive detection of antigen. *Anal. Chem.* **2012,** 84, 7343-7349.

291. Maruyama, M.; Shimada, H.; Suhara, T.; Shinotoh, H.; Ji, B.; Maeda, J.; Zhang, M. R.; Trojanowski, J. Q.; Lee, V. M. Y.; Ono, M.; Masamoto, K.; Takano, H.; Sahara, N.; Iwata, N.; Okamura, N.; Furumoto, S.; Kudo, Y.; Chang, Q.; Saido, T. C.; Takashima, A.; Lewis, J.; Jang, M. K.; Aoki, I.; Ito, H.; Higuchi, M., Imaging of tau pathology in a tauopathy mouse model and in Alzheimer patients compared to normal controls. *Neuron.* **2013,** 79, 1094-1108.

Appendix A: Site-directed Mutagenesis QuikChange Protocol

Detailed instructions are available at the Agilent website (accessed on 3/18/2014): http://www.chem.agilent.com/library/usermanuals/Public/200518.pdf

Materials:

- 10X reaction buffer: 100 mM KCl, 100 mM $(NH_4)_2SO_4$, 200 mM Tris-HCl pH 8.8, 20 mM $MgSO_4$, 1% Triton X-100, 1 mg/mL BSA
- dNTP mix: proprietary
- PFU ultra DNA polymerase, 2.5 U/μL
- DpnI restriction enzyme, 10 U/μL
- XL1-Blue supercompetent *E. coli*
- EB buffer: 10 mM Tris-HCl pH 8.5
- Xho1 and Nco1 restriction enzymes
- BL21 (DE3) competent *E. coli*

Protocol (QuickChange to protein expression):

1. 5 ng/μL plasmid DNA (K18 311/328, see Section 7.3.1) was added with 4 pM forward and reverse primers to master mix containing 10X reaction buffer, dNTP, and PFU ultra in a 200 μL PCR tube.

2. PCR was performed using a melting temperature of 95 °C for 30 seconds, an annealing temperature of 56 ± 2 °C for one minute, and an extension temperature of 68 °C for 12 minutes. Cycling was repeated 18 times.

3. 1 μL DpnI was added to the PCR product and incubated at 37 °C for two hours. This digests and eliminates the non-mutated original DNA.

4. Mutated DNA was transformed into XL1-Blue supercompetent cells.

5. Resulting colonies were amplified and the DNA collected using the Midiprep protocol (Appendix B).

6. 100 ± 20 μL EB buffer was added to the dried DNA and concentrations were found by absorption at 260 nm using the ratio 50 μg/mL = 1.0 a.u.

7. The insert containing the mutated protein sequence was isolated by incubating DNA with Xho1 and Nco1 restriction enzymes at 37 °C for one hour.

8. The resulting cleaved DNA was visualized on an agarose gel, and the MW of the inserts were checked for accuracy (see Figure 7.2).

9. Following sequence confirmation, mutated DNA was transformed into BL21 (DE3) competent cells for expression.

Appendix B: Midiprep Protocol

Detailed instructions can be downloaded at the QIAGEN website (accessed on 3/18/2014): http://www.qiagen.com/knowledge-and-support/resource-center/resource-download.aspx?id=46205595-0440-459e-9d93-50eb02e5707e&lang=en

Materials:

- Buffer P1 (resuspension): 50 mM Tris-HCl pH 8.0, 10 mM EDTA, 100 μg/mL RNase A
- Buffer P2 (lysis): 200 mM NaOH, 1% SDS
- Buffer P3 (neutralization): 3.0 M KCH_3CO_2
- Buffer QBT (equilibration): 750 mM NaCl, 50 mM MOPS pH 7.0, 15% isopropanol, 0.15% Triton X-100
- Buffer QC (wash): 1.0 M NaCl, 50 mM MOPS pH 7.0, 15% isopropanol
- Buffer QF (elution): 1.25 M NaCl, 50 mM Tris-HCl pH 8.5, 15% isopropanol
- QIAGEN-tip column

Protocol:

1. A single colony of XL1-Blue *E. coli* containing the DNA of interest was grown under agitation for 16-17 hours at 37 °C in 50 mL LB medium containing 30 mg/mL kanamycin.

2. Bacterial cells were centrifuged at 6000 X g for 15 minutes at 4 °C, and the pellet was resuspended in 4 mL Buffer P1.

3. 4 mL Buffer P2 was added to resuspended pellet, mixed gently, and incubated at room temperature for five minutes.

4. 4 mL Buffer P3 was added and mixed thoroughly, followed by incubation on ice for 15 minutes.

5. Mixture was centrifuged at 20,000 X g for 30 minutes at 4 °C. Supernatant was centrifuged again for 15 minutes to ensure exclusion of pellet from column.

6. QIAGEN-tip column was equilibrated by addition of 4 mL Buffer QBT. Supernatant was applied to QIAGEN-tip column, which was then washed twice with 10 mL Buffer QC. DNA eluted from the column with 5 mL Buffer QF.

7. DNA precipitated through addition of 3.5 mL isopropanol. This was immediately centrifuged at 15,000 X g for 30 minutes at 4 °C. Pellet was washed with 1.8 mL 70% ethanol and transferred into a 2 mL Eppendorf vial. This was again centrifuged at 15,000 X g for 10 minutes at 4 °C.

8. Supernatant was discarded and pellet air dried fully before addition of EB buffer.

Appendix C: BCA Assay Protocol

Detailed instructions are available at the Pierce website (accessed on 3/18/2014): http://www.piercenet.com/instructions/2161296.pdf

Materials:

- Reagent A: Na_2CO_3, $NaHCO_3$, bicinchoninic acid (BCA, $C_{20}H_{12}N_2O_4$), sodium tartrate ($Na_2C_2H_4O_6$) in 0.1 M NaOH
- Reagent B: 4% $CuSO_4$
- Albumin standard: 2 mg/mL in 0.9% saline, 0.05% NaN_3

Protocol:

1. Working reagent was prepared by mixing 18 mL Reagent A with 350 µL Reagent B. The color changes from blue to green due to complexation of the Cu^{2+}.

2. A calibration curve was prepared with the Albumin standard (below).

3. 85 µL sample (standard curve and unknown(s)) was added to 1.8 mL working reagent. This mixture was incubated for 30 minutes at 37 °C. The observed color change is associated with reduction of Cu^{2+}. Reduction is initiated through coordination of Cu^{2+} with the peptide backbone. Binding is proportional to the number of amino acids present, and the peptide must be at least 3 amino acids in length.

4. The color change was quantified by UV-Vis absorbance at 562 nm. The best fit to the calibration curve is used to calculate the concentration of unknown protein.

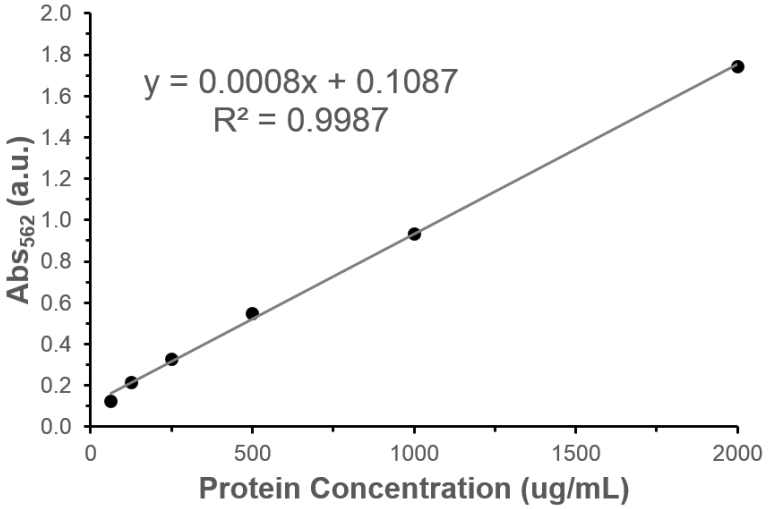

Appendix D: Publications, University of Denver 2011-2014

Meyer, V.; Dinkel, P.D.; Luo, Y.; Yu, G.; Wei, G.; Zheng, J.; Eaton, G.R.; Ma, B.; Nussinov, R.; Eaton, S.S.; Margittai, M., Single mutations in tau modulate the conformational ensemble of fibrils through seed selection, *Angew. Chem. Int. Edit.* **2014**, 53, 1590-1593.

Biller, J.R.; Elajaili, H.; Meyer, V.; Rosen, G.M.; Eaton, S.S.; Eaton, G.R., Electron spin lattice relaxation mechanisms of rapidly-tumbling nitroxide radicals, *J. Magn. Reson.* **2013,** 236, 47-56.

Mitchell, D.G.; Tseitlin, M.; Quine, R.W.; Meyer, V.; Newton, M.E.; Schnegg, A.; George, B.; Eaton, S.S.; Eaton, G.R., X-band rapid-scan EPR of samples with long electron spin relaxation times: A comparison of continuous wave, pulse, and rapid-scan EPR, *Mol. Phys.* **2013**, 111, 2664-2673.

Meyer, V.; Eaton, S.S.; Eaton, G.R., Temperature dependence of electron spin relaxation of 2,2-diphenyl-1-picrylhydrazyl in polystyrene, *Appl. Magn. Reson.* **2013**, 44, 509-517.

Biller, J.R.; Meyer, V.; Elajaili, H.; Rosen, G.M.; Eaton, S.S.; Eaton, G.R., Frequency dependence of electron spin relaxation times in aqueous solution for a nitronyl nitroxide radical and perdeuterated-tempone between 250 MHz and 34 GHz, *J. Magn. Reson.* **2012**, 225, 52-57.

Siddiqua, A.; Luo, Y.; Meyer, V.; Swanson, M.A.; Yu, X.; Wei, G.; Zheng, J.; Eaton, G.R.; Ma, B.; Nussinov, R.; Eaton, S.S.; Margittai, M., Conformational basis for asymmetric seeding barrier in filaments of three- and four-repeat tau, *J. Am. Chem. Soc.* **2012**, 134, 10271-10278.

Biller, J.R.; Meyer, V.; Elajaili, H.; Rosen, G.M.; Kao, J.P.Y.; Eaton, S.S.; Eaton, G.R., Relaxation times and line widths of isotopically-substituted nitroxides in aqueous solution at X-band, *J. Magn. Reson.* **2011**, 212, 370-377.

Mitchell, D.G.; Quine, R.W.; Tseitlin, M.; Weber, R.T.; Meyer, V.; Avery, A.; Eaton, S.S.; Eaton, G.R., Electron spin relaxation and heterogeneity of the 1:1 alpha,gamma-bisdiphenylene-beta-phenylallyl (BDPA)/benzene complex, *J. Phys. Chem. B.* **2011**, 115, 7986-7990.

Mitchell, D.G.; Quine, R.W.; Tseitlin, M.; Meyer, V.; Eaton, S.S.; Eaton, G.R., Comparison of continuous wave, spin echo, and rapid scan EPR of irradiated fused quartz, *Radiat. Meas.* **2011**, 46, 993-996.